Tuning the Physical and Optoelectronic Properties of Phosphorescent Iridium(III) Complexes: Applications to Organic Semiconductor Devices

St. Andrews

Adam Francis Henwood

May 23, 2017

Abstract

This thesis explores the design, synthesis and characterisation of iridium(III) complexes for optoelectronic applications; in particular, cationic $[Ir(C\hat{}N)_2(N\hat{}N)]^+$-type emitters (where C^N is an anionic bidentate cyclometalating ligand such as 2-phenylpyridinato, ppy, and N^N is a neutral bidentate ligand such as 2,2'-bipyridine, bpy) for use in light-emitting electrochemical cells (LEECs). Design strategies aim to achieve high photoluminescence quantum yields (Φ_{PL}) for these complexes.

Chapter 1 provides an overview of the fundamental photophysics of luminescent transition metal complexes, before reviewing state of the art iridium complexes employed in LEEC devices.

Chapter 2 employs a combination of the electron-deficient 2,4-difluorophenylpyridine (dFppy) C^N ligand and various functionalised biimidazole (biim) N^N ligands. Within the family of different biim ligands the emission energy does not vary significantly, but the excited state kinetics differ depending on the rigidity of the biim ligand. Combining the lead biim ligand with a sterically bulkier C^N ligand gives an iridium complex that emits deep blue light with 90% Φ_{PL} in MeCN.

Chapter 3 describes an approach to replacing the electrochemically unstable aryl carbon-fluorine bonds in dFppy, while maintaining the deep blue emission colour observed for the complexes in Chapter 2.

Chapter 4 expands on the concept of rigid biim ligands to bibenzimidazoles (bibenz). Combining conjugated bibenz N^N ligands with more conjugated C^N ligands allows for the emission colour of these complexes to be tuned to the orange/red. The Φ_{PL} necessarily falls due to the energy gap law, but is nevertheless higher than values measured for reference complexes.

Chapter 5 explores the use of an arylazoimidazole ligand with donor-acceptor intraligand

charge transfer characteristics in order to red-shift the emission further. The resultant complex is poorly emissive, but shows a panchromic absorption profile and high molar absorptivity, which is unusual for iridium(III) complexes. The absorption profile can be tuned as a function of the protonation state of the imidazole.

1. Candidate's declarations:

I, Adam Francis Henwood, hereby certify that this thesis, which is approximately 45,000 words in length, has been written by me, and that it is the record of work carried out by me, or principally by myself in collaboration with others as acknowledged, and that it has not been submitted in any previous application for a higher degree.

I was admitted as a research student in September, 2013 and as a candidate for the degree of PhD in September, 2013; the higher study for which this is a record was carried out in the University of St Andrews between 2013 and 2017.

(*If you received assistance in writing from anyone other than your supervisor/s*):
I, ….., received assistance in the writing of this thesis in respect of [language, grammar, spelling or syntax], which was provided by ……

Date 12/04/17 signature of candidate Adam Henwood

2. Supervisor's declaration:

I hereby certify that the candidate has fulfilled the conditions of the Resolution and Regulations appropriate for the degree of PhD in the University of St Andrews and that the candidate is qualified to submit this thesis in application for that degree.

Date 12/04/17 signature of supervisor Eli Zysman-Colman

3. Permission for publication: (*to be signed by both candidate and supervisor*)

In submitting this thesis to the University of St Andrews I understand that I am giving permission for it to be made available for use in accordance with the regulations of the University Library for the time being in force, subject to any copyright vested in the work not being affected thereby. I also understand that the title and the abstract will be published, and that a copy of the work may be made and supplied to any bona fide library or research worker, that my thesis will be electronically accessible for personal or research use unless exempt by award of an embargo as requested below, and that the library has the right to migrate my thesis into new electronic forms as required to ensure continued access to the thesis. I have obtained any third-party copyright permissions that may be required in order to allow such access and migration, or have requested the appropriate embargo below.

The following is an agreed request by candidate and supervisor regarding the publication of this thesis:

PRINTED COPY

~~a) No embargo on print copy~~

b) Embargo on all or part of print copy for a period of 1 years (maximum five) on the following ground(s):
   - Publication would be commercially damaging to the researcher, or to the supervisor, or the University
   - Publication would preclude future publication
   - Publication would be in breach of laws or ethics

~~c) Permanent or longer term embargo on all or part of print copy for a period of … years (the request will be referred to the Pro-Provost and permission will be granted only in exceptional circumstances).~~

Supporting statement for printed embargo request if greater than 2 years:

ELECTRONIC COPY

~~a) No embargo on electronic copy~~

b) Embargo on all or part of electronic copy for a period of 1 years (maximum five) on the following ground(s):
   - Publication would be commercially damaging to the researcher, or to the supervisor, or the University
   - Publication would preclude future publication
   - Publication would be in breach of law or ethics

~~c) Permanent or longer term embargo on all or part of electronic copy for a period of … years (the request will be referred to the Pro-Provost and permission will be granted only in exceptional circumstances).~~

Supporting statement for electronic embargo request if greater than 2 years:

ABSTRACT AND TITLE EMBARGOES

An embargo on the full text copy of your thesis in the electronic and printed formats will be granted automatically in the first instance. This embargo includes the abstract and title except that the title will be used in the graduation booklet.

If you have selected an embargo option indicate below if you wish to allow the thesis abstract and/or title to be published. If you do not complete the section below the title and abstract will remain embargoed along with the text of the thesis.

a) I agree to the title and abstract being published YES
b) I require an embargo on abstract NO
c) I require an embargo on title NO

Date 12/04/17 signature of candidate Adam Francis Henwood signature of supervisor Eli Zysman-Colman

Please note initial embargos can be requested for a maximum of five years. An embargo on a thesis submitted to the Faculty of Science or Medicine is rarely granted for more than two years in the first instance, without good justification. The Library will not lift an embargo before confirming with the student and supervisor that they do not intend to request a continuation. In the absence of an agreed response from both student and supervisor, the Head of School will be consulted. Please note that the total period of an embargo, including any continuation, is not expected to exceed ten years.
Where part of a thesis is to be embargoed, please specify the part and the reason.

Declaration

I fully acknowledge that the work presented herein is my own. However, the nature of the research undertaken during my PhD is highly interdisciplinary, and thus contributions from collaborators and co-authors are listed below.

Chapter 1: I am the primary author of the text. Major aspects of this text have been published:

1. Adam F. Henwood and Eli Zysman-Colman, *Top. Curr. Chem.*, 2016, **374**, 1.

2. Adam F. Henwood and Eli Zysman-Colman, *Chem. Commun.*, 2017, **53**, 807.

Chapter 2: Synthesis was carried out by me and Dr. Sloane Evariste. The spectroscopy described in this chapter was performed by me. All of the data analysis was carried out by me. The NMR temperature studies were carried out by Melanja Smith. Single crystal data collection and structure solving was performed by Prof. Alexandra M. Z. Slawin (complexes **64** and **66**) and Dr. David B. Cordes (complexes **14**, **68** and **69**). Density Functional Theory (DFT) calculations were carried out by Dr. Eli Zysman-Colman. Light-Emitting Electrochemical Cells (LEECs) were fabricated by Dr. Antonio Pertegas Ojeda in the group of Dr. Henk Bolink. Organic Light-Emitting Diodes (OLEDs) were fabricated by Dr. Ashu K. Bansal in the group of Prof. Ifor D. W. Samuel. I am the primary author of the text. The work described in this chapter has been published:

1. Adam F. Henwood, Sloane Evariste, Alexandra M. Z. Slawin and Eli Zysman-Colman, *Faraday Discuss.*, 2014, **174**, 165.

2. Adam F. Henwood, Ashu K. Bansal, David B. Cordes, Alexandra M. Z. Slawin, Ifor D. W. Samuel, Eli Zysman-Colman, *J. Mater. Chem. C*, 2016, **4**, 3726.

Chapter 3: Synthesis of the organic ligands and iridium(III) dimers was performed by Tomas W. Rees in the group of Dr. Etienne Baranoff. Synthesis of the cationic iridium(III) complexes was performed by me. Spectroscopy described in this chapter was performed

by me. The NMR temperature studies were carried out by Melanja Smith. Single crystal data collection and structure solving was performed by David. B. Cordes. LEECs were fabricated by Maria Cristina Momblona Rincon and Dr. Antonio Pertegas Ojeda in the group of Dr. Henk Bolink. I am the primary author of the text.

Chapter 4: Synthesis of the organic ligands and iridium(III) dimers was performed by me, Megane Morin, Diego Rota Martir and Daniel Anton Garcia. Synthesis of the cationic iridium(III) complexes was performed by me and Daniel Anton Garcia. Spectroscopy described in this chapter was performed by me and Daniel Anton Garcia. The NMR temperature studies were carried out by Melanja Smith. Single crystal data collection and structure solving was performed by David. B. Cordes. DFT calculations were carried out by Prof. Michael Buehl. I am the primary author of the text.

Chapter 5: Synthesis of the organic ligand and was performed by Dr. Yue Hu in the group of Prof. Neil Robertson. Synthesis of the iridium(III) complexes was performed by me. The spectroscopy described in this chapter was performed by me and Dr. Muhammad T. Sajjad in the group of Prof. Ifor D. W. Samuel. DFT calculations were performed by Dr. Yue Hu in the group of Prof. Neil Robertson. Organic photovoltaic (OPV) devices were fabricated by Dr. Gopala K. V. V. Thalluri and Dr. Sanjay S. Ghosh in the group of Prof. Ifor D. W. Samuel. Single crystal data collection and structure solving was performed by David. B. Cordes. I am the primary author of the text. The work in this chapter has been published:

1. Adam F. Henwood, Yue Hu, Muhammad T. Sajjad, Gopala Krishna V. V. Thalluri, Sanjay S. Ghosh, David B. Cordes, Alexandra M. Z. Slawin, Ifor D. W. Samuel, Neil Robertson, Eli Zysman-Colman, *Chem. Eur. J*, 2015, **21**, 19128.

Acknowledgements

Isaac Newton is often credited with standing on the shoulders of giants, but Wikipedia reliably informs me that the tosaphist Isaiah di Trani (c. 1180 – 1250) spoke well before him on this matter:

> Who sees further: a dwarf or a giant? Surely a giant, for his eyes are situated at a higher level than those of the dwarf. But if the dwarf is placed on the shoulders of the giant, who sees further? So too we are dwarfs astride the shoulders of giants. We master their wisdom and move beyond it. Due to their wisdom we grow wise and are able to say all that we say, *but not because we are greater than they.*

I would go further: in life, we are a culmination of actions and people who have come before us. My own PhD has been no different. It only exists because of the people who have directly and indirectly touched my life in the last three and half years. Thus I hope not to miss anyone out who has helped me through my journey.

So many people inside and outside St. Andrews need to be thanked. Firstly, I have to thank Dr. Eli Zysman-Colman, who under surprising circumstances, brought me to St. Andrews rather than Canada, and has worked tirelessly to provide me with the help and support I needed throughout my time here.

Thank you to all of the St. Andrews chemistry staff, in the stores or in the services: in particular, Dr. David B. Cordes and Prof. Alexandra M. Z. Slawin for X-ray crystallography and Melanja Smith and Dr. Tomas Lebl for NMR. Thank you also to the many collaborators on the various projects I have worked on: Tomas Rees and Dr. Etienne Baranoff for various chemistry projects; Dr. Yue Hu and Prof. Neil Robertson for the panchromic absorption project; Dr. Ashu Bansal and Prof. Ifor D. W. Samuel for the OLEDs; Dr. Antonio Pertegas Ojeda and Dr. Henk Bolink for the LEECs.

With each year I have spent in St. Andrews, countless colleagues and friends have come and gone that I have to thank. My first year began by counting glassware in the lab, but thanks to Martin Donaldson, Cameron O'Brien, Bec Spicer and Sarah Flook this changed to nights getting lost in the Union (and of course the Lizard) and black tie functions. Dr. Nail Shavaleev's arrival led to the invention of the Friday evening routine of well-done steak and tea at the Grill House, followed by beer at the Criterion. My second year saw the second PhD cohort join the group: Diego Rota Martir and Claus Hierlinger (the original 'Polads'). Thank you to these guys, as well as Mark Huyton and Mattia (number 1) Averardi for helping me discover the joys and dangers of lab darts. Finally, the latest batch of people to make their way through the group: Laura Abad Galan (who despite protesting to the contrary, was definitely one of the guys) Dave Hall (who was unequivocally not one of the guys), Nidhi Sharma (who cooked great food), Ben Armitage (who was the greatest Yorkshire member the group ever had) and Mattia (number 2) Fontani. You are all great guys, and it was my pleasure to work with you. Thank you also to the rest of the EZC group for our great time together. I wish you all the best.

Closer to home, I need to thank all of my family. The Henwood family motto '*justus esto et non metue*' loosely translates as '*be just and fear not*' and these are principles that my family have strived to instil in me since I was a child. In following my pursuits, my parents have always been supportive even when things have not been easy, and I have a brother who made no emotional contributions to my PhD, but whose more lucrative career aspirations have made him somewhat of my financial backer during this period of my life. My extended South African family have always cheered me from the sidelines, so I thank all of them as well.

Finally, Sarah: I met her in an office in September 2013 as a project student, and tried to look cool while stacking textbooks, and now in April 2017 she is still with me: the most important person in my life. During my time in St. Andrews we have been through a lot together, from the aforementioned adventures in the Lizard, the Union and Winter/Grad/Other Balls, to trekking around Eastern Europe and the rural parts of the Kingdom of Fife. You are the only one who has been there throughout, putting up with my potato-ishness, my sending you photos of other random dogs and occasionally my doing a PhD as well. Thank you.

Contents

Abbreviations, Acronyms and Terminology

Acronym	**Expansion**
Alq_3	(tris(8-hydroxyquinolinato)aluminium(III)
Ar-BIAN	bis(iminoarylacenaphthene)
bpy	2,2'-bipyridine
CBP	4,4'-bis(*N*-carbazolyl)-1,1'-biphenyl
CE	Current Efficiency
CFL	Compact Fluorescent Lighting
CIE	Commission Internationale de l'Eclairage
Cp*	pentamethylcyclopentadienyl
CT	Charge Transfer
CV	Cyclic Voltammetry
D-A	Donor-Acceptor
DCM	Dichloromethane
dFMesppy	2-(2,4-difluorophenyl)-4-(2,4,6-trimethylphenyl)pyridinato
dFppy	2-(2,4-difluorophenyl)-pyridinato
DFT	Density Functional Theory
dMebibenz	1,1'-dimethyl-2,2'-bibenzimidazole
dMebiim	1,1'-dimethyl-2,2'-biimidazole
DOTCI	3,3'-diethyl-2,2'-oxathiacarbocyanine iodide
DSSC	Dye-Sensitised Solar Cell
dtbubpy	4,4'-di-*tert*-butyl-2,2'-bipyridine
EA	Elemental Analysis

Acronym	**Expansion**
EBL	Electron Blocking Layer
ECL	Electrochemiluminescence
EL	Electroluminescence
EQE	External Quantum Efficiency
ETL	Electron Transport Layer
Fc	Ferrocene
HBL	Hole Blocking Layer
HG	Host-Guest
HIL	Hole Injection Layer
HOMO	Highest Occupied Molecular Orbital
HRMS	High Resolution Mass Spectrometry
HTL	Hole Transport Layer
H_2bibenz	1,1'-(1*H*,1'*H*)-2,2'-bibenzimidazole
H_2biim	1,1'-(1*H*,1'*H*)-2,2'-biimidazole
IC	Internal Conversion
IL	Ionic Liquid
IQE	Internal Quantum Efficiency
IR	Infrared
ISC	Intersystem Crossing
ITO	Indium Tin Oxide
iTMC	Ionic Transition Metal Complex
k_{nr}	non-radiative rate constant
k_r	radiative rate constant
LC	Ligand-Centred
LED	Light-Emitting Diode
LEEC	Light-Emitting Electrochemical Cell
LLCT	Ligand-to-Ligand Charge Transfer
LMCT	Ligand-to-Metal Charge Transfer
LUMO	Lowest Unoccupied Molecular Orbital
MC	Metal-Centred

Acronym	**Expansion**
mCP	1,3-Bis(*N*-carbazolyl)benzene
Mesppy	2-phenyl-4-(2,4,6-trimethylphenyl)pyridinato
Mesnpy	2-(naphthalen-1-yl)-4-(2,4,6-trimethylphenyl)pyridinato
MLCT	Metal-to-Ligand Charge Transfer
MO	Molecular Orbital
NHC	*N*-Heterocyclic Carbene
OECD	Organisation for Economic Co-operation and Development
OLED	Organic Light-Emitting Diode
OPV	Organic Photovoltaic
OXD7	1,3-bis(5-(4-(*tert*-butyl)phenyl-1,3,4-oxadiazol-2-yl)benzene
o-Xylbibenz	1,1'-(α,α'-*o*-Xylylene)-2,2'-bibenzimidazole
o-Xylbiim	1,1'-(α,α'-*o*-Xylylene)-2,2'-biimidazole
P3HT	Poly(3-hexylthiophen-2,5-diyl)
PCET	Proton-Coupled Electron Transfer
PEDOT:PSS	Poly(3,4-ethylenedioxythiophene)polystyrene sulfonate
PL	Photoluminescence
PLEEC	Polymer Light-Emitting Electrochemical Cell
PMMA	Poly(methylmethacrylate)
ppy	2-phenylpyridinato
PtOEP	Octaethylporphyrinplatinum(II)
PVK	Poly(9-vinylcarbazole)
Φ_{PL}	Photoluminescence Quantum Yield
SCE	Saturated Calomel Electrode
S_n	n^{th} Singlet State
SOC	Spin-Orbit Coupling
SSL	Solid-State Lighting
$t_{1/2}$	Device lifetime
TADF	Thermally Activated Delayed Fluorescence
TDDFT	Time-Dependent Density Functional Theory
T_n	n^{th} Triplet State

Acronym	**Expansion**
t_{on}	Device turn-on time
TPBI	1,3-bis(5-(4-(*tert*-butyl)phenyl-1,3,4-oxadiazol-2-yl)benzene
TTA	Triplet-Triplet Annihilation
UV	Ultraviolet
WOLED	White Organic Light-Emitting Diode
X^Y	Bidentate Ligand
ξ	Spin-Orbit Coupling Constant
z	Atomic Number

Chapter 1

Phosphorescent Transition Metal Complexes

Since Paris and Brandt's seminal report[1] observing phosphorescence from the now famous complex, tris(2,2'-bipyridyl)ruthenium(II) dichloride $[Ru(bpy)_3]Cl_2$ (Figure 1.1), phosphorescent transition metal complexes have consistently stimulated academic interest. The rich photophysical properties of such materials has led to their use in a wide range of applications.[2–9] For example, their light absorbing capabilities have made these complexes favourable choices for applications in solar cells,[10] as photocatalysts for both inorganic[11] and organic[8;12] reactions, as sensitizers for energy and electron transfer[13–15] and for use in light operated nanotechnologies,[16] such as molecular wires,[17;18] switches[19] and molecular motors.[20;21] On the other hand, and equally as important, these complexes can also be highly emissive and thus of interest for light emitting devices,[9;22;23] as biological probes[24] and in sensors.[25]

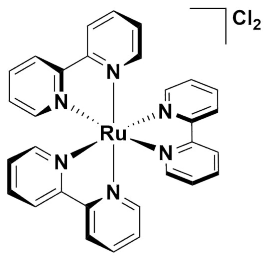

1

Figure 1.1: The first phosphorescent transition metal complex reported.[1]

Unlike many first row transition complexes, where the electronic states are typically 'metal-centred' (MC) in nature, second and third row complexes such as $[Ru(bpy)_3]Cl_2$ display symmetry-allowed electronic transitions such as metal-to-ligand charge transfer (MLCT) states which are low energy and highly absorptive in nature.[10;26] Furthermore, the high spin-orbit coupling (SOC) constants displayed by second and third row complexes enables the relaxation of the spin selection rule, which allows for efficient emission from the triplet state, making them powerful alternatives to conventional organic molecules which mostly only undergo emission from the singlet state.[27] Since these excited state processes underpin these highly desirable properties, an understanding of how they arise is crucial for providing the basis for exploring them in detail. Thus, in this first chapter a molecular orbital (MO) theory approach will be used to explain the light absorption and then light emission processes, highlighting the important kinetic considerations that underpin these processes. This MO description will allow for an explanation as to the importance of the

choice of metal, outlining why iridium(III) complexes have been explored most widely as the phosphor of choice for artificial lighting applications. Having established the choice of metal, this chapter will give a brief outline of different types of lighting device, before reviewing strategies for optimising different properties (emission colour, solubility, photoluminescence quantum yield) of these complexes for their use in devices.

1.1 Photophysics of Coordination Compounds

1.1.1 MO Theory and Light Absorption

In the simplest example of an octahedral transition metal complex of the form ML_6, such as $[Fe(NH_3)_6]^{2+}$, the six coordinating ligands are purely σ-donating in nature. In this case the ligands decrease the five-fold degeneracy of the valence d-orbitals for a theoretical gas phase metal ion into two sets of orbitals in a fashion illustrated by Figure 1.2.[10] Two orbitals ($d_{x^2-y^2}$ and d_{z^2}) of e_g symmetry are doubly degenerate, and are destabilised in energy by an antibonding interaction with the ligand σ-orbitals. The three triply degenerate orbitals of t_{2g} symmetry (d_{xy}, d_{xz} and d_{yz}) are formally non-bonding in nature and thus do not change in energy upon formation of the complex. Considering the electron distribution in the system, the t_{2g} orbitals constitute the Highest Occupied Molecular Orbitals (HOMOs), and thus the e_g orbitals comprise Lowest Unoccupied Molecular Orbitals (LUMOs). This results in a lowest energy optical transition that can be classified as 'MC' in nature.

Although metal character in an electronic transition is often beneficial (as will be discussed below), MC transitions in centrosymmetric molecules are forbidden by the Laporte symmetry selection rule. Therefore, these transitions are only possible as a result of ligand induced fluxional distortions about the metal centre, resulting in molar absorptivities of these transitions being very low ($\epsilon < 100$ M^{-1} cm^{-1}). Furthermore, these states result in population of anti-bonding $e_g{}^*$ orbitals. This incurs structural distortions in the excited state that lead to rapid non-radiative decay of the excited state by processes such as vibrations, thereby drastically reducing the efficiency of any competing emissive processes.[10] This is a critical issue for many phosphorescent transition metal complexes, and suppressing this phenomenon is a key theme of much of the work that will be discussed in this thesis.

Changing the nature of the HOMO-LUMO transition can be achieved by introducing ligands with vacant orbitals of π-symmetry, such as $[Co(CN)_6]^{3-}$ (Figure 1.3). In this case,

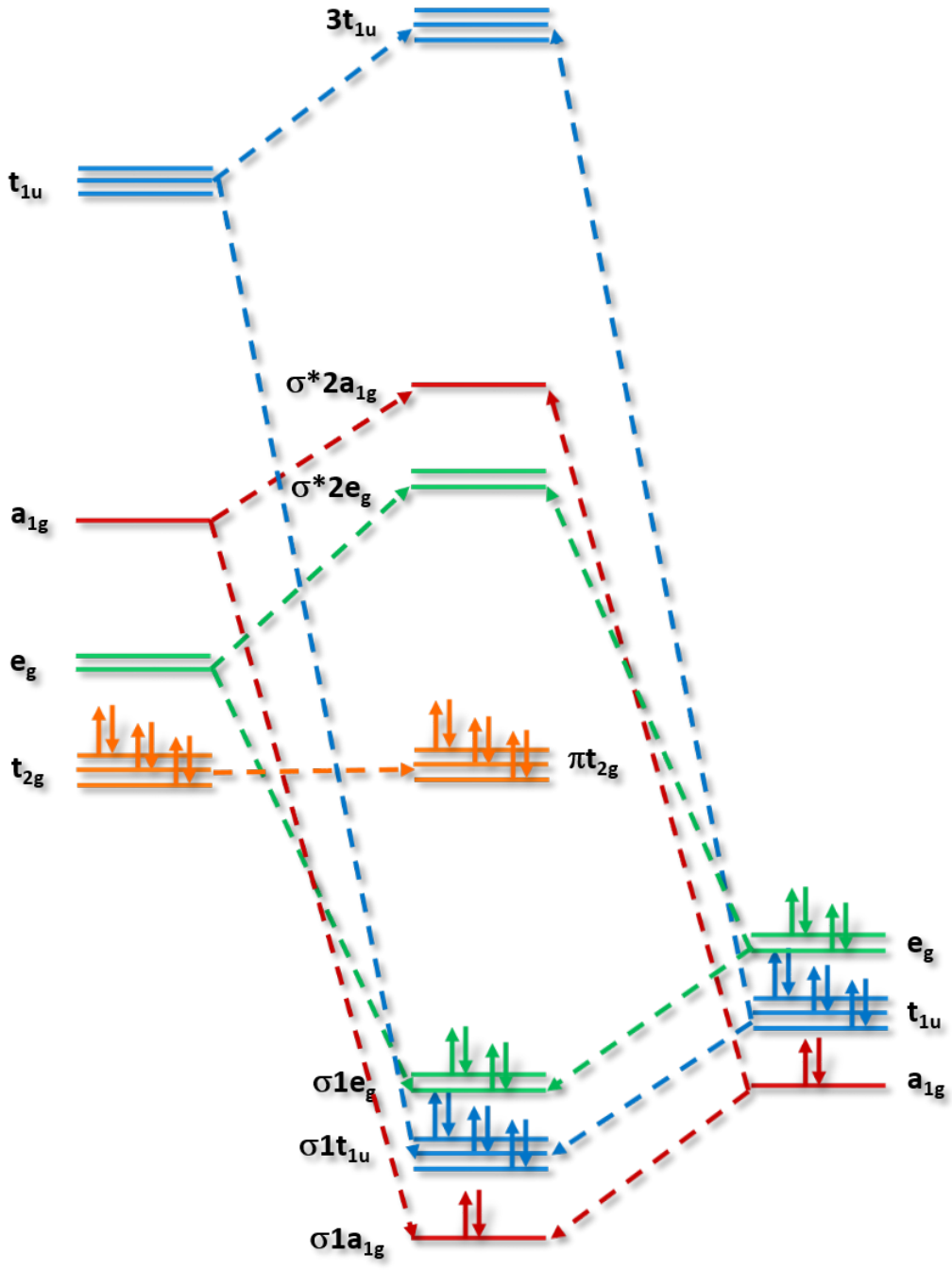

Figure 1.2: MO diagram for a first row transition metal complex containg purely σ-donating ligands such as $[Fe(NH_3)_6]^{2+}$.

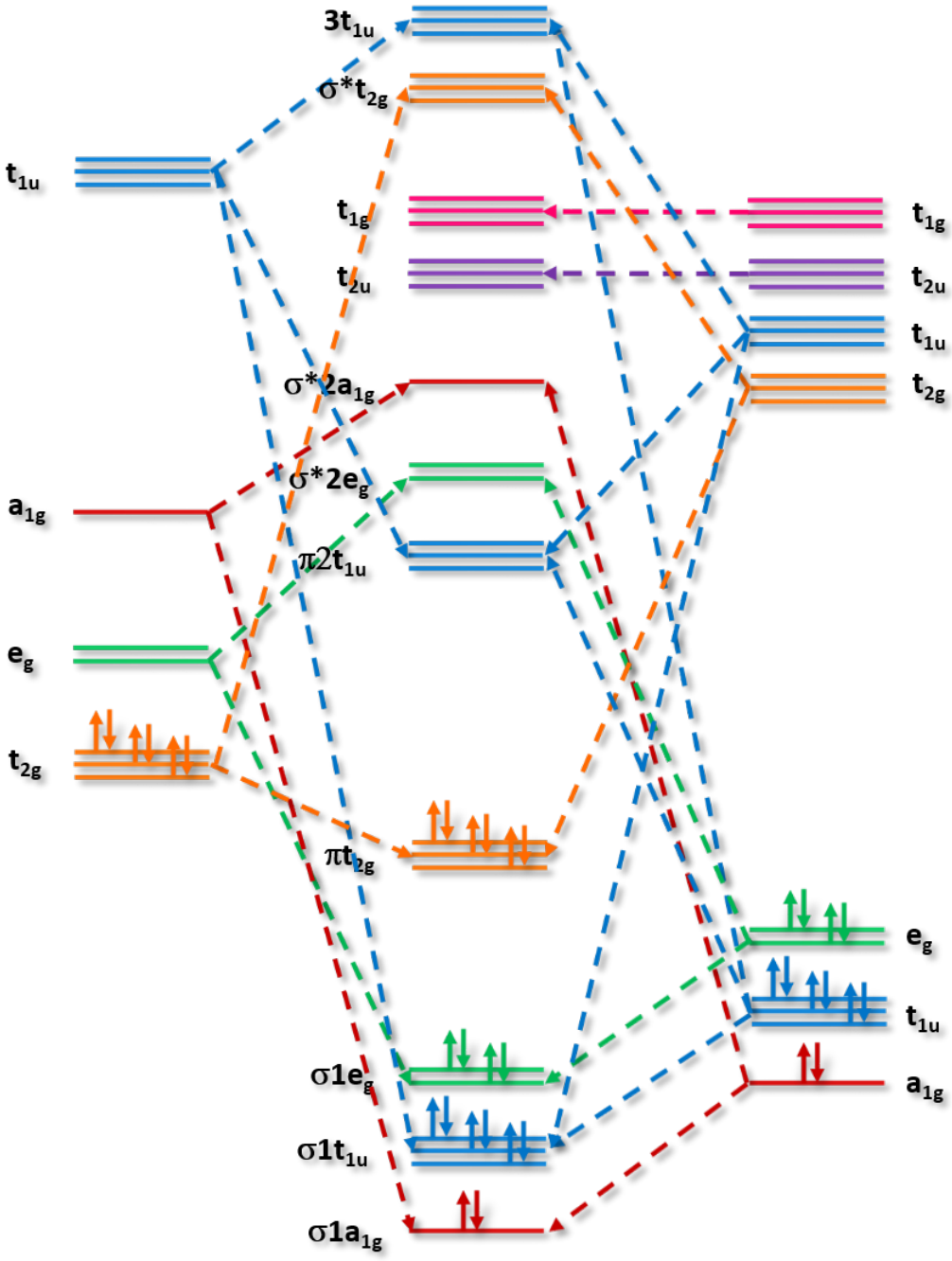

Figure 1.3: MO diagram for a first row transition metal complex containg ligands with vacant orbitals orbitals of π-symmetry, such as $[Co(CN)_6]^{3-}$.

two crucial differences become apparent in the MO diagram: 1) the new set of ligand based t_{2g} orbitals are π-acids, and thus can form a bonding interaction with their previously non-bonding metal based counterparts, stabilising their energy and thus tuning the energy of the HOMO, and 2) the ligand based t_{1u} orbitals lead to the formation of a new set of π-molecular orbitals which, depending on the nature of the ligands, can be lower in energy than the e_g orbitals and thus constitute the LUMO. In this example, the HOMO-LUMO transition is formally an MLCT state. This interaction can be tuned further by varying the ligands, which modulates the electronics of the system. This is the underlying principle behind tuning the emission colour of these complexes.[28;29]

In addition to MC and MLCT states, two other important states to be aware of are ligand-to-metal charge transfer (LMCT) and ligand-centred (LC) transitions. These transitions are summarised in a simplified schematic in Figure 1.4.[28] By comparison to symmetry-forbidden MC states, there are no symmetry restrictions on these other states, and thus they are generally highly absorptive. LC states are localised transitions between energy levels of the same π-networks, and tend to be the most absorptive of the different kinds of transitions. However, since they are localised in similar regions of the molecule, they incur strong exchange interactions which means that their absorption bands tend to be much higher in energy than charge transfer (CT) states (residing in the blue to near-ultraviolet, near-UV, region). CT states, while symmetry allowed, require the movement of the electron from one region of the molecule to another and thus generally occur with lower extinction coefficients than LC-type transitions, but with the caveat of covering lower energies of the absorption spectrum. These bands therefore are crucial for the design of light absorbing materials. From an emission standpoint, all three of these types of states crucially do not incur the same unfavourable excited state distortions exerted by MC states, and thus they can all exhibit luminescence.

1.1.2 The Jablonski Diagram and Light Emission

We have seen how the relative ordering of the orbitals can be modulated by modifying the ligands, and how this can change the nature of the lowest energy transition and thus the nature of absorption. How then, following light absorption, does luminescence occur? The majority of molecules exist in a singlet ground state (S_0), where the electronic configuration is such that the number of electrons in the molecule of one spin orientation match that of the opposing spin orientation.[30] When these molecules absorb a quantum of light corresponding

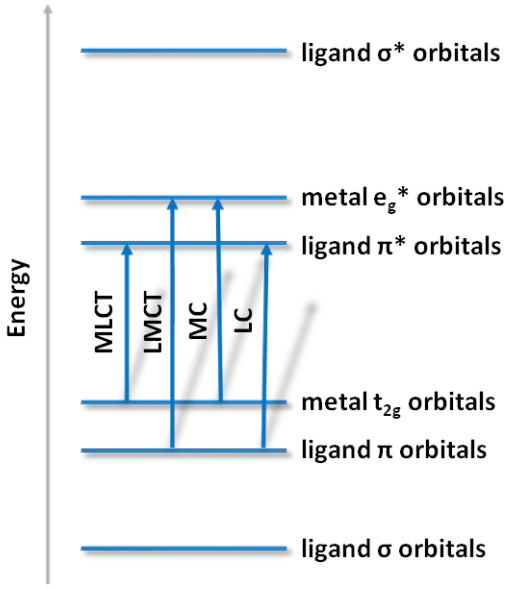

Figure 1.4: Simplified energy diagram showing different states that can characterise a complex. MC states are not desirable when designing luminescent emitters.[28]

to a specific energy, an electron may undergo an electronic excitation, usually from the HOMO, to a higher energy level to generate a singlet excited state (S_n).[31] Kasha's rule states that this is followed by the excited molecule rapidly relaxing to the metastable, lowest singlet exited state (S_1) via non-radiative vibrational decay pathways termed internal conversions (IC) – a process that occurs on a timescale much faster than that of any competing processes.[32] This metastable state may then deactivate back to the ground state via further IC processes, or via an emission process adhering to the spin selection rule ($\Delta S = 0$ for an electronic transition) whereby the excited electron, in anti-parallel spin to the ground state electron, relaxes back to the ground state with concomitant photon emission. When emission is not prohibited by the spin selection rule, this process is termed '*fluorescence*'. These excited state processes are summarised schematically in the Jablonski energy diagram (Figure 1.5).

Considering these phenomena kinetically, each process can be described in terms of rate constants. Typically, the most important rate constant is the rate constant of radiative decay (k_r), which quantifies the rate at which a molecule in its excited state relaxes back to the ground state by the process of emitting light. Since all other processes are (normally) non-emissive, they are typically described by the rate constant of non-radiative decay (k_{nr}), which is a summation of the rate constants of all other processes that can lead to

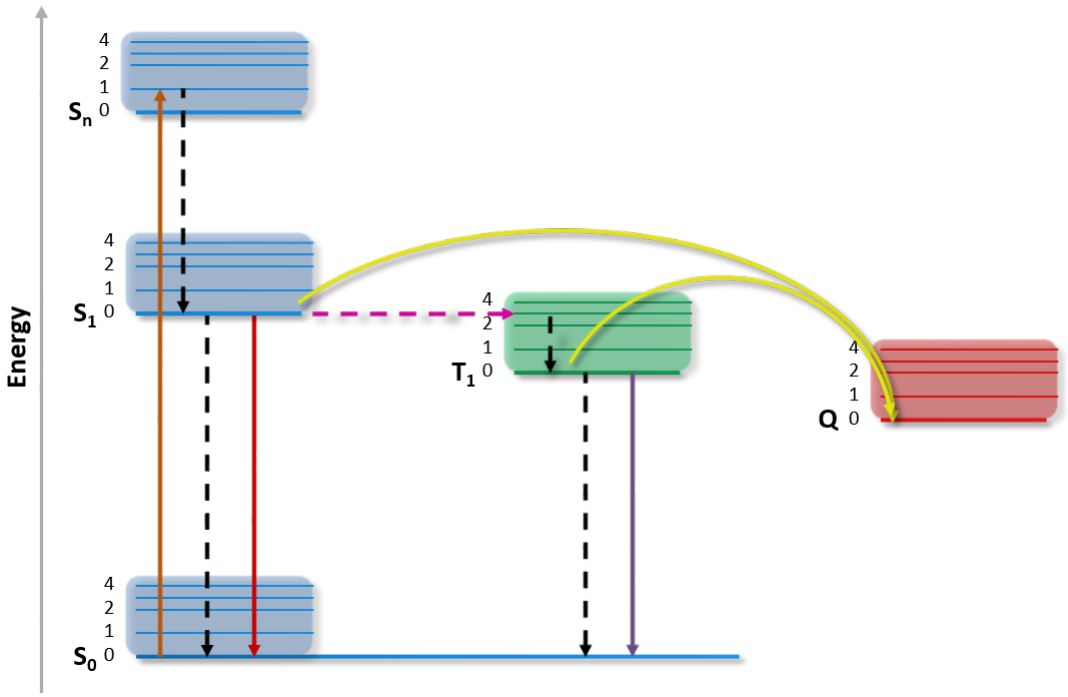

Figure 1.5: Jablonski diagram showing possible excited state kinetic processes for a photophysically active transition metal complex following absorption (orange) to an excited singlet state (blue, S_n): internal conversions (black dashed arrows, IC), fluorescence (red arrow), excited state quenching by energy or electron transfer (yellow arrow) to a quenching species (Q), intersystem crossing (pink dashed arrow, ISC), the excited triplet states (green, T_n) and phosphorescence (purple arrow).[31]

deactivation of the excited state. The most important information that can be gleaned from these values is the photoluminescence quantum yield, Φ_{PL}, which is calculated as the ratio of k_r over all possible excited state processes. Practically, this number quantifies the ratio of photons emitted by the chromophore to photons absorbed, allowing for the efficiency of the emitter to be quantified. A number as close to one as possible is desired, and is achieved by maximising k_r while simultaneously restricting k_{nr}.[33]

$$\Phi_{\mathrm{PL}} = \frac{k_r}{k_r + k_{nr}}$$

Although the situation describing fluorescence is useful for many conjugated organic molecules, it is not necessarily applicable in situations where a (heavy) metal is incorporated into the system. To understand this, we must consider SOC effects.[27;34] For heavy atoms, the high charge on the atomic nucleus exerts significant force on the orbiting electrons, resulting in the orbital motion of the electrons becoming so fast that they interact with

their own spin. In these situations, total orbital angular momentum is conserved during an electronic transition even when the spin state is changed. Practically, this means that the spin selection rule forbidding emission from different spin states, such as T_1 to S_0 (termed '*phosphorescence*'), becomes relaxed.[33]

SOC does this in two ways. Firstly, direct population of the T_1 state from the S_0 ground state is highly forbidden (even in high SOC environments) and much less probable than excitation to an excited singlet state. However, SOC processes circumvent this barrier by efficiently converting S_1 states into T_1 states by spin flipping in a process called intersystem crossing (ISC). This process occurs for all molecules, but with molecules exerting significant SOC effects, such as heavy metal complexes, ISC occurs at much faster rates than any competing processes, allowing for efficient population of the T_1 state over other processes.[35] In fact, for heavy transition metal complexes such as iridium and platinum, ISC is assumed to be so efficient that all S_1 states generated upon excitation are assumed to be converted to the T_1 state before they can undergo fluorescence, in spite of the competing fluorescence process being formally spin allowed. This allows for the approximation that the equation describing the Φ_{PL} of fluorescent molecules is also applicable to phosphorescent molecules, even though this ignores other possible competing effects.

Once the T_1 state is populated, SOC is also important for enabling relaxation back to the ground state to occur. SOC effects induce coupling between the various ^{3}MLCT substates and their corresponding higher energy ^{1}MLCT states, imbuing them with some singlet character such that $\Delta S \neq 0$ and thus relaxing the spin selection rule otherwise forbidding the transition to occur.[34] Yersin and co-workers have shown that at low temperatures, emission can be observed from each individual ^{3}MLCT substate.[36] However, at room temperature, thermal equilibration between the three substates means that emission is only observed from the substate that couples most efficiently to a higher lying ^{1}MLCT state, implying that it is the 'least forbidden' transition. This also explains the importance of the excited state retaining a high degree of MLCT character, as a transition that is predominantly LC in nature requires SOC to indirectly perturb the ^{3}MLCT states to relax the spin selection rule. As a result, pure ^{3}LC states can have extraordinarily long lifetimes (100s of μs or even more).[33] This is a generally undesirable feature for emitters for lighting applications.

Heavy metals, therefore, are vital to achieving efficient phosphorescence and thus the

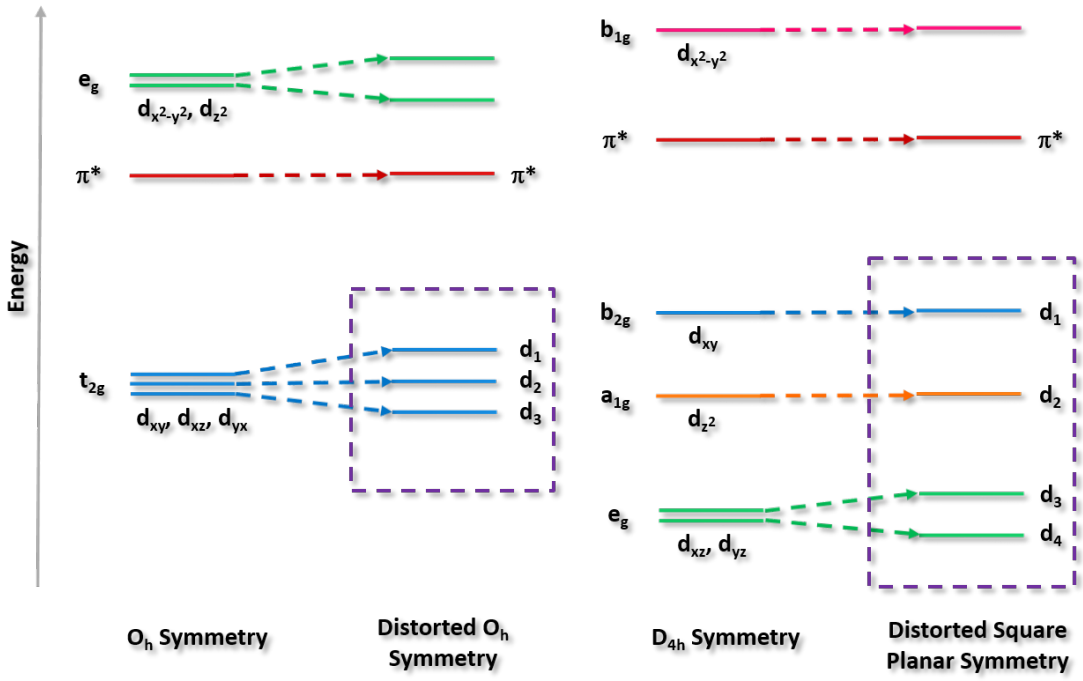

Figure 1.6: Energy diagram showing the splitting of O_h and D_{4h} systems into lower symmetry states. The purple frames highlight filled orbitals for pseudo-octahedral and pseudo-square planar systems, and illustrate the greater energy differences between the d_n states of the pseudo-square planar systems over the corresponding pseudo-octahedral analogues.

choice of metal is crucial to this end. Since SOC essentially governs k_r, maximising SOC will inevitably lead to a more efficient system. As stated, SOC is stronger for heavier metals; in fact, the SOC constant, ξ, is proportional to z^4 (where z is the atomic number) and thus generally speaking heavier elements exert SOC more efficiently. Of d-block metals, the highest SOC constants are 3909 cm^{-1} for iridium, 4480 cm^{-1} for platinum and 5104 cm^{-1} for gold, so it is unsurprising that many complexes based on these metals are highly luminescent.[28] However, although the value of ξ is important, it does not necessarily translate to efficient SOC coupling between singlet and triplet substates. In fact, it has been shown that despite the higher ξ value for platinum over iridium, platinum(II) complexes invariably show lower k_r values than iridium(III) when comparable ligands systems were studied. This can be understood by considering the differences in electronic configurations between octahedral and square planar systems. As mentioned, SOC couples ^{3}MLCT substates of various filled orbitals with higher energy ^{1}MLCT substates *of those states*. The

feasibility of coupling these states is directly related to the energy differences between the different filled ^{3}MLCT substates; smaller energy gaps promote more efficient SOC. From Figure 1.6, it is clear that the energy differences associated with pseudo-octahedral systems are much smaller than the corresponding differences for pseudo-square planar systems. Thus octahedral systems are generally more desirable in order to maximise SOC and thus maximise Φ_{PL}. This is perhaps the premier reason for why iridium(III) complexes are the most extensively employed phosphors in solid-state lighting (SSL) applications.[33;34]

1.2 Solid-State Lighting

Tackling the energy crisis is an increasingly pressing issue, with the need for improving our energy situation becoming increasingly pressing: the 2008 Climate Change Act stipulated that in the UK alone, an 80% reduction in greenhouse emissions from the 1990 baseline must be achieved by 2050. This is an astonishing undertaking, especially considering that since 1990, total energy consumption in OECD (Organization for Economic Co-operation and Development) countries, which includes the UK, has increased by approximately 25%.

Perhaps surprisingly, one of the biggest contributors to this enormous energy cost is artificial lighting. In 2008 artificial lighting constituted 20% of total electrical consumption in the United States,[37] while worldwide this figure is at 19%.[38] Even more concerning is that these numbers are set to increase in line with the growing worldwide population and the rapid economic development of countries like India and China; estimates suggest that global demand for artificial lighting by 2030 will be 80% higher than current consumption levels.[38]

The two possible strategies for curbing this increase in electricity consumption are either to improve the performance of alternative energy sources, or to improve the energy efficiency of current energy consuming technologies. In the former example, there is still scope for improvement in technologies such as solar cells,[39] particularly with regards to young technologies such as perovskite solar cells.[40] These technologies may possibly solve this problem in the long term, but in the short-to-medium term, it might be more desirable to improve the efficiencies of current energy consuming technologies, such as lighting.

Aside from the large energy consumption attributable to artificial lighting, the need for improving its efficiency becomes apparent when compared to other technologies. Indeed, many typical electrical devices such as ovens, toasters and electric motors operate at

efficiencies of greater than 70%, while incandescent light bulbs convert just 5% of energy into visible light.[38] Despite EU regulations banning incandescent bulbs, the current alternative of compact fluorescent lighting (CFL), still only offers efficiencies of about 20%.[38] In fact, even with lighting that is 'energy efficient', the consumption of energy for this basic need is so vast, and still so astonishingly inefficient, that the development of a truly efficient, cheap lighting source would arguably impart a greater impact on world energy consumption in the short to medium term than any other area. Illustrating this point, estimates indicate that adoption of lighting that is 50% efficient would reduce electrical consumption for lighting by 62% and total energy consumption in the USA by 13%.

1.2.1 Organic Light-Emitting Diodes

In addressing this need for increased efficiency, solid-state lighting (SSL) technology has come to the fore. SSL broadly refers to a lighting device that operates through injection of excess holes and electrons, by electrodes, into opposite ends of a solid semiconducting emissive layer. These holes and electrons may then diffuse through the material and recombine with the release of energy as light.[41;42] The ramifications of this process are significant, since it offers the potential for achieving truly 'cold' light, with photon emission being the *principal result* of the device mechanism, rather than a by-product of another dominating mechanism as is the case for incandescence.[23;43]

Two broad classes of SSL exist: inorganic light-emitting diodes (LEDs) and organic light-emitting diodes (OLEDs).[37;38] LEDs are composed of very thin crystalline layers of emissive ternary or quaternary alloys, such as AlGaAs, InGaN or AlGaInP, sandwiched between p-type and n-type binary layers.[41] These binary layers, usually composed of gallium nitride (GaN), act as electron shuttles, injecting electrons (n-type) and holes (p-type) into the emissive layers.[42] The wavelength of light emitted is dictated by the bandgap of the emissive material. Since the bandgap can be modulated as a function of the layer thickness, the emission colour can thus be easily tuned.[38]

Their simple design, exceptional colour tunability and high luminous efficiencies has meant that LEDs have shown exceptional promise as the leading candidate to usurp CFL as the dominant lighting technology.[38;43] However, challenges exist for these materials. A trade-off between surface area and power density exists for this technology that as of yet has limited its potential for industrial scale lighting.[42] Additionally, displays are constructed

from point light sources, rather than a single emitting layer across the display, making glare an issue. Finally, the materials used for these devices are not environmentally friendly, and thus there is a push towards adopting the use of greener materials.[38]

Consequently, of great current academic and commercial interest is the organic complement to LEDs: OLEDs. These devices have a number of advantages over LEDs and other lighting sources: their use of semiconducting plastic materials means that OLED devices can be rollable, flexible, foldable and highly portable, while retaining their functionality even when mechanical stress is applied;[44] they are an innate surface-emitting light source, and thus can be formed on any substrate such as glasses, ceramics and metals, which may lead to interesting design products such as OLED windows;[45;46] finally, their materials are environmentally benign and relatively cheap.[38;46;47]

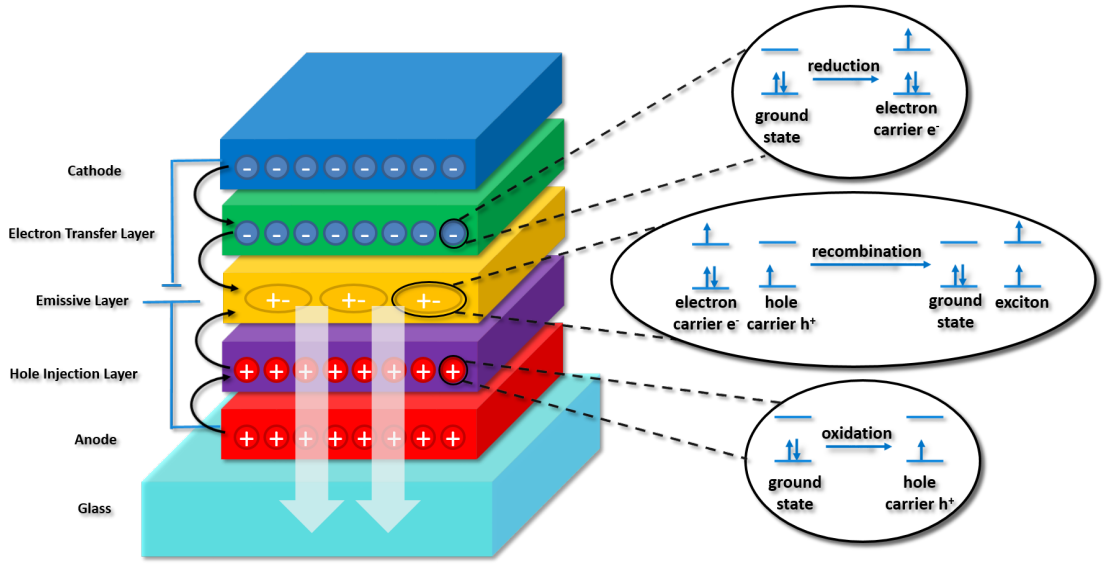

Figure 1.7: Schematic showing typical architecture of an OLED. Charges are injected from the corresponding electrodes, before migrating through the organic layers and combining in the emissive layer. The excited state generated from this process may decay back to the ground state by emitting light.

Figure 1.7 illustrates a typical architecture of an OLED.[48] Like LEDs, OLEDs are multilayered devices fabricated with an emissive layer sandwiched between two electrodes. In a typical device, the cathode and anode inject electrons and holes, respectively, into the organic layers. The individual organic molecules can be considered to be radical cations or anions. The charges then migrate through the device by hopping processes and ideally, the charges meet in the emissive layer, such that they can combine by a double electron transfer

mechanism, leaving one ground state species and one 'exciton' (a bound electron-hole pair). This exciton may then relax back to the ground state by emitting light.

This mechanism of light generation is termed 'electroluminescence' (EL) and has some fundamental differences from photoluminescence (PL). This is because, while for the PL mechanism the S_1 state is always populated before any other state, the EL mechanism generates the excited state in a bimolecular fashion, through the recombination of holes and electrons. This means that even in low SOC systems, such as conjugated organic molecules, triplets are always generated in the device. As the following equations show, three spin states may be triplet in nature, while only one spin state may adopt a singlet configuration.

$$\left.\begin{array}{l} |1,1>=\uparrow\uparrow \\ |1,-1>=\downarrow\downarrow \\ |1,0>=\frac{\uparrow\downarrow+\downarrow\uparrow}{\sqrt{2}} \end{array}\right\} S=1 \qquad \text{(triplet)}$$

$$\left.|0,0>=\frac{\uparrow\downarrow-\downarrow\uparrow}{\sqrt{2}}\right\} S=0 \qquad \text{(singlet)}$$

Thus due to spin statistics, 75% of excitons formed in an OLED are in a triplet spin state. This means that using a fluorescent emitter in an OLED imposes a statistical limit of 25% on their internal quantum efficiencies (IQE, the internal ratio of photons generated from electrons input into the device), making fluorophores generally undesirable for OLED applications.

To address this, phosphorescent transition metal complexes have been studied as emitters for OLEDs, as they are able to harvest all of the excitons formed in the device, in a manner that would allow for theoretical quantum efficiencies of 100% to be possible. This principle was first demonstrated with the use of the red-emitting complex octaethylporphyrinplatinum(II) (PtOEP, **2**).[49] Upon doping this material into an organic host matrix, observed external quantum efficiencies (EQE, the overall device efficiency, quantifying the ratio of photons emitted from the device to electrons input to the device) reached a maximum value of 4% (Figure 1.8), which was a record efficiency for an OLED at the time.[50]

Shortly after PtOEP, the first iridium complex was reported in an OLED: *fac*-[Ir(ppy)$_3$] (complex **3**), now considered the archetypal phosphorescent iridium complex. This complex

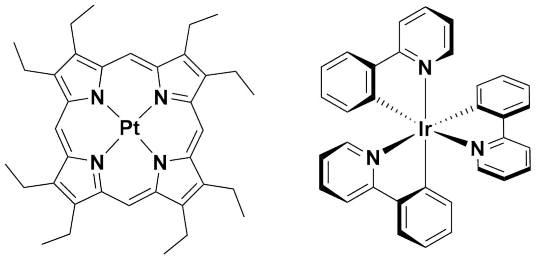

	2	3
$\lambda_{PL(flm)}$ (nm):	650	510
Φ_{PL} (%):	42	97
τ_e (μs):	50	1.6
EQE (%):	4.0	8.0
CIE (x,y):	0.69, 0.30	0.27, 0.63

Figure 1.8: The first phosphorescent complex utilised in an OLED, platinum octaethylporphyrin (PtOEP)[49;50] and the first iridium complex utilised in an OLED, *fac*-[Ir(ppy)$_3$].[51] Their corresponding performances in these reports are also given. Solution-state photophysics in toluene.

is coordinated by three cyclometalating 2-phenylpyridinato (ppy) ligands which bind through a nitrogen atom and a formally anionic carbon atom. These 'C^N' ligands (where C^N denotes a bidentate chelating ligand coordinating through one C atom and one N atom) strongly destabilise the deleterious MC states associated with many of these complexes. As a result, this complex is intensely luminescent, displaying a short excited state lifetime (τ_e = 1.6 μs in toluene) and high quantum yield (Φ_{PL} = 97% in toluene) making it the ideal OLED triplet harvesting candidate, (Figure 1.8).[10;51;52]

In the 18 years since the initial report of **2** in an OLED, device performances have improved considerably, with EQEs reaching 40%. However, the simplest conceivable OLED, in which an organic bilayer is encapsulated between an anode and a cathode, does not give a device with particularly good performance. To achieve these extraordinary efficiencies, multiple organic layers are added to effectively mediate charge transport through the device. Many different layers can be used, such as hole/electron transport layers (HTL, ETL), hole blocking layers (HBL) and/or hole injecting (HIL) layers.[53;54] However, this requires a considerable number of metal/organic and organic/organic contacts, which increases the operating voltage of the device.[46] To circumvent this, air-reactive low work function electrodes such as Ca or Ba are utilised to effect efficient electron injection into the LUMO levels of the adjacent organic layers.[23;55]

This multi-layered architecture poses a significant issue for fabrication. Given that the

latest state-of-the-art in OLED design has been reported to employ up to 15 layers,[23] and examples even exist of 'multi-unit OLEDs' (in which there is a multiply layered structure of multiple alternating emissive units and transparent connecting layers), it is unsurprising that the biggest factor that has hindered widespread commercialisation of OLED technology has been the fabrication cost of the device. Although this is economic for devices such as displays for televesions or phones, it is still a limiting factor in the use of OLEDS for low cost lighting purposes. In all cases, the need for complex multi-layered device architectures and air-sensitive materials necessitates fabrication by vacuum sublimation, which is a technique that is both labour- and cost-intensive.[23] Furthermore, the harsh nature of the vacuum sublimation processing method means that the emissive materials required must be non-ionic and thermally stable, which limits the choice of emissive materials that might be employed.[35;56] The complexity issue is, of course, compounded for white-emitting OLEDs (WOLEDs), which are typically constructed from separate red, green and blue emissive layers.

Another issue for these WOLEDs is that reports to date of devices which are stable, bright and mirror the spectrum of natural light are scarce.[57] This because the generally poorer performances and lower stabilities of blue OLEDs places a limit on the overall performance of WOLEDs.[7;58] The shorter device lifetimes of the blue OLEDs means that as they degrade more quickly than the red or green OLEDs, the colour of the WOLED red shifts away from ideal white. The poorer stability of blue OLEDs can be attributed to the large T_1 energies associated with blue emitters (and the even larger T_1 energies required for the host materials).[58;59] Large T_1 energies necessitate high operating voltages in order to drive the OLEDs,[47] which reduce the stability and thus the overall lifetime of the device. Furthermore, the chemical modifications required to blue shift the emission of the emissive molecule often tends to induce chemical instability in the emitter itself, exacerbating the issue further.[58] Thus it is common to use blue fluorescent emitters instead, but this immediately reduces device IQEs, since the blue triplet excitons formed by the EL mechanism may no longer be harvested.[60]

1.2.2 Light-Emitting Electrochemical Cells

If SSL is to be adopted on an industrial scale to tackle widespread energy wastage by artificial lighting, then the complex architecture of OLEDs must be simplified to mitigate cost. One alternative technology to the OLED for tackling this issue is the light-emitting

electrochemical cell (LEEC). The materials these devices utilise are similar to OLEDs, but they are intrinsically charged and act to perform both the role of charge transport and emission, greatly simplifying the architecture of the device.[23;61–63] This simplicity allows these devices to be fabricated by the cheaper, more scalable method of roll-to-roll solution processing, making the fabrication of large-scale artificial lighting a realistic possibility.[64]

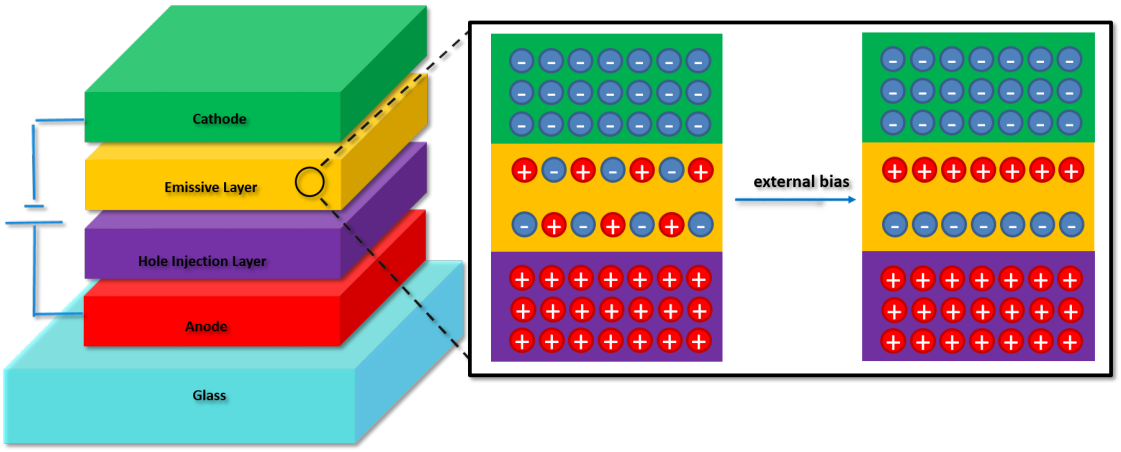

Figure 1.9: Schematic showing typical architecture of a LEEC. Charges are injected from the corresponding electrodes. These charges enforce migration of the anions and cations in the emissive layers to the corresponding interfaces. As the ions migrate, the barrier to charge injection is lowered.

Two families of LEEC are currently of interest: the PLEEC (Polymer Light-Emitting Electrochemical Cell) which contains a mixture of emissive conjugated polymer, ion transport material and inorganic salt;[57;65–67] and the iTMC (ionic transition metal complex) LEEC, which utilises charged organometallic complexes as the emissive layers,[61;68;69] although more recently quantum dot[70;71] and perovskite-based[72;73] devices have emerges as well. Figure 1.9 illustrates the typical architecture of an iTMC LEEC. The device structure has not changed significantly since the original report based on **1**, wherein a single layer of $[Ru(bpy)_3](ClO_4)_2$ was deposited between an indium tin oxide (ITO) anode and an aluminium cathode.[74] However, in recent years it has been more common for devices to use cationic iridium complexes, as they are easily colour tunable, display generally high Φ_{PL} values and show good photo- and chemical stability. Additionally, it is common to find a layer of PEDOT:PSS (poly(3,4-ethylenedioxythiophene)-poly(styrenesulfonate)) is added since it facilitates the formation of uniform iTMC thin films on the ITO substrate and it also improves hole injection. Devices fabricated in the absence of PEDOT:PSS are

prone to forming crystalline-like domains within the film, which can have deleterious effects on the device performance and batch-to-batch reproducibility.[75–77]

The use of charged materials in the emissive layer results in a device operating mechanism unique to LEECs. Upon application of an external bias to the LEEC, there is a large initial barrier to charge injection. However, by using intrinsically charged emissive layers, the constituent ions migrate to the respective electrodes over time, resulting in the formation of an electric double layer that significantly lowers the barrier to charge injection, until eventually charge injection at very low driving voltages (typically ca. 3 V) becomes facile (Figure 1.9).[78] A charge hopping mechanism ensues, akin to that found in an OLED, and emission is realised upon radiative decay of the formed exciton.[23;61]

This lowered charge injection barrier thereby permits the use of air-stable electrodes to operate the LEEC, and negates the need for additional charge transport layers that are normally required for conventional OLEDs. Thus, these devices are structurally simple, and can be printed from solution in air, akin to the printing of newspapers or magazines, making them an attractive, cost-effective technology for large area displays and lighting. This printing method is exceptionally versatile, allowing the deposition of the devices onto virtually any substrate, from glass, metal and flexible plastic substrates to even paper.[79;80]

Like OLEDs, there are a number of challenges that still remain to be addressed with LEECs, including limited device stability[81] and poor colour quality.[82] Furthermore, as with OLEDs, a dearth of efficient blue-emitting LEECs[83–85] has so far hampered the development of white-light-emitting LEECs.[57]

1.3 Tuning the Properties of Transition Metal Complexes by Ligand Substitution

1.3.1 Archetypal Complexes

1.3.1.1 Photophysics

So far, the role of the metal has been discussed extensively, and the importance of iridium(III) in particular as a choice of metal for a phosphorescent emitter has been identified. In this section, the importance of the ligands will be studied in greater detail. For cationic iridium complexes, the archetypal example is $[Ir(ppy)_2(bpy)]^+$ (**4**). Although not the first iridium complex reported to operate in a LEEC (this distinction goes to its cousin,

$[Ir(ppy)_2(dtbubpy)](PF_6)$, **5**, where dtbubpy is 4,4'-di-*tert*-butyl-2,2'-bipyridine)[86], it is the complex that has most frequently been employed as an emitter in a LEEC,[62;81;87;88] and thus serves as a useful standard for comparing the photophysical properties of new emitters.

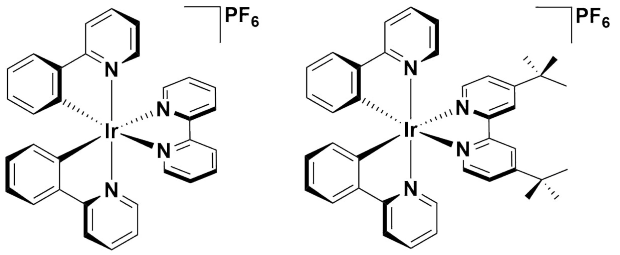

4 **5**

Figure 1.10: Structures of $[Ir(ppy)_2(bpy)]^+$, **4**, and its *tert*-butyl analogue, $[Ir(ppy)_2(dtbubpy)](PF_6)$, **5**, which are widely studied iridium complexes employed in LEEC devices.

The relevant photophysical and electrochemical data for **4** are summarised in Table 1.1. In acetonitrile solution at room temperature **4** is an orange-yellow emitter with a broad, unstructured emission centred at 585 nm, and a triplet lifetime of 0.43 μs (Figure 1.11).[89] This emission profile is characteristic of many $[Ir(C\hat{}N)_2(N\hat{}N)]^+$ complexes, comprising a mixed CT triplet excited state consisting of ^{3}MLCT transitions between the metal and the N$\hat{}$N ancillary ligand and ^{3}LLCT between the phenyl groups of the C$\hat{}$N ligands and the N$\hat{}$N ancillary ligand. The spin density of the triplet state is thus delocalized over the entire complex (Figure 1.12). Upon cooling to 77 K, the emission is hypsochromically shifted but remains unstructured. This rigidochromic blue-shifting of the emission upon cooling is a further hallmark of the mixed CT nature of the emission, which is stabilised at ambient temperature by polar aprotic solvents such as MeCN. Aside from ^{3}MLCT/^{3}LLCT excited states, $[Ir(C\hat{}N)_2(N\hat{}N)]^+$ complexes can also demonstrate structured ^{3}LC emission profiles, and indeed it is not uncommon for cationic iridium complexes to exhibit emission from a mixture of ^{3}LC and ^{3}MLCT/^{3}LLCT states.[34]

The photophysical properties of many iridium complexes in the solid state are very different from what is observed in the solution state. In the case of **4**, the emission energy in thin films compared to MeCN solution is virtually unchanged (a somewhat rare phenomenon), but the Φ_{PL} values differ dramatically. Reports of the Φ_{PL} of **4** in MeCN have

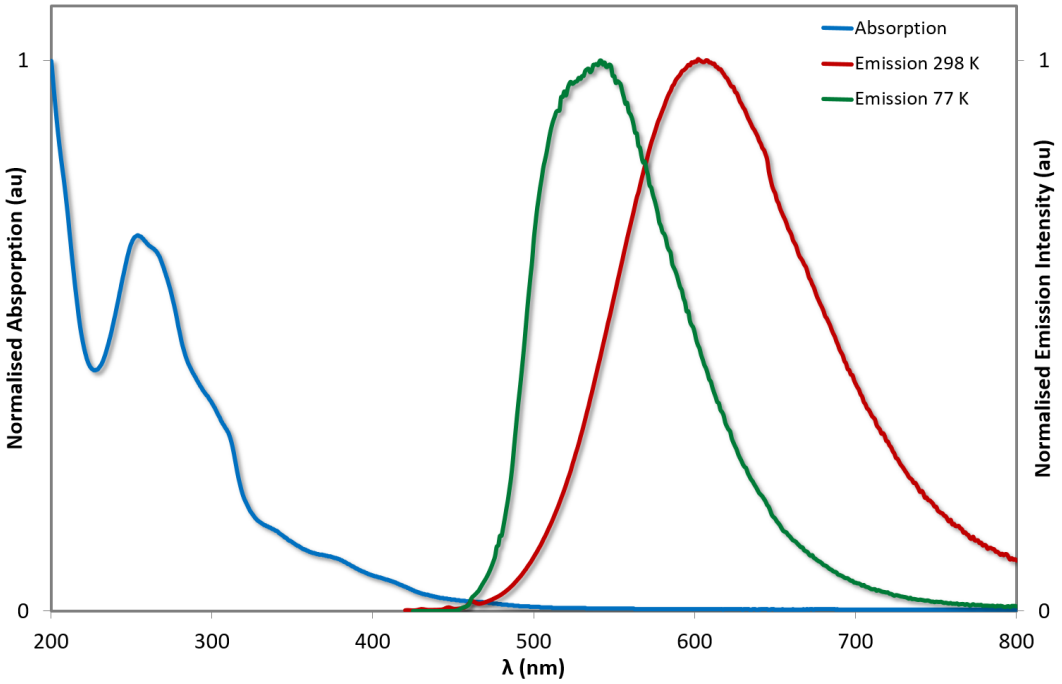

Figure 1.11: UV-vis absorption spectra and emission spectra of **4** in MeCN. 77K emission spectrum of **4** in 2-MeTHF[62;90].

been somewhat variable, ranging from 6 to 14%,[89;91] but ultimately are rather low, while in the 'LEEC' film (containing the complex and an ionic liquid, IL, additive in a 1:1 molar ratio) or in a doped film (5 wt% in poly(methyl methacrylate), PMMA) the Φ_{PL} values are substantially higher (34%[89] and 66%[87], respectively). The increased brightness in the solid state is plausibly attributed to rigidification of the local environment that inhibits molecular motions that otherwise non-radiatively deactivate the excited state. Although clearly a desirable feature, such effects are difficult to predict, with this rigidification phenomenon often in competition with self-quenching processes that lower the Φ_{PL}. Self-quenching is particularly problematic for LEECs since, unlike OLEDs, the emitters are not normally doped into host matrices; typically, the emissive layers are neat films or contain small amounts of IL doped into the host emitter (4:1 and 1:1 weight by weight ratios are the most common configurations), leading to films that show lower Φ_{PL} compared to solution and thus lower device efficiencies as well. Furthermore, the emission energies of these complexes can change substantially in the solid state. Small red-shifts frequently occur due to effects such as aggregate formation but on occasion substantial red-shifting (as high as 71 nm, or 2037 cm^{-1})[92] or even blue-shifting have been reported.[93;94]

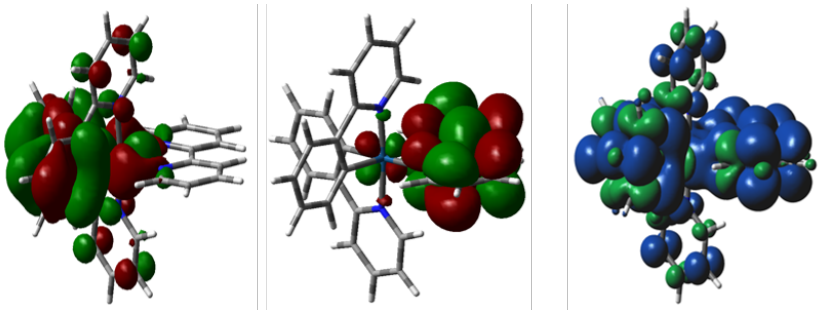

Figure 1.12: DFT computed Kohn-Sham MOs for the HOMO (left) and the LUMO (middle) of **4**, and the computed spin density of the T_1 state (right). DFT [(B3LYP/SBKJC-VDZ for Ir(III)) and (6-31G* for C,H,N)] with CPCM (MeCN).[90]

Aside from characterising the photophysical parameters, it is important to determine the electrochemical properties of such complexes also. Normally, this is done in order to estimate the energies of the HOMO and LUMO levels,[95;96] which is generally important in the context of OLEDs, where aligning the orbital energies of the emitter with those of the host materials and charge transport layers is critical for achieving good performances. For LEECs, this consideration is only important when aligning the energy levels of host-guest systems,[97–99] but not for more traditional 'single-emitter' devices since the emitters here also carry out the role of charge transport. The dual charge transport/light emitting role of the iTMCs in the device is the most important contributing factor for explaining why LEECs are invariably less stable than their OLED counterparts. Thus, an important feature to look for when characterising the electrochemical properties of the emitter is for reversible oxidation and reduction waves, since good reversibility suggests that the emitter might be more resilient to electrochemical degradation when operating in the device.

With the support of density functional theory (DFT) calculations (Figure 1.12), the nature of the oxidation and reduction of **4** has been assigned. The oxidation is ascribed to the $Ir^{III/IV}$ redox couple, along with contributions from the phenyl rings of the cyclometalating ligands. The degree of reversibility of this redox couple depends on the magnitude of the contribution from the C^N ligands; greater phenyl contribution results in a greater degree of irreversible electrochemistry. The reduction is assigned to a highly reversible $bpy^{0/1-}$ redox couple, which is believed to be an important factor in giving devices based on **4** impressive stability metrics ($t_{1/2} = 668$ h, *vide infra*).[87]

An important feature of **4** and its related analogues is the high degree of covalency associated with the metal-ligand bonds. This feature means that unlike, for example,

	4	**Ref.**
λ_{abs} (nm) [ϵ ($/10^4$ M^{-1} cm^{-1}]^a	265 [4.17], 310 [1.29], 375 [0.60], 420 [0.26]	90
$\lambda_{PL(sol)}$ (nm)^{a,b}	585	89
$\lambda_{PL(film)}$ (nm)^c	587	89
$\Phi_{PL(sol)}$ (%)^{b,d}	9	91
$\Phi_{PL(film)}$ (%)^{c,e}	34	89
$\Phi_{PL(film)}$ (%)^e	66	87
τ_e (μs)^{a,b}	0.43	89

Table 1.1: Relevant photophysical data for $[Ir(ppy)_2(bpy)](PF_6)_2$, **4**. ^{a} Measured in MeCN at 298 K. ^{b} Measured under deaerated conditions. ^{c} Film composition: 1:1 iridium complex to ionic liquid. ^{d} Using $[Ru(bpy)_3](PF_6)_2$ as the standard ($\Phi_{PL} = 9.5\%$ in deaerated MeCN). ^{e} Measured using an integrating sphere.

lanthanoid complexes, the ligands of $[Ir(ppy)_2(bpy)]^+$-type complexes exert a significant influence over the photophysical properties of the complex. Thus this property can be exploited to tune the electronics of the system, by adopting a simple ligand substitution strategy (Figure 1.13).[100] In a general strategy, blue-shifting the emission can be achieved by adding electron-withdrawing groups to the phenyl ring of the C^N ligands (stabilising the HOMO) and electron-donating groups to the N^N ligand (destabilising the LUMO). Conversely, electron-donating groups on the C^N ligands and electron-withdrawing groups on the N^N ligand effect a red-shift in the emission.

Although colour tuning in this fashion is facile, there are important subtleties that are often overlooked. In particular, the different possible substitution points (i.e. the regiochemistry) on the C^N or N^N ligands of the complex can lead to overwhelmingly different emission colours observed. A typical example is substitution on the phenyl ring of the C^N ligand, where it is generally accepted that substituents oriented *para*- to the metal more effectively influence the HOMO energy. In addition, HOMO control can also be achieved by substitution on the pyridyl ring of the C^N ligand: when the substituent on the pyridyl ring is *para*- to the phenyl it can effectively influence the energy of the orbitals localised on the phenyl rings (which also can contribute to the HOMO). In recent years Hammett values have come to the fore as a useful qualitative tool for predicting the emission colour of a complex based on incorporation of a particular functionality.[101;102]

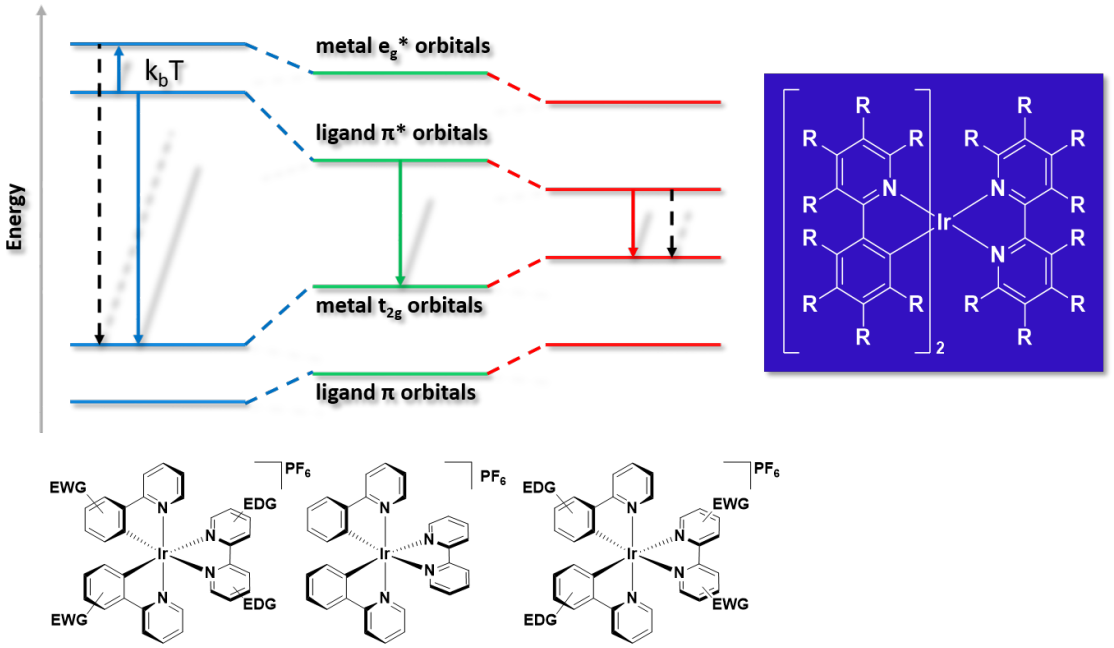

Figure 1.13: General scheme (left) depicting strategy for colour tuning the emission of $[Ir(ppy)_2(bpy)]^+$, **4**. The HOMO is largely localised on the metal centre and the phenyl rings of the cyclometalating ligands, while the LUMO is largely localised on the bpy. This allows for tuning of the emission by appropriate functionalisation of the ligands. Dashed arrows indicate deactivation from the excited state via non-radiative decay. Schematic (right) showing different substitution points on about the ligand scaffold of **4**.

The other consideration that must be taken into account when colour tuning is the quantum yield. At the extremities of the visible spectrum, the Φ_{PL} values tend to drop off precipitously. For the red, this is an expected consequence of the energy gap law, wherein the rate of non-radiative decay increases exponentially with decreasing emission energy, as vibrational modes of the ground state more readily couple to those of the excited state,[103;104] which is the primary deactivation mode when tuning the emission towards the red. For iridium complexes that are being tuned towards blue emission, the energies of the ^{3}MC as well as ^{3}CT and ^{3}LC states are all very strongly destabilised. However, the relative destabilisation of the ^{3}MC states is less pronounced than the emissive ^{3}CT or ^{3}LC states, resulting in population of these ^{3}MC states by thermal processes becoming increasingly feasible as a function of an increasing HOMO-LUMO energy gap.[52] Population of these ^{3}MC states results in efficient quenching of the excited state. Thus tuning Φ_{PL} must always be a consideration when tuning colour as well.

1.3.1.2 Device Performances

Complex **4** is the complex that has been reported the highest number of times in a LEEC. A summary of the data of some LEECs reported employing **4** is given in Table 1.2 while Figure 1.14 shows the use of complex **4** in what is now considered the archetypal device architecture of a LEEC. An additional PEDOT:PSS layer is employed between the ITO anode and the emissive layer, and an IL doptant is added to the emissive layer. In the absence of any IL dopant (Entry 1 in Table 1.2) the device gives good performance, exhibiting a remarkably long device lifetime of 668 h. The authors attribute this stability to the relatively large calculated ^{3}MC-T$_1$ energy gap for **4**.[87] Theory and experimental observations have implicated ^{3}MC states in an elongation of the N$_{\text{pyridyl}}$-Ir bond of the C^N ligands of [Ir(C^N)$_2$(N^N)]$^+$ complexes, which accounts for the efficient non-radiative quenching resulting from these states.[105] In addition, work on ruthenium(II) complexes has suggested that this bond lengthening/breaking process within the ^{3}MC state introduces a free coordination site that allows small molecules such as water to coordinate to the metal, quenching the emission and leading to degradation products within the device.[106;107] Thus, devices employing complexes with a small ^{3}MC-T$_1$ energy gap tend to not be stable unlike the case with **4** where the device stability is enhanced. In addition, the reversible electrochemistry in **4** results in its capacity to act as an effective charge transport material and thereby resist electrochemical degradation processes that also impact device lifetimes.

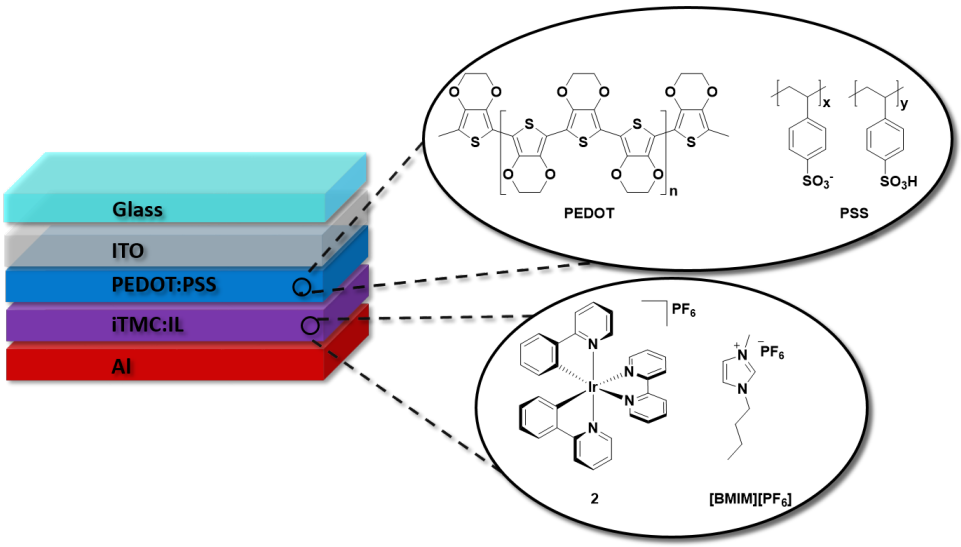

Figure 1.14: Typical device architecture of a LEEC employing **4** as the emissive layer.

Unfortunately, the long device lifetime in Entry 1 is accompanied by a long device

turn on time as well (t_{on} = 70.2h), and thus IL dopants are added to circumvent this. The most common IL used in LEECs is 1-butyl-3-methylimidazolium hexafluorophosphate, [BMIM][PF_6]. Entries 2 and 3 demonstrate the differences in LEEC performance produced by just varying the ratio of 4 and [BMIM][PF_6] in an otherwise identical device configuration.[87] In the absence of IL, an extremely long t_{on} is observed. This is attributed to low ionic mobility of the PF_6^- anions, possibly due to the formation of microcrystalline domains in the film. Addition of IL circumvents this problem, improving ionic conductivity and thus charge transport in the device, in addition to disrupting any possible crystallite formation. Both devices with an IL dopant show improved t_{on} times (7.2 and 0.7 h for Entries 2 and 3, respectively) as well as improved EQEs (3.0 and 5.6%, respectively); where EQE defined as the ratio of electrons injected into the device to photons outcoupled from the device. However, the addition of IL comes at the considerable cost of device stability as measured by its lifetime ($t_{1/2}$, defined as the time taken for the device to reach half of its maximum luminance). In the absence of IL, this device lasts for up to 668 h, but lifetimes are dramatically reduced for the devices constituting iTMC:IL ratios of 4:1 (69 h) and 1:1 (7.8 h). This further reduction of device stability with increasing amounts of IL is representative of the behaviour in LEECs, regardless of iTMC emitter, and illustrates the trade-off between $t_{1/2}$ and t_{on} that has been a significant challenge to overcome. The compromise between attaining good device performance (EQEs, t_{on}) and reasonable device lifetimes has meant that generally the most popular iTMC:IL ratio reported in the literature has been 4:1 weight by weight.

Alternatively, devices reported by Slinker and co-workers explore the effect on the response time of doping in inorganic salt additives with cations of varying sizes (Table 1.2, Entries 4-8).[88] They reasoned that the large size of the iTMC cations renders the complexes essentially stationary in the device, meaning that upon initial application of a bias voltage, the cation density at the cathode is initially much lower than the anion concentration at the anode, leading to an imbalance of charge injection into the device. Thus they reasoned that by doping in small amounts of alkali metal cation hexafluorophosphate salts, faster t_{on} times under constant current conditions could be achieved. Accordingly, the devices employing $LiPF_6$ as the additive showed the best performances (Entries 5 and 6) due to the small size of the Li^+ cation, and thus higher ionic mobility. Crucially, this also led to more balanced charge injection that ultimately improved not just response times, but also luminance values and EQEs.

Entry	Emissive Layer	Bias	t_{on} (h)	L (cd m^{-2})	EQE (%)	$t_{1/2}$ (h)	Ref.
1	**4**	3.0 V	70.2	219	2.2	668	[87]
2	**4**:IL (4:1)	3.0 V	7.2	334	3.0	69	[87]
3	**4**:IL (1:1)	3.0 V	0.7	375	5.6	7.8	[87]
4	**4** + 0.1 wt% KPF_6	1.5 mA	63	1560	1.0	295	[88]
5	**4** + 0.1 wt% $LiPF_6$	1.5 mA	4.6	4950	3.2	37	[88]
6	**4** + 0.3 wt% $LiPF_6$	1.5 mA	0.003	3030	2.0	137	[88]
7	**4** + 0.1 wt% NH_4PF_6	1.5 mA	77	1410	0.9	199	[88]
8	**4**	1.5 mA	49	80	0.8	167	[88]
18	**4**:IL (4:1) + trace Cl^-	100 A m^{-2}		ca. 450			[81]
19	**4**:IL (4:1)	100 A m^{-2}		ca. 900			[81]

Table 1.2: Summary of LEECs reported employing **4**. Definitions: t_{on} defined as the time to reach maximum luminance; L is maximum luminance; EQE is external quantum efficiency; $t_{1/2}$ is the time taken for the device luminance to fall to half the maximum value.

A more concerning aspect of these devices is that their performances are sometimes not reproducible. Housecroft and co-workers have recently addressed this issue, demonstrating that the poor batch-to-batch reproducibility of these devices is attributable, at least in part, to sample purity, implicating trace chloride anions in particular as culpable for negatively affecting the device performance.[81] Using silver salt-assisted syntheses they were able to isolate **4** with improved purity, leading to devices with superior luminance levels (ca. 900 cd m^{-2} Entry 10) compared with those containing trace chloride impurities (ca. 450 cd m^{-2}, Entry 9). High purity samples are crucial for achieving good device performance, and indeed, aside from the presence of Cl^-, trace water has also been implicated in impacting device performances of ruthenium-based LEECs.[107]

1.3.2 Blue-Emitters for LEECs

To date, attaining simultaneously efficient, stable and deep blue-emitting LEECs remains the most pressing issue for LEEC development. The challenge of obtaining high performance blue-emitting devices is well-known for both organic and inorganic light emitting devices, and while it has largely been addressed in the latter case, this topic is still the source of very active research for OLEDs. For example, a recent report detailed the performance of a new champion blue OLED, which showed simultaneously deep blue emission and high device efficiency (EQE = 10.1%).[108] However, this efficiency value still falls well below the efficiencies reported for red or green (EQE 30%), or even sky blue OLEDs (EQE > 20%).[58]

In the case of LEECs, the situation is more dire. To date, no iTMC LEEC has even been reported emitting blue light close to the 'ideal deep blue' CIE (Commission Internationale de l'Eclairage: a method of translating an emission spectrum into a single X,Y coordinate which reflects the colour of a spectrum actually observed by eye) coordinate (CIE: 0.15, 0.06, as defined by the European Broadcast Union, EBU), let alone with good efficiency. Furthermore, the stability of these sky blue LEECs is demonstrably inferior than their OLED counterparts. The generally accepted industry requirements for OLED device lifetimes is more than 20,000 h,[109] while sky blue/blue-green LEECs often display device lifetimes in the region of tens of hours. Given that blue is a necessity in attaining white light from a typical RGB colour combination, overcoming this issue is of pressing concern. A summary of the relevant performance metrics of blue LEECs discussed herein is given in Table 1.3.

1.3.2.1 Efficiency

The widely accepted paradigm to achieve blue emission in $[Ir(C\hat{}N)_2(N\hat{}N)]^+$-type complexes requires that the HOMO be stabilised with electron-withdrawing groups located on the phenyl ring of the C^N ligands and the LUMO be destabilised with electron-donating groups located on the ancillary N^N ligand. The most commonly used electron-withdrawing substituents are fluorine atoms with examples of complexes shown in Figure 1.15. Complex **6** employs the ubiquitous fluorinated C^N ligand 2,4-difluorophenylpyridinato (dFppy) to blue-shift the emission, with further blue-shifting of the emission achieved by incorporating an electron-rich heterocycle within the ligand N^N ligand framework.[110;111] By contrast,

Complex	λ_{PL} (nm)	Φ_{PL} (%)	EQE (%)	$t_{1/2}$ (h)	CIE	λ_{EL} (nm)	Ref.
6	452, 480	20	0.3		0.20, 0.28	460, 486	[110]
7[a]	492	100	14.4	2.17	0.20, 0.36	460, 486	[111]
8	489	24	3.4		0.25, 0.46	497	[112]
9	472, 490	54	7.6		0.22, 0.41	474, 494	[113]
10	472, 501	0.001		24.3	0.43, 0.53	560	[114]
11	477, 500			29.8	0.41, 0.53	556	[115]
12	480, 509	3		15.8	0.26 , 0.48	486, 512	[116]

Table 1.3: Summary of LEECs employing blue-emitting iTMCs. Definitions: λ_{PL} is the solution-state emission maximum in MeCN; Φ_{PL} is the solution-state photoluminescence quantum yield in MeCN; EQE is external quantum efficiency; $t_{1/2}$ is the time taken for the device luminance to fall to half the maximum value; CIE are the Commission Internationale de l'Eclairage defined X,Y coordinates of colour; λ_{EL} is the electroluminescence maximum. [a] Solution state measurements in DCM.

complex **7** incorporates the pyrazole within the C^N ligands.[75] This strategy is most effective when this structural modification occurs within the ancillary ligand, as exemplified by the greater blue-shift in emission observed for **6** (λ_{PL} = 451, 484 nm in MeCN) compared to **7** (λ_{PL} = 492 nm in DCM).

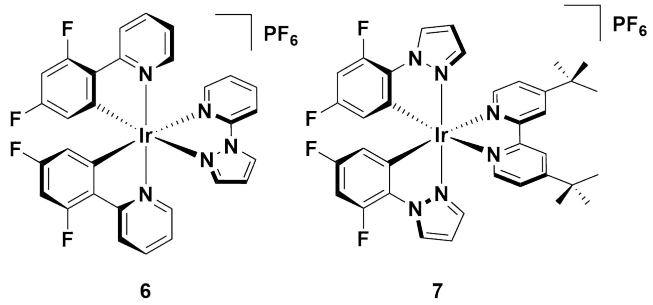

Figure 1.15: Blue-emitting iridium complexes bearing pyrazole-type ligands.

The blue emission in solution observed for **6** translates to its performance in the device, with CIE coordinates in the sky blue (CIE: 0.20, 0.28). Despite being reported in 2008, this LEEC nevertheless remains the bluest reported for any iridium emitter to date. However, the emission observed for this device is still a long way from the ideal 'deep blue' coordinates required in RGB devices (CIE: 0.15, 0.06). Furthermore, this device functions in the absence of IL, which results in essentially impractical turn on times (t_{on} = 7.1 h). When an IL

dopant is added, the response time shortens dramatically (t_{on} = 1.1 h) but the observed colour is also greatly red-shifted (CIE: 0.33, 0.45). In contrast to **6**, the performance of 3 in the device is relatively poor, with low efficiencies and brightness levels reported for both the IL free (EQE = 0.28%, L_{max} = 39 cd m^{-2}) and IL doped devices (EQE = 0.21%, L_{max} = 23 cd m^{-2}).

By contrast, although complex 7 displays an emission profile that is strongly red-shifted compared to **6**, it is a much more efficient emitter in the device. Indeed, this high efficiency has made it a favoured choice of emitter either for blue-emitting LEECs,[75;97;117] or as the blue component in white LEECs.[111;118–120] As a blue/blue-green emitter, the device reported based on **7** displays extraordinarily high device efficiencies (EQE = 14.4%). These values can vary significantly, depending on the device architecture. For example, the first reported LEEC employing this complex gave a comparably low overall EQE of 4.4%, using a typical device architecture of ITO/PEDOT:PSS/Ir/Al. However, it is worth noting that this device displays very high brightness for a LEEC (L_{max} = 1700 cd m^{-2}).[75]

Since then, Wong in particular has explored different means by which charge injection and transport can be improved using this complex as an emitter. For example, it was shown that by doping small amounts (up to 1.0 wt%) of a pure organic near-infrared (NIR) emitting laser dye, 3,3'-diethyl-2,2'-oxathiacarbocyanine iodide, DOTCI, (Figure 1.16) into the emissive layer of complex **7**, higher device efficiencies could be obtained (EQE = 12.8% for 0.01 wt% DOTCI) than without any dopant (EQE = 9.1% for the pristine device).[121] The intrinsic hole transporting properties of **7** leads to the formation of the charge recombination zone near the cathode, which facilitates exciton quenching. This charge imbalance can be mitigated by doping in DOTCI, which has a much higher HOMO than **4** and therefore impedes hole transport, but a similar LUMO energy to **4**, such that the electron mobility remains balanced. Furthermore, the poor spectral overlap between the emission of **7** and the absorption of DOTCI results in minimal quenching of the iridium-based emission by energy transfer to the guest, which would otherwise negatively impact the efficiency of the device.

A different strategy that has been used to improve device efficiencies is by adding steric bulk to the complex to inhibit intermolecular quenching processes. Complexes **8** and **9** demonstrate this strategy (Figure 1.17). Both complexes are blue-green emitters in acetonitrile solution (λ_{PL} = 489 nm for **8** and 472, 490 nm for **9**), with **9** blue-shifted due

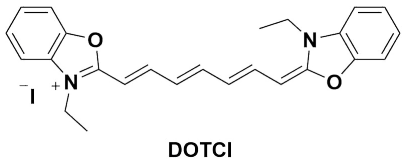

Figure 1.16: Organic dopant used to improve the efficiencies of **7**.

to the additional pyrazole rings incorporated within the cyclometalating ligands. The most important structural difference between **8** and **9** is the presence of the trityl group on the ancillary ligand of **9**. This bulky unit serves to increase the molecular spacing between the emissive molecules in the film, which leads to reduced excited-state self-quenching that negatively impacts the device efficiencies. Indeed, despite **9** being moderately blue-shifted both in solution and in the device (λ_{EL} = 474, 494 nm; CIE: 0.22, 0.41) compared to **8** (λ_{PL} = 497 nm; CIE: 0.25, 0.46), the LEEC with **9** shows greatly improved efficiencies (current efficiency = 8.4 cd A^{-1} for **8** and 18.3 cd A^{-1} for **9**; EQE = 3.4% for **8** and 7.6% for **9**).

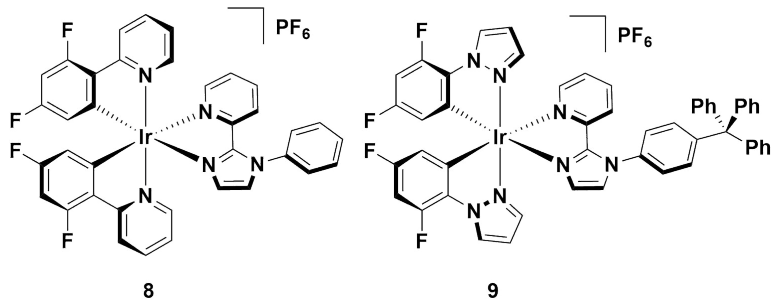

Figure 1.17: Blue-emitting iridium complexes bearing pyridylimidazole ancillary ligands.

1.3.2.2 Stability

Although the examples above have demonstrated that high efficiencies are possible for blue LEECs, so far they have ultimately fallen short of displaying 1) deep blue colour and 2) good device stability. There are many reasons for the poor stability of these devices, but one factor in particular thought to be contributing to poorer device performance is the presence of C_{aryl}-F bonds on the cyclometalating ligands. It has been posited that the highly electron deficient C^N ligands make them susceptible to chemical degradation by nucleophilic aromatic substitution of the fluorine substituents in the device. This phenomenon has been documented to occur in OLEDs,[122] as well as under extreme thermal

conditions.[123] This phenomenon has also been studied in LEECs (see Section 1.3.3). Thus there is interest in designing new emitters that emit blue light without the need for fluorine substituents that might negatively impact the stability. In addition, there is interest in adopting hydrophobic substituents within the ligand framework to impede nucleophiles from coordinating to the iridium centre and quenching the emission. These two strategies are exemplified by complexes **10** and **11**, with **11** in particular representing an all-in-one effort to achieve blue emission without impacting the device stability.

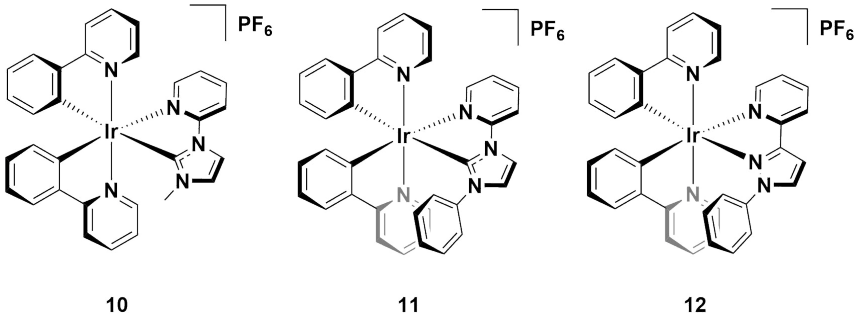

Figure 1.18: Fluorine-free blue-emitting iridium complexes.

Both complexes **10** and **11** use *N*-heterocyclic carbenes (NHCs) within the ancillary ligand. These heterocycles are very strongly σ-donating in nature, and consequently act to destabilise the LUMO of these complexes. The potency of these heterocycles is well known, with near-UV emission having been reported for iridium complexes containing multiple NHCs within the ligand frameworks.[108;124] Thus, despite both complexes bearing just ppy as the C^N ligands, they are both blue-green emitters in acetonitrile solution (λ_{PL} = 472, 501 nm for **10** and 477, 500 nm for **11**), with emission strongly blue-shifted and more ligand-centered compared to **4** (λ_{PL} = 605 nm) thereby demonstrating the feasibility of blue-shifting emission without using fluorine.[114;115]

Aside from the fluorine-free cyclometalating ligands, **11** also features what has become a common strategy of enforcing an intramolecular π-stacking arrangement between the pendant aryl ring on the N^N ligand and one of the phenyl rings of the C^N ligands. This π-stacking motif envelops the metal centre in a supramolecularly caged hydrophobic scaffold that shields it from adventitious attack from nucleophiles that degrade the emitter.[125–127] This design feature is most commonly utilised with six-membered ring systems, such as the N^N ligand 6-phenyl-2,2'-bipyridine, since the intramolecular π-stacking distance is usually shorter than in the case of five-membered rings such as the imidazolium ring in **11**, and is

thus more effective at shielding the iridium core.

The results of combining a fluorine-free ligand scaffold with an intramolecular π-stacking interaction do appear to improve the stability of the emitter. The devices with both **10** and **11** are longer lived ($t_{1/2}$ = 24.3 h for **10** and 29.8 h for **11**) than any of the LEECs with other blue/blue-green emitters discussed so far (e.g. $t_{1/2}$ = 2.17 h for **7**), pointing to some extent to the merits of this strategy. However, it is important to note that the devices based on these materials are also greatly red-shifted. While the emitters are blue-green in solution, the devices based on these complexes are essentially yellow-green in colour (λ_{EL} = 560 nm for **10** and 556 nm for **11**; CIE: 0.43, 0.53 for **10** and 0.41, 0.53 for **11**), which is at least partly accountable for the improved device lifetimes. In addition, although there is a slight improvement in the device lifetime of the LEEC with **11** over that with **10**, this effect is not as pronounced as for some examples that will be discussed below. This is because of the weaker intramolecular π-stacking interaction associated with five-membered ring systems compared to their six-membered counterparts.

Finally, the use of complex **12**, a structurally related analogue of **11**, also attempts to combine strategies for improving stability with strategies for achieving blue emission. The ancillary ligand in this instance contains a pyrazole with coordination through the nitrogen. Complex **12**, like **11**, is fluorine-free and has an intramolecular π-stacking ring. This complex is red-shifted in MeCN solution compared to **10** or **11** (λ_{PL} = 480, 509 nm) but, surprisingly, is much bluer in the device, essentially retaining its solution-state emission characteristics (λ_{EL} = 486, 512 nm; CIE: 0.26, 0.48). The blue-shifted emission appears to impact the stability, however, with a lower device lifetime ($t_{1/2}$ = 15.8 h) compared to the LEECs with **10** or **11**. The lower device stability for the device with **12** is possibly due in part to its higher brightness compared to the LEECs with **10** or **11** (L_{max} = 15.4 cd m^{-2}) for **10**, 16.1 cd m^{-2} for **11** and 37.0 cd m^{-2} for **12**). Nevertheless, although these complexes are the most stable among blue-green LEECs, none of them come close to commercially relevant stability requirements or even to some of the stability metrics reported for yellow or orange devices (1000s of hours).

1.3.3 Green-Emitters for LEECs

Green emitters, like sky-blue emitters, appear to have the same trade-off in device performances: devices based on these complexes have been shown to achieve high efficiencies,

but also relatively low device lifetimes. Since many green-emitting complexes also contain fluorinated cyclometalating ligands, this may account for their shorter device lifetimes compared to yellow or orange LEECs. A summary of the emitters discussed in this section is given in Table 1.4.

Complex	λ_{PL} (nm)	Φ_{PL} (%)	EQE (%)	$t_{1/2}$ (h)	CIE	λ_{EL} (nm)	Ref.
13	535	28	7.1	12	0.35, 0.57	535	[128]
14	512	70	14.9	9	0.30, 0.45	525	[129]
15^a			8.2	98	0.38, 0.57	554	[130]
15^b	552	69	2.9	59.8	0.38, 0.57	554	[93]
16	555	52	2.9	48.3	0.39, 0.56	558	[93]
17	555	59	3.0	55.0	0.42, 0.55	552	[93]
18	554	62	2.9	13.2	0.39, 0.55	555	[93]
19	548	32	2.3	223	0.44, 0.55	555	[89]
20	559	54	2.2	356	0.47, 0.52	570	[89]

Table 1.4: Summary of LEECs employing green-emitting iTMCs. Definitions: λ_{PL} is the solution-state emission maximum in MeCN; Φ_{PL} is the solution-state photoluminescence quantum yield in MeCN; EQE is external quantum efficiency; $t_{1/2}$ is the time taken for the device luminance to fall to half the maximum value; CIE are the Commission Internationale de l'Eclairage defined X,Y coordinates of colour; λ_{EL} is the electroluminescence maximum. ^{a} Operated under pulsed current conditions, with an average current density of 25 A m^{-2}. ^{b} Operated under pulsed current conditions, with an average current density of 100 A m^{-2}.

1.3.3.1 Efficiency

Most LEECs reported, even now, employ constant voltage driving methods as a means of powering the device. Such a method results in generally slow turn-on times, but good performance metrics in terms of brightness and efficiency have been reported. Two of the best performing LEECs were reported employing complexes **13** and **14**. The crucial design feature of **13** is that it contains a bulky 4,5-diaza-9,9'-spirobifluorene ancillary ligand.[128] The bulk of this ligand ensures that intermolecular quenching in the solid state is minimised. Indeed, the photoluminescence quantum yield in the neat film (Φ_{PL} = 31%) is in fact not measurably different compared to the quantum yield in solution (Φ_{PL} = 28%). Ultimately, it is this high neat film quantum yield that accounts for the very good device efficiency

(EQE = 7.1%). Similarly, complex **14** employs the bulky dtbubpy ancillary ligand. In this case, the quantum yields are even higher (Φ_{PL} = 70% in solution and 72% in the film used for the device), giving device efficiencies that are extraordinarily high (EQE = 14.9%).[129]

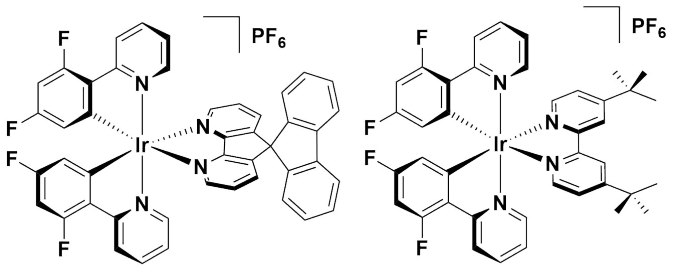

Figure 1.19: Efficient green-emitting devices based on constant voltage driving conditions.

Both of these devices are driven at a constant voltage (2.8 V for **13** and 3.0 V for **14**). This driving method leads to some drawbacks, including long device turn-on times (t_{on} = 1.5 h for **13** and 0.8 h for **14**) and also relatively poor stability ($t_{1/2}$ = 12 h for **13** and 9 h for **14**) for both devices. However, it is worth noting that a pulsed current LEEC based on **14** has been reported, demonstrating much lower efficiencies (EQE = 2.83%) than reported under constant voltage.[93]

In recent years an alternative driving method has become prevalent for operating these devices. Using a pulsed current driving method, high device efficiencies are also possible, but not at the expense of the stability or turn-on times of the devices. Arguably the champion green LEEC published to date is based on complex **15**, which uses a pulsed current driving method to operate the device.[130] In the report, the authors explored driving the devices under a variety of different conditions, including varying the duty cycles from 25% to 100% (the latter of which correlates to operation under constant current) and also the average pulsed current density, from 18.75 to 150 A m^{-2}. After much optimisation, it was found that a 75% duty cycle with a pulsed current density of 25 A m^{-2} led to the best overall device performance. Crucially, it was found that high device efficiencies (EQE = 8.2%) were possible, without adversely affecting the stability ($t_{1/2}$ = 98 h) or the turn on time (t_{on} = 0.2 s). Indeed, these metrics make this LEEC the best overall, certainly when accounting for the slow turn-on times and stabilities reported for the constant voltage LEECs employing **13** and **14**.

1.3.3.2 Stability

Complex **15** has also been reported as part of a larger study into the stability of iridium complexes bearing fluorinated C^N ligands.[93] As previously identified, such complexes are expected to be unstable, due to the reactivity of such aromatic rings bearing fluorine substituents, particularly when bound to the metal. To equivocally study this, Baranoff and co-workers synthesised complexes **15** – **18**, and studied their performance in the LEEC. All four complexes were designed to have similar photophysical properties (λ_{PL} = 552 – 555 nm, Φ_{EL} = 52 – 69%), with complex **18** compensating for the electron withdrawing effects of the additional fluorine atoms on the C^N ligands by adopting moderately electron releasing methyl groups in a *para* relationship with respect to the metal. These similar properties in solution translate into similar device performances as well (EQE = 2.9 – 3.0%, L_{max} = 1028 – 1095 cd m^{-2}), such that the stability values are directly comparable. It was observed that among the four complexes, complex **18**, bearing four fluorine atoms, shows greatly reduced device lifetimes ($t_{1/2}$ = 13.2 h) compared with the other three complexes ($t_{1/2}$ = 48.3 – 59.8 h for complexes 13 – 15). The device lifetimes for complexes 13 – 15 are by comparison rather long for green emitters; indeed, only complexes **19** and **20** are longer lived 'green' emitters in the device.

Complexes **19** and **20** provide a good comparison with **15**. The electroluminescence of these complexes is only slightly red-shifted (CIE: 0.44, 0.55 for **19** and 0.47, 0.52 for **20**; λ_{EL} = 555 nm for **19** and 570 nm for **20**) compared to **15** (CIE: 0.38, 0.57, λ_{EL} = 554 nm), but they show greatly improved stabilities ($t_{1/2}$ = 98 h for **15**, 223 h for **19** and 356 h for **20**). This is attributed to the methyl groups in the ortho- position with respect to the pyridyl nitrogen atoms, which act in a similar fashion to the intramolecularly π-stacking phenyl rings for **11** and **12**. It is plausible also that the lack of fluorine substituents appended to complexes **19** and **20** also adds to their stability in the device.

1.3.4 Yellow/Orange-Emitters for LEECs

Moving from green emitters to yellow/orange leads to a pattern becoming apparent: as the colour of the device shifts from blue to yellow the efficiency of the devices generally decreases, but the stability improves. Indeed, emitters of these colours surpass all others in terms of stability, with the most stable devices reported to date emitting in this colour regime.

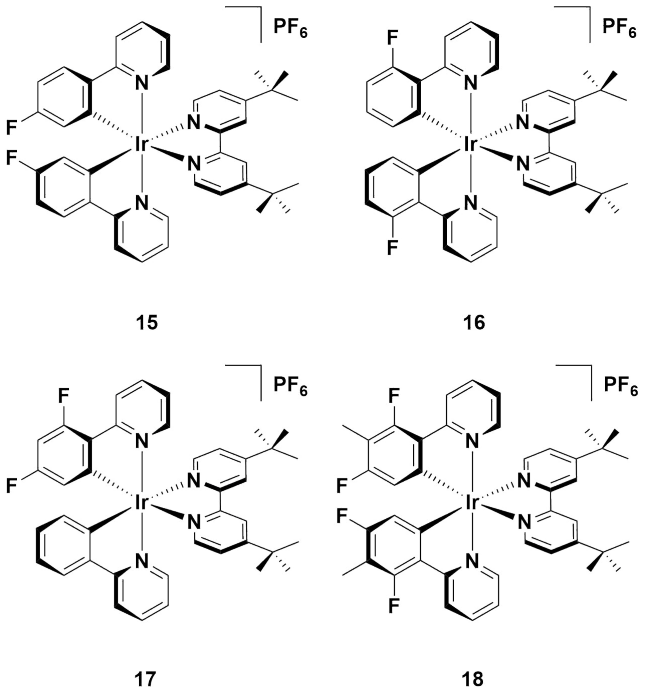

Figure 1.20: Multiply fluorinated green-emitting iridium complexes. The tetra-fluorinated complex displays much faster device degradation than the bis-fluorinated complexes, despite otherwise comparable device performances.

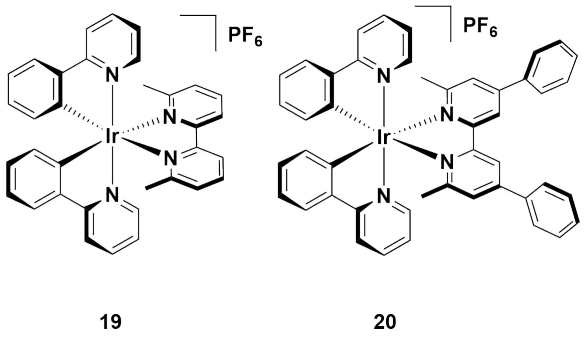

Figure 1.21: High stability green emitters.

1.3.4.1 Efficiency

Efficiencies reported for yellow/orange LEECs tend not to be as high as for green LEECs, although several examples of complexes with comparable efficiencies have been reported. For example, the external quantum efficiencies reported for the devices using **21** and **22** (Figure 1.22) are two of the highest (EQE = 6.1% for both **21** and **22**) reported for this colour to date.[112;127] The origin of the high efficiency for **21** is not explained. In solution this complex is not especially emissive (Φ_{PL} = 9% in MeCN) and no thin film PL data

Complex	λ_{PL} (nm)	Φ_{PL} (%)	EQE (%)	$t_{1/2}$ (h)	CIE	λ_{EL} (nm)	Ref.
21	588	9	6.1		0.53, 0.47	588	[112]
22	595	7	6.1	660			[127]
23	605	23	9.2		0.51, 0.48	580	[117;128]
24	568	59	5.5			566	[131]
25	570	47	4.0			577	[131]
26	595	3	4.0	3000			[126]
27	595	3	1.1	1300			[132]
28	574	2		2000	0.49, 0.50		[133]
29	623	26	0.3	110	0.55, 0.44	594	[134]
30^a	593	5	3.4	950			[127]
30^b				>4000			[135]
31	583	43		2000	0.54, 0.44	589	[136]
32	600	13		2800			[125]
33	611	4		1204			[125]
34	645	2		>2800			[125]

Table 1.5: Summary of LEECs employing yellow/orange-emitting iTMCs. Definitions: λ_{PL} is the solution-state emission maximum in MeCN; Φ_{PL} is the solution-state photoluminescence quantum yield in MeCN; EQE is external quantum efficiency; $t_{1/2}$ is the time taken for the device luminance to fall to half the maximum value; CIE are the Commission Internationale de l'Eclairage defined X,Y coordinates of colour; λ_{EL} is the electroluminescence maximum. ^{a} Operated under constant voltage conditions, with an applied voltage of 3.0 V. ^{b} Operated under pulsed current conditions, with an average current density of 185 A m^{-2}.

is reported. Complex **22** is also poorly emissive in solution (Φ_{PL} = 7% in MeCN) but in this instance the value reported for the Φ_{PL} in the film is much higher (Φ_{PL} = 47% in a film of iridium complex and ionic liquid in 4:1 molar ratio), which accounts for the good device performance. As with other complexes previously discussed, the performance of **22** in the device is attributed to the presence of the bulky hydrophobic substituents on the complex, which contribute to decreased quenching of the excitons formed in the device. An added benefit of the substitutions on the ancillary bipyridine ligand is that they improve the stability of the emitter in the device, with a very good device lifetime compared to many other LEECs reported in the literature ($t_{1/2}$ = 660 h). This result is in contrast with

the LEECs using complexes **11** and **12**, wherein the shielding of the iridium centre by the intramolecular π-stacking interaction was mitigated somewhat by the use of five-membered pyrazole and imidazolium rings.

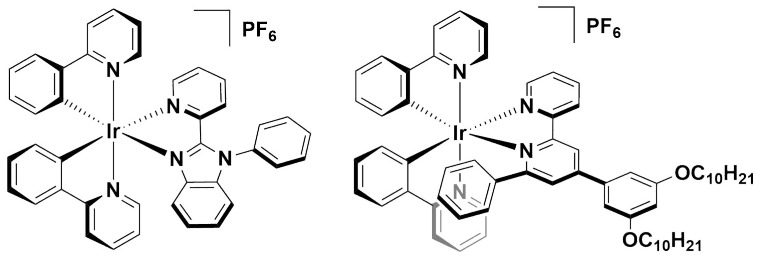

21 **22**

Figure 1.22: Yellow/orange emitters showing high device efficiencies.

The highest efficiency yellow/orange device reported to date is complex **23**, which is the fluorine-free analogue of complex **13**, using the same 4,5-diaza-9,9'-spirobifluorene compound as the diimine ligand.[117;128] Steric bulk of this ligand remains an important factor in preventing intermolecular quenching in the device by increasing the spacing between the chromophores, leading to a reasonably bright emitter in solution (Φ_{PL} = 23%) and solid state (Φ_{PL} = 33% in the 'LEEC' film containing the iridium complex and ionic liquid in a 1.3:1.0 molar ratio). Its initial device efficiency was reported to be 7.1% using a simple LEEC architecture [ITO/Ir:[BMIM][PF_6] (1.3:1.0 molar ratio)/Ag]. However, studies on improving the carrier injection efficiency of the device have since led to a record quantum efficiency (EQE = 9.2%) reported for a yellow/orange device, based on a related device architecture [ITO/PEDOT:PSS/Ir:[BMIM][PF_6]/Ag. This improved performance is likely to be due to the fact that **23** has preferred electron-transporting characteristics,[117] and thus PEDOT:PSS, which is effective as a hole injecting layer, helps to balance charge transport in the device.

It is curious to note however, that analogues of **23**, using the same diazafluorenyl-type ligand (**24** and **25**) are in fact brighter in solution than **23** (Φ_{PL} = 59% and 47%, respectively), but display poorer performance in the device.[131] These emitters were designed to explore strategies for improving the turn-on time of the LEEC, with the charged groups appended to **25** anticipated to increase the rate of ion separation in the emissive layer, similar to a previously reported series of complexes bearing cationic ammonium substituents,[137] and thus more quickly lower the barrier to charge injection into the device. This effect is

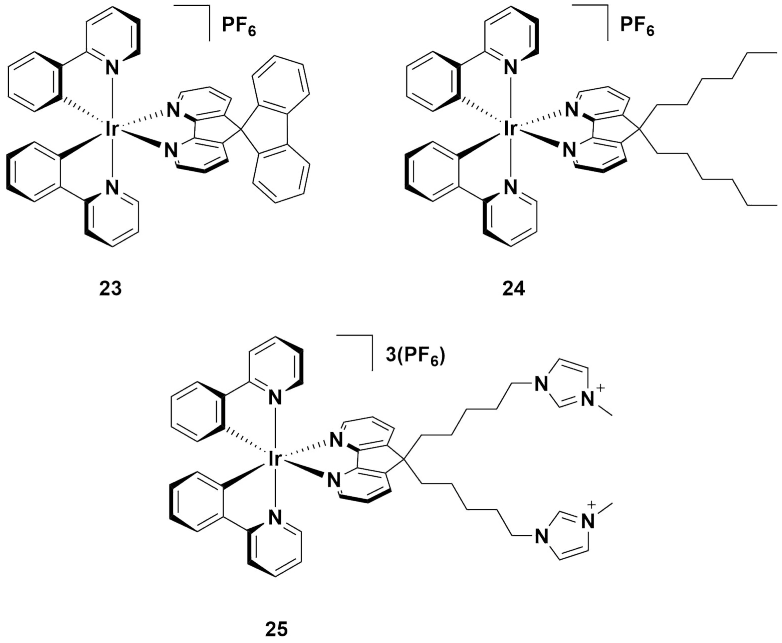

Figure 1.23: High efficiency yellow/orange emitter (**23**) and related analogues (**24** and **25**).

achieved (t_{on} = 1.1 h for **24** and 0.2 h for **25**) but at the detriment of the performance of the emitter in the device (EQE = 5.5% for 23 and 4.0% for 24), suggesting that even minor changes to functionality peripheral to the electronics of the emitter can nevertheless have a significant effect on the efficiency (Figure 1.23).

1.3.4.2 Stability

Complex **26** is the first example reported of a complex containing the intramolecular π-stacking motif alluded to previously. Within **26**, there is a short centroid-to-centroid distance of 3.48 Å between the phenyl ring on the bpy and one of the cyclometalating phenyl rings. This tight interaction maintains the structural integrity of the inner coordination sphere, even when the anti-bonding e_g orbitals of the ^{3}MC states are populated, prohibiting extension of $N_{pyridyl}$-Ir bond of the C^N ligands, and thus inhibiting potential nucleophiles from coordinating to the metal centre upon population of the ^{3}MC states. The devices reported based on this emitter were operated under constant voltage and two device lifetime values have been reported ($t_{1/2}$ = ca. 1300 h[127;132;138] or 3000 h[126]), with the longer value resulting from operating the device with a pre-biasing method (Figure 1.24).

Although the intramolecular π-stack is an effective strategy for increasing device stability, it does have limits: complex **27**, with two incorporated π-stacking phenyl rings on the

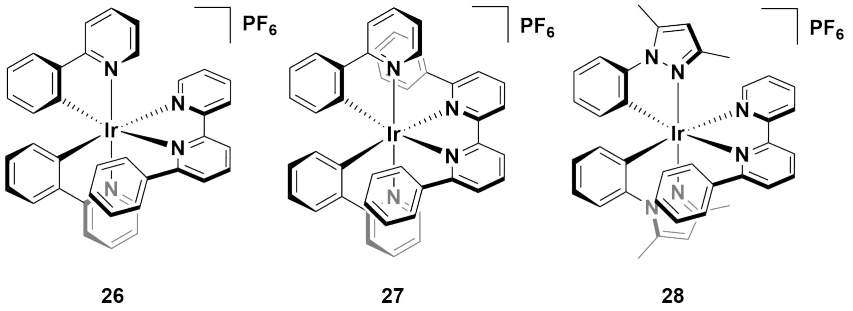

Figure 1.24: High stability LEECs operated under constant voltage conditions.

ancillary ligand results in poorer device performance compared to that with **26**.[132] In a comparable study, devices based on **26** and **27** both show long lifetimes ($t_{1/2}$ = 1300 h for **26** and **27**). However, the luminance values of **26** (L_{max} = 110 cd m^{-2}) are higher than for **27** (L_{max} = 70 cd m^{-2}). Devices with different luminance levels are not necessarily comparable in terms of stability, since brighter devices intrinsically degrade more quickly. Thus, to compare devices of different luminance levels it has been argued that considering the total photon flux emitted from the device once the luminance reaches 1/5 of the maximum value, $E_{t1/5}$, is a more accurate assessment of its stability. In this instance, **26** showed higher $E_{t1/5}$ values (13.6 J) than **27** (6.9 J), and thus it was concluded to be the more stable emitter. This lower stability was rationalized on the basis that the although the additional π-stacking ring further shields the metal centre, in order to maximize this dual π-stacking interaction, a distortion of the inner coordination-sphere of the complex is required. This distortion, counter to the design principle, actually makes the ^{3}MC states more thermally accessible, thus promoting exciton quenching and making the complex more susceptible to degradation reactions in the device.

An alternative strategy designed to protect the iridium from adventitious attack of small molecule nucleophiles is shown for complex **28**.[133] Here, the methyl groups appended to the pyrazole rings add an additional steric shield to the metal centre similar to complexes **19** and **20**. This strategy confers excellent stability to the LEEC with the device with **28** showing higher lifetimes ($t_{1/2}$ = 2000 h) than those reported using **26** as the reference emitter ($t_{1/2}$ = 1290 h). Indeed, based on the performances of a variety of complexes bearing hydrophobic substituents, it has become a generally accepted paradigm that such motifs appear to improve the stability of the emitter in the device. For example, the phenyl rings on the 5,5'-positions of the ancillary ligand of complex **29** do not form any kind

of intramolecular π-stacking motif, or act as a steric shield as the methyl groups do for complexes **19**, **20** or **28**. Nevertheless, the hydrophobicity of these rings appear to lead to good device performances, with good brightness (L_{max} = 130 cd m^{-2}) and a reasonable device lifetime ($t_{1/2}$ = 110 h).[134]

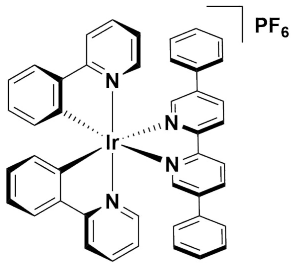

29

Figure 1.25: Stable LEEC employing hydrophobic substituents.

Given the aforementioned benefits of pulsed current LEECs, it is plausible that were pulsed current LEECs based on complexes **26**–**29** be reported, they would perform even better. Complex **30**, which is the methoxy analogue of **22**, is a good example of the contrasting performances of an emitter in a LEEC under constant voltage and pulsed current conditions. Under constant driving voltage, the device was reported to show good stability ($t_{1/2}$ = 950 h),[127] but this is well below the value reported for the same emitter operated under pulsed current conditions ($t_{1/2}$ = 4000 h).[135] Indeed, this latter lifetime is the longest reported for any iridium-based LEEC to date. The long lifetime in the device is coupled with higher brightness (L_{max} = 650 cd m^{-2} under pulsed current and 183 cd m^{-2} under constant voltage), which suggests that it is in fact even more stable under pulsed current conditions than the device lifetimes suggest, although $E_{t1/5}$ values are not reported for either device. It is worth noting that the current efficiency (CE) of the device under constant voltage conditions is higher than under pulsued current (CE = 8.2 cd A^{-1} under constant voltage versus 3.6 cd A^{-1} for pulsed current).

The merits of the pulsed current driving method are exemplified by the device with **31**. An extensive literature survey suggests that this complex is the only emitter reported with a device lifetime of greater than one thousand hours ($t_{1/2}$ = 2000 h) that does not have an intramolecular π-stacking motif. The device with this complex also shows a higher efficiency than that with **30** (CE = 6.5 cd A^{-1}) under pulsed current driving.[136]

Finally, complex **32** represents arguably the most stable emitter reported to date.[125] The

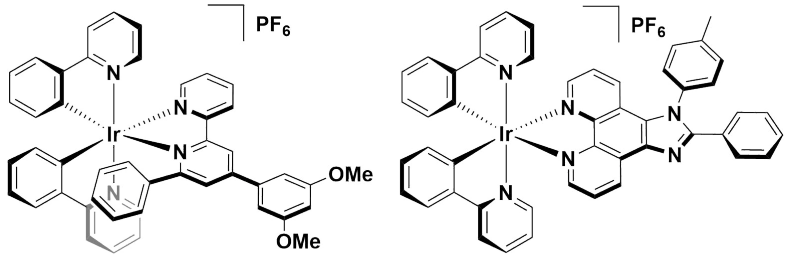

30 31

Figure 1.26: High stability LEECs operated under pulsed current conditions.

values reported for complexes **32** – **34** are from operating the devices at an exceptionally high current density of 300 A m^{-2}. Typically, pulsed-current LEECs are operated at average current densities of 50 – 100 A m^{-2} (**30** was operated at an average of 185 A m^{-2} and **31** at 100 A m^{-2}); however, at these current densities no discernible degradation of the devices could be observed and thus a much higher average current density was required. The high stability of the device at these current densities for all three complexes ($t_{1/2}$ = 2800 h for **32**, 1204 h for **33**, and >2800 h for **34**) is attributed to the use of silver salts during the synthesis to minimise the presence of chloride impurities, which as discussed in Section 1.3.1.2, are detrimental to the performance of iTMCs in the device.

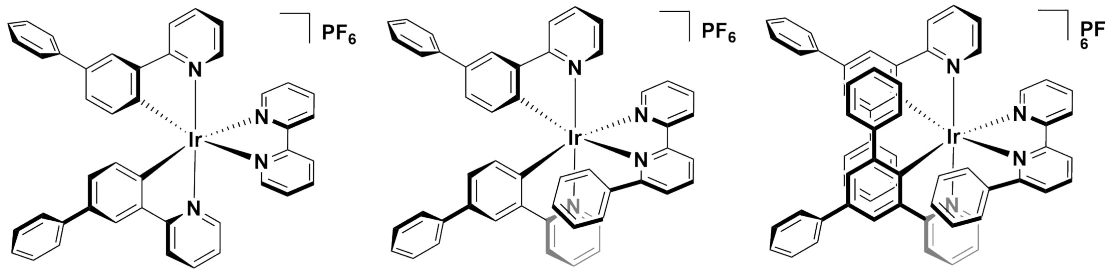

32 33 34

Figure 1.27: Champion-pulsed current LEEC for stability (**32**) and related analogues (**33** and **34**).

Although the device lifetime data would suggest that **34** is the most stable in the device, no $E_{t1/5}$ values are reported to affirm this assertion. In fact, comparing the luminance values for the three devices demonstrates that the device based on **32** is in fact much brighter (L_{max} = 1024 cd m^{-2}) than either complexes **33** (L_{max} = 676 cd m^{-2}) or **34** (L_{max} = 261 cd m^{-2}), suggesting that **32** is more stable than **34**. Although such high stability values are welcome for these devices, it is perhaps surprising that **32** is the most stable,

since it is also the simplest of these structures, with only two hydrophobic phenyl rings attached to the C^N and no intramolecular π-stacking motifs as in **33** and **34**. These results illustrate that there are still challenges for correlating the structure of an emitter to its performance in the device.

1.3.5 Red-Emitters for LEECs

Although the challenge of designing blue emitters is still the greatest for LEECs (no LEEC so far has been reported to even achieve deep-blue emission, let alone with good device performance), only a small number of LEECs have been reported to have CIE coordinates close to the ideal red value (CIE 0.66, 0.33) and, like the blue LEECs reported to date, these devices all show poorer stability compared with yellow/orange LEECs (Table 1.6).

Complex	λ_{PL} (nm)	Φ_{PL} (%)	EQE (%)	$t_{1/2}$ (h)	CIE	λ_{EL} (nm)	Ref.
35	624	0.7	7.4		0.67, 0.32	635	[75]
36[a]	627	3	2.6		0.66, 0.33	650	[112]
37	556	24	9.5	8.2	0.59, 0.40	624	[92]
38	573	58	2.7	9.8	0.50, 0.41	616	[92]
39	619	55	3.3		0.65, 0.34	644	[139]
40	666	2.6	0.08	6.3	0.68, 0.33	666	[140]
41	608	6	1.7	25	0.59, 0.41	607	[141]
42	687	2		0.5	0.71, 0.28	630	[142]
43	687	1		37	0.69, 0.29	660	[142]

Table 1.6: Summary of LEECs employing red-emitting iTMCs. Definitions: λ_{PL} is the solution-state emission maximum in MeCN; Φ_{PL} is the solution-state photoluminescence quantum yield in MeCN; EQE is external quantum efficiency; $t_{1/2}$ is the time taken for the device luminance to fall to half the maximum value; CIE are the Commission Internationale de l'Eclairage defined X,Y coordinates of colour; λ_{EL} is the electroluminescence maximum.

1.3.5.1 Efficiency

Although heterocycles such as pyrazoles and imidazoles are rarely used for red emission (due to their strong σ-donating character and their tendency to induce a blue-shift in the emission compared with pyridyl rings), two of the best red-emitting devices nevertheless utilise such heterocycles. Complex **35** utilises a phenylpyrazole-type cyclometalating ligand

but compensates for its blue-shifting effect by incorporation of the highly conjugated 2,2'-biquinoline ancillary ligand to red shift the emission.[75] Similarly, the LUMO destabilising capabilities of the imidazole ring contained within the ancillary ligand of **36** are also compensated for by the anellation of the imidazole ligand and appended quinoline.[112] Both of these complexes are red emitters (λ_{PL} = 624 nm for **35** and 627 nm for **36**) in MeCN solution but they are only poorly emissive (Φ_{PL} = 0.7% for 34 and 3% for 35), presumably as a function of the energy gap law. Photoluminescence quantum yield data in the solid state is not reported for either of these emitters so it is not possible to correlate these to the device performances. However, somewhat surprisingly given the low Φ_{PL} values in solution, high efficiencies are reported for both devices, particularly the device based on **35**, (EQE = 7.4% for **35** and 2.6% for **36**), making them among the best red devices reported to date. In addition, the colour of both devices essentially coincides with the pure red CIE coordinate (CIE 0.67, 0.32 for **35** and 0.66, 0.33 for **36**).

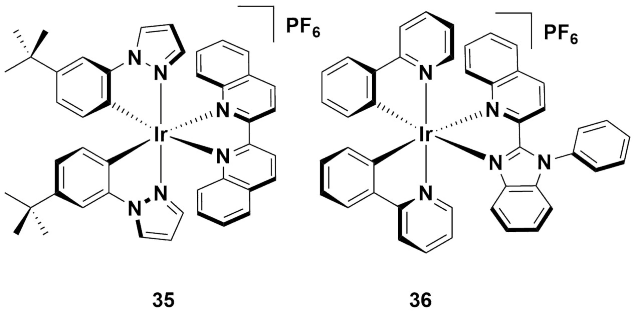

Figure 1.28: High efficiency, red-emitting iridium complexes.

One of the intrinsic issues with blue emitters is that the emission is frequently red-shifted in the device. For red emitters, this feature can act as an advantage, exemplified by complexes **37** and **38**.[92] In solution these complexes emit yellow light (λ_{PL} = 573 nm for **36** and 556 nm for **37**), but in neat film (λ_{PL} = 627 nm for **36** and 625 nm for **37**) and in the device (λ_{EL} = 624 nm for **36** and 616 nm for **37**) the emission is strongly red-shifted. The authors attribute this red shift to the possible formation of excimers in the condensed phase, due to strong π-π intermolecular stacking interactions observed in the crystal structures of both **37** and **38**. Crucially, this red shift in emission observed in the LEEC is accompanied with impressive device performance, particularly for **37**, which shows the highest device efficiency of any red or yellow/orange device reported to date (EQE = 9.5% for **37** and 2.7% for **38**). This high efficiency certainly qualifies **37** as the champion red-emitting device

reported to date. However, it is worth noting that the CIE coordinates of these devices (CIE 0.59, 0.40 for **37** and 0.50, 0.41 for **38**) are blue-shifted compared to the pure red CIE coordinates (CIE: 0.66, 0.33) required for RGB colour coordinates.

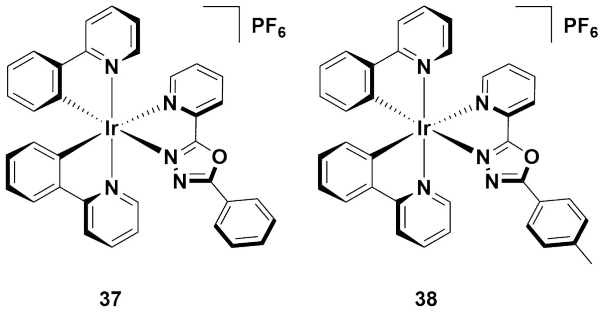

Figure 1.29: High efficiency, red-emitting iridium complexes.

Finally, complex **39** is an interesting red emitter.[139] The extended conjugation of the perylenediimide unit was used to achieve deep-red emission, while also functioning as an electron-transporting moiety to balance the hole conducting properties of the iridium component. However, it was found that the iridium(III) chromophore essentially does not contribute to the photophysics of the compound. The short emission lifetime (τ_e = 3.0 ns) and high quantum yield (Φ_{PL} = 55%) for a red emitter (λ_{PL} = 619 nm) point instead towards fluorescence directly from the perylenediimide chromophore; an assignment supported by theoretical calculations that implicated only the perylenediimide unit in the electronics of the HOMO or LUMO. Thus, the iridium in this case acts only as an appended charged unit to enable this material to function in the LEEC.

Crucially, the short emission lifetime is suggested to help in circumventing non-radiative quenching pathways in which typical triplet emitters are susceptible, leading to a good efficiency (EQE = 3.27%) for a red-emitting device (CIE 0.65, 0.34). Although a useful feature, it is unclear if this compound is purely a singlet emitter, or whether it is in fact harvesting triplets as well, which is an important feature of typical phosphorescent iridium complexes. In this instance, it is possible that this strategy is in fact wasting the triplets generated in the emissive layer, defeating the object of utilizing an iridium-based material in the first place.

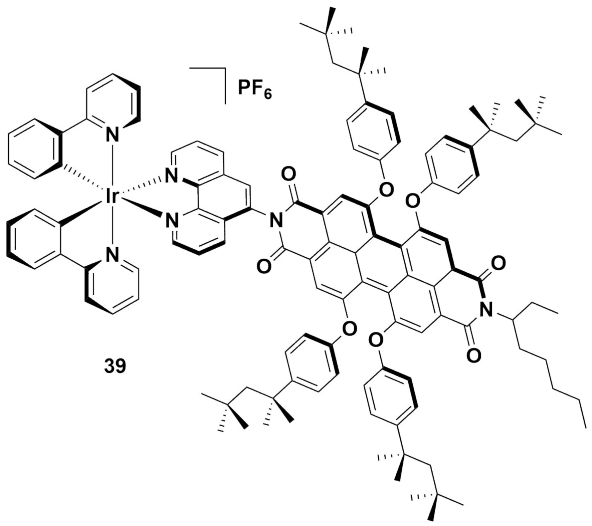

Figure 1.30: Deep-red-emitting iridium complex with good device efficiency.

1.3.5.2 Stability

Complex **40** employs a 2,5-dipyridyl(pyrazine) ancillary ligand which shows significantly red-shifted emission compared to complexes such as **4** as a result of the electron-withdrawing nature of the non-coordinating nitrogen on the pyrazine ring.[140] Thus, in this instance, the electron-withdrawing nitrogen acts to strongly stabilise the LUMO and red-shift the emission. Further narrowing of the HOMO-LUMO gap comes by way of the non-coordinating pyridyl ring, which extends the conjugation on the ancillary ligand, red-shifting the emission further, both in solution (λ_{PL} = 666 nm) and the device (CIE 0.68, 0.33; λ_{EL} = 666 nm). Although the efficiency of the device is low (EQE = 0.08%), the lifetime ($t_{1/2}$ = 6.3 h) is rather long for a deep-red-emitting device. As with the examples below, much shorter device lifetimes compared with yellow/orange seems to be a general feature of deep-red-emitting LEECs.

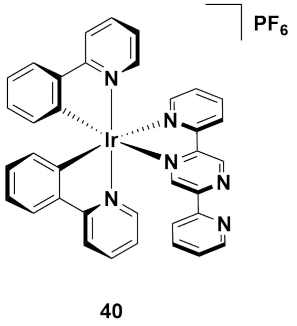

Figure 1.31: Iridium complex with good stability for a deep-red LEEC.

A number of red emitting intramolecularly π-stacked complexes have been reported but

few of them demonstrate any appreciable stability when compared to their yellow/orange analogues. Indeed, even in the case of the most stable of the red-emitting complex bearing an intramolecularly π-stacking motif, **41**, the device lifetime ($t_{1/2}$ = 25 h) is still very short compared with many other devices employing intramolecularly π-stacked complexes.[141] Although the luminance levels for this device are good (L_{max} = 626 cd m^{-2}), the yellow-emitting devices utilising structurally related complexes **33** and **34** are brighter and of course significantly longer lived. Clearly the stability of deep-red emitters is still lagging some way behind other devices reported to date.

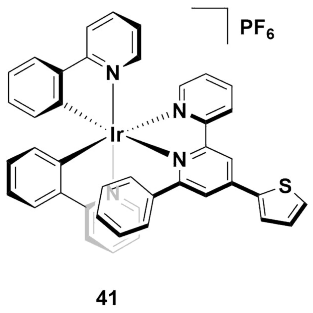

41

Figure 1.32: Intramolecularly π-stacked deep-red-emitting iridium complex.

An alternative strategy reported for improving the stability of this class of emitters is that shown in a comparative study between complexes **42** and **43**. Complex **42** displays deep red emission (λ_{PL} = 687 nm) as a result of the strongly electron-withdrawing ester groups appended to the ancillary ligand, which stabilise the LUMO. As with other red emitters discussed so far, the lifetime of the device based on **42** is short ($t_{1/2}$ = 0.52 h). However, covalently tethering the emitter to a polymer backbone (**43**) was found to give a material that upon spin coating gave a more uniform distribution of the complex within the emissive layer, reducing aggregate formation and also increasing the spatial distribution of the emitters within the device. These factors all acted to improve the stability, with a significant enhancement in the device lifetime with of **43** ($t_{1/2}$ = 37 h) compared to the device with **42**. Although in absolute terms the lifetime of **43** is still poor, it is nevertheless the longest of any red device (CIE 0.69, 0.29) reported to date, suggesting that this is a viable, underexplored strategy for improving the stability of the emitters in the devices, as well as highlighting similar challenges in achieving stable red LEECs as discussed for achieving stable blue LEECs.

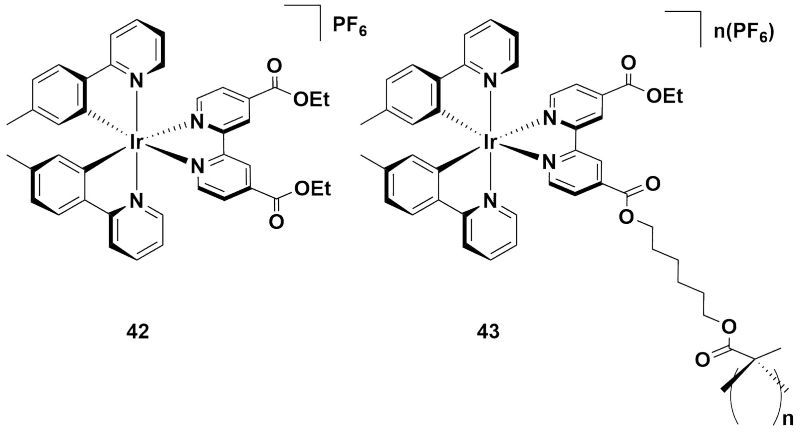

Figure 1.33: Deep-red-emitting iridium complex and its corresponding polymeric analogue, which shows greatly enhanced stability.

1.4 Objectives

This introduction has explored different ways of improving the properties of cationic iridium(III) complexes for LEECs, through the lens of colour tuning. This will inform the aims and objects of this thesis. Principally, the aim of this thesis is to design new iridium(III) complexes with improved properties, such as Φ_{PL} or colour, for optoelectronic applications. Chapter 2 will explore the design of new iridium complexes which exhibit deep-blue emission, which, as discussed, is a challenge. A particular focus will be placed on achieving *bright* deep-blue emission, which becomes difficult as the energy of the emission increases, due to the presence of typically low-lying MC states. Chapter 3 will build on the results of Chapter 2, but will focus on improving this ligand design, utilising a physical-organic approach, based on Hammett parameters, to design new ligands that also achieve deep-blue emission, but not at the expense of the stability of the emitter in the device. Chapter 4 moves from deep-blue to orange/red, with a view to applying the principles of improving Φ_{PL} to emitters that are susceptible to quenching by the energy gap law. Finally, Chapter 5 will focus on the design of even more red-shifted complexes, utilising an ancillary N^N ligand with donor-acceptor character that significantly red-shifts the absorption of the corresponding complexes beyond the normal profiles associated with $[Ir(C^N)_2(N^N)]^+$ complexes.

Chapter 2

Brightly Blue-Emitting Iridium Complexes

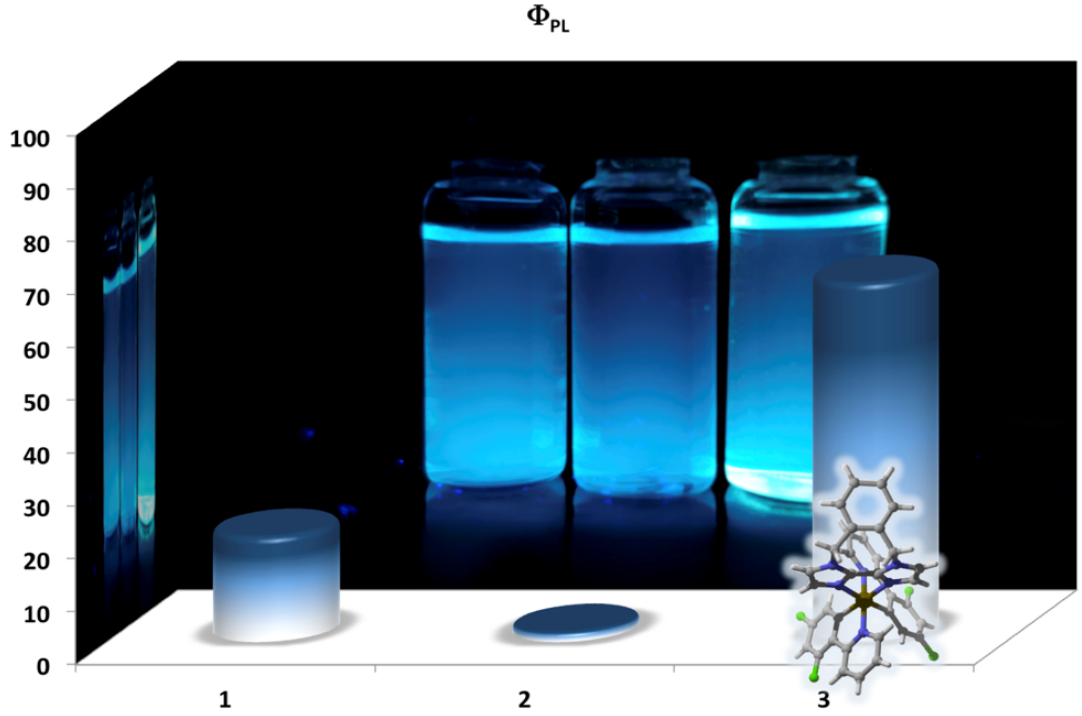

2.1 Introduction

2.1.1 Background

The previous chapter discussed some of the problems with fabricating devices based on phosphorescent blue emitters, particularly relating to their stability. In addition, Figure 1.13 outlined the deleterious effects of low-lying ^{3}MC states on the Φ_{PL} of these emitters.[52] Thus there is an urgent need for the design of new emitters that simultaneously emit *deep blue* and bright light.

This is apparent when surveying the literature for blue-emitting complexes bearing electron rich diimine ligands. For example, complex **6** was discussed in Chapter 1 as one of the leading blue-emitting complexes in LEECs, with emission in MeCN (λ_{PL} = 452, 480 nm)[110] significantly blue-shifted compared to the archetype complexes **4** (λ_{PL} = 585 nm)[89] or **14** (λ_{PL} = 512).[129] It is also blue-shifted compared to its ppy analogue (**44**). However, it is also relatively poorly emissive (Φ_{PL} = 20%), and lower in Φ_{PL} than **44** (Φ_{PL} = 23%), which ultimately results in a lower LEEC device efficiency as well (EQE = 0.3% for **6** and 1.6% for **44**).[110]

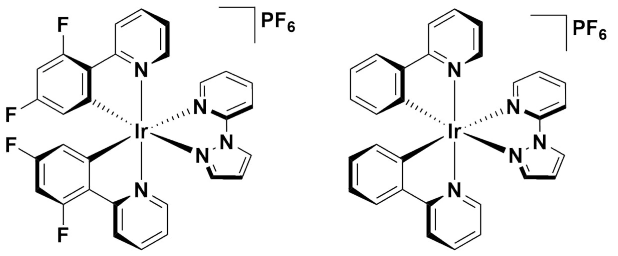

Complex:	6	44
λ_{PL} (nm):	451, 484	475, 503
Φ_{PL} (%):	20	23
η_{ext} (%):	0.3	1.6
CIE (x,y):	0.20, 0.28	0.29, 0.50

Figure 2.1: Blue-emitting iridium complexes containing pyrazole within the N^N ligand. Photophysics reported in MeCN.[110]

Adopting 1,2,3-triazoles instead of pyrazoles within the N^N framework also leads to deep blue emission (λ_{PL} = 452, 480 nm for **45**),[143] although the emission colour of **45** falls within the same regime as **6**, suggesting that as the emission becomes more ^{3}LC in nature, it becomes more difficult to destablise the LUMO further. This is exemplified by complexes **46** and **47**, which are designed to be bluer anologues of **45** by incorporating

1,2,3-triazoles within the C^N ligand framework, in addition to the triazole incorporated within N^N ligand.[84] Theoretical and experimental observations have shown that such phenyl-1,2,3-triazoles typically destabilise the LUMO, rather than the HOMO, despite their situation within the C^N ligand framework.[144;145] This is in contrast to ligands such as phenylpyrazoles, which stabilise the HOMO by their π-accepting properties.[75;146;147] However, complex **47**, which is structurally analogous **45**, also falls within the same solution state emission regime as **6** (λ_{PL} = 452 nm) and with lower quantum yield (Φ_{PL} = 0.05% for **47**) than **6** or **45**. However, this complex also displays emission that is more ^{3}CT in character, rather than ^{3}LC, compared to **6** or **45**, which is desirable due to the higher k_r values typically associated with such states. Complex **46** is expectedly red-shifted compared to **47**, with an enhanced, but still low, solution state quantum yield (λ_{PL} = 485 nm, Φ_{PL} = 0.2% for **46**). Curiously, in contrast to photophysics in solution, the device based on **46** is bluer than that of **47**.[84]

Trying to blue-shift the emission further by incorporating another triazole within the N^N ligand framework to give bis-1,2,3-triazoles does appear to be an effective strategy, with complex **48** displaying emission that is significantly blue-shifted compared to complexes such as **4** or **5** and also even the fluorinated analogue of **5**, complex **14** (λ_{PL} = 512 nm). Adopting phenyl-1,2,3-triazoles as the cyclometalating ligands does not significantly blue-shift the emission, although again the emission becomes more ^{3}CT in character. When the C^N ligand in **49** is modified to incorporate a 2,4-difluorophenyl ring, in this instance the emission does appear to blue-shift. However, the resultant complex **50** is photo-unstable, with this bis-triazole undergoing a photo-ejection mechanism.[148;149] Low temperature emission spectra could nevertheless be measured, with this complex emitting in the near UV (λ_{PL} = 393 nm at 77 K).

Examples of N^C: (where C: is an *N*-heterocyclic carbene) bearing complexes, such as **10** and **11**, were discussed previously as complexes which were sky-blue (λ_{PL} = 472, 501 nm for **10** and 477, 501 nm for **11**) in spite of their ppy cyclometalating ligands, but also poessessing very low quantum yields (Φ_{PL} = > 1% for **10** and **11**). This is true also for other NHC-containing complexes, such as **51** and its dFppy analogue **52**, which are both poorly emissive in solution (Φ_{PL} = 0.9% for **51** and 3% for **52**).[150] Curiously, adopting two NHCs to give a C:^C: ligand does not lead to any discernible blue-shift in the emission (λ_{PL} = 450 nm for **52** compared to 452, 482 nm for **53** and 452, 480 nm for **54**) but does lead to an enhancement in the Φ_{PL} (Φ_{PL} = 20% for **53** and 20% for **54**).[151] The emission can,

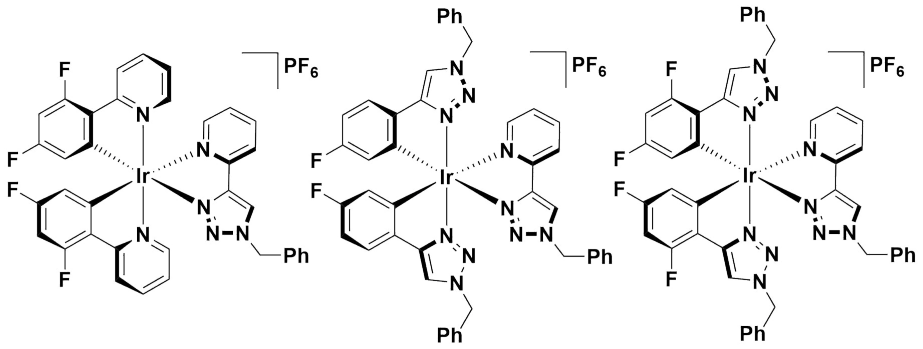

Complex:	45	46	47
λ_{PL} (nm):	452, 483	485	452
Φ_{PL} (%):	22	0.2	0.05
η_{ext} (%):	-	0.1	0.4
CIE (x,y):	-	0.26, 0.36	0.28, 0.45

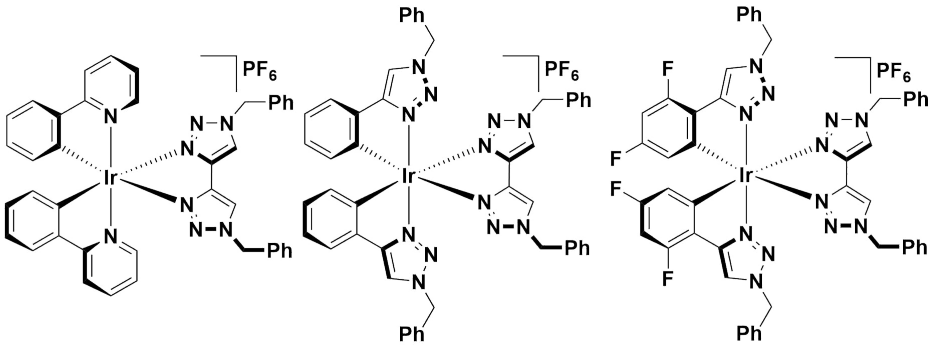

Complex:	48	49	50
λ_{PL} (nm):	481, 511	495	393 (at 77 K)
Φ_{PL} (%):	3	3	-

Figure 2.2: Blue-emitting iridium complexes containing 1,2,3-triazoles within the N^N ligand. Photophysics reported in DCM for complex **45** and MeCN for complexes **46** – **50**.[84;143;148]

however, be blue-shifted marginally further by incorporating a nitrogen atom with then phenyl ring of the C^N ligand, which in a *para*-relationship with respect to the metal acts as an electron-withdrawing group to stabilise the HOMO (λ_{PL} = 440 nm) but the quantum is also lowered (Φ_{PL} = 13%).[152] Ultimately, all of these numbers are still significantly lower than those reported for neutral analogues, such as **56** which is arguably the most efficient deep blue emitting iridium complex reported to date (λ_{PL} = 418 nm; Φ_{PL} = 76%).[108]

Finally, imidazoles are isomers of pyrazoles/NHCs which, aside from their use in SSL, have also spurred interest in more diverse applications as a result of their distal nitrogen atoms. For example, these -NH moieties have been exploited for their hydrogen-bonding properties, allowing the construction of supramolecular assemblies,[153;154] the design of

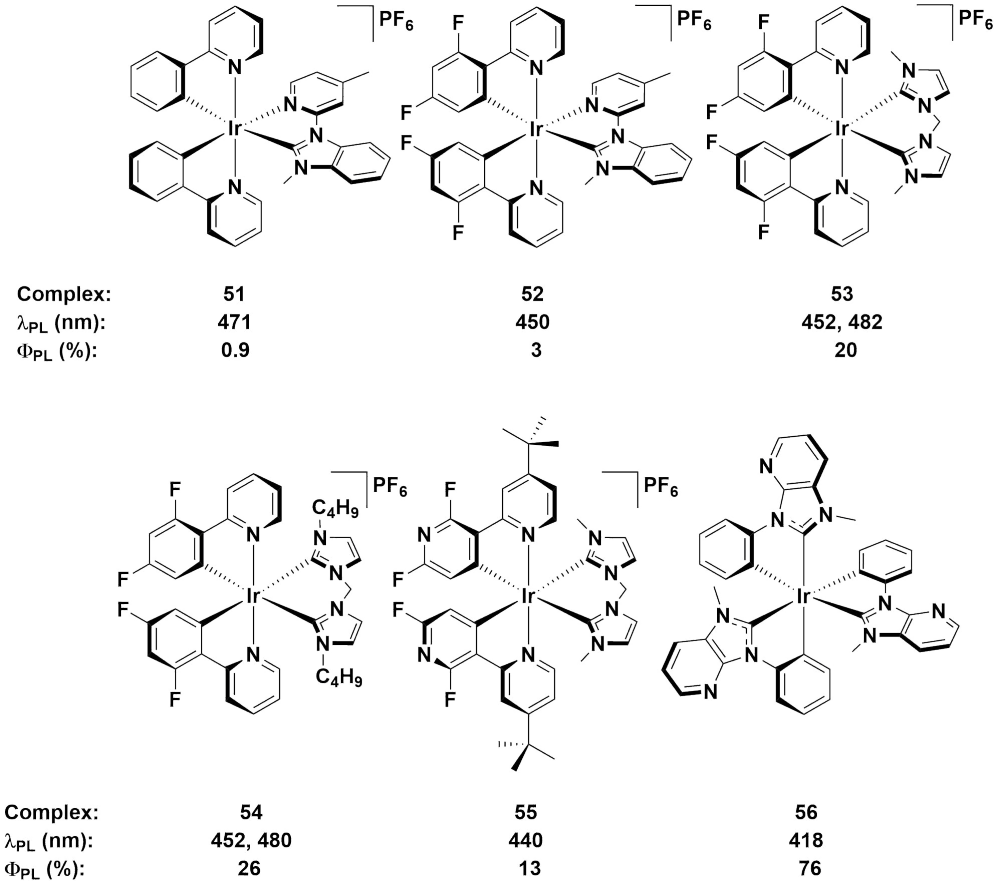

Figure 2.3: Blue-emitting iridium complexes containing NHCs within the N^N ligand. Photophysics reported in MeCN for complex **51**, **52** and **55**; in DCM for complexes **53** and **54**; 2-MeTHF for complex **56**.[108;150–152]

sensors[155–157] and bioimaging agents,[158;159] as well as for the design of systems to study excited state proton-coupled electron transfer (PCET).[160;161]

Optoelectronically, these heterocycles blue-shift the emission in a similar fashion to NHCs and pyrazoles, with complexes **57** and **58**, employing the ligands 1*H*,1'*H*-2,2'-biimidazole (H_2biim) and 1,1'-dimethyl-2,2'-biimidazole (dMebiim), both showing blue-green emission in solution (λ_{PL} = 484, 514 nm in DCM for **57** and 496 nm in MeCN for **58**). A quantum yield is not reported for **57**, but the value for **58** is low (Φ_{PL} = 5%). Complex **59** is expectedly blue-shifted (λ_{PL} = 456, 484 nm in DCM) and also poorly emissive (Φ_{PL} = 10%), although it is worth noting that the reference used for measuring the quantum yield of **59** (Φ_{PL} = 40% for *fac*-[Ir(ppy)$_3$]) is now defunct (Φ_{PL} = 97%)[52] and so the quantum yield for **59** is likely to be higher (ca. 25%).

So far, several of the complexes discussed have had emission spectra reported to be

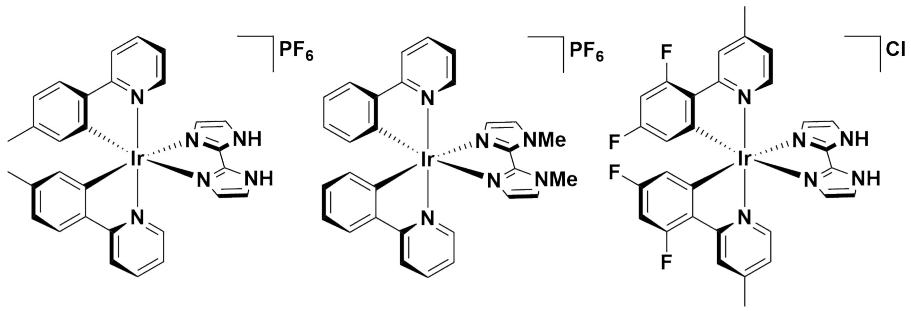

Complex:	57	58	59
λ_{PL} (nm):	484, 514	496	456, 484
Φ_{PL} (%):	-	5	10

Figure 2.4: Blue/blue-green-emitting iridium complexes containing biimidazole N^N ligands. Photophysics reported in DCM for complexes **57**[161] and **59**,[162] and in MeCN for complex **58**.[112]

deep blue in colour ($\lambda_{PL} < 460$ nm) but have also been poorly emissive ($\Phi_{PL} = 26\%$ for the most emissive, complex **54**). Thus research efforts have also been expended in increasing the quantum yields of such complexes. This can be done in two ways: increasing k_r, or decreasing k_{nr}. Increasing k_r is more difficult, since the SOC of the metal is constant, while often controlling the interplay between ^{3}CT and ^{3}LC states of the complex is not straightforward (i.e. designing emitters that emit explicitly from ^{3}MLCT/^{3}LLCT states), particularly in the blue where often the energies of the orbitals localised on the N^N ligands are destabilised to the point where the N^N ligands are no longer chromophoric, and the excited state becomes localised on the principally on the C^N ligand. In the past few years, studies on multimetallic assemblies have shown that such compounds can in fact display increased radiative rate constants compared to their mono-metallic analogues, by virtue of the increased SOC effects exerted by multiple metal centres. Such systems are rarely applicable to the blue since these assemblies are necessarily more conjugated and thus red-shifted in emission compared to their mono-metallic counterparts.[163–165]

Thus for blue emission, decreasing k_{nr} is a more viable strategy. This can be done in two main ways: 1) employing higher-order ter-,[151 167] tetra-,[168–170] or even hexadentate[171] chelates which act to rigidify the ligand scaffold and thus prohibit *intra*molecular ligand vibrations contributing to k_{nr}; 2) incorporate bulky substituents within the ligand scaffold which shield the metal centre from *inter*molecular quenching processes such as concentration quenching. Complex **8** and its trityl functionalised analogue **9** were examples of these, while complexes **60** – **63** further demonstrate this principle. Complex **60** is a reasonably emissive

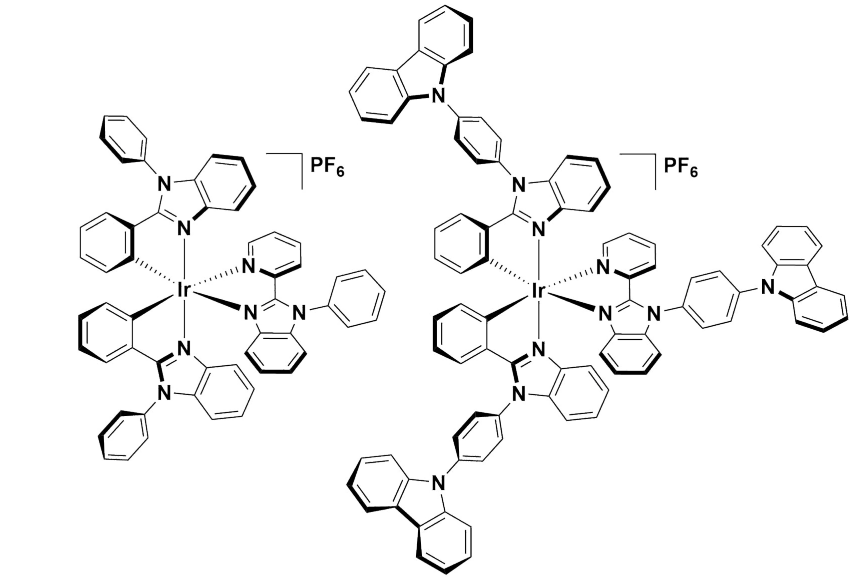

Complex:	60	61
λ_{PL} (nm):	571	577
Φ_{PL} (%):	18	31

Figure 2.5: Yellow-emitting iridium complexes containing benzimidazole C^N and N^N ligands. Complex **61** is more emissive due to the added bulk of the carbazolyl substituents. Photophysics reported in neat film for complexes **60** and **61**.[166]

yellow emitter (λ_{PL} = 569 nm in DCM and 571 nm in neat film) with a high quantum yield in solution (Φ_{PL} = 60% in DCM) that is greatly diminished in the solid state (Φ_{PL} = 18% in neat film). Complex **61** is an analogue of **60** that has carbazolyl substiuents appended to the C^N and N^N ligands. This complex emits in the same region as **60** (λ_{PL} = 570 nm in DCM and 577 nm in neat film) but with a diminished solution state quantum yield (Φ_{PL} = 44% in DCM), presumably due to increased quenching of the excited state by rotation of the carbazolyl units. However, in the solid state, the quantum yield is enhanced compared to that of **60** (Φ_{PL} = 31% in neat film), and this is attributed to the increased steric bulk of these units reducing concentration quenching, as well as restricted rotational freedom of the carbazolyl units.[166]

For complexes **62** and **63** this effect is even more pronouced. Complex **62**, known in the literature as FIrpic, is the most widely employed sky-blue emitter for vacuum-sublimed OLEDs to date.[173] However, its poor solubility makes it an unfavourable candidate for solution-processed OLEDs. It was recently reported that appending mesityl subtituents in complex **63** could accomplish a number of roles to improve the performance of the emitter in the device: 1) the mesityl unit confers improved solubility to allow formation of high

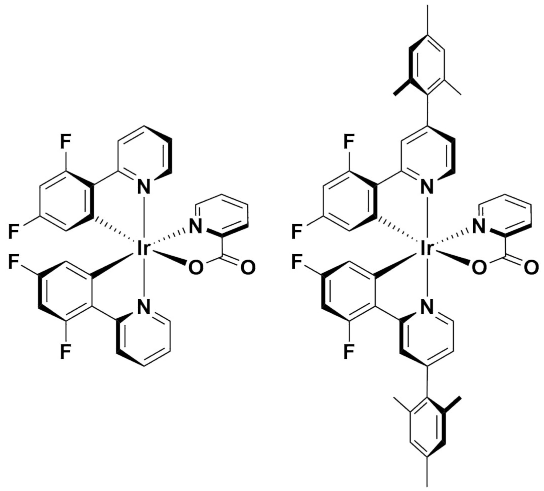

Complex:	62	63
λ_{PL} (nm):	469	475
Φ_{PL} (%):	54	92

Figure 2.6: Sky blue-emitting complex **62** (FIrpic) and its mesityl functionalised analogue **63**.[172]

quality spin-coated thin films from solution; 2) the increased steric bulk of the mesityl unit inhibits intermoleculer quenching processes, giving much brighter emission both in solution and in the device; 3) the mutual orthogonality of the mesityl group with respect to the cyclometalating ligand truncates any extension of the π-conjugation which would invoke an unwanted red-shift in emission. Accordingly, complex **63** emits in the same regime as **62** (λ_{PL} = 469 nm for **62** and 475 nm for **63**) but with vastly improved quantum yields (Φ_{PL} = 54% for **62** and 92% for **63**).[172]

2.1.2 Chapter Outline

It is clear from the preceding literature that combining bright emission with deep blue colour is a challenge, particularly for cationic complexes where the best examples reported are either not bright enough (e.g. complex **55**) or blue enough (complexes **7** or **9**; λ_{PL} = 489 nm and 472, 490 nm, respectively). In this chapter, a combination of strategies is employed to design cationic emitters that are simultaneously deep blue *and* efficient emitters. The first strategy outlines efforts to suppress *intra*molecular processes contributing to k_{nr}. It was surmised that the low quantum yield observed for complex **58**, despite its blue-green emission, was due to undesired twisting of the dMebiim ligand from the imposed steric strain of the methyl groups. It was thus hypothesized that adopting a tethering motif

between the two non-coordinating biimidazole nitrogen atoms would prohibit alleviation of the torsional strain, rigidifying the complex and resulting in a concomitant increase in Φ_{PL}. Four target complexes were identified (Figure 2.7) to test this hypothesis.[174] Complexes **64** and **65** would act as control complexes to study the effects of varying the steric bulk on the distal nitrogen atoms, while complexes **66** and **67** were the lead complexes. Crucially, from an optoelectronic perspective, all of these complexes should behave similarly to complex **59**, which was a deep blue emitter in solution. This is particularly important for complexes **66** and **67**, and thus the tethering units have been designed to be strictly non-conjugated with respect to the N^N ligand, and thus their influence should only be discernible in the excited state kinetics, rather than optoelectronics.

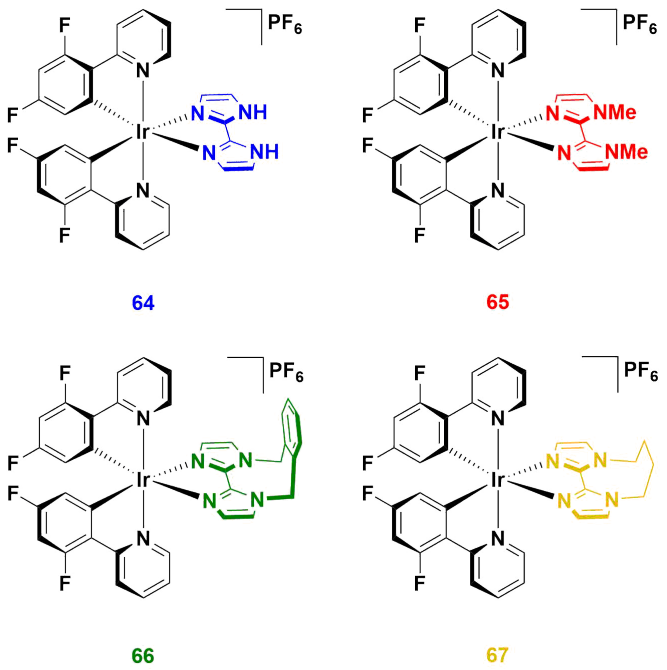

Figure 2.7: First generation of complexes containing biimidazole-type N^N ligands.[174]

The second strategy builds on the first, but in this instance targets the suppression of *inter*molecular processes contributing to k_{nr}. In particular, adopting the mesityl strategy employed effectively for complex **63** and several related analogues[91;175;176] in an effort to combine deep blue emission with near unitary quantum yields. For reference, complex **14** and its mesityl analogue **68** were synthesised to study the effects of the mesityl group. Complex **69** was the lead complex, designed to combine optimised C^N ligands with an optimised N^N ligand.[177]

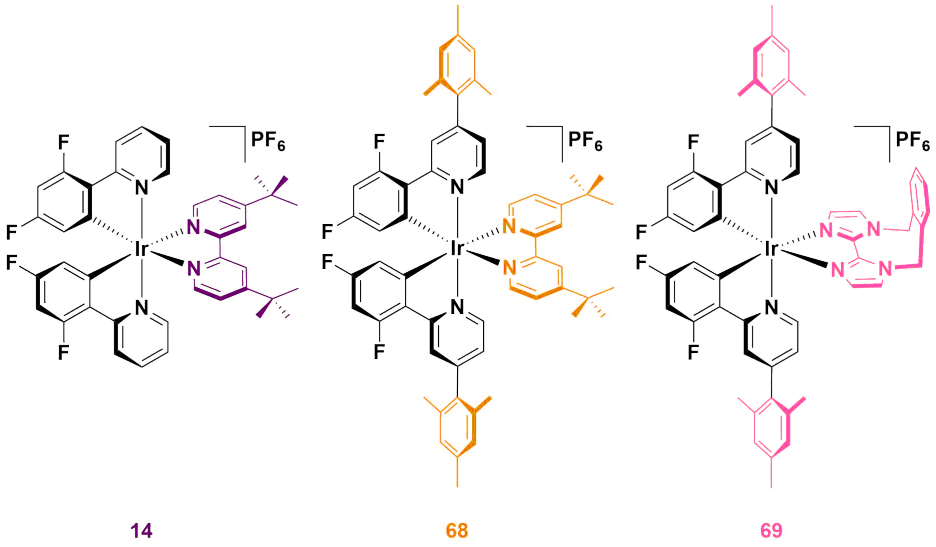

Figure 2.8: Second generation biimidazole-complex and reference analogues.[177]

2.2 Synthesis and Characterisation

2.2.1 Ligand Syntheses

The cyclometalating ligand 2-(2',4'-difluorophenyl)pyridine (dFppy) was chosen as this is the most common electron-deficient C^N ligand reported and would allow **64** to serve as an appropriate benchmark complex. The dFppy ligand was prepared in good yield in a similar manner to that reported previously,[178] by Suzuki-Miyaura cross-coupling 2,4-difluorophenylboronic acid and 2-bromopyridine. It had been reported that the analogous mesityl C^N ligand, 2-(2,4-difluorophenyl)-4-(2,4,6-trimethylphenyl)pyridine (dFMesppy), could be prepared by sequential Suzuki-Miyaura cross-coupling reactions starting from 2-chloro-4-iodopyridine, with first mesitylboronic acid and then 2,4-difluorophenylboronic acid as the corresponding coupling partners.[172] However, while the second was found to be straightforward, isolation of the 2-chloro-4-mesitylpyridine intermediate after the first step is more problematic.

The original procedure stipulated carrying out the reaction in a 1:1 stoichiometric ratio of mesitylboronic acid and 2-chloro-4-iodopyridine, presumably to avoid secondary cross-coupling at the 2-position of the pyridine. However, it was observed that mesitylboronic acid is prone to deborylation as a competitive undesired side reaction under these conditions, due to the bulk of the methyl groups in the 2,6-positions. The starting pyridine was thus always recovered from the reaction when carried out in this manner. Since the starting material

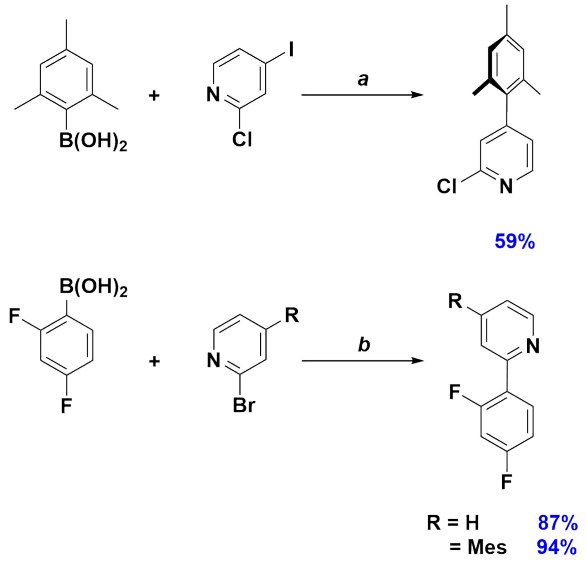

Figure 2.9: Synthesis of C^N ligands. Reagents and conditions: [a] K_2CO_3, 1,4-dioxane/water (2:1 v/v), $Pd(PPh_3)_4$ (5 mol%), N_2, 100 °C, 72 h. [b] Na_2CO_3, 1,4-dioxane/water (2:1 v/v), $Pd(PPh_3)_4$ (5 mol%), N_2, 100 °C, 19 h.

has virtually the same R_f as the product, isolating the desired precursor is not possible by column chromatography alone, requiring an additional Kugelrohr distillation step to obtain the product in good purity. To facilitate the purification process, it was determined that adding a large excess of boronic acid (1.5 – 1.8 equivalents) leads to complete consumption of the starting material, and crucially any side products generated from over cross coupling under these conditions were separable by column chromatography.

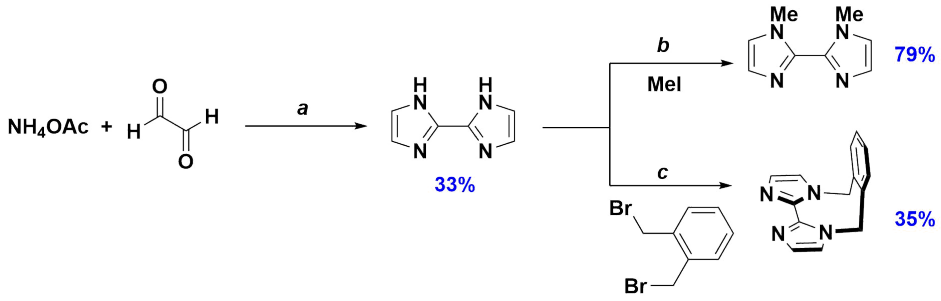

Figure 2.10: Synthesis of N^N ligands. Reagents and conditions: [a] H_2O, 40 °C, 8 h. [b] NaOH (35% w/v), DMF, RT, 12 h. [c] NaOH (35% w/v), MeCN, 82 °C, 12 h.

H_2biim was prepared in moderate yield by the condensation of glyoxal in the presence of ammonium acetate.[179;180] 1,1'-Dimethyl-2,2'-biimidazole (dMebiim) could be obtained by alkylation of H_2biim using methyl iodide in the presence of DMF and aqueous sodium hy-

droxide base at room temperature. Obtaining the alkylated product 1,1'-(α,α'-*o*-Xylylene)-2,2'-biimidazole (*o*-Xylbiim) was more difficult. The original report of this compound stipulates similar reaction conditions to dMebiim, but purification by sublimation is arduous and difficult to scale up.[179] Thus an alternative synthesis, wherein H_2biim was alkylated in MeCN instead was carried out. The compound could be purified by dissolving in DCM, and adding an excess of diethyl ether, which precipitated the impurities. Filtration and evaporation of the solvent gave the pure ligand. By contrast, despite repeated alkylation attempts, the butylene linked analogue ligand, Bubiim, was not able to be isolated in good purity.

2.2.2 Complex Syntheses

Initially, the dichloro-bridged iridium dimers $[Ir(C\hat{}N)_2(\mu\text{-}Cl)]_2$ were synthesised following Nonoyama's method,[181] in which the precursor dimer complex is obtained from refluxing $IrCl_3.3H_2O$ in the presence of C^N ligand in a high boiling alcoholic solvent, such as 2-methoxyethanol or 2-ethoxyethanol, for 19 – 24 h. Typically such dimers are isolated as a mixture of products (such as diastereomers) and so are used directly in the next step. However, it was observed that the dimers used from such a synthesis gave crude mixtures that also contained significant additional impurities, and in certain instances the resultant crude mixtures could sometimes not be purified at all, despite repeated column chromatography and recrystallisation steps. Indeed in some instances X-ray quality crystals could even be obtained from such recrystallisations, but nevertheless analysis of the bulk sample inevitably revealed presence of these impurities.

For example, Figure 2.11 shows the ^{19}F NMR of complex 14 following column chromatography. In addition to the two expected signals integrating in a 1:1 ratio (corresponding to the symmetric 4' and 6' fluorine atoms of each C^N ligand) there are three additional signals. It is now established in the literature that complexes bearing fluorinated cyclometalating ligands such as dFppy are unstable when subjected to harsh conditions, with reports of degradation of complexes in OLEDs,[122] LEECs (complexes **15** – **18**)[93] as well as in the presence of extreme heat.[123;182;183] Thus on the basis of these literature reports, the observation of three additional ^{19}F signals was attributed to loss of a single fluorine atom on one of the C^N ligands, which de-symmetrises each of remaining three fluorine atoms. To address this, the $[Ir(C\hat{}N)_2(\mu\text{-}Cl)]_2$ dimers were prepared using the iridium(I) precursor $[Ir(COD)(\mu\text{-}Cl)]_2$ (where COD is 1,5-cyclooctadiene), since these reactions have been shown

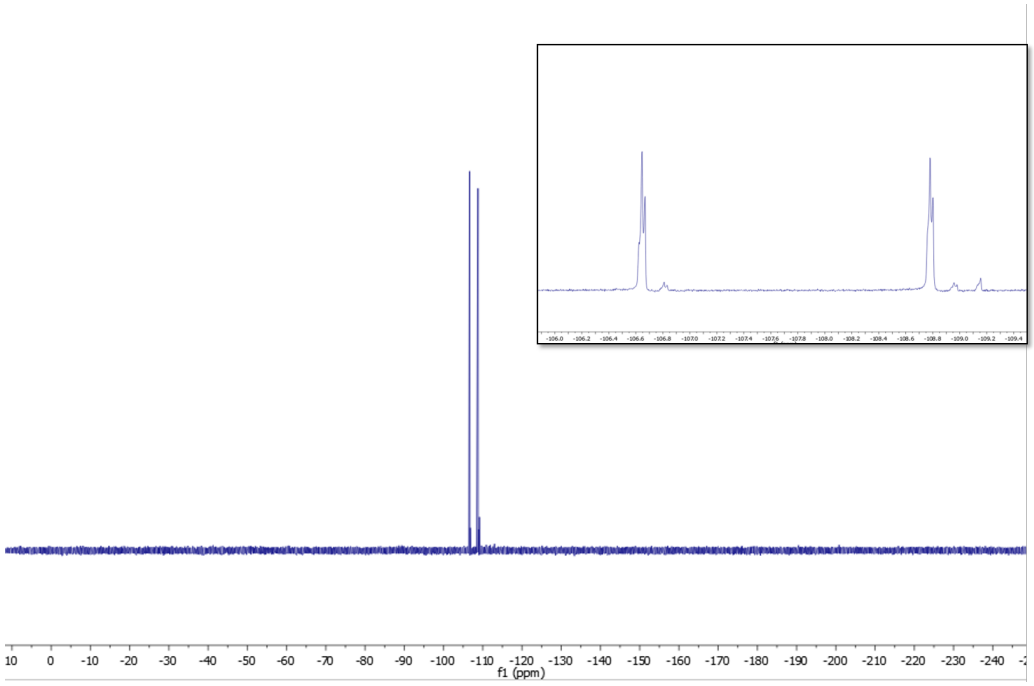

Figure 2.11: ^{19}F NMR spectrum of **14** synthesised from a batch of [Ir(dFppy)$_2$(μ-Cl)]$_2$ prepared by Nonoyama's method.[181] Inset: a close up of the spectrum showing the presence of additional ^{19}F resonances, attributed to the mono-defluorinated side product.

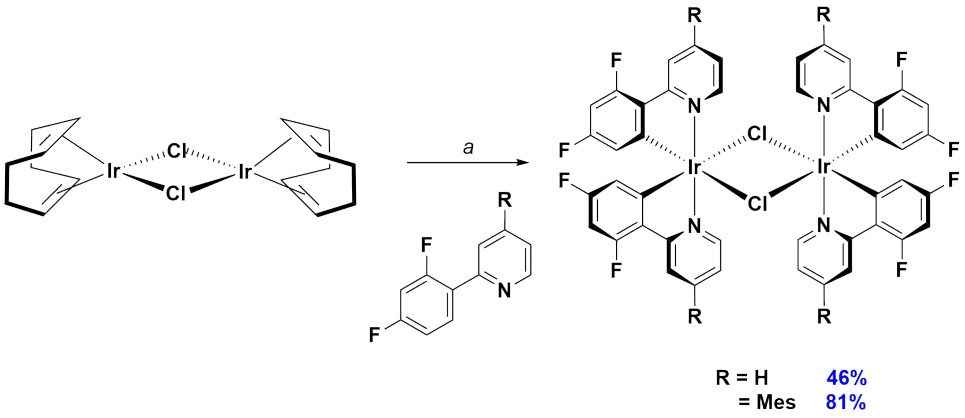

Figure 2.12: Synthesis of [Ir(C^N)$_2$(μ-Cl)]$_2$ dimers. Reagents and conditions: [a] 2-EtOC$_2$H$_4$OH, N$_2$, 110 °C, 3 h.

to proceed much more quickly (usually 3 h) and with the formation of much cleaner dimers that facilitate the purification of the subsequent complexes (Figure 2.12).[184–186] The complexes could then be synthesised in good yields by heating the dimers in a DCM/MeOH mixture with a slight excess of N^N ligand. Purification by column chromatography gave the materials as their chloride salts, which could be exchanged by a metathesis reaction

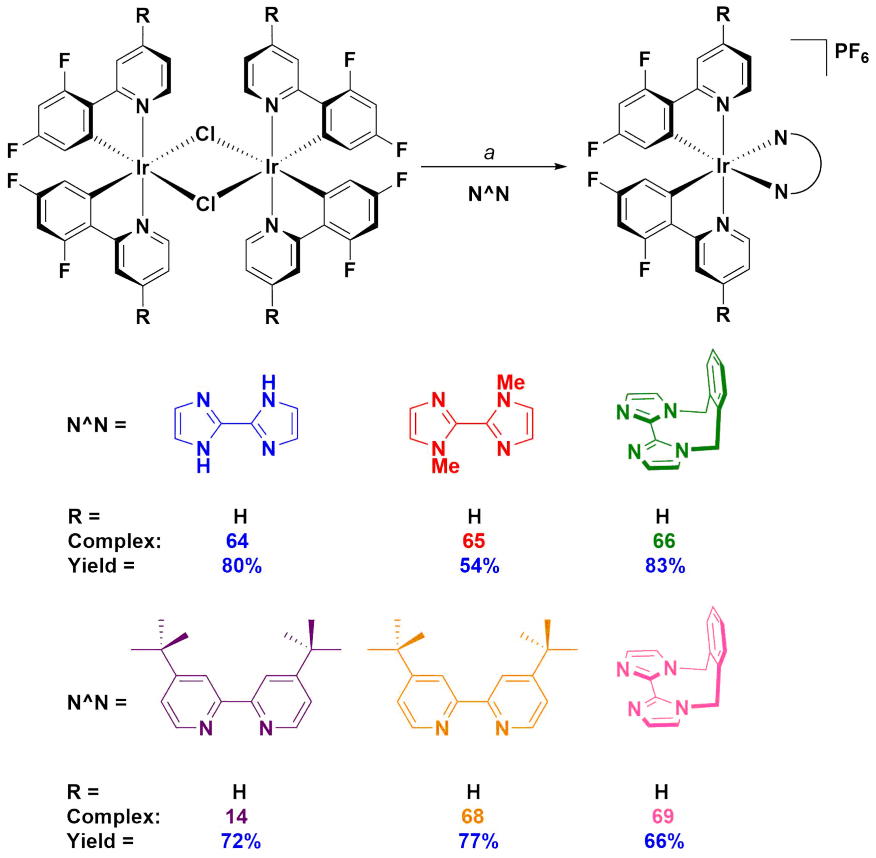

Figure 2.13: Synthesis of $[Ir(C\hat{}N)_2(N\hat{}N)](PF_6)$ complexes. Reagents and conditions: [a] i) DCM/MeOH (1:1 v/v), 40 ℃, N_2, 19 h ii) excess NH_4PF_6 (aq).

with excess aqueous NH_4PF_6.

2.2.3 Complex Characterisation

All complexes were characterised by ^1H, ^{19}F and ^{13}C NMR spectrocopy, although the poor solubility profiles of complexes **64**, **65** and **66** prohibited obtaining good ^{13}C spectra for these compounds. This poor solubility also meant their solution-state characterisation was carried out in DMSO-d_6, while complexes **14**, **68** and **69** were soluble in many other organic solvents such as $CDCl_3$, CD_2Cl_2 and CD_3CN. In addition, all the complexes were further characterised by high resolution mass spectrometry (HRMS) and elemental analysis (EA). Finally, X-ray quality crystals were grown of complexes **14** (suprisingly, despite several reports of this complex in the literature, single crystal data has not previously been reported),[129;185;186] **64**, **66**, **68** and **69**.

While the ^1H NMR spectra of complexes such as **64** and **65** are sharp and well-resolved, the ^1H NMR spectra of the complexes containing *o*-Xylbiim as the N^N ligand (**66** and **69**) give more ^1H resonances than expected (Figure 2.14).

The complexity of these spectra at room temperature was attributed to slow fluxional motion of the *o*-xylyl group, due to the conformational rigidity of the *o*-Xylbiim ligand. Since these complexes are isolated as a mixture of Δ and Λ isomers, this slow ring inversion process results in the detection of two or more diastereomeric atropisomers at this temperature. A similar feature is observed in the ^{19}F NMR spectrum, where the loss of pseudo-C_2 symmetry on the NMR timescale results in each ^{19}F atom experiencing its own unique magnetic environment. Thus the ^{19}F NMR spectrum of, for example, complex **69** presents itself as a spectrum of three peaks, two of which correspond to one fluorine atom and another resembling a broad multiplet that integrates to double the intensity of the other two peaks. Additionally, for complexes bearing the mesityl ring (complexes **68** and **69**) there is the additional slow rotation of the mesityl ring with respect to the C^N ligand, such that each of the methyl signals are unique by ^1H NMR.

Heating a solution of **66** and **69** in DMSO-d_6 results in sharpening of the ^1H signals as the rate of ring flipping of the *o*-Xylbiim ligand becomes fast on the NMR timescale (Figure 2.15). For **69**, this is accompanied by an increased rotation speed of the mesityl rings such that the methyl groups in an *ortho*- relationship with respect to the $C^N_{pyridyl}$ rings are no longer distinguishable. Using Eyring analysis, the barrier to ring flipping of

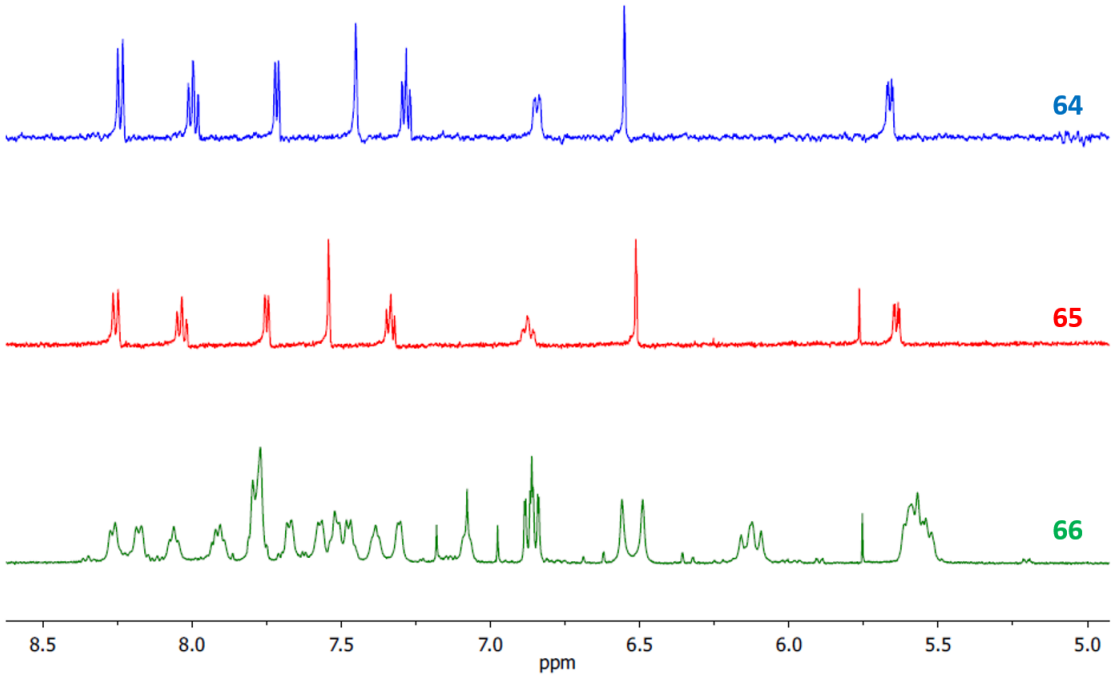

Figure 2.14: Stacked plot of ^{1}H NMR spectra of complexes **64**, **65** and **66** at room temperature in DMSO-d_6.

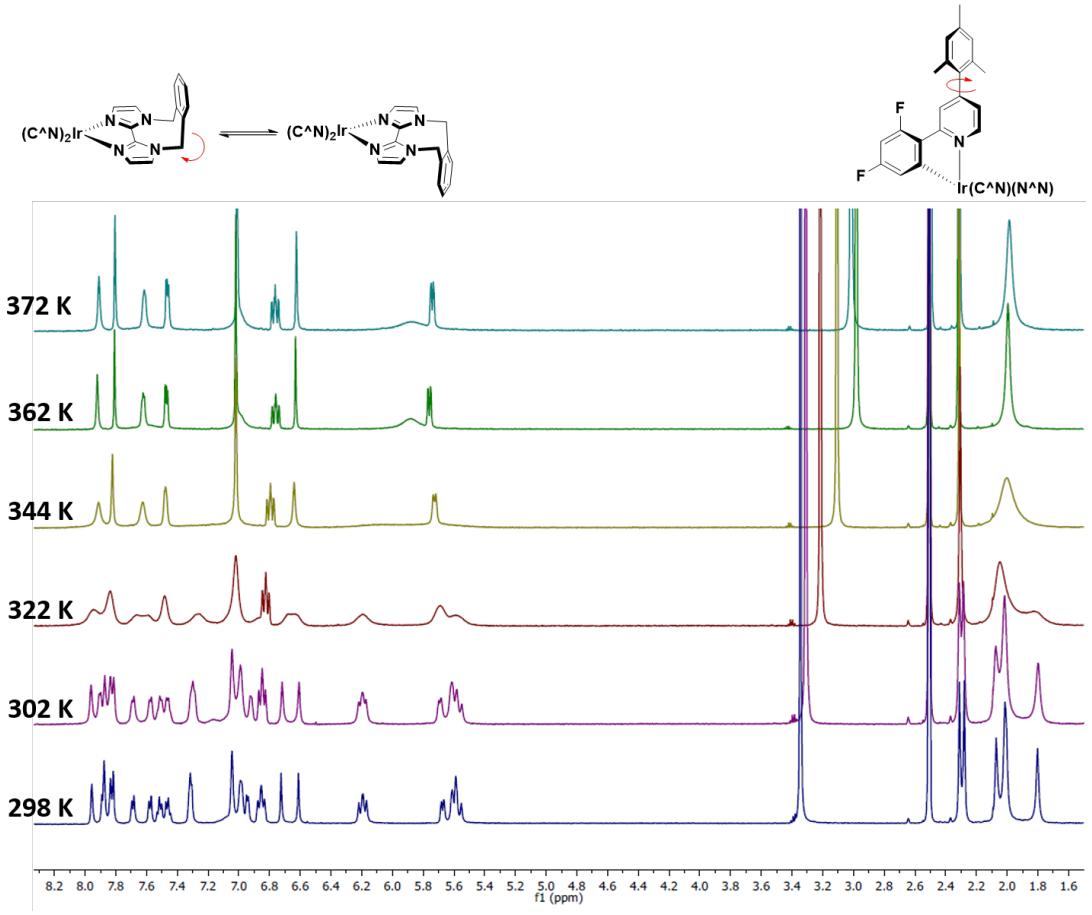

Figure 2.15: ^{1}H NMR temperature study complex **69** in DMSO-d_6 from 298 K to 372 K. Schemes showing the motion of **69** at high temperature are shown.

the *o*-Xylbiim ligand can be determined:[187]

$$\Delta G^{\ddagger} = -RT_c \cdot \ln\left(\frac{k_{\text{exch}}h}{k_B T_c}\right)$$

where $\Delta G^{\ddagger}$ is the Gibbs free energy of activation, R is the gas constant, T_c is the coalescence temperature, h is Planck's constant, k_B is Boltzmann's constant and k_{exch} is the rate constant of exchange, found with:

$$k_{\text{exch}} = \frac{\pi\Delta\nu_0}{\sqrt{2}}$$

where $\Delta\nu_0$ is the difference in ppm of the two coelescing signals at room temperature. Carrying out the appropriate analysis on complexes **66** and **69** give respective Gibbs free energy barriers to inversion of +83 (based on the doublet at 6.5 ppm) and +72 kJ mol^{-1} (based on the doublet at 6.7 ppm).

Suitable single crystals for X-ray diffraction analysis (Figure 2.16) were grown by vapour diffusion of Et_2O into MeCN (complexes **64**, **14** and **69**); Et_2O into DCM/MeOH (complex **66**); and $^{i}Pr_2O$ into MeCN (complex **68**). Analysis of X-ray structures is useful not just for elucidating molecular structure, but also because it can provide information as to the performance of the emitter in the devices, which operate in the solid state. Although solution processed devices are fabricated by spin-coating methods, which are intended to deposit wholly amorphous films, intermediate-range ordering within spin-coated films of materials such as $[Ru(bpy)_3](PF_6)_2$ has nonetheless been observed,[76] with such crystallinity believed to be an important factor in influencing the performance of the corresponding electroluminescent devices,[77] particularly in instances where the excited state is observed to change from solution to the solid state.[92;188;189]

All five complexes show the expected distorted octahedral geometry, with the $C\hat{}N_{pyridyl}$ nitrogen atoms in a *trans* disposition. In all of the complexes, the C^N ligands behave in a similar manner, with the Ir-C (1.98 – 2.03 Å) and Ir-$N_{C\hat{}N}$ (2.03 – 2.05 Å) bond lengths, and N-Ir-C bite angles (79.7 – 81.2°) all falling within a similar regime, suggesting that the nature of the N^N ligand (sterics, electronics) does not significantly influence the metal-C^N interactions. In all cases, shorter Ir-C bond lengths compared to Ir-$N_{C\hat{}N}$ are observed, indicative of a strong metal-carbanionic bond. The mesityl functionality appears to have very little influence over the coordination geometry as well. This is probably due to the large pyridyl-mesityl torsion angles (69.2 – 88.6°), which results in these mesityl rings being decoupled from the electronics of the C^N ligand.

Looking at the N^N ligands, the biimidazole complexes all have uniformly longer Ir-$N_{N\hat{}N}$ bond lengths (2.14 – 2.17 Å) than the bipyridine analogues (2.12 – 2.13 Å). This is a direct result of the complexes maintaining similar N-Ir-N bond angles (79.7 – 81.2°), which suggests that a direct result of employing a 5,5-ring system such as biimidazole is a moderately weaker Ir-N bond. Similar bond angles to the metal are reported in other biimidazole-to-metal crystal structures such as with iron (H_2biim = 80.4°, *o*-Xylbiim = 75.4°)[190] and with rhodium (H_2biim = 79.2°).[191] The N^N ligands are all relatively planar, which is important for maintaing the octahedral geometry of the metal and thus not inadvertently introducing undesirable non-radiative pathways.[132;152]

The packing of the complexes in the solid state reveals some interesting trends. Complex **64** is able to form strong hydrogen bonding interactions between the N-H hydrogen atoms

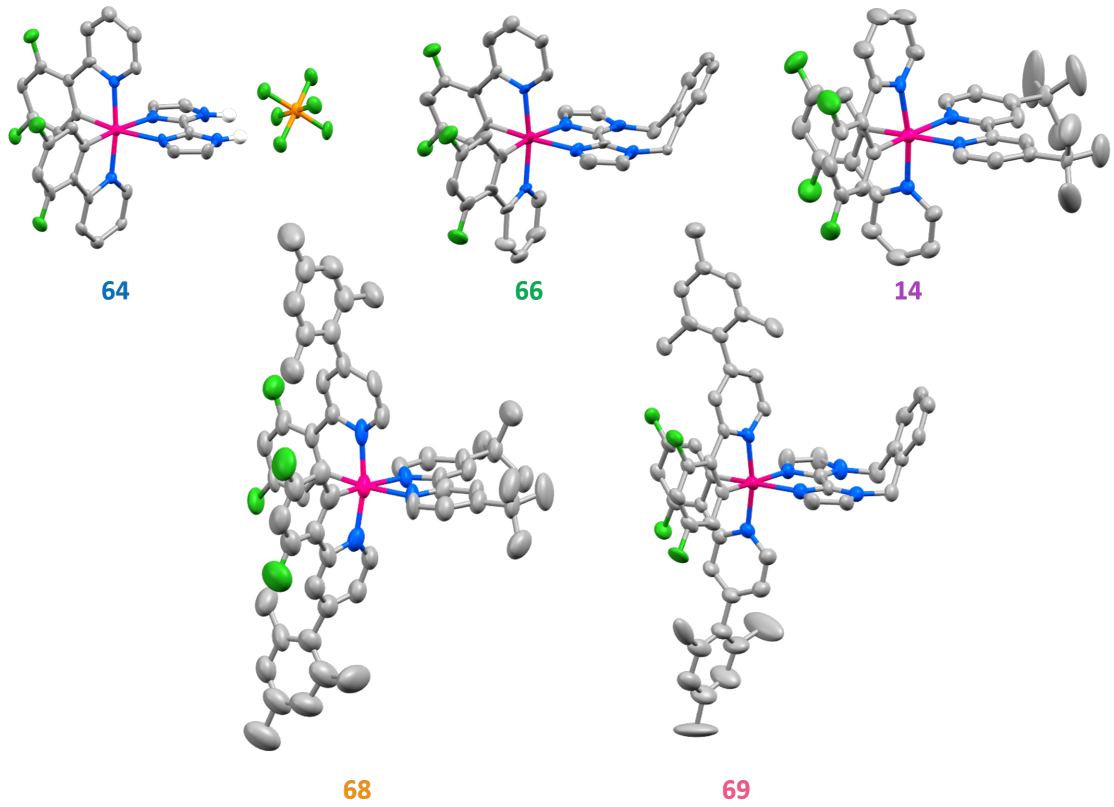

Figure 2.16: X-ray crystal structures of complexes **64**, **66**, **14**, **68** and **69**. Solvent molecules and C-H hydrogen atoms have been removed for clarity; counterions have been removed for clarity except for complex **64**, which forms a strong hydrogen bonding interaction between the N-H hydrogen atoms and the hexafluorophosphate anion. Thermal ellipsoids at 50% probability level.

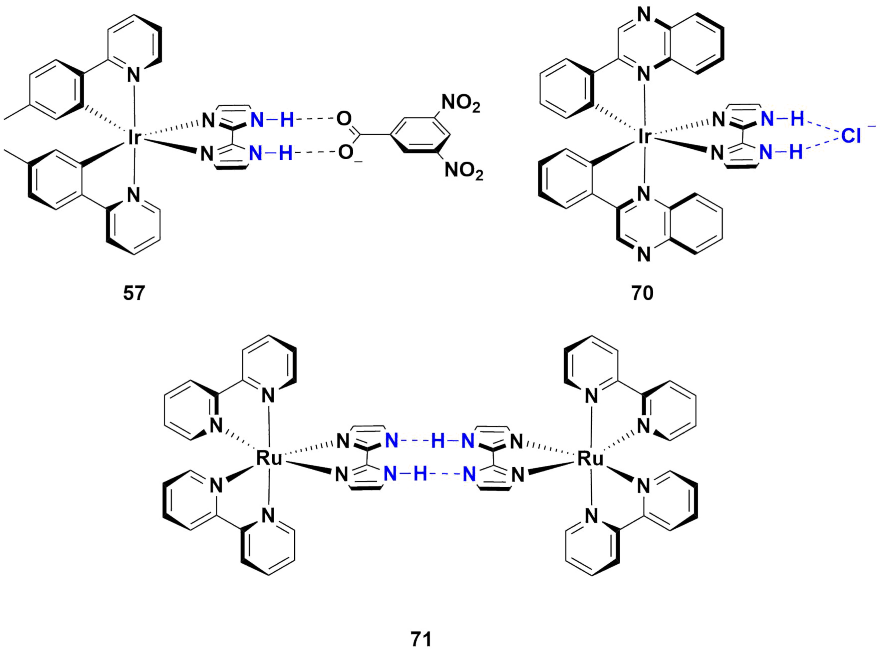

Figure 2.17: Examples of hydrogen-bonded biimidazole containing transition metal complexes.

and the hexafluorophosphate anion, similar to iridium complexes bearing pyridylimidazole-type ligands[155] and also other complexes bearing H_2biim as the ancillary ligand (Figure 2.17). For example, a crystal of complex **57** as its dinitrobenzoate salt has been reported, showing a strong interaction with the benzoate functionality, as well as complex **70** which forms a tight hydrogen-bonding interaction with its chloride counteranion.[192] This interaction is not specific to iridium, with examples in particular of ruthenium biimidazole complexes forming hydrogen bonding interactions with polyoxometalates,[154] cyanometallates[153] and even self-hydrogen bonded dimers when the H_2biim ligand is mono-deprotonated (complex **71**).[153;193] By contrast, complexes **66**, **14**, **68** and **69** show minimal interactions with their counteranions.

An analysis of the extended crystal packing reveals features that explain several photophysical phenomena observed in the solid state (*vide infra*). Complexes **66**, **14**, **68** and **69** all show similar shortest Ir-Ir internuclear distances (**66**: 8.830(5) Å, **14**: 8.5148(9) Å, **68**: 9.000(3) Å, **69**: 8.8803(7) Å), despite the other differences observed in intermolecular interactions. Complex **14**, appended with the bulky dtbubpy ligand, shows no strong intermolecular interactions in the solid state, with only weak C-H–π hydrogen bonds observed. In contrast, **66** forms ordered channels (Figure 2.18, top left) as a result of face-to-face

Complex	Bond Length (Å)			Bond Angle (°)		Torsion (°)
	Ir-C	Ir-$N_{C\hat{}N}$	Ir-$N_{N\hat{}N}$	N-Ir-C	N-Ir-N	N-C-C-N
64	2.019(10)	2.038(8)	2.158(8)	80.8(3)	76.1(2)	-2.3(12)
	2.033(8)	2.027(8)	2.173(6)	81.2(4)		
66	2.00(3)	2.051(13)	2.16(2)	79.7(7)	76.4(8)	8(2)
	1.98(2)	2.051(14)	2.136(18)	80.8(8)		
14	2.005(9)	2.035(6)	2.126(6)	81.0(3)	76.3(2)	6.1(9)
	2.013(7)	2.043(6)	2.127(7)	80.0(3)		
68	1.978(14)	2.032(13)	2.121(8)	81.2(6)	76.2(4)	0.9(18)
	2.020(11)	2.043(12)	2.128(9)	80.4(5)		
69	2.001(9)	2.048(6)	2.145(11)	79.9(3)	76.1(4)	-0.9(12)
	2.025(13)	2.041(8)	2.135(8)	80.6(4)		

Table 2.1: Selected crystallographic parameters for complexes **64**, **66**, **14**, **68** and **69**. The torsion angle is measuring the planarity of the N^N ligand.

π-stacking interactions between the *o*-Xylyl groups of neighbouring N^N ligands.

Despite the added bulk resulting from the mesityl groups present in **68** and **69**, these complexes show additional intermolecular interactions, with the complexes positioned such that two difluorophenyl rings of adjacent complexes are correctly positioned to facilitate a π-stacking interaction, with respective centroid–centroid distances of 3.628(8) and 3.531(7) Å (Figure 2.18, top right and bottom right). This interaction is facilitated by the propensity of fluorinated phenyl rings to more readily form π-stacking interactions than fluorine-free rings.[194] Indeed iridium complexes reported to contain the analogous fluorine-free cyclometalating ligand 2-phenyl-4-(2,4,6-trimethylphenyl)pyridine (Mesppy) do not appear to contain such π-stacking interactions,[176] suggesting these interactions are occuring in spite of the presence of the mesityl units. These interactions are strengthened by further mutual C-H–π contacts between the same adjacent complexes.

Finally, as with complex **66**, the packing in **69** is further ordered through a secondary π-stacking interaction between the Xylyl rings of the *o*-Xylbiim ligand of adjacent complexes. This combination of π-interactions results in the formation of strongly interacting chains of molecules running along the crystallographic *ab*-diagonal axis, with alternating long [15.0779(8) Å] and short [8.8803(7) Å] iridium-iridium distances (Figure 2.18).

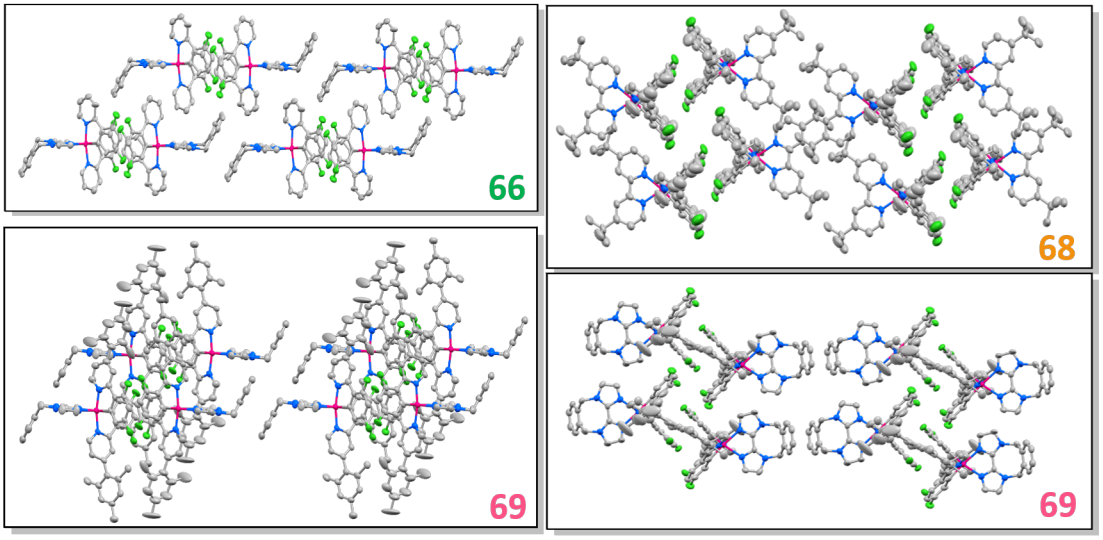

Figure 2.18: X-ray packing of: complex **66** viewed along the plane of the N^N ligand (top left); complex **68** viewed along the N_{C^N}-Ir-N_{C^N} axes (top right); complex **69** viewed along the plane of the N^N ligand (bottom left); complex **69** viewed along the N_{C^N}-Ir-N_{C^N} axes (bottom right).

2.3 Theoretical Calculations

A combined DFT and time-dependent DFT (TDDFT) study of complexes **64**, **65** and **66** was undertaken, and compared to the butylene-tethered analogue complex **67**, with a view to understanding how modifying the substituents on the distal nitrogen atoms affect the geometry of the complexes, as well as rationalising the photophyical properties of the isolated complexes.[195–200] The complexes were modeled using Gaussian 09[201] at the B3LYP[202–204] level of theory with the SBKJC-DVZ[205–208] basis set for iridium, 6-31G* for heavy atoms directly coordinated to iridium and 3-21G* for all other atoms[205;209–217] in the presence of the solvent MeCN.[218]

The geometry of the ground state structures was fully optimised without the imposition of symmetry restrictions. Each complex adopts a pseudo-octahedral geometry. Selected structural parameters for these complexes are summarised in Table 2.2. Computed geometries for **64** and **66** generally reproduce those found in the crystal structure, although the Ir-N_{N^N} and Ir-N_{C^N} bonds for **64** and **66** are predicted to be elongated by around 0.02 Å, while there is a slightly more pronounced torsion between the two imidazole fragments in the crystal structure of **66** of 8°. The geometries of the triplet state were optimised using spin-unrestricted DFT calculations at the UB3LYP level. In the triplet state, the Ir-N_{N^N} is

Complex	64		65		66		67	
	S_0	T_1	S_0	T_1	S_0	T_1	S_0	T_1
Ir-$N_{N^\wedge N}$	2.197	2.214	2.170	2.190	2.820	2.194	2.019	2.201
Ir-$N_{C^\wedge N}$	2.074	2.065	2.073	2.064	2.074	2.065	2.076	2.067
Ir-$C_{C^\wedge N}$	2.020	2.007	2.023	2.009	2.021	2.009	2.021	2.008
N-Ir-N	75.4	75.1	74.3	74.3	74.9	74.5	75.1	74.8
N-Ir-C	80.4	81.2	80.4	81.3	80.4	81.2	80.4	81.1
N-C-C-N	0.1	1.6	3.1	11.5	1.4	1.5	8.7	9.2

Table 2.2: Selected calculated average structural parameters for complexes **64**, **65**, **66** and **67**. The torsion angle is measuring the planarity of the N^N ligand. Bond lengths in Å and bond angles in °.

predicted to be slightly elongated compared to the ground state, while modest bond length contractions are predicted between the iridium center and the C^N ligands. Structural differences manifest most markedly in the N-C-C-N torsion of the N^N ligands. In particular, there is a large change in the N-C-C-N torsion observed for complex **65** when moving from the S_0 to T_1 states, with the T_1 state acting to minimise the repulsive interactions of the methyl groups. Complex **67** is predicted to have a much larger N-C-C-N torsional twist than **64** and **66** in both the S_0 and T_1. The relative flexiblity of the butylene linker allows for a degree of conformational compensation in the N-C-C-N dihedral angle in order to minimize the repulsive interactions of bridge, in a similar manner to the T_1 state of **65**, and thus these two complexes are predicted to have considerable non-radiative contributions to the excited state. By contrast, complex **66** exhibits the most rigid conformation and thus would be expected to have the lowest k_{nr} of these four complexes.

Figure 2.19 show a comparison of the relative energies of the five highest energy occupied and five lowest energy unoccupied molecular orbitals (MOs) for 1-3. The HOMO is localised on both the aryl ring of the C^N ligands and the iridium atom (t_{2g}); the LUMO is also situated on the dFppy ligands but with an increased contribution from the pyridyl rings as well. The HOMO-LUMO gap is predicted to be large for all three complexes, in the region of 4.16 eV. Alkylating the N^N ligand does not significantly perturb the energies of the frontier molecular orbitals.

Qualitatively, TDDFT analysis for **64** – **66** predicts a T_1 state that is predominantly ^{3}LC on the C^N ligands with some ^{3}MLCT admixture from the iridium t_{2g} orbitals to

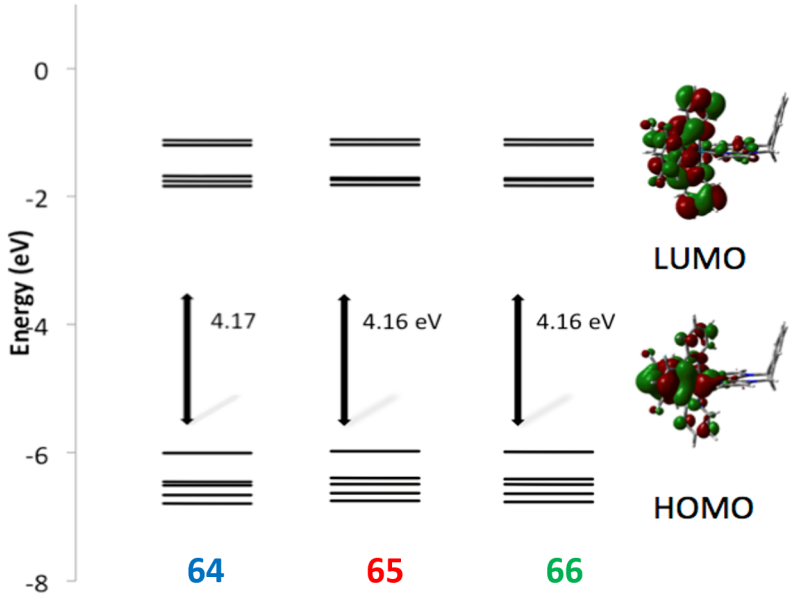

Figure 2.19: Calculated energy level scheme for the Kohn-Sham orbitals between HOMO−4 to LUMO+4 of **64**, **65** and **66**, and the associated DFT calculated HOMO-LUMO energy gap (in eV). Electron density contour plots for **66** (0.002 e bohr^{-3}). The contour plots for **64** and **65** mirror those of **66**.

the C^N ligands (Figure 2.20). The spin densities for the T_1 state for **64** – **67** are shown in Figure 6 and all show similar topologies with the spin density localised on one of the two dFppy ligands, implying an emission resulting from a ^{3}LC state. This assignment is consistent the observed structured emission of these complexes (*vide infra*).

The emission energy was predicted using two different methodologies. The phosphorescence is estimated as the difference between the T_1 and S_0 states in their respective optimised geometries ($E_{0,0}$), which is a good indicator of the $E_{0,0}$ emission measured at 77

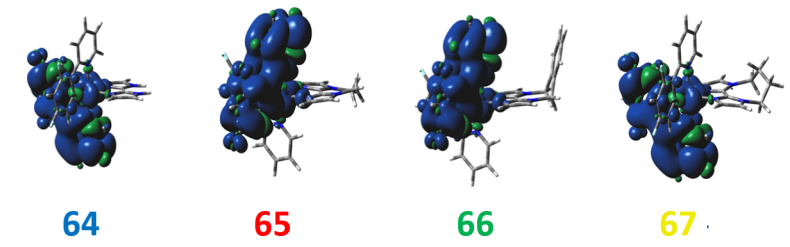

Figure 2.20: Calculated spin density contours of the T_1 state for complexes **64** – **67** (isocontour value of 0.0004 au).

K. For **64** – **66**, an emission at 430 nm was predicted. The λ_{max} at 77 K ranged from 451 – 453 nm. The adiabatic electronic emission (E_{AE}) is determined from the vertical energy difference between the T_1 and S_0 states at the optimised geometry of the T_1 state. For **64** – **66**, an emission at 487 nm was predicted.

2.4 Optoelectronic Characterisation

2.4.1 Electrochemistry

Cyclic voltammetry (CV) in deaerated MeCN at 298 K was undertaken to measure the energies of the frontier MOs of the synthesised complexes, which is crucial for device fabrication purposes. *n*-NBu_4PF_6 was used as the supporting electrolyte and the Fc/Fc^+ redox couple was used as the internal standard. All potentials are referenced with respect to the saturated calomel electrode (SCE, $Fc/Fc^+ = 0.38$ V in MeCN).[219] The poor solubility of **64**, **65** and **66** in MeCN gave poorly resolved CV traces, and thus only weak oxidations could be discerned in the observable solvent windows. The improved solubility of complexes **14**, **68** and **69** meant that well resolved CV traces of these complexes could be measured, and are shown in Figure 2.21. The HOMO energy levels of all complexes were determined from the following:[95]

$$E_{HOMO} = -[E_{ox\ vs\ Fc/Fc^+} + 4.8]eV$$

The analogous calculation using $E_{red\ vs\ Fc/Fc^+}$ could be used to calculate the LUMO energies of complexes **14**, **68** and **69** but the lack of a well resolved reduction wave in the accessible solvent window for complexes **64** – **66** necessitated estimating the LUMO energies by subtracting the $E_{0,0}$ (estimated from the intersection point of the absorption and emission spectra) from the E_{HOMO} energy. However, this is known to give an inaccurate number since it is determined from the optical gap, and thus does not account for the exciton binding energy.[96] Table 2.3 summarises the relevant electrochemical data.

The oxidation potentials of all the complexes are in a similar regime ($E_{1/2(ox)} = 1.37$ – 1.60 V), and are all reversible or quasi-reversible, which is a result of the oxidation being predominantly comprised of the Ir^{III}/Ir^{IV} redox couple with varying contributions from the C^N ligands. The DFT calculations (*vide infra*) for complexes **64** – **66** corroborate this analysis. This is a general trend for $[Ir(C\hat{}N)_2(N\hat{}N)]^+$ complexes,[90] and indeed similar

Complex	$E_{1/2(ox)}$ (V)	$E_{1/2(red)}$ (V)	$E_{0,0}$ (eV)	E_{HOMO} (eV)	E_{LUMO} (eV)
64	1.51	-	-2.85	-5.93	-3.08
65	1.45	-	-2.95	-5.87	-2.92
66	1.44	-	-2.90	-5.86	-2.96
14	1.60	-1.36	-2.95	-6.02	-3.06
68	1.59	-1.36	-2.81	-6.01	-3.06
69	1.37	-1.99	-2.84	-5.79	-2.47

Table 2.3: Electrochemical data for complexes **64**, **65**, **66**, **14**, **68** and **69**. Measurements were carried out in MeCN at a scan rate of 100 mV s^{-1} with Fc/Fc^+ employed as an internal standard, and data reported *vs* SCE (Fc/Fc^+ = 0.38 V in MeCN.

conclusions have been made from electrochemical measurements and DFT calculations previously reported for **14**.[186] It is worth noting, however, that the oxidation potentials of **14** and **68** are marginally higher (more stabilised) than for the biimidazole containing analogues. This demonstrates that although the biimidazole ligands are not directly involved in the oxidation process, their strongly electron-releasing characteristics nevertheless influence the largely metal-localised HOMOs of these complexes. Introduction of the mesityl rings in particularly **68** and to some extent **69** appears to have a negligible effect on the oxidation potential of these complexes.

The reductions of **64** – **66** are irreverisble and could not be easily distinguished from the solvent window. The reduction of **69** is discernible, but is also largely irreversible and close to the boundary of the solvent window. However, it is clearly significantly more negative in potential ($E_{1/2(red)}$ = -1.99 V) than the analogous reductions of **14** and **68** ($E_{1/2(red)}$ = -1.36 V for both complexes), which is indicative of the LUMO destabilising power of the *o*-Xylbiim ligand compared to dtbubpy. This compensates for the moderately less positive oxidation potential observed for **69** compared to **14** and **68**. The reductions of **14** and **68** are well-resolved, highly reversible waves characteristic of reduction of dtbubpy.

Electrochemical data in DCM had previously been reported for **14**. The previously reported values ($E_{1/2(ox)}$: 1.55 V; $E_{1/2(red)}$: -1.42 V vs SCE)[186] are similar to those measured here ($E_{1/2(ox)}$: 1.60 V; $E_{1/2(red)}$: -1.36 V vs SCE), but modestly shifted to more negative potentials. Complex **59** is the most similar structurally to complexes **64** – **66** and **69**. The oxidation potential for this complex in DCM ($E_{1/2(red)}$ = 1.59 V) was reported to be marginally higher than complexes, **64** – **66** and **69**, which is likely due to the difference in

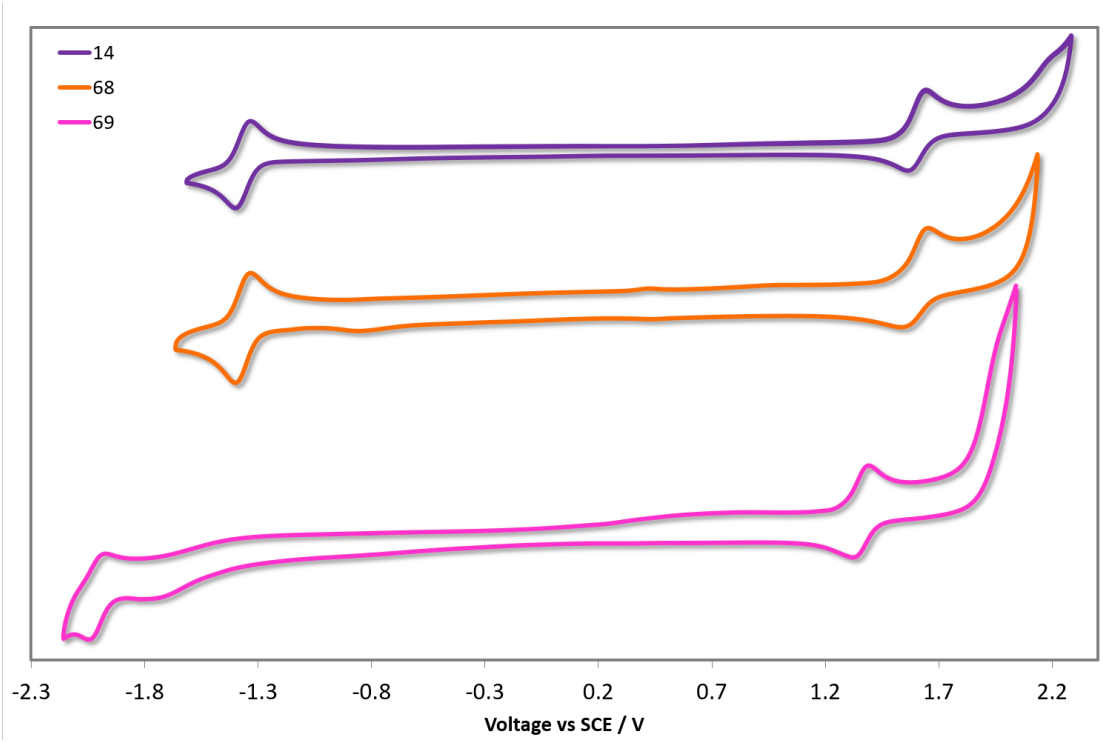

Figure 2.21: CV traces of complexes **14**, **68** and **69** in MeCN solution, reported versus SCE ($Fc/Fc^+ = 0.38$ V in MeCN)[219] redox couple. Scan rates were at 100 mV s^{-1}, and are in the positive scan direction.

Complex	λ_{abs} (nm) [ϵ ($/10^4$ M^{-1} cm^{-1}]
64[a]	245 [3.5], 264 [2.7], 300 [1.4], 365 [0.3], 420 [0.05], 445 [0.01]
65[a]	253 [3.1], 279(sh) [2.6], 303(sh) [1.7], 316(sh) [1.3], 370 [0.4], 422(sh) [0.07], 450 [0.02]
66[a]	251 [4.0], 279(sh) [3.2], 314(sh) [1.8], 368(sh) [0.5], 420 [0.07], 450 [0.02]
14[b]	249 [6.00], 261(sh) [5.46], 298 [3.02], 307(sh) [2.74], 365 [0.48], 420 [0.08], 450 [0.04]
68[b]	257 [6.25], 297(sh) [3.60], 309(sh) [3.21], 330(sh) [1.66], 368 [0.65], 420 [0.11], 449 [0.04]
69[b]	258 [4.84], 281(sh) [4.33], 306(sh) [2.73], 321(sh) [2.13], 371 [0.77], 422 [0.12], 450 [0.04]

Table 2.4: Absorption maxima and their corresponding molar absorptivities for complexes **64**, **65**, **66**, **14**, **68** and **69**. [a] Measured in aerated MeOH at room temperature. [b] Measured in aerated MeCN at room temperature.

solvent.

2.4.2 UV-Vis Absorption

As mentioned, complexes **64**, **65** and **66** are poorly soluble in most organic solvents, and thus their photophysics were studied in MeOH, in which they were sparingly soluble. Complexes **14**, **68** and **69** by contrast are highly soluble and so their photophysical properties were studied in MeCN which is the most common solvent used to study cationic iridium(III) complexes. The absorption spectra of all complexes are shown in Figure 2.22, while their absorption bands and molar absorptivities are summarised in Table 2.4.

The absorption spectra for complexes **64**, **65** and **66** are relatively unstructured, typical for iridium-biimidazole complexes,[112;162] with the intense band at around 250 nm region assigned to spin-allowed $^1\pi$-π^* transitions. All three complexes also demonstrate a distinct lower energy absorption band at about 370 nm, as well as a small tail into the near UV region. These bands are also present in complex **59** and were ascribed to a mix of π-π^* and MLCT transitions.[162] Alkylation of the H_2biim ligand leads to a more structured absorption profile, particularly between 250 – 370 nm.

The profile observed for **14** generally reproduces that reported in the literature, with

the principal band at 249 nm and a shoulder at 298 nm assigned as typical π-π*transitions associated with this family of complexes.[186] The bands at energies lower than 360 nm are assigned as a combination of ^{1}MLCT/^{1}LLCT and ^{3}MLCT/^{3}LLCT transitions.[29] The crucial design feature of the mesityl groups observed in the crystal structure of **68** appears to also be operative in solution. No red-shift in the absorption profile is observed, while this moiety confers only an increase in molar absorptivities across the spectrum. An additional shoulder at 261 nm present in **14** is not observed in **68**.

Although the absorption spectrum of **66** was recorded in MeOH, the photophysics of this complex is predominantly LC in nature (*vide infra*) and thus there is expected to be very little solvatochromic differences observed when studying the absorption of **69** in MeCN. Indeed, as observed when comparing **14** and **68**, the presence of the mesityl substituents in **69** have minimal impact on the absorption profile with only modest increases in the molar absorptivities compared to **66**. The shoulder at 281 nm for **69** is considerably more pronounced than the shoulder at 279 nm for **66** , which is likely the result of π-π* transitions localised on the mesityl ring.

2.4.3 Solution-State Photoluminescence

A summary of the relevant photophysical parameters of the complexes studied is given in Table 3.4. The photophysics of complexes **64**, **65** and **66** were recorded in deaerated MeOH solution at 298 K (Figure 2.23) and in a 1:1 MeOH/EtOH glass at 77 K (Figure 2.24), while complexes **14**, **68** and **69** were studied in dearated MeCN solution at 298 K (Figure 2.25). The photophysical properties of **69** were also studied in dearated MeOH solution at 298 K so as to compare with complexes **64** – **66** (Figure 2.23).

The structured emission profiles at 298 K in MeOH for complexes **64**, **65**, **66** and **69** arise from emission that is a predominantly ^{3}LC T_1 state (Figure 2.23). This is in agreement with DFT calculations which predict the spin density of the T_1 state of complexes **64** – **66** to be localised almost exclusively in the C^N ligands. Low temperature measurements on complexes **64** – **66** further corroborate this assertion, with vibronic bands that become sharper and more distinct at 77 K while undergoing no rigidochromic shift in the emission maxima. At both 298 and 77 K, two high-energy emission maxima are observed at around 455 nm and 484 nm, along with lower vibronic emission peaks tailing out to about 650 nm. Complex **64** is only modestly red-shifted (λ_{PL} = 464, 490 nm) at room temperature

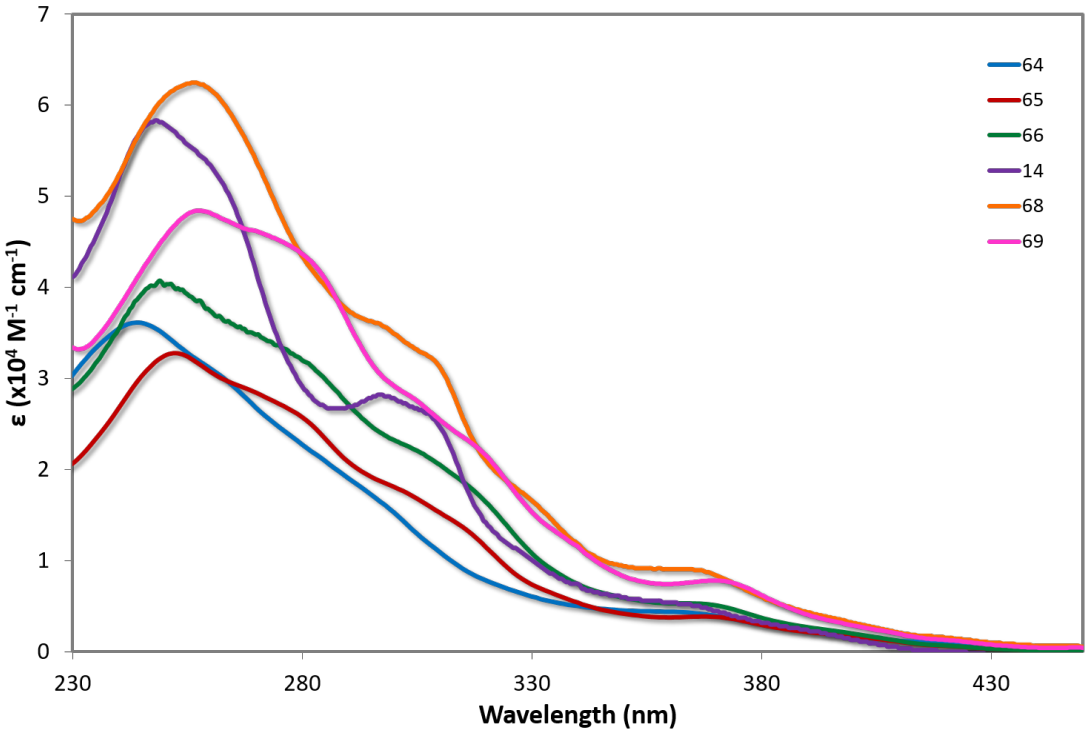

Figure 2.22: Absorption spectra of complexes **64**, **65** and **66** in aerated MeOH solution at room temperature, and absorption spectra of complexes **14**, **68** and **69** in aerated MeCN solution at room temperature.

	λ_{PL} (nm) [a]		Φ_{PL} (%) [b]	τ_e (μs) [c]		k_r [d]	k_{nr} [d]
	77 K	298 K	298 K	77 K	298 K	($/10^5$ s^{-1})	($/10^5$ s^{-1})
64[d]	453, 486	464, 490	20	3.68	1.56	1.28	5.13
65[d]	451, 484	457, 486	2	3.72	0.091	2.20	108
66[d]	450, 483	457, 487	68	3.96	3.84	1.77	0.83
14[e]	-	515	72	-	1.36	5.29	2.06
68[e]	-	515	80	-	1.37	5.84	1.46
69[d]	-	458, 489	82	-	2.26	3.63	0.80
69[e]	-	459, 487	90	-	2.19	4.11	0.46

Table 2.5: Relevant solution-state and low temperature photophysical data for complexes **64** – **66**, **14**, **68** and **69**. [a] λ_{exc}: 360 nm. [b] Quinine sulfate used as the reference (λ_{PL} = 54.6% in 0.5 M H_2SO_4 at 298 K).[220] [b] λ_{exc}: 378 nm. [c] Measurements at 298 K in deaerated MeOH and at 77 K in MeOH/EtOH glass. [d] Measurements at 298 K in deaerated MeCN. [e] Measurements at 298 K in deaerated MeOH.

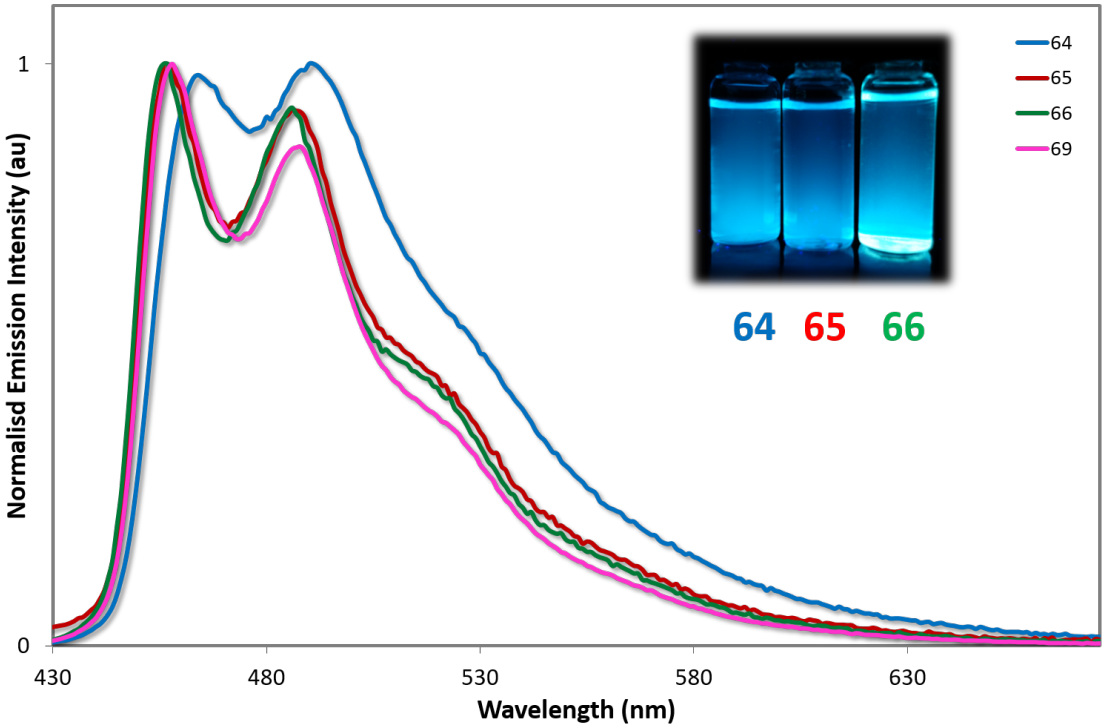

Figure 2.23: Normalised emission spectra of complexes **64**, **65**, **66** and **69** in deaerated MeOH solution at room temperature. λ_{exc}: 360 nm. Inset: MeOH solutions of complexes **64**, **65** and **66** illuminated under UV light.

compared to **65** (λ_{PL} = 457, 486 nm) and **66** (λ_{PL} = 457, 487 nm), which show virtually overlapping emission profiles. The near identical emission spectra across the three complexes verifies the assertion that the electronics across the series are unchanging, with only a slight blue shift in emission arising from incorporating the moderately electron-releasing alkyl groups in place of the parent protons. Similarly, the emission profile of **69** in MeOH (λ_{PL} = 458, 489 nm) is also virtually coincident with **65** and **66**, indicating that the methyl groups on the mesityl rings disrupt any conjugation of these rings into the C^N ligands.

Although the optoelectronics are similar for complexes **64** – **66**, the excited state kinetics are decidedly different. At low temperature the lifetimes of these complexes are all in the microsecond regime, with complex **66** showing an excited state lifetime (τ_e = 3.96 μs) that is only marginally longer than complexes **64** (τ_e = 3.68 μs) or **65** (τ_e = 3.71 μs). These lifetimes point towards phosphorescent emission for all three complexes at low temperature.

Moving to room temperature, the lifetime of **66** is essentially unchanged (τ_e = 3.84 μs), while the lifetime of **64** is diminished but remains in the microsecond regime (τ_e = 1.56 μs).

By contrast, the lifetime of complex **65** drops off precipitously (τ_e = 0.091 μs), pointing towards substantive contributions to k_{nr} for this complex. On the basis of the distorted T_1 state computed by DFT, the primary non-radiative decay pathway for complex **65** is surmised to be fluxional rotation about the biimidazole carbon-carbon bond, promoted by the steric clash of the methyl groups on the distal nitrogens. Evidence that this process is dynamic comes from the much longer lifetime observed for **65** at low temperature than at room temperature, which suggests that constraining the dMebiim ligand in a rigid medium prohibits this deleterious, fluxional process. Furthermore, although complex **64** does not have any steric factors promoting distortion of the N^N ligand out of the plane in as drastic a manner as **65**, the distal nitrogens are not conformationally locked and thus free to rotate under thermal coercion at room temperature. Thus, rigidifying the ligand scaffold by using a tether as in complex **66** mirrors the rigid environment experienced by all three complexes at low temperature, leading to a lifetime that is essentially the same at room temperature as at 77 K. In essence, tethering the distal nitrogens suppresses significant *intra*molecular contributions to k_{nr}.

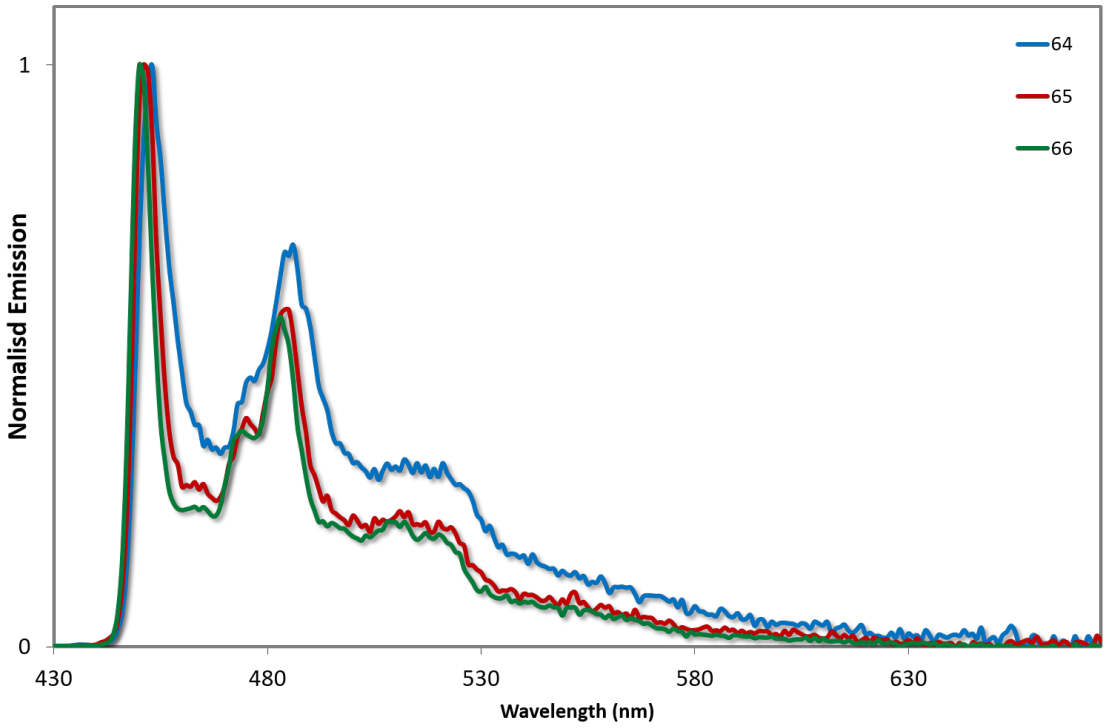

Figure 2.24: Normalised emission spectra of complexes **64**, **65** and **66** in 1:1 MeOH/EtOH glass at 77 K. λ_{exc}: 360 nm.

The pattern observed for the lifetimes of complexes **64** – **66** is mirrored in the measured

quantum yields. Complex **64** is only moderately emissive (Φ_{PL} = 20%) while the emission of **65** (Φ_{PL} = 2%) is significantly quenched. Amazingly, the quantum yield measured for **66** (Φ_{PL} = 68%) is much higher than both **64** and **65**. These figures are reflected in the excited state kinetics. All of the values for k_r are similar for **64** – **66** (ranging from 1.28 to 2.20 $\times 10^5$ s^{-1}), which is indicative of emission from the same state (i.e. ^{3}LC emission) and thus similar SOC effects exerted by the metal centre for all three complexes. By contrast, values for k_{nr} values differ dramatically across the series. Complex **65** has a k_{nr} value (k_{nr} = 107.69 $\times 10^5$ s^{-1}) that is two orders of magnitude larger than that calculated for **64** (k_{nr}= 5.13 $\times 10^5$ s^{-1}). The brightest complex, **66**, has a calculated k_{nr} (k_{nr} = 0.83 $\times 10^5$ s^{-1}) which is even lower than **64**, demonstrating the restriction in vibrational contributions to k_{nr} upon tethering the ancillary ligand. Recent studies on iridium complexes bearing biimidazoles substituted with phenyl rings[221] or extended alkyl chains[222] also report complexes with low quantum yields, in line with the observations made here.

Moving to complexes **14** and **68**, these complexes are also phosphorescent emitters, but show room temperature lifetimes in MeCN (τ_e = 1.36 μs for **14** and 1.37 μs for **68**) that are the shortest among those studied (apart from **65**). These relatively short lifetimes point towards emission from a mixed ^{3}MLCT/^{3}LLCT state. The broad, unstructured emission profiles are also indicative of emission from ^{3}CT states. The photophysical properties of **14** have been reported previously, and the data measured here (Φ_{PL} = 72%; τ_e = 1.36 μ; λ_{PL} = 515 nm) is in accordance with the literature **14** (Φ_{PL} = 70 – 71%; τ_e = 1.25 – 1.40 μ; λ_{PL} = 512 nm).[129;186] As with complexes **66** and **69**, the emission profiles of **14** and **68** virtually overlap, demonstrating that the mesityl rings of **68** are maintaining their mutually orthogonal relationship with respect to the C^N ligands in solution. This observation is consistent with the absorption spectroscopy and the electrochemistry.

Again, however, while the optoelectronics remain unchanged by the mesityl substituion, the excited state kinetics are different. The quantum yield observed for **68** (Φ_{PL} = 80%) is higher than for **14** (Φ_{PL} = 72%), despite exhibiting virtually the same excited state lifetime; the result of a combination of slightly increased radiative rate constant (k_r = 5.29 $\times 10^5$ s^{-1} for **14** and 5.84 $\times 10^5$ s^{-1} for **68**) and decreased non-radiative rate constant (k_{nr} = 2.06 $\times 10^5$ s^{-1} for **14** and 1.46 $\times 10^5$ s^{-1} for **68**) for the mesityl analogue. Making the analogous comparison for complexes **66** and **69** in MeOH, it is clear that combining the rigid N^N ligand with a sterically bulky C^N ligand leads to an even greater enhancement of the quantum yield (Φ_{PL} = 68% for **66** and 82% for **69**). In this instance, the enhanced

luminescence is almost entirely due to an increase in the radiative rate constant (k_r = 1.77 $\times 10^5$ s^{-1} for **66** and 3.63 $\times 10^5$ s^{-1} for **69**) resulting from the reduced concentration quenching promoted by the bulky mesityl groups.

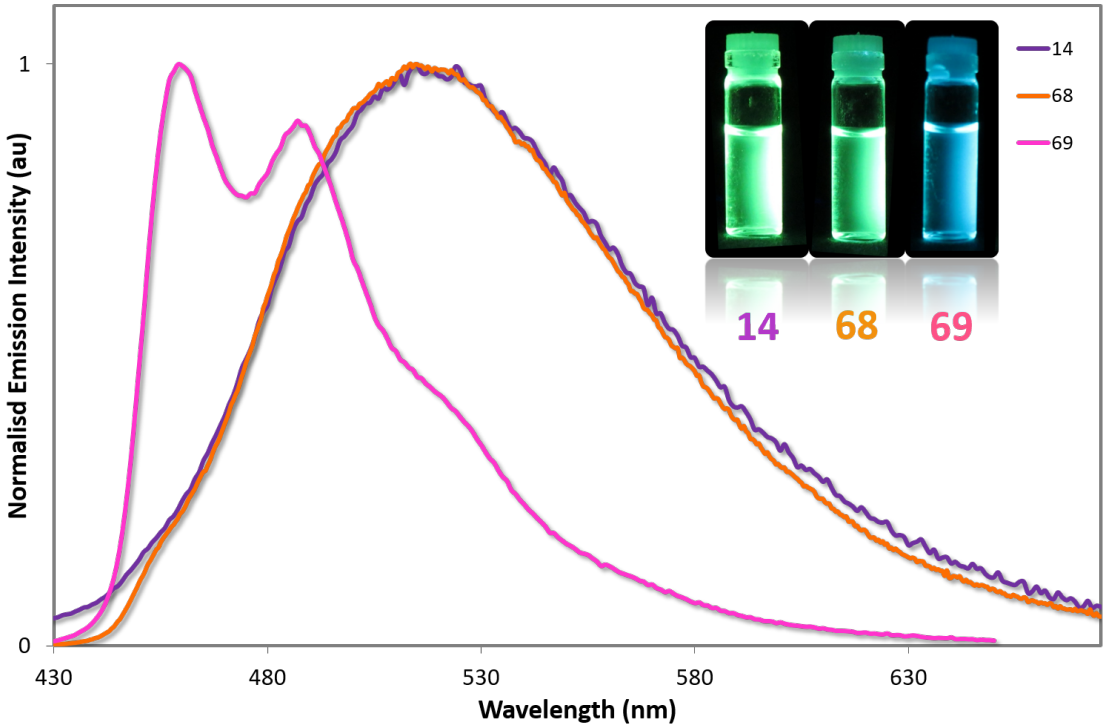

Figure 2.25: Normalised emission spectra of complexes **14**, **68** and **69** in deaerated MeCN solution at room temperature. λ_{exc}: 360 nm. Inset: MeCN solutions of complexes **14**, **68** and **69** illuminated under UV light.

In MeCN solution, complex **69** is even more emissive, with a near unitary quantum yield of 90%. The increased quantum yield of **69** compared with **14** and **68** is likely to be due to a combination of energy gap law effects arising from the blue-shifted emission of **69**, as well as the rigidifying effects of the N^N ligand. Ultimately, the results demonstrate that rational design of a blue emitter with near unitary quantum yield can be achieved by careful consideration of the different *inter*- and *intra*molecular contributions to k_{nr}.

Analysis from an extensive literature survey suggests that this is the highest photoluminescence quantum yield for a blue cationic complex reported to date; all cationic iridium emitters that have a bluer λ_{max} are significantly less efficient. See for example, complex **6** which is moderately bluer (λ_{PL} = 452, 480 nm) but less emissive (Φ_{PL} = 20%)[110] or the NHC complexes **51** – **55**,[150–152] which can show deep blue emission (λ_{PL} = 440 nm for

Complex [a]	λ_{PL} (nm) [b]	Φ_{PL} (%) [c]	τ_e (μs) [d]
14 (neat film)	520	62	0.41 (41%), 0.85 (59%)
14 (doped film)	518	90	1.75
68 (neat film)	508	54	0.39 (68%), 1.23 (34%)
68 (doped film)	474, 502	97	1.63
69 (neat film)	465, 492	43	0.19 (29%), 1.23 (71%)
69 (doped film)	462, 492	89	1.92

Table 2.6: Relevant solid-state photophysical data for complexes **14**, **68** and **69**. [a] Neat films were dip coated from MeCN solution, while doped films were dip coated from a DCM solution of 5 wt% of the complex in PMMA. [b] λ_{exc}: 360 nm. [c] Measured using an integrating sphere. ments at 298 K in deaerated MeOH and at 77 K in MeOH/EtOH glass; λ_{exc}: 360 nm for neat films; λ_{exc}: 300 nm for doped films. [d] λ_{exc}: 378 nm.

complex **55**) but also with low quantum yields (Φ_{PL} = 0.9 – 29%). While this is no doubt in part due to more thermally accessible MC states in these emitters as a function of a larger HOMO-LUMO gap, this result nevertheless demonstrates the potency of this ligand design. High quantum yields, on the other hand, have been reported, such as for complex **9** (Φ_{PL} = 54%), which incorporates a bulky trityl group into the N^N ligand framework. However, this complex is still less emissive than **69** and red-shifted in colour (λ_{PL} = 472, 490 nm).[113]

2.4.4 Solid-State Photoluminescence

The improved solubility of complexes **14**, **68** and **69** facilitated spin coating samples of these complexes to measure their photophysical properties in the solid state, with a view to correlating these measurements to the crystal packing observations. Measurements were carried out both in neat and doped (5 wt% in PMMA) films. The results are collated in Table 2.6 and the spectra shown in Figures 2.26 and 2.27. In contrast to the solution-state photophysics, the quantum yields for these complexes decrease across the series (Φ_{PL} = 62% for **14**, 54% for **68** and 43% for **69**). The decrease in quantum yield may be linked to the propensity of **68** and particularly **69** to form more ordered crystal packing arrays than **14**, which may make these complexes more susceptible to concentration quenching processes by means of aggregate formation.[223;224]

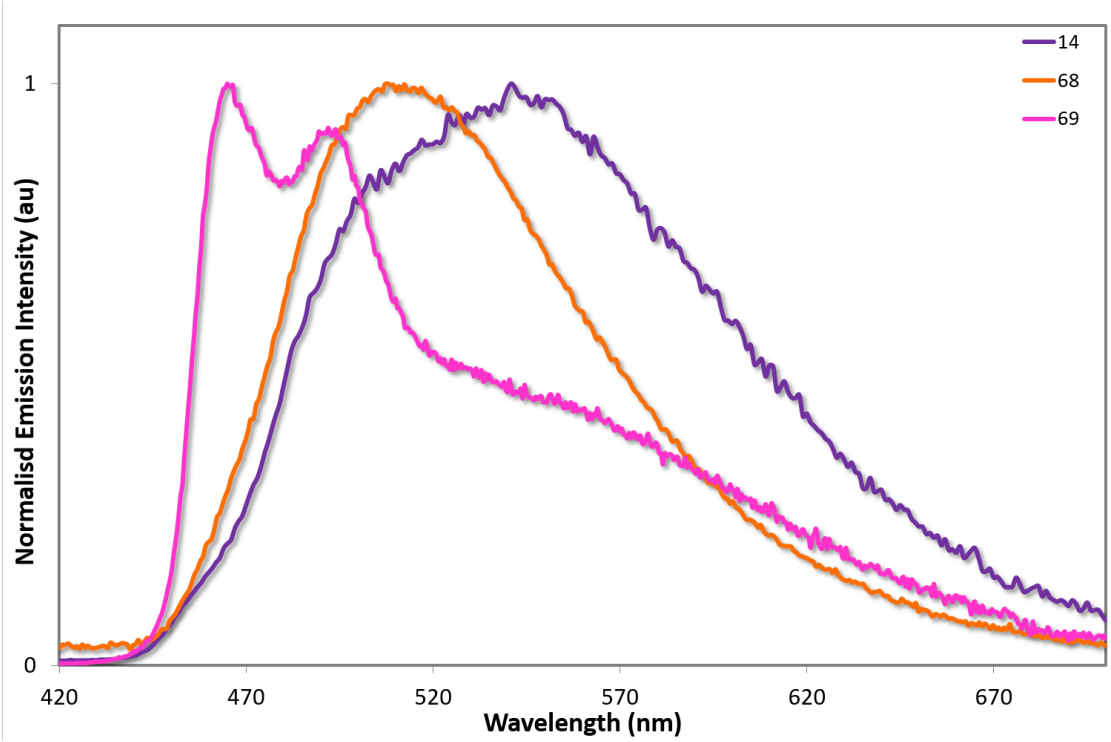

Figure 2.26: Emission spectra of **14**, **68** and **69** in neat film. λ_{exc}: 360 nm.

By contrast, the photoluminescence quantum yields of the doped films, as expected, are independent of crystal packing effects, with exceptionally high values for all three complexes. The quantum yield for **14** was previously reported to be 96%,[129] while here it is measured to be 90%. Under identical conditions, the quantum yield of **68** is essentially unitary at 97%! In addition, the emission profile of **68** is blue-shifted and more ^{3}LC in nature than for **14**. Complex **69** is virtually as bright in the solid state (Φ_{PL} = 89%) as in MeCN solution (Φ_{PL} = 90%), indicating that the rigidifying effects in the solid state are limited for this complex since this has already largely been achieved by the N^N ligand.

All of these quantum yields are remarkably high for charged iridium complexes in the solid state. Indeed, only a few ionic iridium(III) complexes have been reported to have higher quantum yields in the solid-state. It is worth noting that although complexes **68** and **69** show significantly diminished quantum yields in neat film compared to solution or doped films, these values still compare well with both 'classic' iridium complexes which do not possess large, bulky substituents, such as complex **3**, *fac*-[Ir(ppy)$_3$] (Φ_{PL} = 97% in a 1.5 mol% CBP (4,4'-bis(*N*-carbazolyl)-1,1'-biphenyl) film compared to Φ_{PL} = 3% in neat film) and FIrpic (Φ_{PL} = 99% in 1.4 mol% mCP (1,3-Bis(*N*-carbazolyl)benzene), compared to Φ_{PL} = 15% in neat film),[225] as well as with other iridium complexes bearing bulky ligand

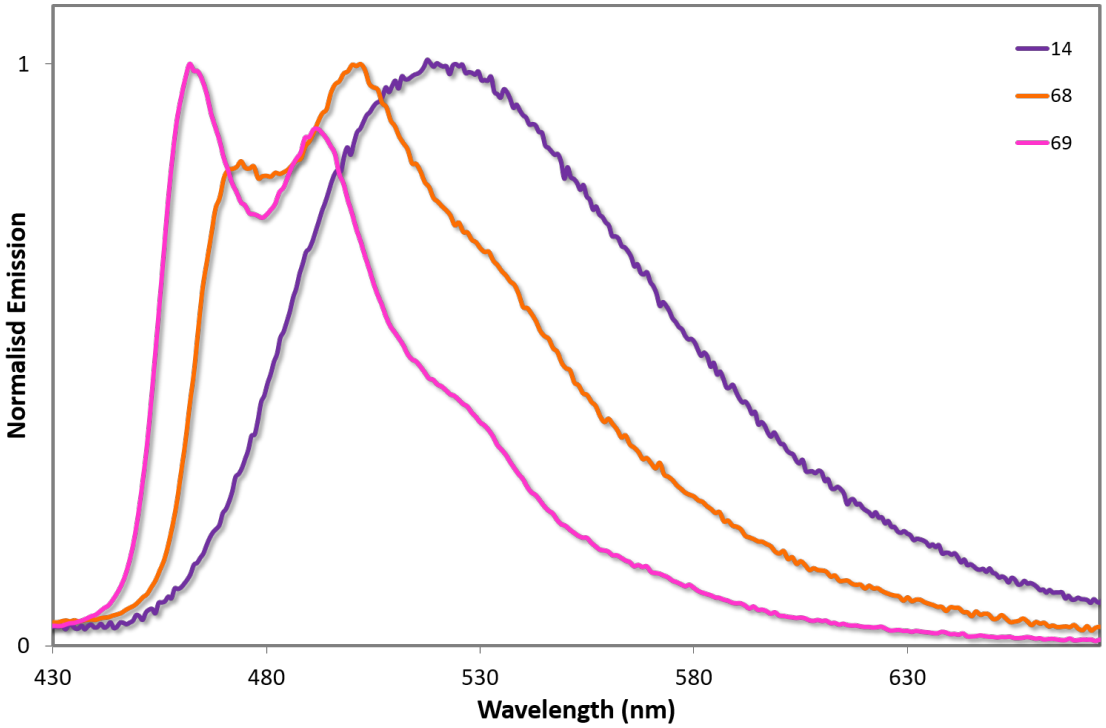

Figure 2.27: Emission spectra of **14**, **68** and **69** in doped film (5 wt% in PMMA). λ_{exc}: 300 nm.

functionalities such as complex **13** (Φ_{PL} = 42% in a 1.5 mol% mCP film compared to Φ_{PL} = 31% in neat film).[128] Complex **7**, however, shows an exceedingly high quantum yield in the neat film (Φ_{PL} = 75%) with sky-blue emission (λ_{PL} = 474 nm).[120]

In doped film, aside from the quantum yield of 96% reported previously for **14**,[129] only nine cationic complexes have been reported previously with quantum yields of similar magnitude (in 5 wt% doped PMMA films). For instance, a series of emitters based on 2,4-difluorophenylpyrazole and varying N^N ligands were reported with three compounds within the study showing quantum yields ranging from 89 to 100%, but with greener emission than **69** (λ_{PL} = 500 – 510 nm).[83] Complexes **15** – **18** also showed this behaviour, with high quantum yields (Φ_{PL} = 82 – 93%) in the green regime (λ_{PL} = 503 – 519 nm) of the visible spectrum.[93] A family of complexes reported containing cyclometalating ligands decorated with electron-withdrawing sulfone groups on the phenyl moiety all displayed near-quantitative quauntum yields in the solid state, ranging from 86 – 94%, and displaying blue-green emission (λ_{PL} = 487 – 505 nm).[147] Complex **9**, bearing a tritylphenyl functionalised phenylimidazole ancillary ligand, is the bluest (λ_{PL} = 474 nm) example with doped film emission data, with a high quantum yield of 79%.[113] Nevertheless this is less

bright and more red-shifted in emission than **69**.

2.5 Light-Emitting Devices

2.5.1 LEECs

Complex **69** was tested in a series of LEEC devices to see how its photophysical properties translate into EL. The optimised device architecture is given in Figure 2.28 and the EL spectra for this LEEC are shown in Figure 2.29, while the relevant device parameters for the three configurations tested are given in Table 2.7. For all devices, PEDOT:PSS was used to improve the interface between the emissive layer and the anode, as well as to facilitate hole injection. Two archetypal emissive layers were tested: one based on a pristine iTMC film, and one comprised of a mixture of iTMC and IL (4:1 iTMC to IL ratio). However, these configurations have been reported to display red-shifted EL spectra for blue emitters compared to their photoluminescence.[152;188] To avoid this, a host-guest (HG) configuration was also studied (Figure 2.28), with a neutral phosphine oxide material (**SPPO13**) acting to improve electron transport through the emissive layer, and a carbazole-based material appended with a cationic imidazolium cation (**NMS25**) which has hole-transporting characteristics and facilitates the turn-on time of the device in a similar manner to a conventional ionic liquid.[98]

Emissive Layer	L_{max} (cd m^{-2})	P. E. (lm W^{-1})	C. E. (cd A^{-1})	EQE (%)
69 (pristine)	107	0.6	2.1	0.8
69:IL (4:1)	69	0.4	1.4	0.5
69:HG (1:9)	433	1.1	5.7	2.5

Table 2.7: Relevant LEEC performance data for complex **69**. Definitions: L_{max} is maximum luminance; P. E. is power efficiency; C. E. is current efficiency, EQE is external quantum efficiency. Devices operated under pulsed current, with an average pulsed current density of 50 A m^{-2}.

The device based on the HG configuration gave significantly improved device performances compared to when an IL or pristine film configuration was used. Both higher luminance values (L_{max} = 433 cd m^{-2} for the HG device compared to 107 cd m^{-2} for the pristine device) and overall device efficiencies (EQE = 2.5% for the HG device compared to 0.8% for the pristine device) were observed for the HG device. This points towards a device

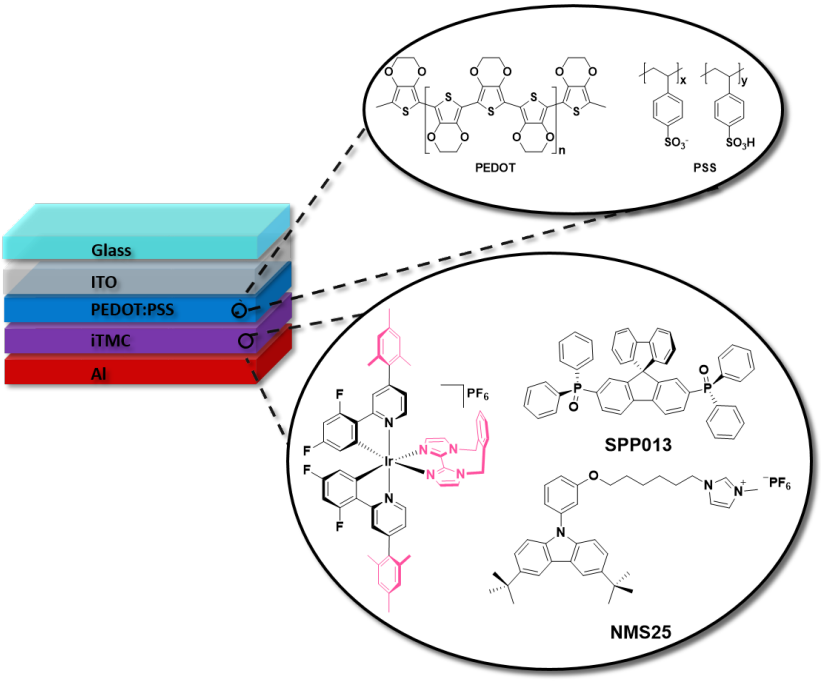

Figure 2.28: Host-guest LEEC architecture of **69**.

with a better balance of charge transport through the emissive layer. The EL spectrum of **69** in the HG configuration resembles that of the photoluminescence spectra, with a structured profile pointing towards emission from a principally ^{3}LC state. However, over time the spectrum appears to red-shift, with the vibronic band at 464 nm diminishing while the band at 526 nm becomes more prevalent. This is tentatively ascribed to the loss of one or more fluorine atoms from the C^N ligands, which as mentioned is a well-accepted phenomenon in the literature.[93;122;123] Furthermore, the observation of mono-defluorinated species in the ^{19}F NMR spectra in crude samples of **14**, **68** and **69** before work up suggests that these complexes are prone to C-F bond cleavage, facilitated by conditions such as heat or electrical stimulus. Thus although **69** gives good device performances, like many other blue emitting devices its performance is hindered by its stability.

2.5.2 OLEDs

Coincidentally with studying LEECs, complex **69**, as well as complexes **14** and **68**, were used as emitters in solution-processed OLEDs (Figure 2.30). The emitter was embedded in an OXD7/mCP host (where OXD7 is 1,3-bis(5-(4-(*tert*-butyl)phenyl-1,3,4-oxadiazol-2-yl)benzene, and sandwiched between organic layers of PVK (where PVK is poly(9-vinylcarbazole) and TPBI (where TPBI is 1,3,5-tris(1-phenyl-1*H*-benzimidazol-2-

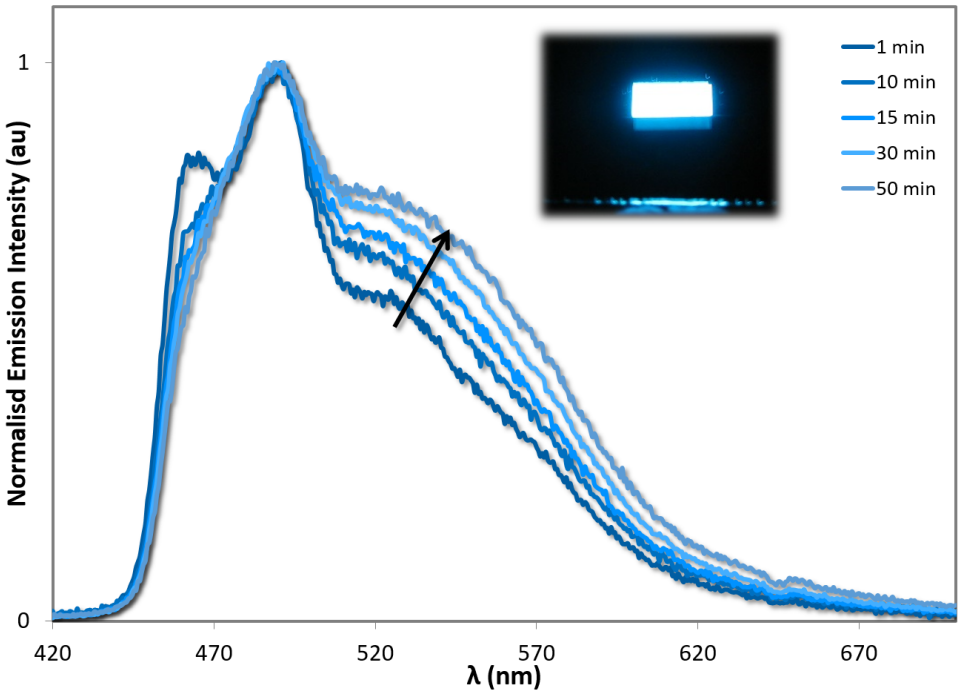

Figure 2.29: Electroluminescence spectra of HG-LEEC containing **69**. The spectrum observed red-shifts over time. Inset: image of LEEC under operation.

yl)benzene)). PVK facilitates the injection of holes, while the electron transport layer TPBI blocks the holes from penetrating into the cathode due to a deep lying HOMO, reducing current leakage. As opposed to LEECs, this multi-layer structure helps to confine the excitons within the emitting layer, leading to improved device performance. Except for TPBI and the contacts, all the layers were deposited by solution-processing methods. The relevant device parameters are summarised in Table 2.8, and the EL spectra for the OLEDs fabricated are given in Figure 2.31.

The EL spectra follow the trend observed for the doped films. The spectrum of **14** is broad and featureless, while **68** is slightly blue-shifted and more structured. Complex **69** is the most structured and also the bluest. The CIE colour coordinates of the OLEDs follow the trend expected for the EL spectra, with the CIE coordinates of **14** (0.25, 0.48) red-shifted compared to the mesityl containing complex **68** (0.21, 0.40). The replacement of the dtbubpy ligand in **68** with the *o*-Xylbiim ligand in **69** does not lead to substantially bluer CIE coordinates, which were found to be 0.21, 0.37. In the EL spectra, the emission from mCP:OXD-7 (expected at around 410 nm) disappears completely, indicating that complete energy transfer occurs from the host system to all of the emissive complexes.

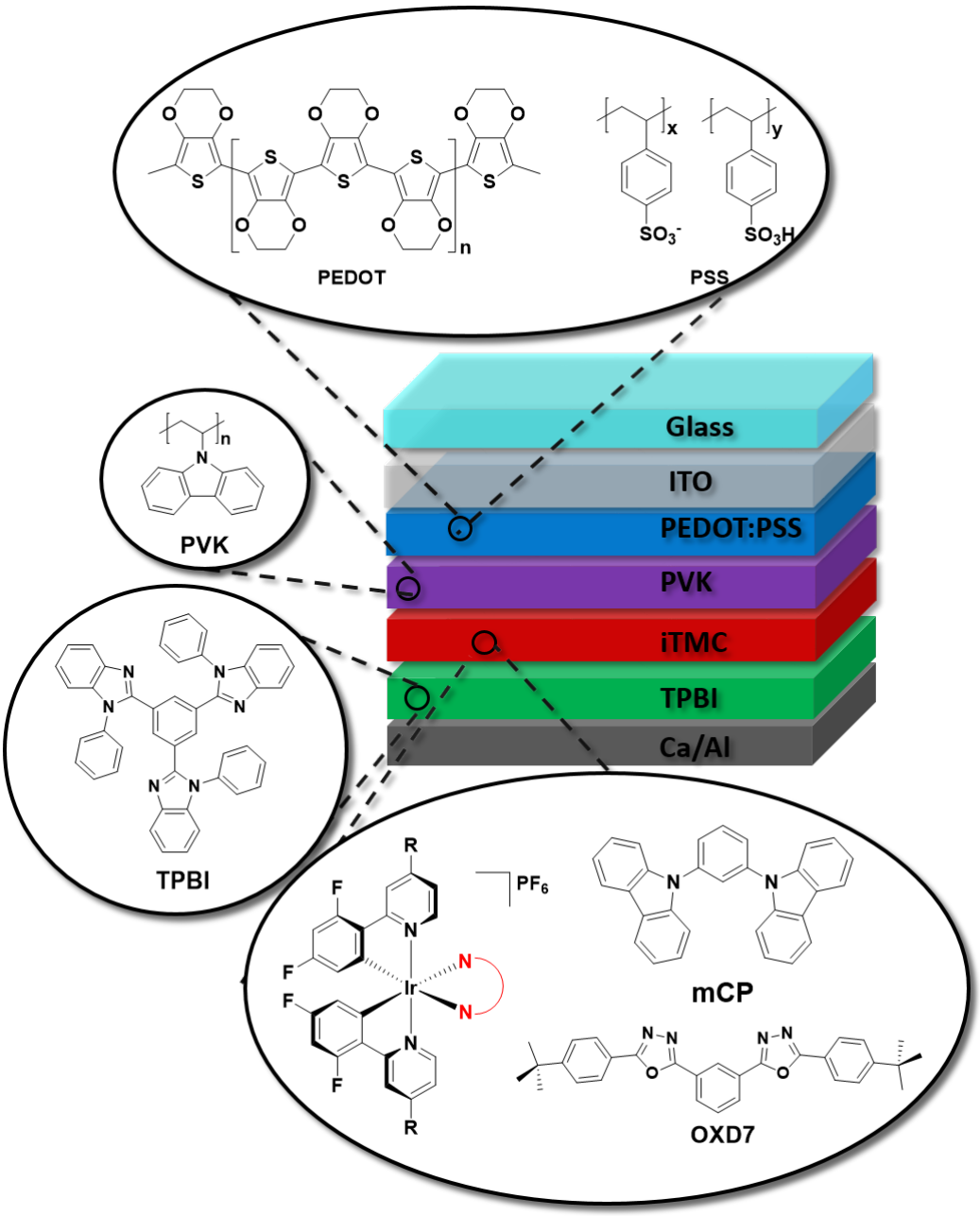

Figure 2.30: OLED architecture used for complexes **14**, **68** and **69**.

Complex	Turn-on (V)	L_{max} (cd m^{-2})	P. E. (lm W^{-1})	EQE (%)	CIE (x, y)
14	6.4	1790	6.2	5.4	0.25, 0.48
68	6.2	2935	4.8	4.0	0.21, 0.40
69	4.8	1086	4.4	3.4	0.21, 0.37

Table 2.8: Relevant OLED performance data for complexes **14**, **68** and **69**. Definitions: L_{max} is maximum luminance; P. E. is power efficiency; EQE is external quantum efficiency. Devices operated under pulsed current, with an average pulsed current density of 50 A m^{-2}.

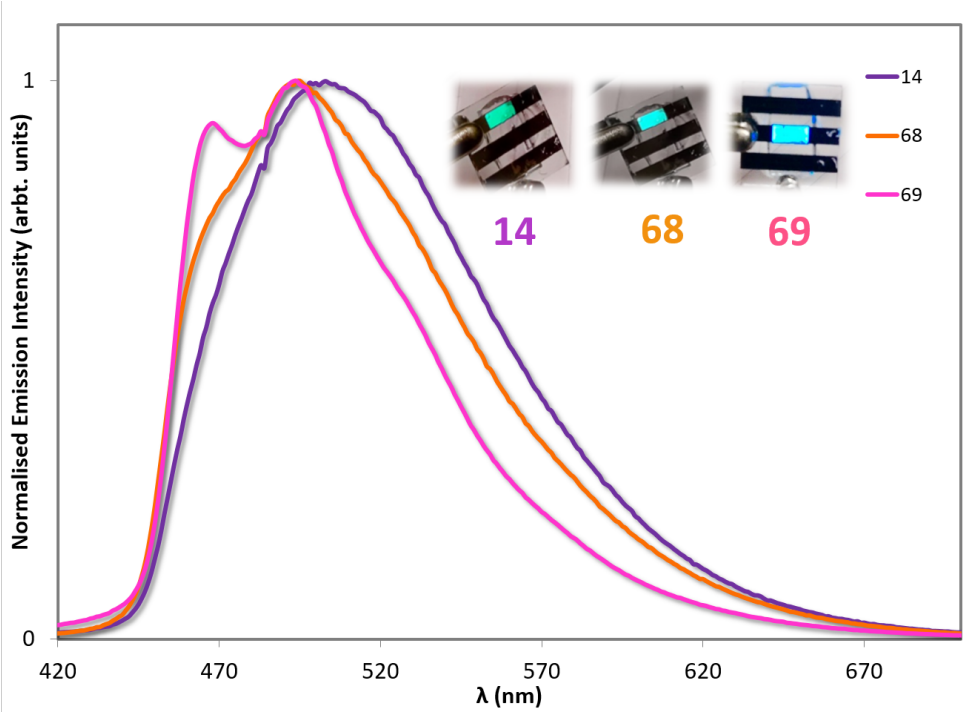

Figure 2.31: Electroluminescence spectra of complexes **14**, **68** and **69**. Inset: images of OLEDs under operation.

The turn-on voltage is lowest for the device made with **69** as the active layer, which is 4.8 V. The turn-on voltages for the other devices are higher at around 6.3 V. The highest luminance value is obtained for the device based on **68** (L_{max} = 2935 cd m^{-2}), while the highest EQE is that of complex **14** (EQE = 5.4%) The efficiencies of these devices are reduced at high brightness, which is likely due to the deterioration of charge carrier balance in the device at high current density and the increase of non-radiative quenching processes, including triplet-triplet annihilation (TTA).[226] These results suggest the performance of the devices can be optimised further by improving the charge balance.

Comparing these devices to that based on **63** shows that **63** has a higher overall efficiency (EQE: 10.4% for the optimised device).[172] However, this device employs a neutral emitter, whereas the emitters used here are ionic. Thus it is useful to compare these emitters to those based on charged emitters used in OLEDs, of which there are only a few examples.[227–232] The most efficient of these comes from a series of studies based on complex **44**, wherein counterions of different size and electron-transporting capability were employed to control charge transport in the device. The premier example utilised a derivative of the well-studied electron-transporting OXD-7 material, functionalised with an anionic sulfonate group. This

resulted in a solution-processed OLED with significantly improved performance (EQE = 9.8%) compared to the device employing the PF_6^- counterion (EQE = 3.5%).[231] This suggests that the performances of the devices based on **14**, **68** and **69** could possibly be improved by modifying the counteranion.

In addition, two examples of OLEDs employing cationic emitters that have been fabricated by vacuum sublimation have been reported.[233;234] The best of these is that based on complex **72**, which by utilising a conjugated diphenylamine-fluorenylpyridine C^N ligand, allows the inherently poor volatility of cationic iridium complexes to be overcome. These devices show reasonable external quantum efficiencies, peaking at an EQE of 6.5%.[234] The solution-processed devices reported here are not quite as efficient, but offer the distinct advantages of simpler processing and the possibility of being patterned by printing processes.

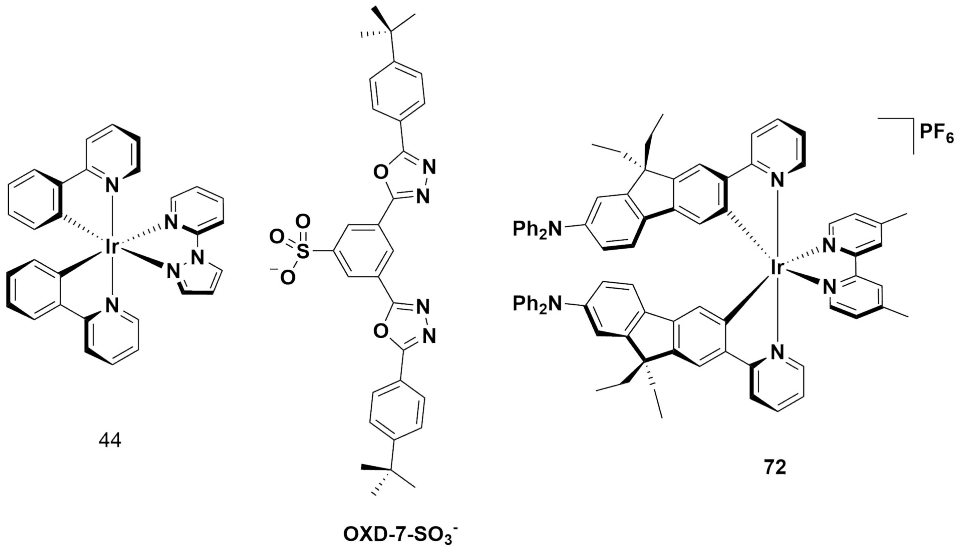

Figure 2.32: Iridium complex with an electron transporting counteranion for a solution-processed OLED (**44** and **OXD-7-SO$_3^-$**,[231] and a sublimable cationic iridium complex for a vacuum-deposited OLED.[234]

2.6 Conclusions

The synthesis and characterisation of a family of novel biimidazole-containing iridium complexes of the form $[Ir(C^N)_2(N^N)](PF_6)$ has been discussed, wherein the biimidazole ligand has been optimised to suppress *intra*molecular contributions to k_{nr} and the C^N

ligand has been optimised to suppress *inter*molecular contributions to k_r. Combining these strategies has lead to the design of a cationic blue-emitting complex (λ_{PL} = 459, 487 nm) with among the highest quantum yields reported in solution and the solid-state (complex **69**). Complex **69** was studied in a LEEC, displaying blue emission, but also poor stability. This complex and two reference complexes (**14** and **68**) were studied in solution-processed OLEDs, giving reasonable performance (EQE = 3.4 – 5.4%) and sky blue light (CIE: 0.21, 0.37 for complex **69**).

Chapter 3

Blue-Emitting Iridium Complexes with Cyclometalating Pyrimidines: Ligand Design Informed by Hammett Parameters

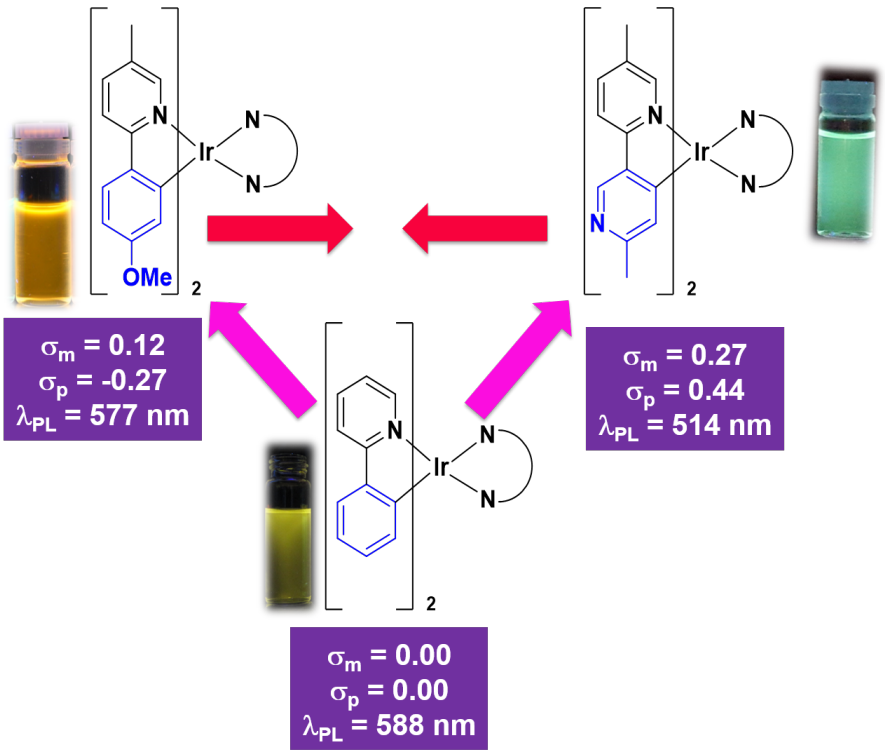

3.1 Introduction

3.1.1 Background

The previous chapter discussed some of the problems with utilising iridium complexes with fluorinated cyclometalating ligands. In addition to the literature precedent, the LEEC based on complex **69** illustrated the undesirable results of utilising fluorinated C^N ligands, demonstrating poor stability in the device, as well as a red-shifting feature that points towards defluorination of this complex under electroluminescent conditions. Thus there is a desire to design new blue emitting complexes that do not contain C_{aryl}-F bonds.

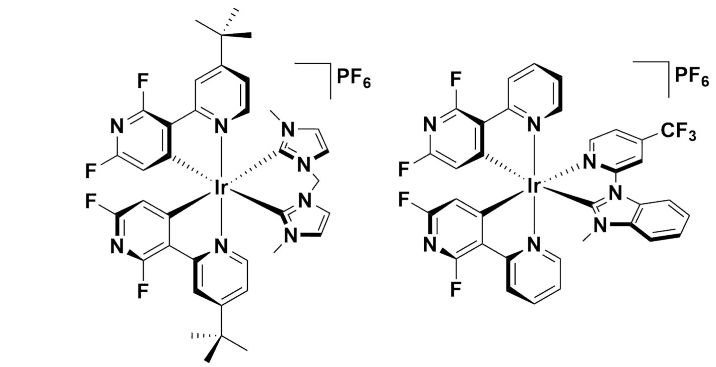

Complex:	55	73
λ_{PL} (nm):	440	464
Φ_{PL} (%):	13	9

Complex:	74	75
λ_{PL} (nm):	465, 480	440, 470
Φ_{PL} (%):	-	87

Figure 3.1: Selected examples of cationic (**55**[152] and **73**[235]) and neutral (**74**[101] and **75**[236]) complexes bearing the 2',6'-difluoro-2,3'-bipyridine C^N ligand.

One avenue being explored for blue-shifting the emission of these complexes is replacing the phenyl ring of the heterocycle with a different heterocycle altogether.[237] Originally, this principle was demonstrated with the fluorinated C^N ligand 2',6'-difluoro-2,3'-bipyridine,

of which complex **55** was an example discussed in Chapter 2. Some other examples are given in Figure 3.1. Only a few examples of cationic emitters utilising this C^N ligand are reported[152;235] but examples of neutral complexes are more numerous.[237;238] These complexes utilise the electron-withdrawing properties of the cyclometalated pyridine to stabilise the HOMO energy in concert with the fluorine atoms on the pyridine ring. However, the ancillary ligand normally needs to be modified to push the emission into the deep-blue. For example, **55** (λ_{PL} = 440 nm),[152] bearing a strongly electron-donating bis-NHC ligand, and **75**, bearing an anionic pyrazolate ligand (λ_{PL} = 440, 470 nm),[236] are both deep-blue emitters. However, **73**, contains an ancillary ligand with diminished electron-donating capabilities as a result of the -CF_3 group (λ_{PL} = 464 nm),[235] and **74**, which only contains a 2,4-pentanedionate (acac) ancillary ligand (λ_{PL} = 465, 480 nm),[101] are only sky-blue in colour.

In order to replace the fluorine atoms on these ligands, recent research has focused on correlating the electron-withdrawing or donating capabilities of a particular substituent, as quantified by its Hammett value, to the capability of the substituent to blue-shift or red-shift the emission profile of the complex.[101;102] The Hammett value in particular is important, since it relates the electron-withdrawing or donating capabilities of a particular substituent to its *regiochemistry*. For example, in devising new ways of blue-shifting the emission of these complexes, methoxy substituents have come to the fore, despite being typically thought of as electron-donating functionalities. Indeed, this is the case in the *ortho*- and *para*-positions, as borne out by a negative Hammett value (σ_p = -0.27), but this functional group is in fact inductively electron-*withdrawing* in a *meta*-position (σ_m = +0.12). Thus in the correct position on the ring, this group can be used to blue-shift the emission of these complexes in place of fluorine atoms. Some examples of such complexes are given in Figure 3.2. In a proof of concept, complex **76** was designed to mimic the properties of complex **62**, FIrpic. It was shown to have very similar photophysical properties (λ_{PL} = 466 nm for **76** and 469 nm for FIrpic; Φ_{PL} = 54% for **76** and 61% for FIrpic in MeCN) as well as almost co-incident electrochemical properties ($E_{1/2(ox)}$ = 0.93 V for **76** and FIrpic in DMF *vs* the Fc/Fc^+ couple).[101] The emission of complex **77** is blue-shifted (λ_{PL} = 454 nm) compared to **76** due to the incorporation of two alkoxy groups into the C^N ligand framework, with the alkoxy substituents designed to improve the solubility of these emitters as well.[183] Complex **78** is one of only four cationic complexes reported to contain fluorine-free cyclometalated 2,3'-bipyridines, all of which show green/blue emission

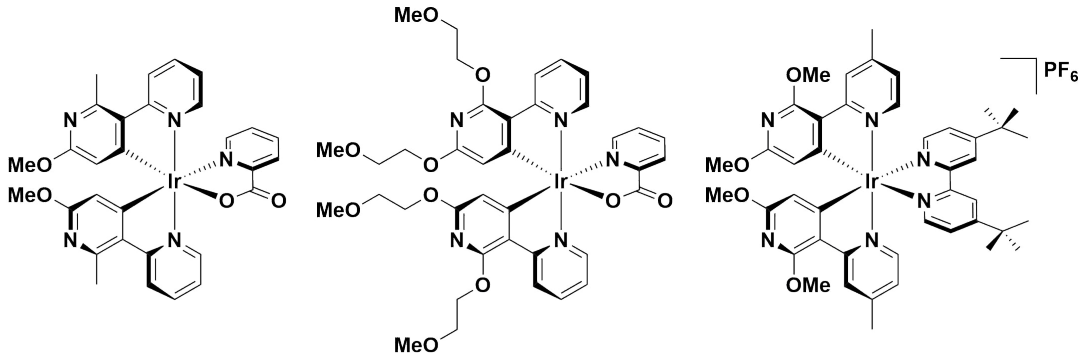

Complex:	76	77	78
λ_{PL} (nm):	466, 492	454	517
Φ_{PL} (%):	54	75	53

Figure 3.2: Selected examples of blue/blue-green emitting 'fluorine-free' iridium complexes bearing cyclometalated 2,3'-bipyridine ligands with alkoxy substituents.[85;101;183]

(λ_{PL} = 517 nm),[85] which is noticeably red-shifted in colour compared to complexes **76** and **77**. This demonstrates the difficulty in designing bluer cationic emitters compared to their neutral counterparts.

Although Hammett parameters can be a useful tool for qualitatively predicting the emission properties of a particular complex, there are instances where such predictions are not straightforward. This is apparent when considering that for many systems, particularly neutral iridium complexes, the HOMO is localised on the metal and the phenyl of the C^N ligand, while the LUMO is localised on the pyridine of the C^N ligand. Thus in these instances, substituents on the phenyl ring of the C^N ligand can have a profound effect on both the HOMO *and* the LUMO. Complexes **79** and **80** demonstrate this effect. Complex **79** contains the 2',6'-difluoro-2,3'-bipyridine cyclometalating ligand, and is a blue emitter in solution (λ_{PL} = 457 nm). Adopting -CF_3 substituents in place of fluorine atoms leads to a red-shift in the emission. The larger σ_m value for -CF_3 (σ_m = +0.43) compared with fluorine (σ_m = +0.34) would suggest that the -CF_3 groups should blue-shift the emission. However, the σ_p value for fluorine is close to zero (σ_m = +0.06), compared with a large positive value for -CF_3 (σ_p = +0.54), which results in a lower LUMO energy for **80** compared with **79** and thus red-shifted emission.[239;240]

A different strategy that has been employed recently is shown in Figure 3.4, whereby the electron-withdrawing nitrogen atom is methylated. The quaternised nitrogen is even more electron-withdrawing due to the additional positive charge, facilitating a significant

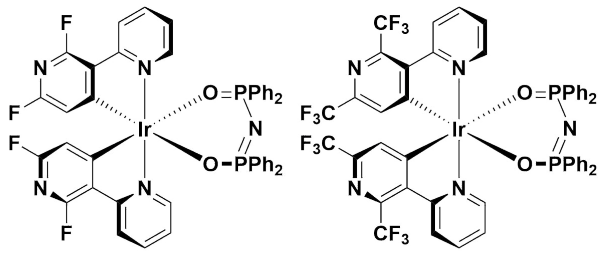

Complex:	79	80
λ_{PL} (nm):	457	500
Φ_{PL} (%):	7	63

Figure 3.3: Blue/blue-green emitting 'fluorine-free' iridium complexes bearing cyclometalated 2,3'-bipyridine ligands substituted with -CF_3 substituents, and its fluorinated analogue.[239;240]

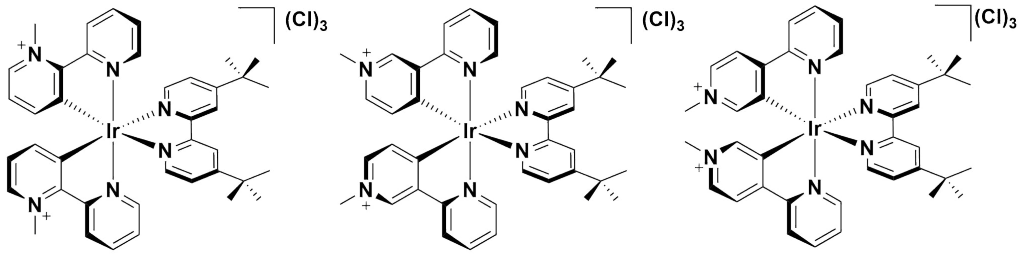

Complex:	81	82	83
λ_{PL} (nm):	530, 588	440, 468	522, 553
Φ_{PL} (%):	43	45	52

Figure 3.4: Selected examples of blue/blue-green emitting 'fluorine-free' iridium complexes bearing cyclometalated *N*-methylatated bipyridinium ligands.[241;242]

blue-shift in the emission. Furthermore, the increased charge on the complex confers these complexes with interesting properties, such as water solubility (as the chloride salt) or as potentially interesting candidates for LEECs, where higher charge on the complex can improve device turn-on times.[131;137] However, this high charge does impede the purification process for these complexes, requiring expensive sephadex chromatography to purify rather than traditional purification methods employed for cationic iridium(III) complexes.

Again, the photophysics of these complexes is entirely dependent on the regiochemistry. When the methylated nitrogen is situated in a *meta*-relationship with respect to the metal (**81** and **83**) the emission is only green in colour (λ_{PL} = 530 nm for **81** and 522 nm for **83**). When situated *para*- to the metal, the emission is overwhelmingly shifted into the deep blue (λ_{PL} = 440, 468 nm for **82**) with a high quantum yield for a deep-blue cationic

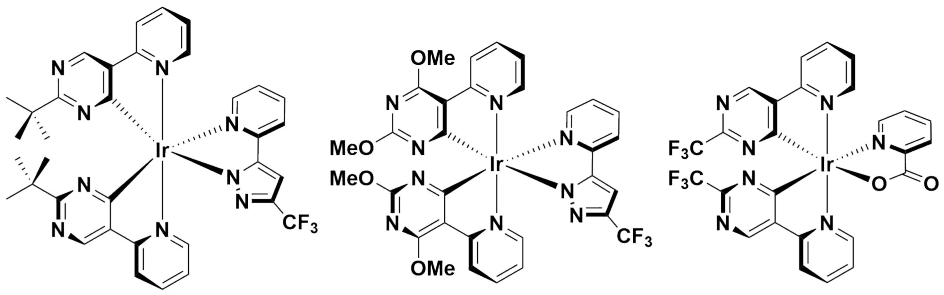

Complex:	84	85	86
λ_{PL} (nm):	456, 488	444, 472	470, 503
Φ_{PL} (%):	63	91	12

Figure 3.5: Selected examples of blue/blue-green emitting 'fluorine-free' iridium complexes bearing cyclometalated 5-(pyridin-2-yl)pyrimidine ligands.[243–245]

emitter (Φ_{PL} = 45%).[241;242] Encouragingly, complex **82** only employs dtbubpy as the N^N ligand, leaving open the possibility to push the emission even further into the blue by using a more blue-shifting N^N ligand.

Recently, the work on cyclometalated 2,3'-bipyridines has been extended to cyclometalated 5-(pyridin-2-yl)pyrimidine ligands, wherein the incorporation of an additional nitrogen atom within the C^N ligand framework blue-shifts the emission even further.[243–246] Examples are given in Figure 3.5. Complex **84** combines the pyrimidyl cyclometalating ligand with the anionic pyrazolate to blue-shift the emission (λ_{PL} = 456, 488 nm), and this is pushed even further into the blue by complex **85** ((λ_{PL} = 444, 570 nm) which combines the pyrimidyl moiety with the methoxy strategy discussed for complexes **76** – **78**. By contrast, complex **86** (λ_{PL} = 470, 503 nm) is red-shifted compared to **84** and **85**, since the ancillary picolinate ligand is not as effective at destabilising the LUMO energy as the pyrazolate N^N ligand used in **84** and **85**. Finally, studies on the regiochemical relationship of the pyrimidyl nitrogens with respect to the metal were again shown to be important, with all examples showing that isomers where the nitrogens are in a 4,6-relationship (*meta*, *meta*) are red-shifted compared to when they are in a 3,5-relationship (*ortho*, *para*).

3.1.2 Chapter Outline

In this chapter, the first examples of cationic iridium complexes bearing cyclometalated 5-(pyridin-2-yl)pyrimidine ligands are reported (Figure 3.6). Combinations of four different ligands were studied. For the C^N ligands, the same cyclometalating pyrimidyl ring

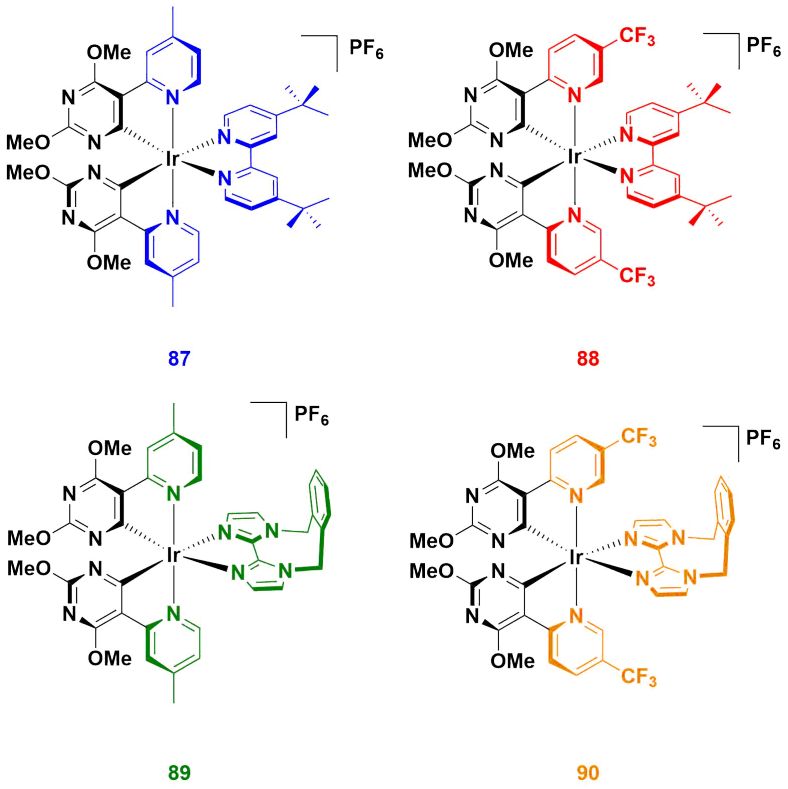

Figure 3.6: Targets complexes synthesised in this study.

(2,4-dimethoxypyrimidine) was chosen. The pyridyl ring of the C^N ligand was varied either to contain a methyl group *para* to the metal centre (5-(4-methylpyridin-2-yl)-2,4-dimethoxypyrimidine, Mepypyrm), or to contain a trifluoromethyl group *para* to the pyrimidyl ring (5-(5-(trifluoromethyl)pyridine-2-yl)-2,4-dimethoxypyrimidine, CF_3pypyrm). For the N^N ligands, dtbubpy was used to understand the effects on the photophysical properties of the new C^N ligands on the complexes (**87** and **88**) in comparison to well-studied systems. In addition, the *o*-Xylbiim ligand was used to see if the emission of the subsequent complexes (**89** and **90**) could be blue-shifted further than their dtbubpy analogues.

Given the paucity of cationic iridium complexes bearing cyclometalated heterocycles, it is helpful to compare complexes **87** – **90** to reference complexes with well-characterised photophysical properties. Thus for this study, complex **14** will be used as a reference to compare the electronics of the dFppy C^N ligand with the new Mepypyrm and CF_3pypyrm ligands, while **69** will provide a reference for the *o*-Xylbiim complexes **89** and **90**. Complex **78** is structurally very similar to **87** except the cyclometalating heterocycle is a pyridine and not a pyrimidine (2',6'-dimethoxy-4-methyl-2,3'-bipyridine, 5-Mepypy), and thus serves

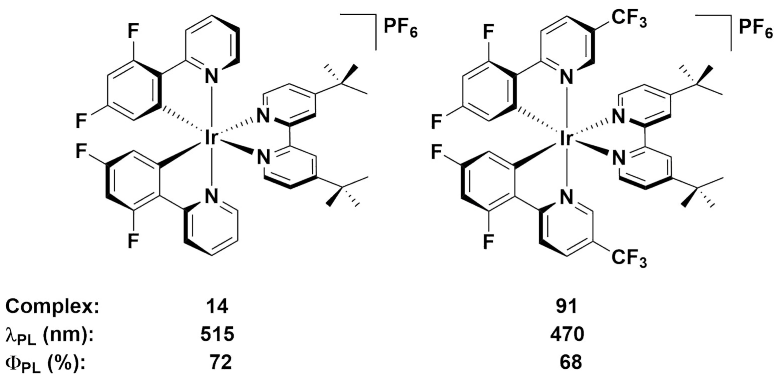

Figure 3.7: Reference complex **14** and its -CF_3 substituted analogue.[247]

as a basis to understand the effects of the additional nitrogen atom contained within the pyrimidine ring on the optoelectronic properties of the complex. Finally, complex **91**,[247] like complexes **88** and **90**, has a -CF_3 substituent incorporated into the pyridine ring of the C^N ligands (2-(2,4-difluorophenyl)-5-(trifluoromethyl)pyridine, dFCF_3ppy), making this an important complex for understanding the difference in electronics between Mepypyrm and CF_3pypyrm.

3.2 Synthesis and Characterisation

3.2.1 Syntheses of Ligands and Complexes

The two C^N cyclometalating ligands could be made in two steps. Lithiation of 5-bromo-2,4-dimethoxypyrimidine with *n*-BuLi and quenching with trimethylborate afforded, after hydrolysis with HCl, the corresponding boronic acid. Both C^N ligands were then obtained through a Suzuki-Miyaura[248] cross-coupling reaction with the appropriate substituted halopyridine. Synthesis of the chloro-bridged dimers proceeded by refluxing the C^N ligand in 2-ethoxyethanol with [Ir(COD)(μ-Cl)]$_2$ as the iridium source, and then complexes **87** – **90** were obtained by cleavage of the isolated crude dimers with an excess of N^N ligand in refluxing DCM/MeOH solution. The anion metathesis step was initially carried out using NH_4PF_6, but to avoid protonation of the pyrimidine rings on the complexes (*vide infra*) KPF_6 was used subsequently instead.

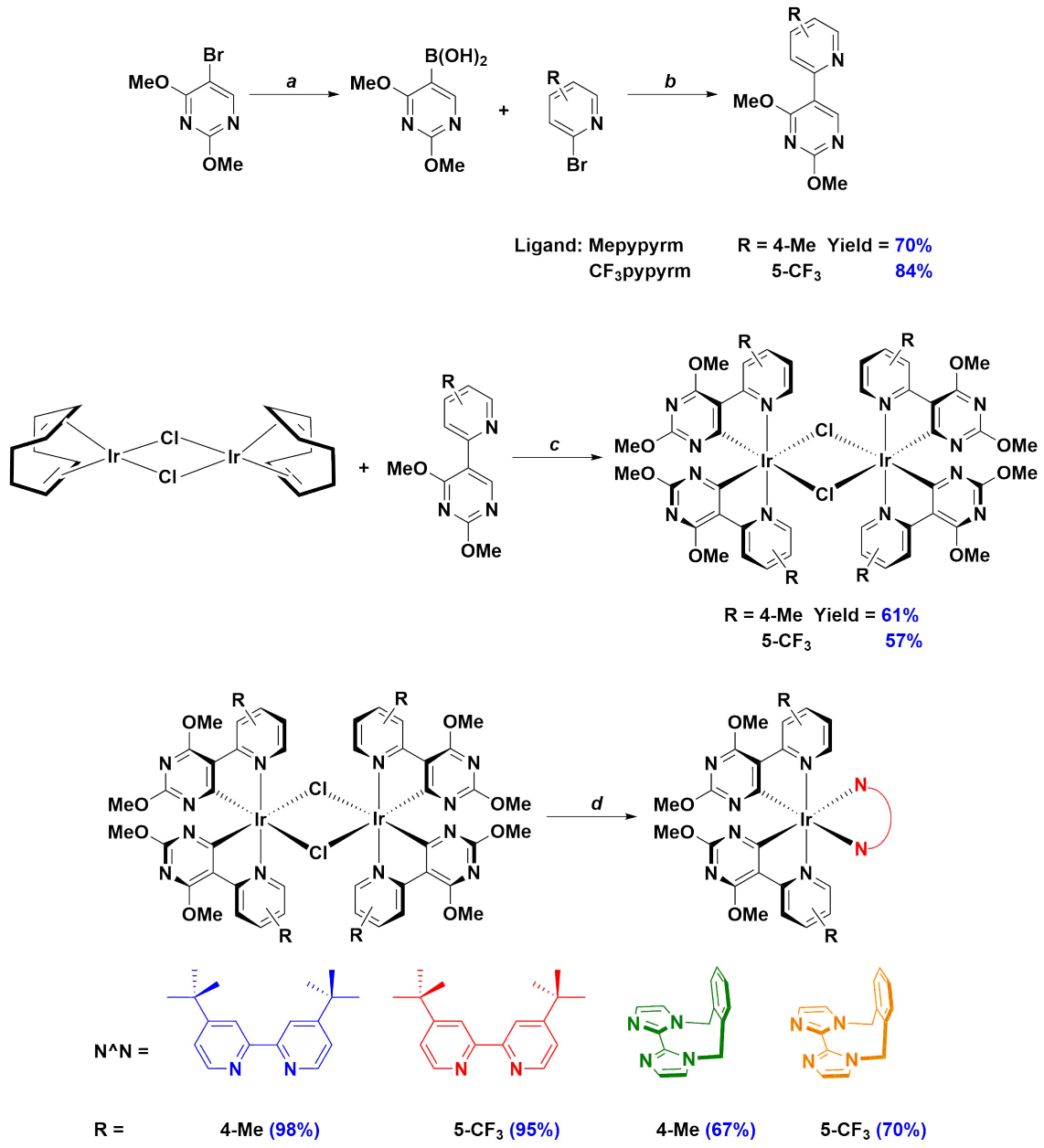

Figure 3.8: Synthesis of C^N ligands and complexes. Reagents and conditions: [a] i) *n*-BuLi (1.3 equiv., 2.5 M in Hexanes), THF, N_2, −78 °C 1h; ii) $B(OMe)_3$ (1.5 equiv.), rt, 16 h; iii) HCl, 16 h, rt. [b] K_2CO_3 (3.0 equiv.), 1,4-dioxane/water (2:1 v/v), $Pd(PPh_3)_4$ (5 mol%), 80 °C 16 h. [c] 2-$EtOC_2H_4OH$, 110 °C N_2, 3 h. [d] i) DCM/MeOH (1:1 v/v), 40 °C 19 h, N_2; ii) Excess KPF_6 (aq).

3.2.2 Complex Characterisation

All complexes were characterised by ^{1}H, ^{13}C and, for complexes **88** and **90**, ^{19}F NMR spectroscopy. In addition, all the complexes were further characterised by high resolution mass spectrometry (HRMS) and elemental analysis (EA). Additionally, the structures of the four complexes were determined by single crystal X-ray diffraction.

The X-ray crystal structures of complexes **87** – **90** are shown in Figure 3.9, and the relevant crystallographic parameters are given in Table 3.1. In the solid-state, all four complexes show the expected distorted octahedral geometry about the iridium centre, with two C^N ligands coordinating through the pyridyl nitrogen atoms in a mutually *trans* configuration and the cyclometalating carbon atoms of the pyrimidine rings mutually *cis* to each other. The coordination sphere is completed by coordination through the nitrogen atoms of the N^N ligands (Figure 3.9). It was surprising to observe to observe that in contrast to complexes **87** and **88**, the crystal structures of **89** and **90** are not monocationic. In both cases one of the pyrimidyl nitrogen atoms of each of complexes is protonated, which is hypothesized to arise from the initial use of NH_4PF_6 as the anion metathesis reagent. In the case of **89**, the complex is a dication with two PF_6^- anions present for charge balance and a hydrogen bond (2.134 Å) between the protonated pyrimidine ring and an acetonitrile solvent molecule. Complex **90** crystallises as a dimeric pair of protonated (**90a**) and non-protonated (**90**) complexes, which form a tight hydrogen bond (1.984 Å) between the protonated pyrimidine ring of **90a** and the non-protonated pyrimidine ring of **90b**. Thus, in the crystal structure there are three PF_6^- anions for charge balance: one for each cyclometalated complex, and one for the additional proton.

For complexes **87** and **88**, an unusual structural feature is observed, where only one of the Ir-C_{C^N} bond lengths is shorter than the Ir-N_{C^N} bond lengths from the same C^N ligand (Table 3.1). This is not typical of cyclometalated iridium complexes as the Ir-C_{C^N} bonds are generally considered to be stronger than the Ir-N_{C^N} bonds, and thus they would all be expected to be shorter. By contrast, complexes **89**, **90a** and **90b** show more conventional behaviour.

In solution, batches of **87** and **88** prepared using NH_4PF_6 as the anion metathesis reagent gave unusually broad and featureless ^{1}H NMR spectra, which were attributed to the formation of hydrogen-bonded assemblies due to protonation of the pyridimine rings, as was observed in the crystal structures of **89** and **90**. Figure 3.10 shows a comparison of the

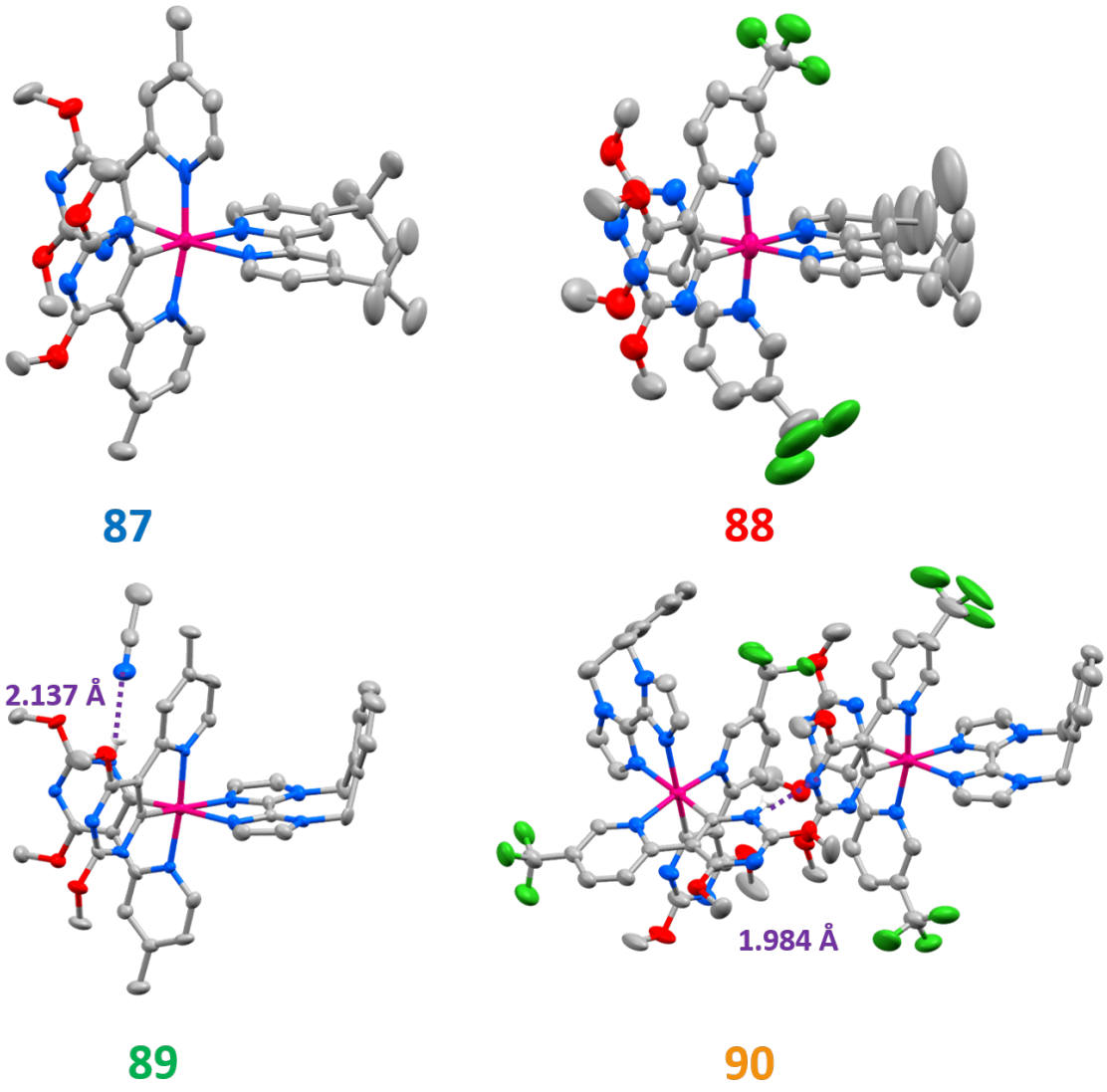

Figure 3.9: X-ray crystal structures of complexes **87** – **90**. Counterions, C-H hydrogen atoms and non-hydrogen bonding solvent molecules have been removed for clarity. Atom labelling: hydrogen (white), carbon (grey), nitrogen (blue), oxygen (red), fluorine (green), iridium (pink). Hydrogen bonding of the protonated pyrimidine rings in 3 and 4 is denoted with a dashed purple line.

Complex	Bond Length (Å)			Bond Angle (°)	
	Ir-C	Ir-N_{C^N}	Ir-N_{N^N}	N-Ir-C	N-Ir-N
87	1.993(19)	2.030(19)	2.134(16)	79.5(8)	75.6(6)
	2.014(17)	1.949(19)	2.146(15)	79.5(8)	
88	1.997(15)	1.98(2)	2.138(13)	80.7(8)	76.6(5)
	1.950(17)	2.04(2)	2.119(15)	80.7(8)	
89	1.968(7)	2.049(6)	2.109(6)	79.9(3)	75.5(2)
	1.950(17)	2.04(2)	2.119(15)	80.7(8)	
90a	1.980(6)	2.051(5)	2.099(5)	80.2(2)	75.85(19)
	1.970(6)	2.040(5)	2.138(5)	79.9(2)	
90b	1.964(6)	2.029(5)	2.118(5)	79.8(2)	75.6(2)
	1.989(6)	2.035(5)	2.136(5)	79.7(2)	

Table 3.1: Selected crystallographic parameters for complexes **87**, **88**, **89** and the dimeric pair **90a** and **90b**.

^{1}H NMR spectra of batches of complex **88** prepared using NH_4PF_6 and KPF_6, showing the sharper features present for the batch prepared using KPF_6. Addition of K_2CO_3 to a solution of complex prepared using NH_4PF_6 resulted in deprotonatation of the complex to give the expected sharp spectrum. In order to ensure valid comparison across the series of complexes, all photophysical measurements were carried out on samples prepared using KPF_6. Elemental analysis confirmed they are in their monocationic forms.

The ^{1}H NMR spectra of non-protonated samples of complexes **89** and **90** are expectedly broad, as a result of slow fluxional motion of the o-Xylbiim ligand on the NMR timescale as was observed for complexes **89** and **90**. Heating the samples resulted in simplification of the spectra due to the dynamic pseudo C2-symmetric geometry. An example variable temperature NMR spectrum of complex **90** is given in Figure 3.11. Eyring analysis on the barrier to inversion for 3 and 4 gave similar activation energies to each other ($\Delta G^{\ddagger}$ = 83 kJ mol^{-1} for complexes **89** and **90**, respectively) as well as to complexes **66** ($\Delta G^{\ddagger}$ = 72 kJ mol^{-1}) and **69** ($\Delta G^{\ddagger}$ = 82 kJ mol^{-1}).

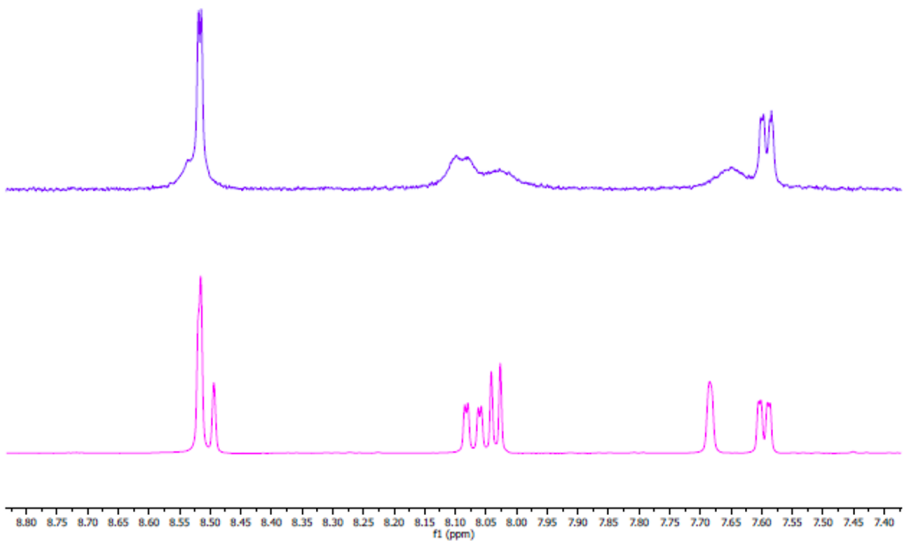

Figure 3.10: Aromatic region of the ^{1}H NMR spectra for **88** in CD_3CN prepared using NH_4PF_6 (top) or KP_6 (bottom) as the anion metathesis reagent.

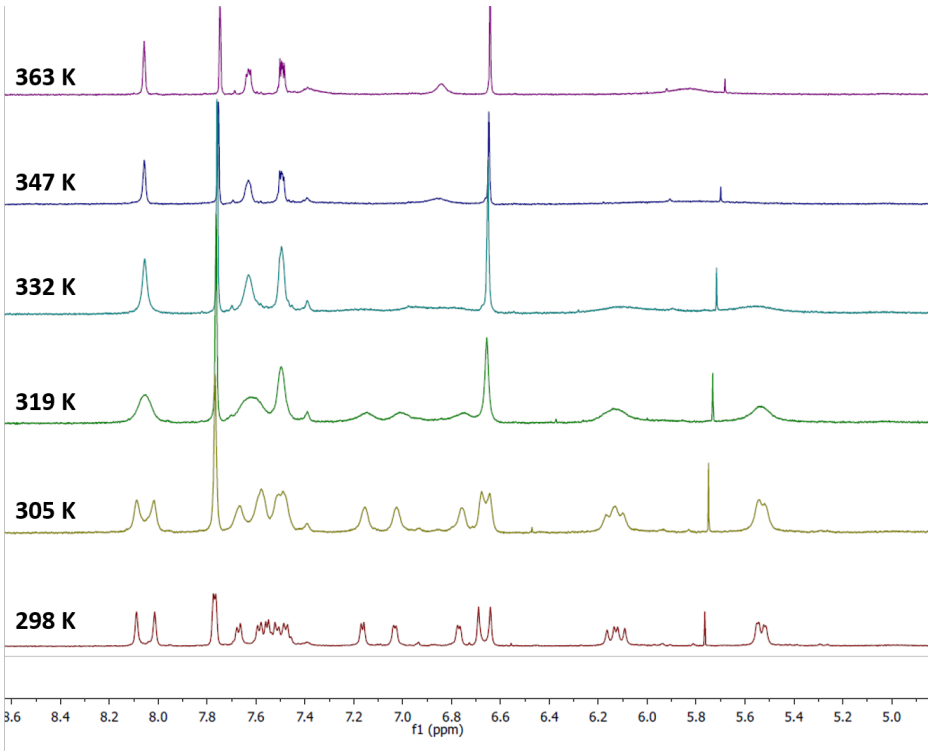

Figure 3.11: ^{1}H NMR spectra for the aromatic region of complex **90** in DMSO-d_6 as a function of temperature.

3.3 Optoelectronic Characterisation

3.3.1 Electrochemistry

Electrochemical measurements on **87** – **90** were carried out in deaerated MeCN. The CV traces are shown in Figure 3.12 while the relevant electrochemical data is given in Table 3.2. The first oxidation wave in **87** was found to be quasi-reversible while those of **88** – **90** were found to be irreversible. The oxidation potential for **87** ($E_{1/2(ox)}$ = 1.53 V) is cathodically shifted compared to **88** ($E_{1/2(ox)}$ = 1.70 V) indicating that the -CF_3 group is exerting a stabilising influence on the HOMO of **88**. This is consistent with the analogous comparison of complexes **14** ($E_{1/2(ox)}$ = 1.60 V) and **91** ($E_{1/2(ox)}$ = 1.69 V) though the effect is more pronounced in **88** compared to **87** due to the concomitant removal of the electron-donating methyl group, which is not present in **14**. A slightly less positive oxidation potential is observed for **87** compared to **14**, which indicates that dFppy more strongly stabilises the HOMO than the Mepypyrm C^N ligand. There is only a small difference in the oxidation potential measured for **78** ($E_{1/2(ox)}$ = 1.51 V) compared to **87**, demonstrating that the additional nitrogen atom in the pyrimidine has only a modest influence on the HOMO. In contrast to **87** and **14**, complex **88** has a virtually identical oxidation potential to **91** ($E_{1/2(ox)}$ = 1.69 V), demonstrating the importance of the influence of the -CF_3 substitution in the C^N ligand design.

Complex	$E_{1/2(ox)}$ (V)	$E_{1/2(red)}$ (V)	ΔE (V)	E_{HOMO} (eV)	E_{LUMO} (eV)
87	1.53	-1.39	2.92	-5.95	-3.03
88	1.70	-1.38	3.08	-6.12	-3.04
89	1.46	-2.00	3.46	-5.88	-2.42
90	1.65	-1.74	-3.39	-6.07	-2.68
14	1.60	-1.36	2.96	-6.02	-3.06
69	1.37	-1.99	3.36	-5.79	-2.47
78	1.51	-1.41	2.92	-5.93	-3.01
91	1.69	-1.37	-3.06	-6.11	-3.05

Table 3.2: Electrochemical data for complexes **87**, **88**, **89**, **90**, **14**, **69**, **78** and **91**. Measurements were carried out in MeCN at a scan rate of 100 mV s^{-1} with Fc/Fc^+ employed as an internal standard, and data reported *vs* SCE (Fc/Fc^+ = 0.38 V in MeCN).

As was observed for **87** and **88**, the oxidation potential of **89** ($E_{1/2(ox)}$ = 1.46 V) is

cathodically shifted compared to 90 ($E_{1/2(ox)}$ = 1.65 V). Both the *o*-Xylbiim complexes 89 and 90 show marginally cathodically shifted oxidation waves compared to their corresponding dtbubpy analogues 87 and 88; a consequence of the electron-releasing nature of the biimidazole N^N ligand. A similar comparison exists with complexes **14** and **69** ($E_{1/2(ox)}$ = 1.37 V).

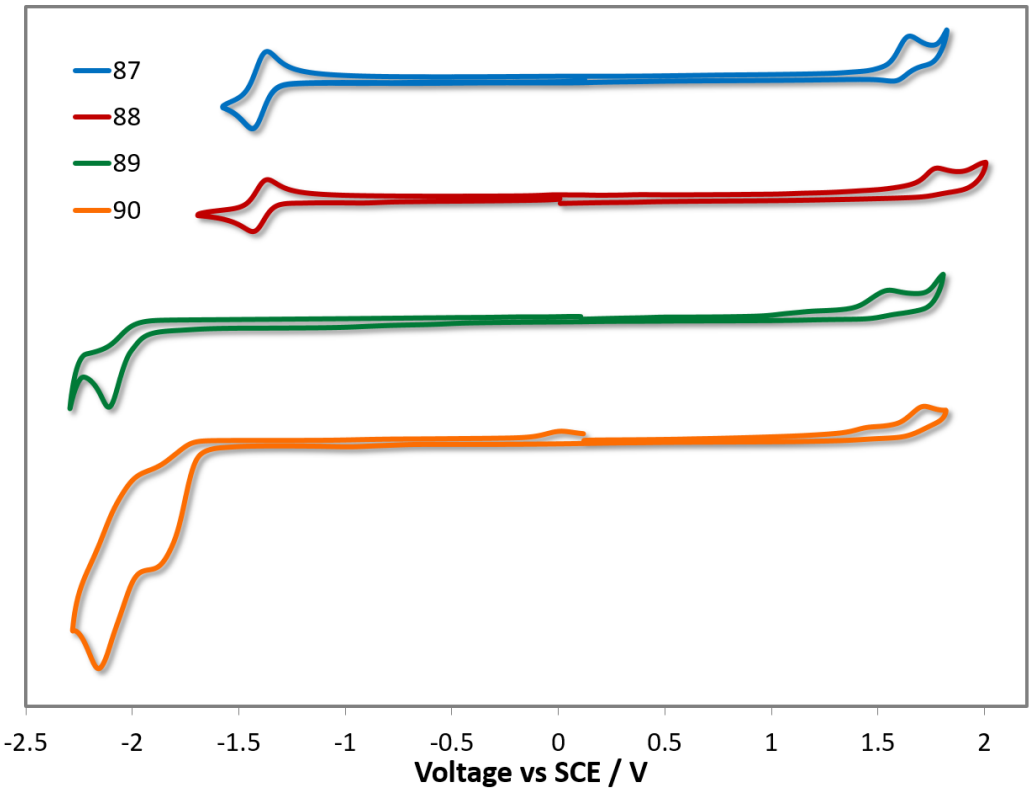

Figure 3.12: CV traces of complexes 87, 88, 89 and 90 in MeCN solution, reported versus SCE (Fc/Fc^+ = 0.38 V in MeCN).[219] Scan rates were at 100 mV s^{-1}, and are in the positive scan direction.

Determining trends for the observed reduction potentials is less straightforward. For complexes 87 and 88, a reversible reduction at virtually the same potential ($E_{1/2(red)}$ = -1.39 V for 87 and -1.38 V for 88) was attributed to reduction of the dtbubpy ligand. Complexes **14**, **78** and **91** likewise show reversible reduction waves in a similar range ($E_{1/2(red)}$ = -1.36 V for **14**, -1.41 for **78** and -1.37 for **91**). For complexes 89 and 90, the reduction waves are observed at significantly lower potentials ($E_{1/2(red)}$ = -2.00 V for 89, -1.74 V for 90) and are irreversible in nature. The nature of the reductions in 89 and 90 can be inferred by scanning beyond the reduction potentials of the dtbubpy ligand for complexes 87 and 88 (Figure 3.13). Complex 87 exhibits a second irreversible reduction at

the same potential ($E_{1/2(red)}$ = -2.00 V) as the reduction for **89**, which strongly suggests reduction of the pyridine ring of the C^N ligand. However, it is worth noting that the reduction wave in **69**, which was attributed to reduction of the *o*-Xylbiim ligand, is also at almost the same potential ($E_{1/2(red)}$ = -1.99 V). It is therefore plausible that the reduction wave of complex **89** might instead be due to the reduction of the N^N ligand. For complex **90**, there are at least two observable reduction processes that can be attributed to either or both the reduction of the *o*-Xylbiim ligand and the pyridyl ring of the C^N ligand. A similar set of multi-electron reductions are observed for complex **88** ($E_{1/2(red)}$ = -1.86 V) and these are anodically shifted compared to the second reduction observed for **87**. This behaviour mirrors the anodic shift observed in the first reduction of **90** compared to **89** and is consistent with direct reduction of a more electron deficient CF_3-substituted pyridine ring. Finally, complex **91** is reported to have a second reduction ($E_{1/2(red)}$ = -1.68 V) that was attributed to the reduction of the dFCF_3ppy ligand in a similar regime to the first reduction of **90**.

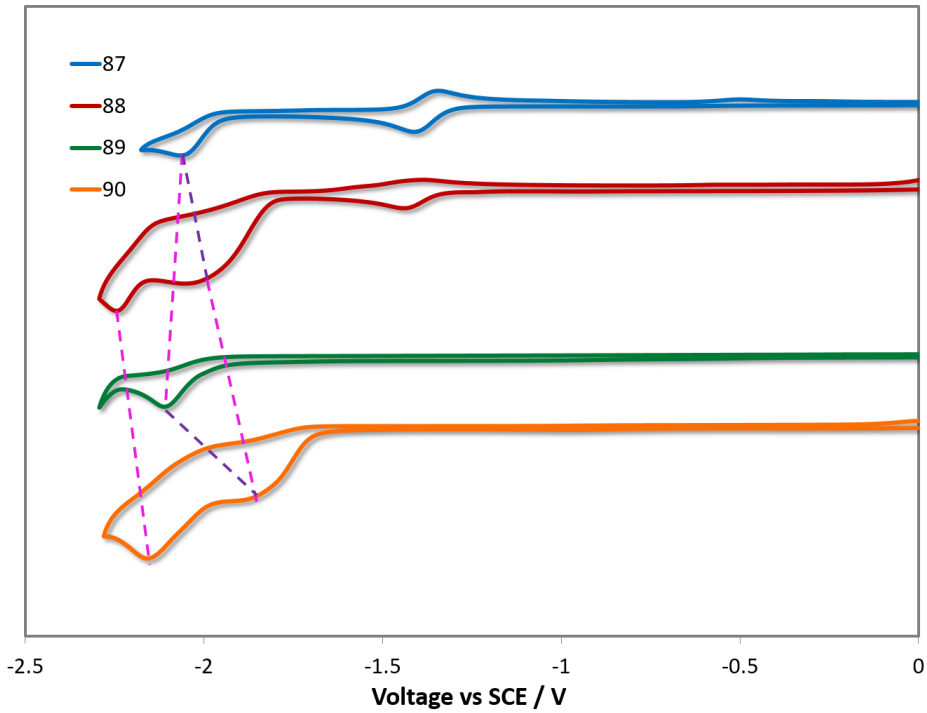

Figure 3.13: CV traces of complexes **14**, **68** and **69** in MeCN solution, reported versus SCE (Fc/Fc^+ = 0.38 V in MeCN)[219] redox couple. Scan rates were at 100 mV s^{-1}, and are in the positive scan direction.

3.3.2 UV-Vis Absorption

The UV-vis absorption spectra for complexes **87** – **90** are shown in Figure 3.14 and the molar absorptivity data is given in Table 3.3. In the high-energy region of the spectrum (250 – 325 nm), $^1\pi$-π^* transitions for all complexes dominate and the features of the spectra are determined by the nature of the N^N ligand. The principal $^1\pi$-π^* bands for complexes **87** and **88** are blue-shifted (λ_{abs} = 264 nm for **87** and 261 nm for **88**) and more intense than for **89** and **90** (λ_{abs} = 268 nm for **89** and 276 nm for **90**), which is in accordance with what was observed previously between complexes containing dtbubpy or *o*-Xylbiim as the N^N ligand. In addition, two bands are observed for **87** and **88** (λ_{abs} = 300 and 311 nm for **87** and 297 and 311 nm for **88**) that are not present for **89** and **90**, which suggest that these bands involve uniquely the dtbubpy N^N ligand.

Complex	λ_{abs} (nm) [ϵ ($/10^4$ M^{-1} cm^{-1}]
87	264 [6.5], 300 [3.5], 311(sh) [3.1], 335 [1.7], 361 [0.9]
88	261 [5.6], 275(sh) [4.6], 297(sh) [3.1], 311 [2.5], 350 [1.5], 384 [0.7]
89	268 [3.9], 322 [1.5], 339 [1.2], 369 [0.4]
90	276 [4.1], 315(sh) [1.8], 352 [1.2], 388 [0.4]

Table 3.3: Absorption maxima and their corresponding molar absorptivities for complexes **87**, **88**, **89** and **90**. [a] Measured in aerated MeCN at room temperature.

At lower energies, the trends are reversed, with the absorption features insensitive to the nature of the N^N ligand but strongly affected by the nature of the C^N ligand. Complexes **87** and **89** have a pair of poorly resolved absorption bands (λ_{abs} = 335 and 362 nm for **87** and 339 and 369 nm for **89**). Complexes **88** and **90** have a similar pair of absorption bands but these bands are well-resolved and red-shifted (λ_{abs} = 350 and 384 nm for **88** and 352 and 388 nm for **90**). The similarity of the absorption spectra suggests that these bands constitute transitions localised on the C^N ligands. However, their much lower absorptivity values compared to the higher energy absorption bands implies that they are not likely to comprise significant π-π^* contributions. Instead, the lower absorptivities of these bands for the four complexes is indicative of charge transfer contributions from the metal to the pyridine on the C^N ligand (^{1}MLCT), as well as from the methoxy substituents into the pyridyl rings (^{1}ILCT). The red-shift observed for complexes **88** and **90** corroborates this charge transfer assertion, due to stabilisation of the orbitals on the pyridyl ring by the

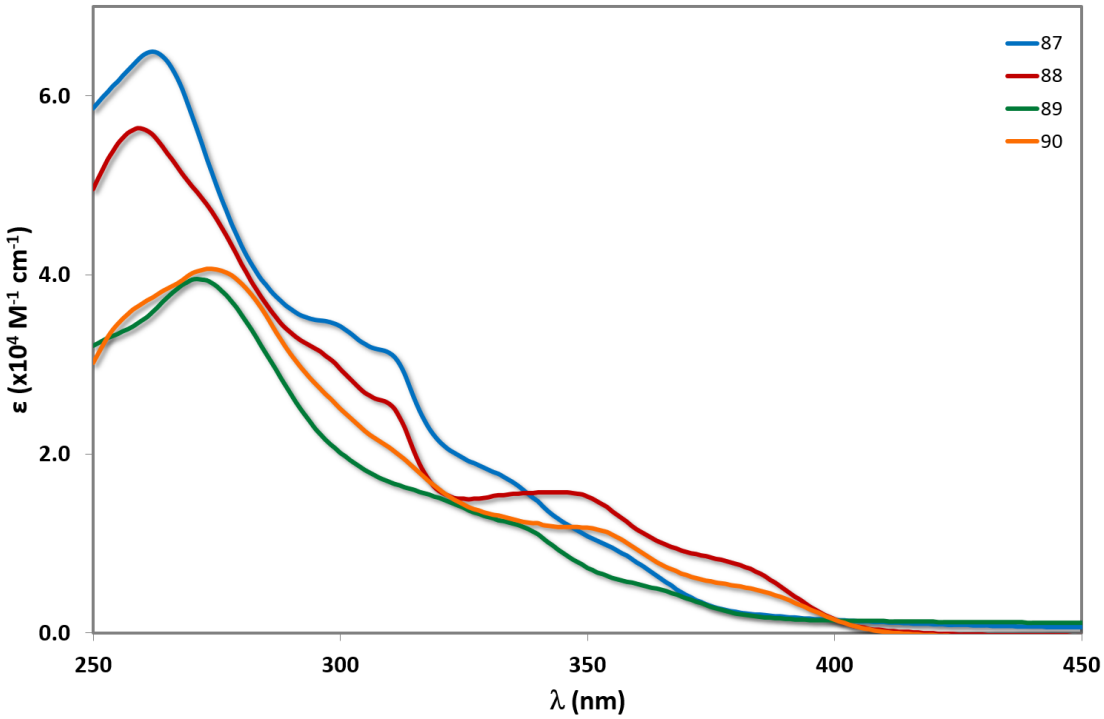

Figure 3.14: UV-Vis absorption spectra of complexes **87** – **90** in MeCN solution.

electron-withdrawing -CF_3 group, and is in accordance with an anodic shift in the second reduction potentials of **88** compared to **87** and the first reduction potential of **90** compared to **89**. Although the principal bands for complexes **87** and **89** are blue-shifted, there is weak absorption beyond the onset of absorption for complexes **88** and **90**, suggesting that the lowest energy transition is in fact higher in energy for complexes **88** and **90** than for **87** and **89**.

3.3.3 Photoluminescence

The photophysical properties of these complexes were studied in MeCN solution at 298 K. Their emission profiles are shown in Figure 3.15, and the relevant photophysical data are given in Table 3.4. Complex **87** is a green emitter, with broad, unstructured emission that is characteristic of a mixed charge transfer state between both the metal to the N^N ligand (^{3}MLCT) and the C^N ligands to the N^N ligand (^{3}LLCT). The photophysical properties of **87** (λ_{PL} = 515 nm, Φ_{PL} = 81%) are remarkably similar to **14** (λ_{PL} = 515 nm, Φ_{PL} = 72%) and **78** (λ_{PL} = 517 nm, Φ_{PL} = 53%), suggesting that the additional nitrogen in the pyrimidyl ring in this instance does not have a significant influence on the energy of the T_1 state.

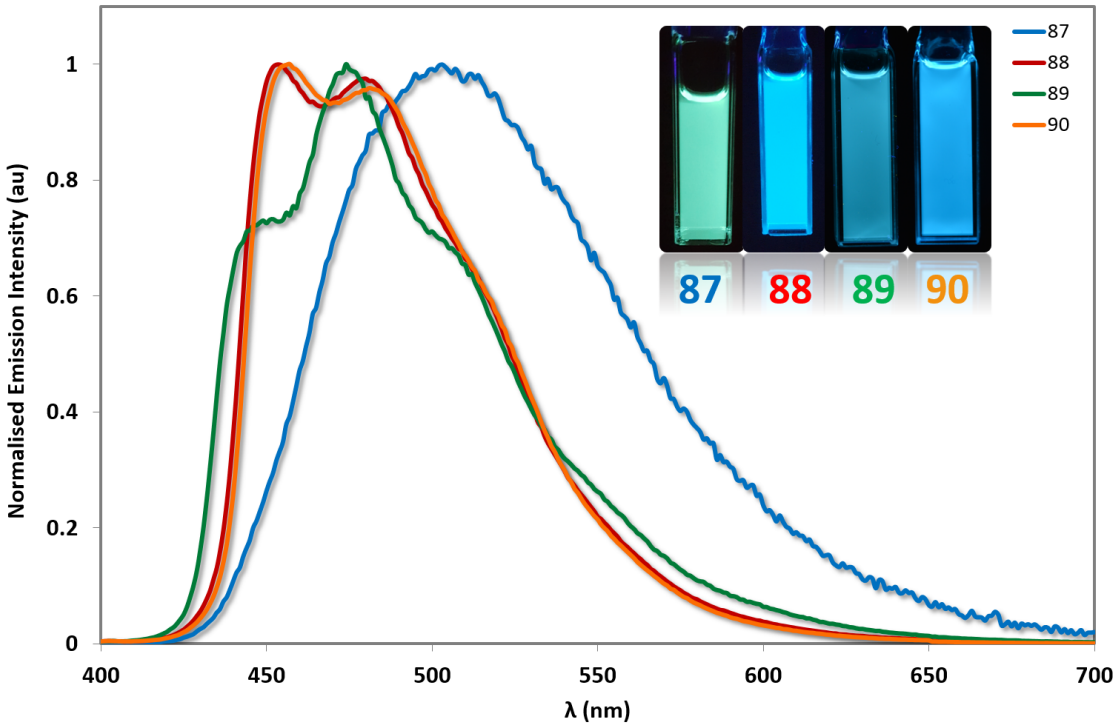

Figure 3.15: Emission spectra of complexes **87** – **90** in deaerated MeCN solution at 298 K. Inset: MeCN solutions of complexes **87**, **88**, **89** and **90** illuminated under UV light.

By contrast, **88** displays structured ^{3}LC emission localized on the C^N ligands that is significantly blue-shifted (λ_{PL} = 454, 481 nm, Φ_{PL} = 77%) compared to **87**. Analogously, complex **91** is blue-shifted (λ_{PL} = 470 nm, Φ_{PL} = 68%) compared to complex **14**, demonstrating that the -CF_3 group exerts a significant blue-shifting effect on the emission energy. However, the blue-shifted emission of **88** compared to **91** implies a synergistic blue-shifting effect between the -CF_3 moiety and the pyrimidine compared to the dFCF_3ppy ligand.

While complex **87** showed emission from a mixed ^{3}MLCT/^{3}LLCT state, the use of the *o*-Xylbiim ligand in **89** and **90** renders the N^N ligand non-chromophoric and thus the emission of **89** originates from a blue-shifted, highly vibronic ^{3}LC state (λ_{PL} = 446, 475, 510 nm, Φ_{PL} = 80%). The principal vibronic bands in **89** virtually coincide with those of complex **88**, but the relative intensities differ; for complex **89**, the most intense band is at 475 nm, while the band at 446 nm appears as a less intense shoulder. In the case of **88**, the emission intensities of both bands are very similar, with the band at 454 nm only marginally more intense than that at 481 nm. Finally, complex **89** has a third shoulder at 510 nm that is almost totally suppressed in the case of **88**. Thus, **88** appears bluer than **89** due to a smaller contribution to the emission from the blue-green region of the spectrum.

Complex	λ_{PL} (nm) [a]	CIE (x, y)	Φ_{PL} (%) [b]	τ_e (μs) [c]	k_r ($/10^5$ s^{-1})	k_{nr} ($/10^5$ s^{-1})
87[c]	515	0.20, 0.41	81	1.36	5.96	1.40
88[c]	454, 481	0.14, 0.19	77	4.21	1.82	0.55
89[c]	446, 475, 510	0.16, 0.23	80	9.01	0.89	0.22
90[d]	457, 483	0.15, 0.23	73	4.77	1.53	0.57
14	515	-	72	1.36	5.29	2.09
69	459, 487	-	90	2.19	4.11	0.46
78	517	-	53	1.30	4.08	3.62
91	470	-	68	2.30	2.96	1.39

Table 3.4: Relevant solution-state photophysical data for complexes **87** – **90**, **14**, **69**, **78** and **91**. [a] λ_{exc}: 360 nm. [b] Quinine sulfate used as the reference (Φ_{PL} = 54.6% in 0.5 M H_2SO_4 at 298 K).[220] [c] λ_{exc}: 378 nm.

The blue-shift in emission observed for **89** compared with **87** is not mirrored in the analogous comparison between **90** and **88**. In this instance, the emission profile of **90** (λ_{PL} = 457, 483 nm, Φ_{PL} = 73%), overlaps almost coincidentally with **88** albeit with a small red-shift in the former. It is therefore apparent that when the -CF_3 group is incorporated into the C^N ligand, the emission becomes totally localised on the cyclometalating ligand and the ancillary ligand exerts almost no influence.

The relatively long excited state lifetimes (τ_e > 4 µs) and small radiative constants ($k_r < 2 \times 10^5$ s^{-1}) further support the predominantly ^{3}LC character of the emissive triplet state in complexes **88** – **90**. By contrast, complex **87** displays a shorter lifetime (τ_e = 1.36 µs) and larger radiative rate constant ($k_r = 5.96 \times 10^5$ s^{-1}) which is in line with a CT-based triplet excited state. The optoelectronic properties of complex **88** are therefore remarkable: the global LUMO of the complex resides on the N^N ligand (as determined by the electrochemistry), which is expected to result in a d_π-$\pi^*_{N^N}$ MLCT/LLCT state of lower energy than the π_{C^N}-$\pi^*_{C^N}$ ^{3}LC state, emission appears to originate from the higher energy ^{3}LC state.

This is an important feature, especially when the reference complexes are considered. Comparing **87** with **14** leads to the conclusion that these two complexes are photophysically indistinct, with both exhibiting emission from a ^{3}MLCT/^{3}LLCT state, as well as similar excited lifetimes and quantum yields. Thus, it can be concluded that in this instance

the optoelectronic properties exerted by the Mepypyrm C^N ligand on the corresponding complex compared to dFppy are essentially the same. By contrast, when the analogous comparison is made between CF_3pypyrm (**88**) and dFCF_3ppy (**91**), the photophysical properties of these complexes diverge drastically; **91** is blue-shifted compared to **14**, but it nevertheless emits from a predominantly ^{3}MLCT/^{3}LLCT state, with a chromophoric contribution from the dtbubpy N^N ligand. On the other hand, the CF_3pypyrm C^N ligand renders the dtbubpy ancillary ligand non-chromophoric, which is highly unusual for iridium(III) complexes bearing these N^N ligands.

This unusual feature of the CF_3pypyrm C^N is mirrored by the photophysics of **90**, which has virtually identical photophysical properties to complex **88** (similar emission maximum, shape of the emission spectrum, Φ_{PL}, excited state lifetime, and radiative and non-radiative constants) despite the presence of the *o*-Xylbiim ancillary ligand which has a much higher energy LUMO compared to dtbubpy.

Finally, complex **69** is the bluest among the reference complexes (λ_{PL} = 459, 487 nm, Φ_{PL} = 90%) due to the adoption of the *o*-Xylbiim ligand as the N^N ligand. Although it is moderately more emissive, complexes **88** and **90** are modestly blue-shifted in emission, showing that it is possible to achieve significantly blue-shifted emission in cationic iridium complexes without employing C-F_{aryl} bonds.

3.4 Conclusions and Further Work

The first examples of cationic iridium(III) complexes bearing cyclometalating pyrimidyl rings has been reported. By replacing the ubiquitous difluorophenyl ring with a judiciously designed pyrimidine ring, which combines electron-withdrawing nitrogen atoms and ambivalent methoxy substituents (electron-donating in an *ortho* and *para* position and electron-withdrawing in a *meta* position), new C^N ligands capable of blue-shifting the emission of $[Ir(C^N)_2(N^N)]^+$ complexes can be achieved without employing C_{aryl}-F bonds. Additional modifications to the pyridine ring of the C^N, such as methyl in a *para* relationship with respect to the metal (Mepypyrm) or a -CF_3 substituent situated in a *para* relationship with respect to the pyrimidine, can blue-shift the emission even further, with the -CF_3 group being a particularly effective exponent. Remarkably, the optoelectronics of the complexes bearing the CF_3pypyrm C^N ligand were found to be independent of the N^N ligand used to complete the coordination sphere, even when ligands with a relatively

low-lying ground state LUMO (dtbubpy) were employed. Crucially, the ligand is also better at blue-shifting the emission than its fluorinated dFCF_3ppy analogue, pointing towards the merits of adopting the dimethoxypyrimidine ring in place of difluorophenyl.

Future work based on these complexes will entail the fabrication of LEECs to discern the efficacy of these new C_{aryl}-F free complexes in devices. Theoretical calculations are also in progress in particular to characterise the nature of the HOMO, LUMO and the triplet excited state, and in particular their divergent characteristics observed experimentally.

Chapter 4

Conjugated Bibenzimidazole Ligands for Enhanced Photoluminescence Quantum Yields of Orange/Red-Emitting Iridium(III) Complexes

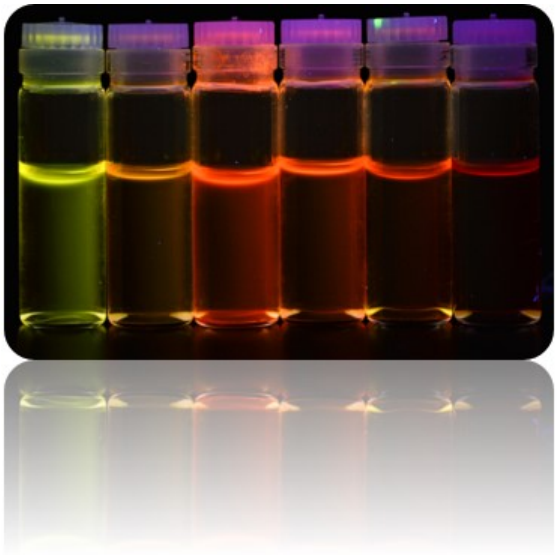

4.1 Introduction

4.1.1 Background

Chapters 2 and 3 have so far explored the use of electron-deficient C^N ligands and electron-rich N^N ligands in order to blue-shift the emission these complexes. In particular, the *o*-Xylbiim ligand was found to be effective at simultaneously blue-shifting the emission and increasing the photoluminescence quantum yield as a result of the rigidifying xylylene linker restricting intramolecular non-radiative decay pathways contributing to k_{nr}. This is particularly challenging, since the thermal population of MC states becomes facile when the HOMO-LUMO gap is large.

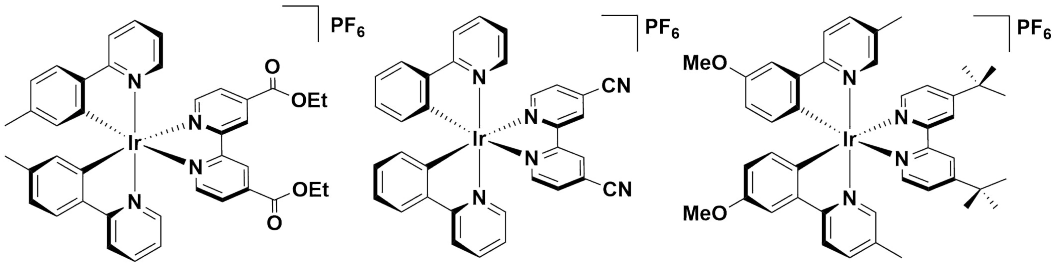

Complex:	42	91	92
λ_{PL} (nm):	687	608, 651	680
Φ_{PL} (%):	2	1	0.3

Figure 4.1: Red-emitting iridium complexes bearing electron-withdrawing groups to stabilise the LUMO (**42**,[142] **91**[249]) and electron-donating groups to destabilise the HOMO (**92**[250]). Photophysics in MeCN (complexes **42** and **92**) and in DCM (complex **91**).

An equally difficult challenge is the design of highly emissive red-emitting complexes, since the energy gap law dictates that a smaller HOMO-LUMO gap facilitates vibronic coupling of the ground state with the excited state, leading to an exponential increase in k_{nr} as a function of lower emission energy.[103;104] Red-shifting the emission profile of cationic iridium complexes is generally achieved in two ways: 1) by incorporating electron donating and withdrawing groups, respectively, within the C^N and N^N ligand frameworks, the HOMO and LUMO energies can be appropriately tuned so as to narrow the energy gap, and thus red-shift the emission; 2) by increasing the conjugation across the ligand scaffolds, the emission of these complexes will also become red-shifted in colour. Some examples are discussed below.

Complex **42** was discussed as a deep-red emitter as a result of the electron-withdrawing

ester groups on the ancillary ligand, although it has a low Φ_{PL}.[142] Similar properties are reported for the cyano-substituted complex **91**.[249] Complex **92** employs methoxy substituents in a *para* relationship with respect to the metal, and achieves strongly red-shifted emission compared to complexes such as **4** (λ_{PL} = 585 nm in MeCN), or its analogue with methoxy in a *meta* relationship with the metal (λ_{PL} = 585 nm in MeCN).[250] However, as with **42** and **91**, this comes at the expense of very low quantum yield (Φ_{PL} = 0.3%).

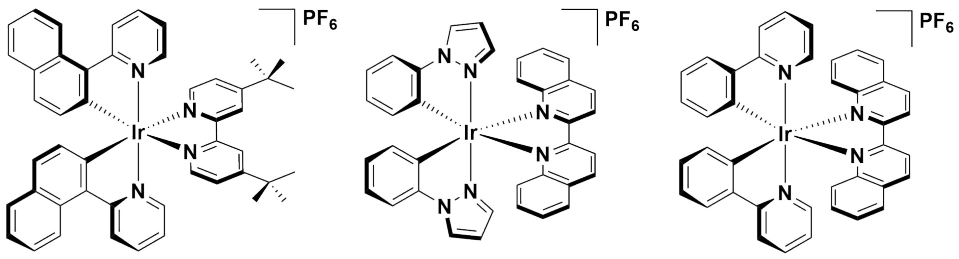

Complex:	93	94	95
λ_{PL} (nm):	590, 626	616	656
Φ_{PL} (%):	1	2	20

Figure 4.2: Red-emitting iridium complexes bearing conjugated C^N (**93**,[251]) and N^N ligands (**94**[75], **95**[252]). Photophysics in MeCN (complexes **93** and **94**) and in DCM (complex **95**).

Examples of extending the conjugation of the ligand scaffold were discussed in Chapter 1. Some additional examples are given in Figure 4.2. The π system can be expanded either on the pyridine of the C^N ligand[253;254] or on the phenyl ring of the C^N ligand,[255] such as complex **93**,[251] as well as on the ancillary N^N ligands in complexes **94**[75] and **95**.[252;256] All of these complexes are red emitters, with **93** and **94** showing low quantum yields (Φ_{PL} = 1% for **93** and 2% for **94**). Surprisingly, complex **95** shows a much higher quantum yield (Φ_{PL} = 20%), despite being red-shifted in colour and having a very similar structure to **94**.

Similarly, complexes bearing benzimidazoles are red-shifted in emission compared to their imidazole analogues.[158;258] Comparing complexes **57**[161] and **58**[112] with their closely related analogues **96**,[257] containing the annelated 1*H*,1'*H*-2,2'-bibenzimidazole (H_2bibenz) N^N ligand and **97**,[257] containing 1,1'-dimethyl-2,2'-bibenzimidazole (dMebibenz), it is evident that the extended conjugation along the bibenzimidazole core acts to red-shift the emission. However, two features are apparent for **96** and **97** that make them different to the biimidazole complexes studied here. Firstly, in Chapter 2 the alkylated complexes were *blue*-shifted in colour compared to when the ligand employed was H_2biim, which is

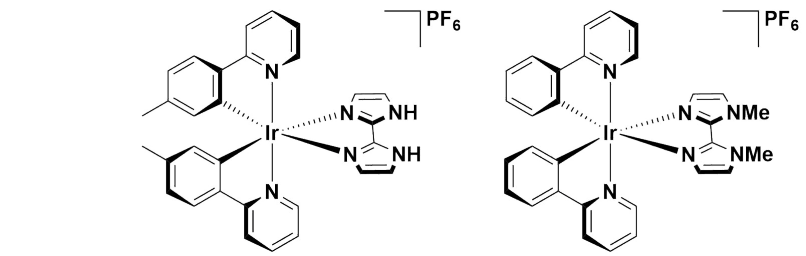

Complex:	57	58
λ_{PL} (nm):	484, 514	496
Φ_{PL} (%):	-	8

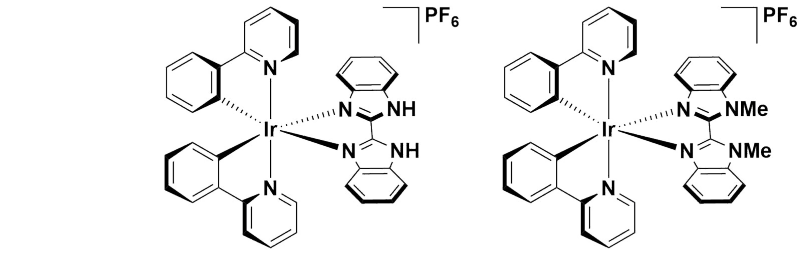

Complex:	96	97
λ_{PL} (nm):	534	593
Φ_{PL} (%):	33	24

Figure 4.3: Comparison between biimidazole complexes discussed in Chapter 2 (**57**[161] and **58**[112]) and closely related bibenzimidazole complexes **96** and **97**.[257] Photophysics reported in DCM for complexes **57**, **96** and **97** and in MeCN for complex **58**.

in contrast to the greatly red-shifted emission reported for **97** compared to **96**. Secondly, the Φ_{PL} of **97** is lower than for **96**, which is what would be expected based on the studies in Chapter 2. However, the differences in Φ_{PL} are not as significant, and may also be attributable in part to the red-shifted emission of **97** compared to **96** as well.

4.1.2 Chapter Outline

In this chapter, the use of H_2bibenz and its tethered analogue, 1,1'-(α,α'-*o*-xylylene)-2,2'-bibenzimidazole (*o*-Xylbibenz), are explored as N^N ligands for the design of orange/red emitting cationic iridium(III) complexes. As discussed, the extended conjugation of the benzimidazole rings necessarily red-shift the emission, while the rigid *o*-Xylbibenz N^N ligand is designed to mirror the *o*-Xylbiim ligand, by impeding the ground state vibrational modes from coupling to the excited state, thereby reducing k_{nr} and increasing Φ_{PL}. In addition, given the efficacy of the mesityl ring at further increasing Φ_{PL}, this motif has also been adopted here.

To evaluate these strategies, six new cationic iridium complexes were targeted. Complexes **98** and **99** are designed to study the difference in photophysical properties between H_2bibenz and *o*-Xylbibenz. The C^N ligand employed is the fluorine-free analogue of dFMesppy, 2-phenyl-4-(2,4,6-trimethylphenyl)pyridine, Mesppy. Complexes **100** and **101** are analogues of **98** and **99**, but possess a more conjugated C^N ligand (2-(napthalen-1-yl)-4-(2,4,6-trimethylphenyl)pyridine (Mesnpy) designed to promote a further red-shift in the emission. In addition, complex **102** employs the same Mesnpy ligand in concert with dtbubpy. Comparing this complex with **93** will indicate whether the mesityl in **102** is enhancing the Φ_{PL}, while comparing **102** with **100** and **101** will allow for a comparison of the optoelectronic properties of H_2bibenz and *o*-Xylbibenz with dtbubpy. Finally, complex **103** incorporates the more conjugated 2,2'-biquinoline (biq) ligand within the coordination sphere, allowing it to serve as a benchmark for the other complexes.

4.2 Synthesis and Characterisation

4.2.1 Ligand and Dimer Syntheses

The reagents and conditions used in the syntheses of all organic compounds are given in Figure 4.5. The N^N ligand H_2bibenz was synthesised in two steps in good yield from *o*-nitroaniline, which was reduced using $SnCl_2$ to give the diamine and subsequently condensed

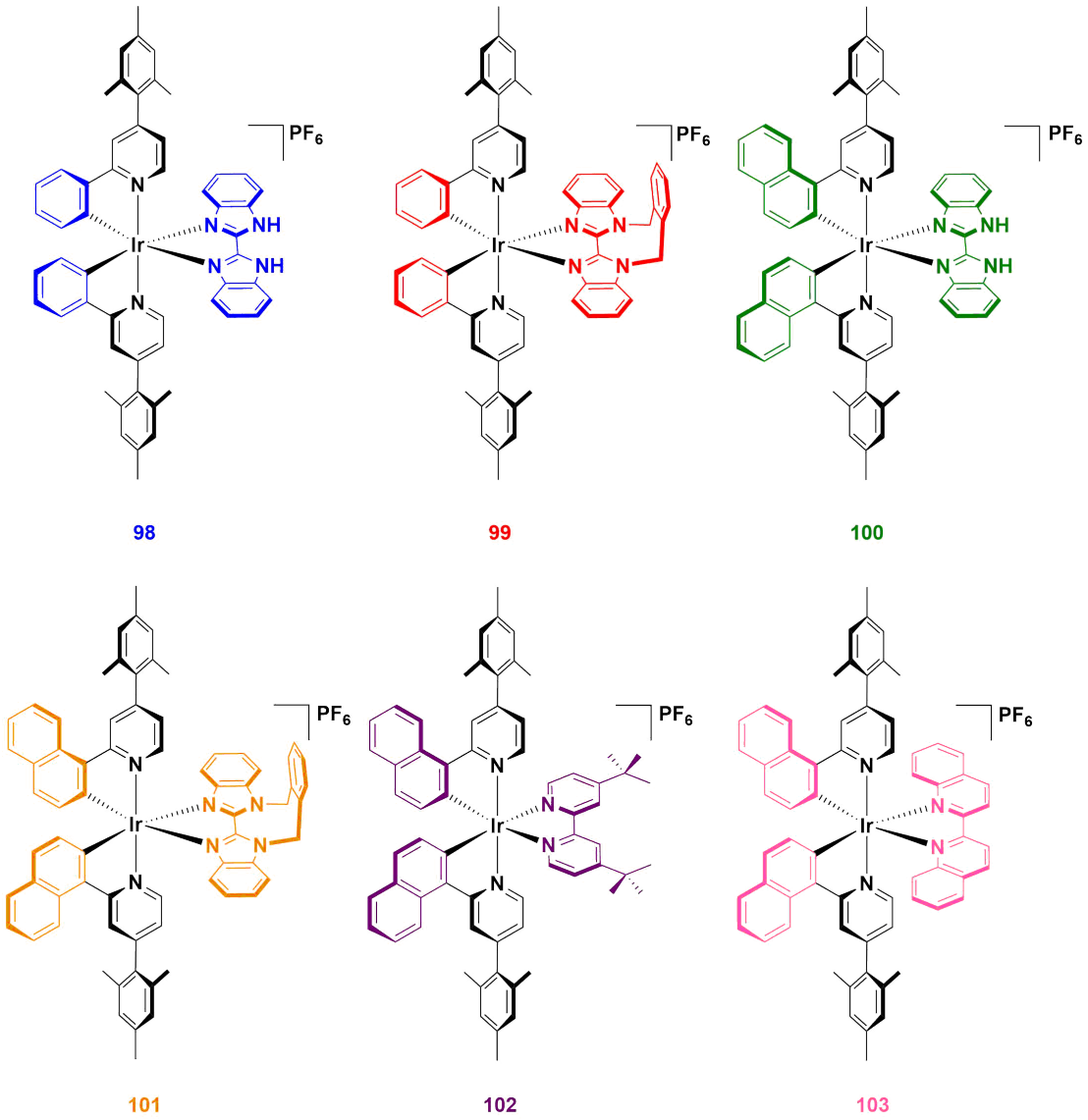

Figure 4.4: Complexes studied in this chapter.

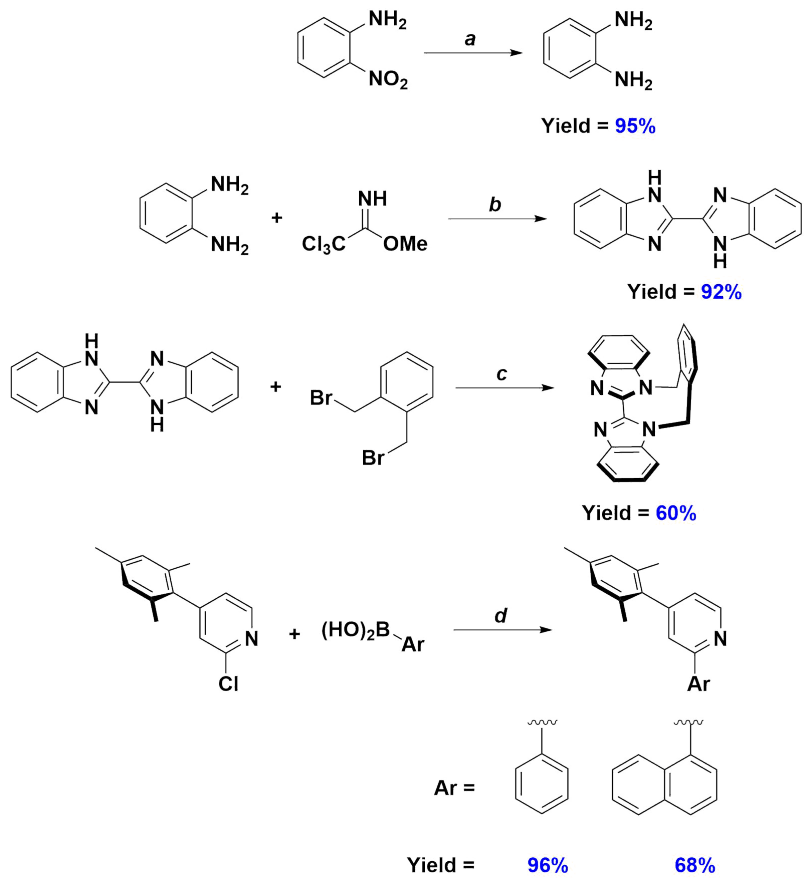

Figure 4.5: Synthesis of organic intermediates and ligands. Reagents and conditions: [a] $SnCl_2$ (3.6 equiv.), EtOH, HCl, 60 °C, 16 h, N_2. [b] i) MeOH, HCl, 0 °C, 3 h, N2 ii) K_2CO_3 (1.0 equiv.), rt, 39 h, N_2. [c] MeCN, $NaOH_{(aq)}$ (5.6 equiv.), 80 °C, 19 h, N_2. [d] $Pd(PPh_3)_4$ (5 mol%), K_2CO_3 (2.8 equiv.), 1,4-dioxane/water (3:1 v/v), 100 °C, 19 h, N_2.

with 2,2,2,-trichloroacetimidate.[259] Alkylation was carried out in the same manner as for *o*-Xylbiim, by refluxing H_2bibenz in MeCN with α,α'-dibromo-*o*-xylene and base.[190]

The cyclometalating ligands were synthesised in an analogous fashion to dFMesppy, by using the same 2-chloro-4-(2,4,6-trimethylphenyl)pyridine intermediate and coupling with the appropriate arylboronic acid under Suzuki-Miyaura conditions.[248] The intermediate dichloro-bridged iridium dimers were synthesised using $[Ir(COD)(\mu\text{-}Cl)]_2$ in the presence of refluxing 2-ethoxyethanol in good yields for iridium dimers. The reagents and conditions used in the dimer syntheses is given in Figure 4.6.

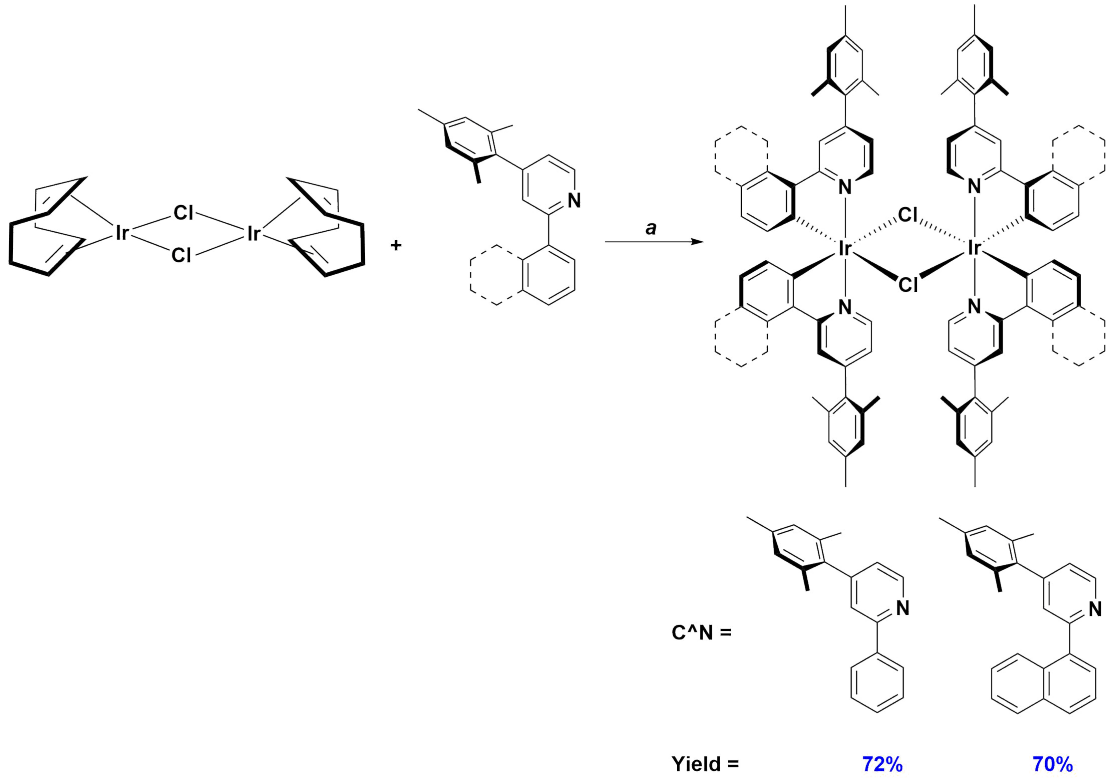

Figure 4.6: Synthesis of dimers. Reagents and conditions: [a] 2-ethoxyethanool, 120 °C, 3 h, N_2.

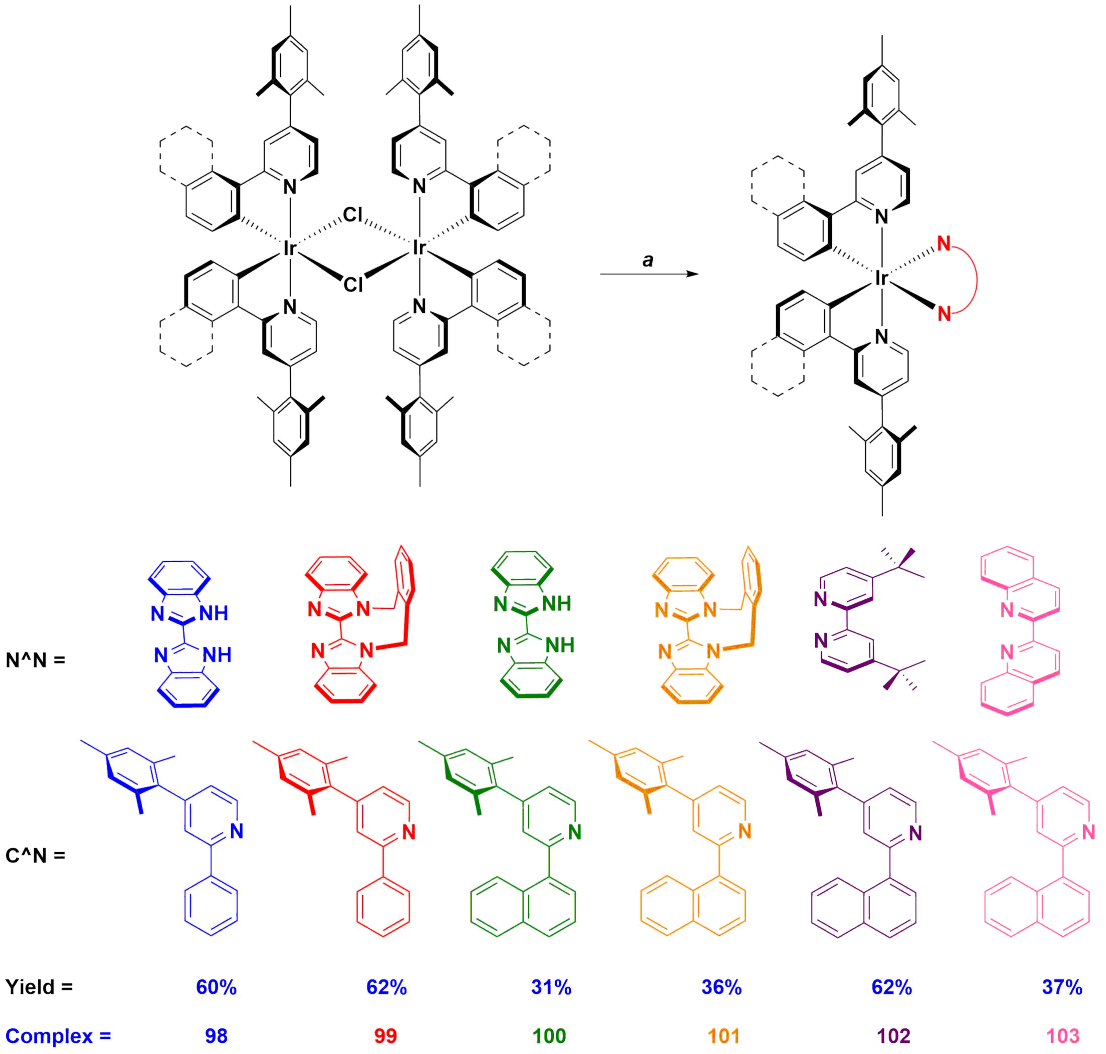

Figure 4.7: Synthesis of complexes **98** – **103**. Reagents and conditions: [a] $AgPF_6$ (2.1 equiv.), DCM/MeOH (1:1 v/v), rt, 3 h, N_2; N^N ligand (2.1 equiv.), rt, 3 h, N_2.

4.2.2 Complex Syntheses

The mononuclear iridium complexes were obtained in a similar manner to that reported by Housecroft *et al.*,[125] wherein a mixture of the iridium dimers and excess $AgPF_6$ were stirred in a solution of DCM/MeOH before filtering through celite to remove the silver impurities. Subsequent addition of the N^N ligand gave the final complexes, which were purified first by silica gel chromatography followed by recrystallization. This protocol is designed to eliminate the presence of chloride impurities in the samples, which can impact the performance of the LEECs.[81]

4.2.3 Structural Characterisation

All complexes were characterised by ^{1}H and ^{13}C NMR spectroscopy, high-resolution mass spectrometry (HRMS) and melting point analysis. All complexes were shown to be analytically pure by elemental analysis (EA). Finally, the structure of the Mesnpy C^N ligand, as well as the structures of complexes **98** and **100** – **103** were unequivocally determined by single crystal X-ray diffraction.

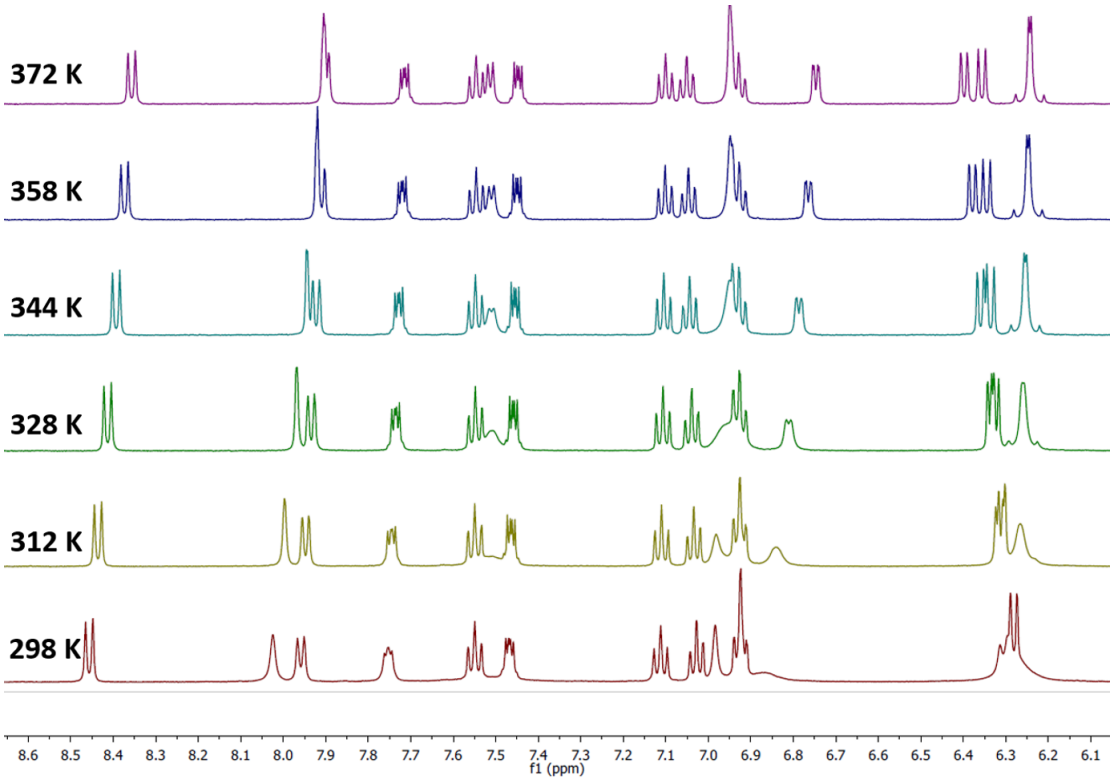

Figure 4.8: Variable temperature ^{1}H NMR study of complex **99** in DMSO-d_6.

The *o*-Xylbiim complexes studies in Chapters 2 and 3 displayed broad, featureless ^{1}H NMR spectra, as well as additional signals indicative of diastereomeric mixtures. The complexity of these spectra was attributed to diastereomeric atropisomerism, due to slow inversion kinetics of the *o*-Xylbiim between its two conformations coupled with the stereochemistry at iridium. By contrast, complexes **99** and **101**, bearing the *o*-Xylbibenz ligand, exhibit sharper signals at room temperature, with only two broad signals at ca. 6.3 and 6.7 ppm. The sharper signals at room temperature, as well as simpler signal patters are indicative of a lower barrier to ring inversion of the *o*-Xylbibenz complexes than for the analogous [Ir(C^N)$_2$(*o*-Xylbiim)](PF$_6$) complexes. To better understand the conformational dynamics present, both complexes were heated in solutions of DMSO-d_6. An example high

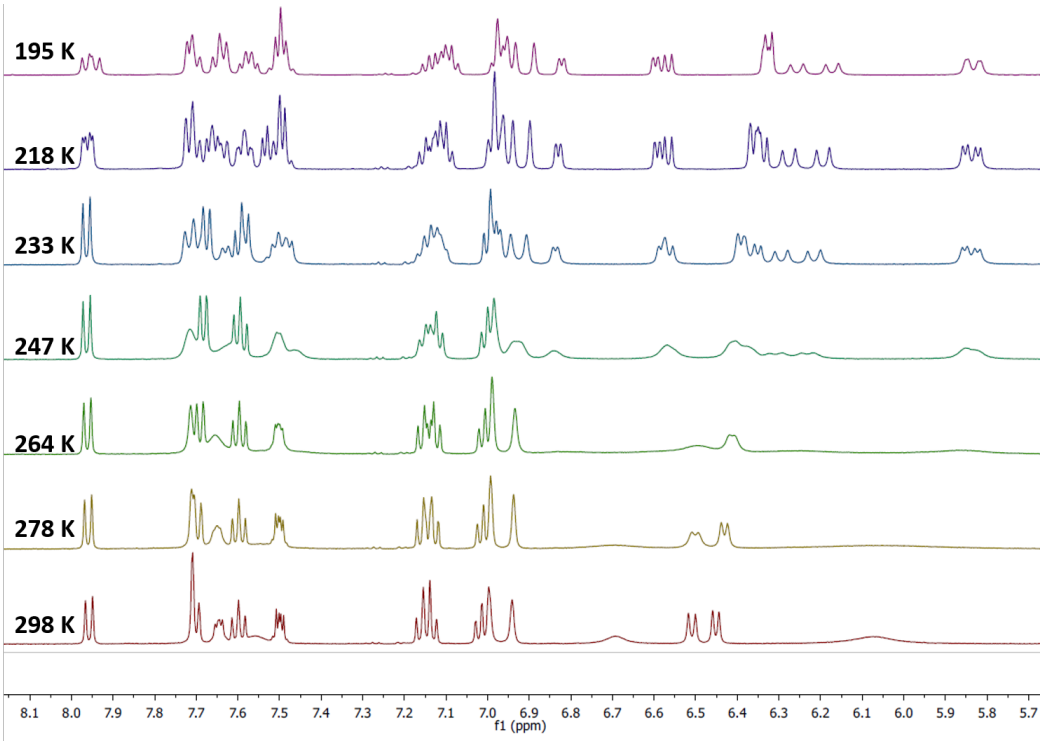

Figure 4.9: Variable temperature ^{1}H NMR study of complex **99** in CD_2Cl_2.

temperature spectrum of complex **99** in DMSO-d_6 is shown in Figure 4.8. In contrast to the *o*-Xylbiim complexes, the form of the spectra changes only minimally as a function of temperature, with the signal at 6.9 ppm becoming more resolved and the signal at 6.3 ppm decoalescing with increasing temperature. By contrast, at low temperature ($<$ 250 K) the ^{1}H NMR spectra of **99** begins to exhibit similar features to those observed at room temperature for the [Ir(C^N)$_2$(*o*-Xylbiim)](PF$_6$) complexes. In particular, the broad signals at 6.7 ppm and 6.0 ppm desymmetrise into respective pairs of doublets and doublet of doublets. Analogous behaviour is also observed for complex **101**. This behaviour appears to confirm that the barrier to ring inversion is lower for the complexes bearing *o*-Xylbiben as the N^N ligand. Further studies are ongoing to affirm the nature of these dynamic processes.

In contrast to the C^N ligands dFMesppy[177] and Mesppy,[260] which are viscous oils at room temperature, the naphthyl analogue Mesnpy forms white crystals upon cooling, facilitated by face-to-face π-π stacking of adjacent naphthalene rings (Figure 4.10). As expected, the methyl groups on the mesityl ring induce a large torsion angle between the mesityl and pyridine rings (79.61°). In addition, there is a significant (43.17°) torsional twist between the naphthalene and the pyridine. Short naphthalene-naphthalene centroid-to-

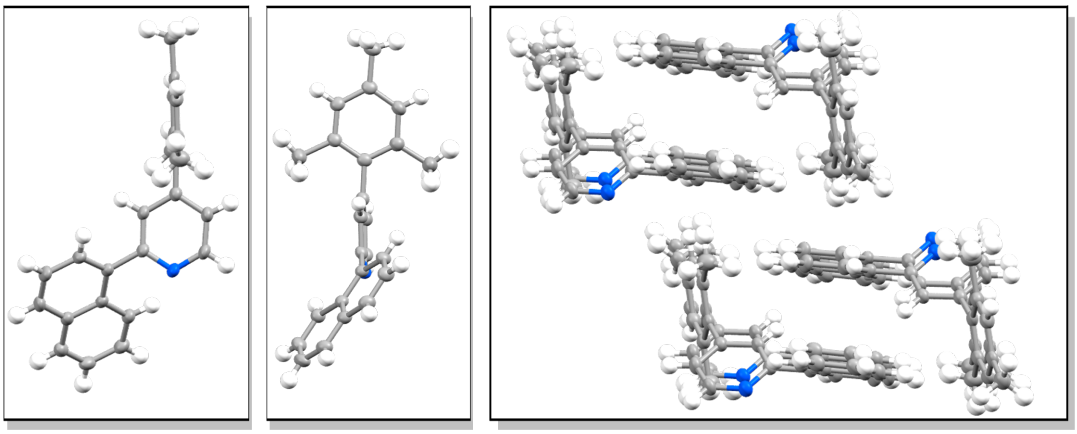

Figure 4.10: X-ray crystal structures of Mesnpy viewed facing the pyridine (left) and the mesityl (centre). Packing of Mesnpy (right) showing dimers forming 2-dimensional channels.

centroid distances (3.165 Å) are indicative of π-π stacking interactions between naphthalene rings within the crystal and lead to the formation of 2-dimensional channels in the extended packing array.

The crystal structures of of complexes **98** and **100** – **103** show the expected distorted octahedral geometries with the pyridyl nitrogen atoms of the C^N ligands in the usual *trans* configuration. As with H_2biim complexes, the complexes bearing H_2bibenz form tight hydrogen bonds between the -NH hydrogen atoms and the PF_6^- anions (1.876 Åfor complex **98** and 1.976 Åfor complex **100**). In all cases, the mesityl rings adopt a highly twisted conformation with respect to the C^N ligand (66.13 – 86.11°). Further, the distortion of the naphthalene ring with respect to the pyridine observed in the crystal structure of Mesnpy is also observed in the structures of **100** – **103**. While there is essentially no torsional twist between the phenyl and pyridine rings of complex **98** (0.54 – 4.94°), the analogous torsional distortions are all significantly larger for complexes **100** – **103** (15.15 – 30.98°), which is a result of the naphthalene rings minimising steric interactions with the pyridine rings.

4.3 Optoelectronic Characterisation

4.3.1 Electrochemistry

Electrochemical measurements on **98** – **103** were carried out in MeCN. The CV traces are shown in Figure 4.12 while the relevant electrochemical data are given in Table 4.1. The oxidation potentials of the complexes are sensitive to the nature of the C^N ligand. The

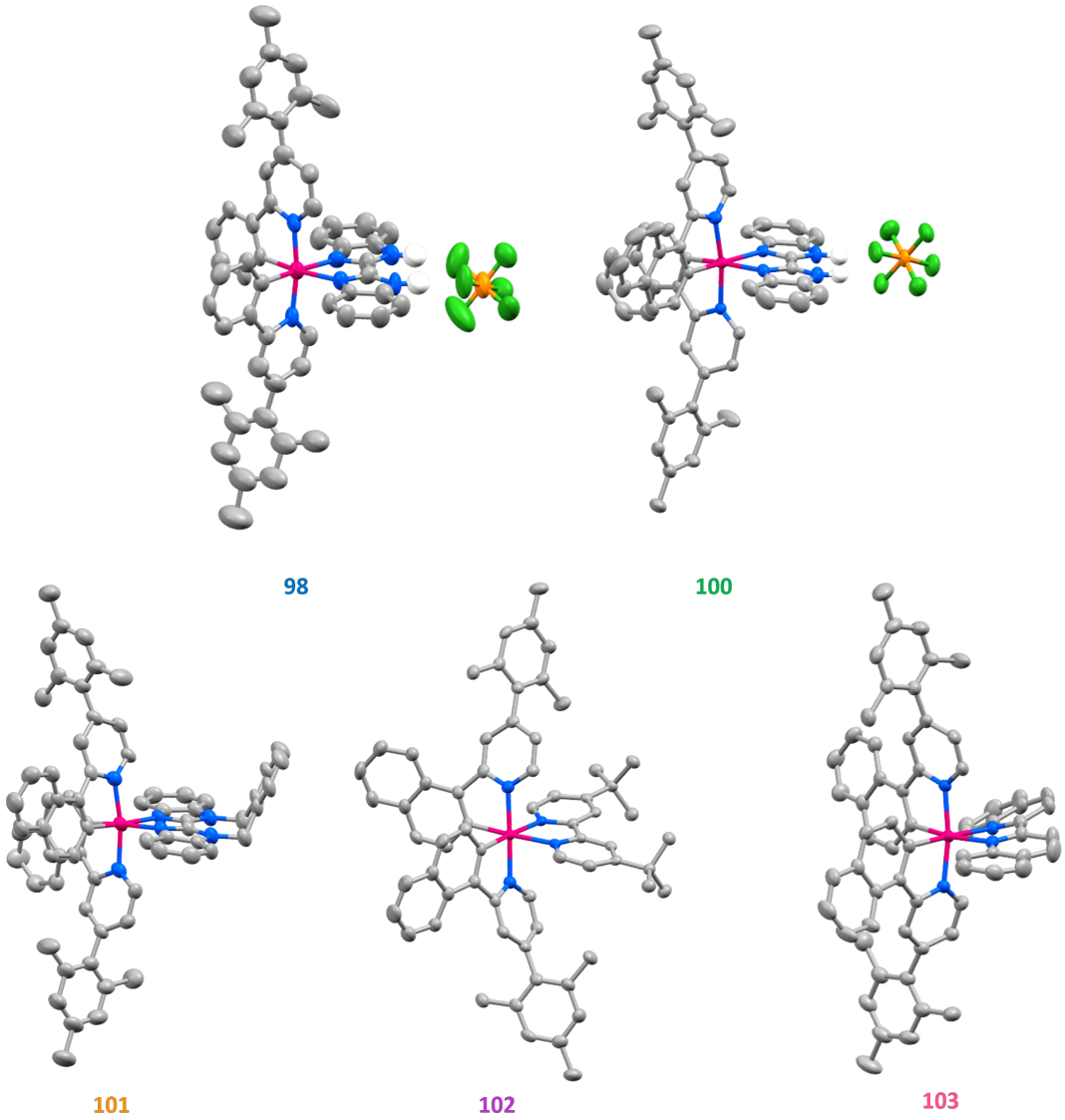

Figure 4.11: X-ray crystal structures of complexes **98**, **100**, **101**, **102** and **103**. Solvent molecules and C-H hydrogen atoms have been removed for clarity; counterions have been removed for clarity except for complexes **98** and **100**, which form strong hydrogen bonding interactions between the N-H hydrogen atoms and the hexafluorophosphate anions.

Complex	$E_{1/2(ox)}$ (V)	$E_{1/2(red)}$ (V)	ΔE (V)	E_{HOMO} (eV)	E_{LUMO} (eV)
98	1.26	-1.34	2.57	-6.05	-3.46
99	1.28	-1.40	2.68	-6.08	-3.40
100	1.18	-1.33	2.46	-5.98	-3.47
101	1.14	-1.47	2.61	-5.94	-3.33
102	1.20	-1.41	2.61	-6.00	-3.39
103	0.99	-1.09	2.08	-5.79	-3.71

Table 4.1: Electrochemical data for complexes **98** – **103**. Measurements were carried out in MeCN at a scan rate of 100 mV s^{-1} with Fc/Fc^+ employed as an internal standard, and data reported *vs* SCE ($Fc/Fc^+ = 0.38$ V in MeCN).

first oxidation waves of **98** and **99** ($E_{1/2(ox)}$ = 1.26 V for **98** and 1.28 V for **99**) bearing the Mesppy C^N ligand are quasi-reversible, while the oxidation waves in **100** and **101** are reversible and shifted cathodically ($E_{1/2(ox)}$ = 1.18 V for **100** and 1.14 V for **101**) due to the increased conjugation on the Mesnpy C^N ligands. By contrast, the oxidation potentials are insensitive to whether the N^N ligand employed is H_2bibenz or *o*-Xylbibenz.

The difference in oxidation potential of **102** ($E_{1/2(ox)}$ = 1.20 V) compared with its mesityl-free analogue **93** ($E_{1/2(ox)}$ = 1.13 V) is small, indicating that the mesityl ring is largely decoupled from the electronics of the system, as described previously. From the CV data presented here, the dtbubpy, H_2bibenz and *o*-Xylbibenz ligands are electronically very similar in their capacity to influence the oxidation potential of the respective complexes **102**, **100** and **101**. This is in stark contrast to the analogous complexes in Chapter 2, where the oxidation potential of $[Ir(dFMesppy)_2(o\text{-Xylbiim})](PF_6)$ was found to be significantly cathodically shifted compared to $[Ir(dFMesppy)_2(dtbubpy)](PF_6)$. Thus the electron-releasing nature of the imidazole heterocycles are offset by the greater π-accepting character of the H_2bibenz and *o*-Xylbibenz N^N ligands.

Finally, in contrast to the complexes **98** – **102**, the oxidation of **103** is completely irreversible and is significantly further cathodically shifted ($E_{1/2(ox)}$ = 0.99 V); the result of the very strong π-accepting properties of the biq ligand. In addition, the significantly lower oxidation potential of **103** compared to the previously reported oxidation for **93** ($E_{1/2(ox)}$ = 1.42 V) and **95** ($E_{1/2(ox)}$ = 1.24 V) suggests that the naphthyl ring is also acting to facilitate the oxidation process.

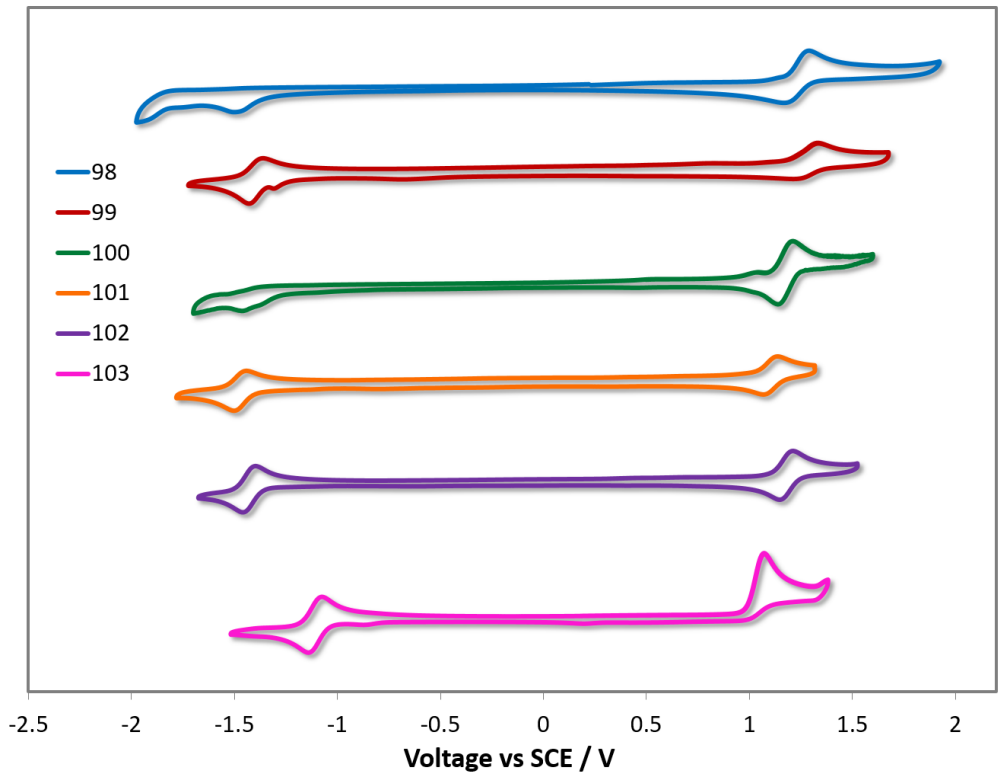

Figure 4.12: CV traces of complexes **98** – **103** in MeCN solution, reported versus SCE (Fc/Fc^+ = 0.38 V in MeCN).[219] Scan rates were at 100 mV s^{-1}, and are in the positive scan direction.

From these data, the first oxidations of **98** – **103** arise from the Ir^{III}/Ir^{IV} redox couple along with contributions from the aryl component of the CˆN ligands. However, the NˆN ligands are nevertheless capable of exerting an influence over the oxidation potentials as a function of the significant metal-based character of the oxidation, and the subsequent sensitivity of the metal-based orbitals to the electronics of the surrounding coordination sphere.

The reduction potentials are more sensitive to the nature of the NˆN ligand and reflect an ancillary ligand-based reduction; thus they are much less sensitive to the nature of the CˆN ligands. For example, the reduction potentials of **98** and **100** ($E_{1/2(red)}$ = -1.34 for **98** and -1.33 V for **100**), bearing H_2bibenz as the NˆN ligand, are completely irreversible and virtually identical. By contrast, the reductions of **99** and **101**, bearing *o*-Xylbibenz, are modestly cathodically shifted compared, and reversible in nature) ($E_{1/2(red)}$ = -1.40 for **99** and -1.47 V for **101**).

As was observed with the oxidation, there is a small anodic shift in the reduction potential of **102** ($E_{1/2(ox)}$ = -1.41 V) compared to **101**. The result is that the electrochemical gaps determined for **101** (2.53 V) and **102** (2.51 V) are identical, indicating that the *o*-Xylbibenz ligand possesses similar electronics proerties to the dtbubpy ligand. By contrast, the reduction potential of $[Ir(dFMesppy)_2(o\text{-Xylbiim})](PF_6)$ is significantly anodically shifted compared to $[Ir(dFMesppy)_2(dtbubpy)](PF_6)$. Finally, the reduction potential of **103** ($E_{1/2(red)}$ = -1.09 for **103**) is significantly stabilised compared to those of **98** – **102**, which reflects the increased conjugation present in the biq ligand.

Preliminary DFT calculations (Figure 4.13) generally corroborate the principal trends assigned here. For each of the six complexes, the HOMO comprises almost equal contributions of iridium d-orbitals and cyclometalating aryl rings while, the LUMO is localized essentially exclusively on the NˆN ligand. Calculations generally predict the expected destabilization of the HOMO as a function of increasing the conjugation of the CˆN ligands. However, the energy of the HOMO of **103** is predicted to be stabilised compared to complexes **100** – **102**, which is in contrast to the experimental findings. In the case of complexes **98** and **100**, bearing the H_2bibenz ligands, their predicted LUMO energies are slightly higher than for complexes **99** and **101**, which contain the *o*-Xylbibenz ligand. This trend is opposite to that observed for the CV experiments where **99** and **101** show more negative reduction potentials than **98** and **100**. Furthermore, DFT calculations predict a LUMO level in **102** that is destabilized compared to **98** – **101**, which is not observed experimentally. The

LUMO of **103** is predicted to be greatly stabilised compared to the other complexes, in line with the electrochemistry.

4.3.2 UV-Vis Absorption

The UV-vis absorption spectra for **98** – **103** are shown in Figure 4.14 and the molar absorptivity data are given in Table 4.2. In the high-energy region of the spectrum (250 – 400 nm), π-π^* transitions with high molar absorptivity dominate for all complexes. Among these, two distinct sets of transitions can be identified (250 – 300 nm and 300 – 400 nm). For complexes **98** and **99**, a single distinct higher energy π-π^* transition (λ_{abs} = 263 nm for **98** and 270 nm for **99**) is observed, along with poorly resolved shoulders (λ_{abs} = 282 nm for **98** and 289 nm for **99**). For complexes **100** and **101**, similar transitions (λ_{abs} = 264 nm for **100** and 263 nm for **101**) are accompanied by well-resolved absorption bands (λ_{abs} = 295 nm for **100** and 291 nm for **101**) that are more strongly absorptive and red-shifted compared to the corresponding shoulders present in **98** and **99**. These absorption bands are therefore assigned to π-π^* transitions on the cyclometalating ligands. Higher absorptivities are also observed for complexes bearing *o*-Xylbibenz (**99** and **101**) compared to H_2bibenz (**98** and **100**) due to additional xylylene-centred π-π^* transitions. The absorption spectrum of **102** shows a similar profile in the high energy region to those of **98** – **101** with a band at 266 nm along with two shoulders at 285 and 294 nm. For **103**, the absorption spectrum in the high-energy region is dominated by a highly absorbing π-π^* transition (λ_{abs} = 265 nm), obscuring the naphthyl-localised shoulder (λ_{abs} = 294 nm).

In the region between 300 – 400 nm, each complex possesses two well-defined, highly absorbing bands. The bands in this region are assigned to π-π^* transitions involving the N^N ligand, evidenced by the near identical absorption maxima between **98** and **100** for this pair of bands (λ_{abs} = 322, 340 nm for **98** and 325, 339 nm for **100**); it is worth noting a moderately increased molar absorptivity observed for **100** compared to **98**. Similarly, these bands in **99** and **101** coincide (λ_{abs} = 335, 352 nm for **99** and 337, 351 nm for **101**) and are more strongly resolved, bathochromically-shifted and significantly more absorptive than their analogous bands in complexes **98** and **100**. The increased absorptivity observed for complexes **99** and **101** can be attributed to additional π-π^* contributions from the xylylene bridge. The bands at 310 and 339 nm for **102** are hypsochromically shifted compared to those clustered between 322 – 339 and 340 – 361 nm, respectively, that are present in **98** – **101**. The pair of bands observed for **103** at 354 and 370 nm are the most red-shifted, due

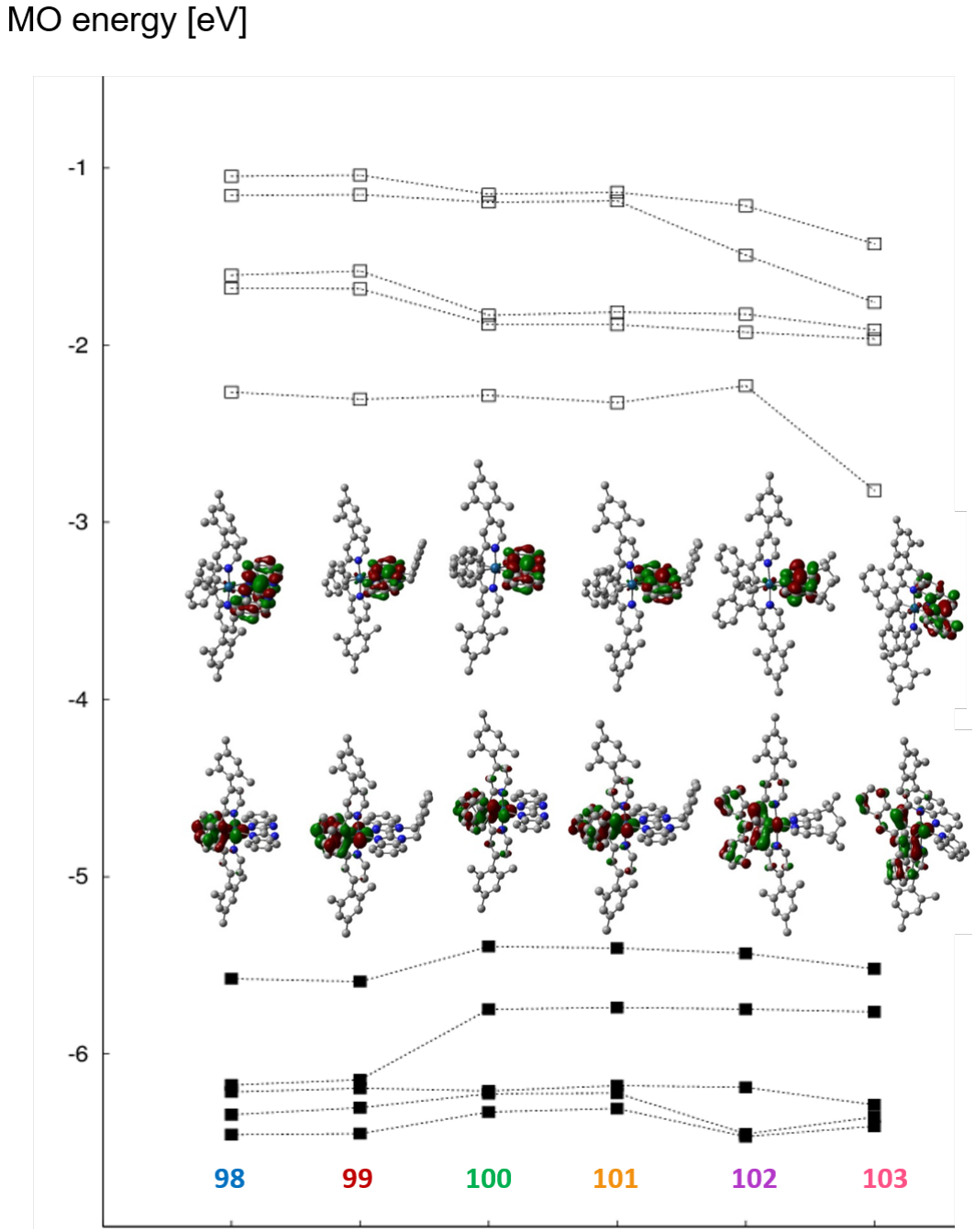

Figure 4.13: Variation of the frontier MO energies (in eV) of complexes **98** – **103** as a function of the ligand environment (singlet ground states, B3LYP level); the five highest occupied and the file lowest unoccupied orbital levels are shown. In the centre, plots of the HOMOs (below) and LUMOs (above) are included (H atoms omitted for clarity, isodensity value 0.04 a.u.).

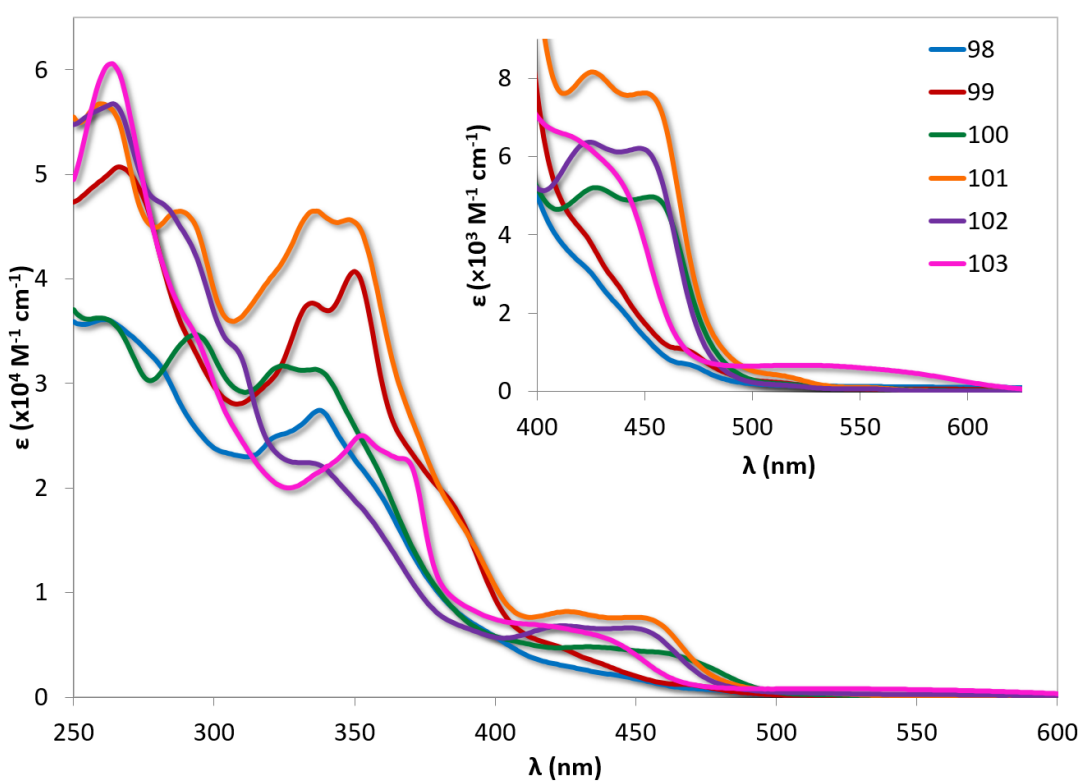

Figure 4.14: UV-Vis absorption spectra of complexes **98** – **103** in MeCN solution.

Complex	λ_{abs} (nm) [ϵ ($/10^4$ M^{-1} cm^{-1}]
98	263 [3.60], 282(sh) [3.12], 322 [3.50], 340 [2.70], 361(sh) [1.86], 402 [0.55], 431 [0.27], 449 [0.18], 479 [0.07]
99	270 [5.01], 289(sh) [3.31], 335 [3.77], 352 [4.01], 386(sh) [1.80], 425 [0.46], 442 [0.28], 471 [0.12], 517 [0.02]
100	264 [3.60], 295 [3.45], 325 [3.17], 339 [3.10], 361(sh) [2.01], 436 [0.48], 463 [0.41], 517 [0.02], 559 [0.01]
101	263 [5.63], 291 [4.60], 319(sh) [3.97], 337 [4.65], 351 [4.52], 374(sh) [2.40], 391(sh) [1.52], 427 [0.82], 458 [0.71], 519 [0.04], 556 [0.01]
102	266 [5.64], 285(sh) [4.63], 294(sh) [4.19], 310 [3.23], 339 [2.20], 358(sh) [1.62], 391 [0.65], 422 [0.68], 454 [0.63], 517 [0.01], 555 [0.01]
103	265 [6.03], 294(sh) [3.43], 354 [2.49], 370 [2.22], 420 [0.68], 443(sh)[0.52], 570 [0.06]

Table 4.2: Absorption maxima and their corresponding molar absorptivities for complexes **98** – **103**. [a] Measured in aerated MeCN at room temperature.

to the great π-accepting character of the biq ligand.

The absorption bands beyond 450 nm are assigned as charge-transfer transitions on the basis of their lower absorptivity values compared to the π-π^*. Surprisingly, these transitions are insensitive to the nature of the N^N ligands, and instead are strongly affected by the nature of the C^N ligand, implying an unusual metal-to-C^N ligand MLCT transition; distinct from the typical metal-to-N^N ligand MLCT transitions generally associated with $[Ir(C^N)_2(N^N)]^+$ complexes.[62;90;261] These conclusions are substantiated by comparing complexes **98** and **99**, which show poorly resolved shoulders (λ_{abs} = 431 nm for **98** and 425 nm for **99**) and a low intensity absorption band (λ_{abs} = 449 nm for **98** and 442 nm for **99**) that are blue-shifted compared with the cluster of more strongly absorptive and well-resolved bands present in **100**, **101** and **102** (λ_{abs} = 436, 463 nm for **100**, 427, 458 nm for **101** and 422, 454 nm for **102**) and a further red-shifted low intensity band at ca. 555 nm (λ_{abs} = 559 nm for **100**, 556 nm for **101** and 555 nm for **102**). Thus, the presence of the naphthyl rings in **100** – **102** results in an enhanced and lower energy absorption profile compared to complexes **98** and **99**. The absorption profile for complex **103** is distinct with only a single blue-shifted band at 443 nm. This, however, is coupled with a relatively strongly absorptive, broad band centred at 539 nm and absorptive up to ca. 640 nm, that is attributed to a spin-forbidden CT transition. Similar transitions are present for complexes **98** – **102**, but these are even less absorptive and have absorption onsets that are significantly blue-shifted ($\lambda_{abs} < 585$ nm for the onset of absorption of complexes **100** – **102**). TDDFT computations are in progress to confirm these assignments.

4.3.3 Photoluminescence

The emission spectra for **98** – **103** are shown in Figure 4.15 and the relevant photophysical data are given in Table 4.3. The DFT computed triplet spin density plots are also shown in Figure 4.16. Complex **98** is a green/yellow emitter (λ_{PL} = 500, 527 nm), with a narrow, somewhat structured emission profile. The short emission lifetime (τ_e= 1.26 µs) coupled with the spin density distribution delocalised across both ligands and the iridium centre are features indicative of an excited state that is predominantly ^{3}CT in character while the emission profile suggests that there is also some ^{3}LC character. The emission of **96** is red-shifted (λ_{PL} = 534 nm in DCM) and unstructured in nature.[257] The more polar solvent MeCN solvent can hydrogen-bond with the NH moieties of the H_2bibenz ligand, polarising this bond and increasing electron density on the H_2bibenz ligand, thereby destabilising

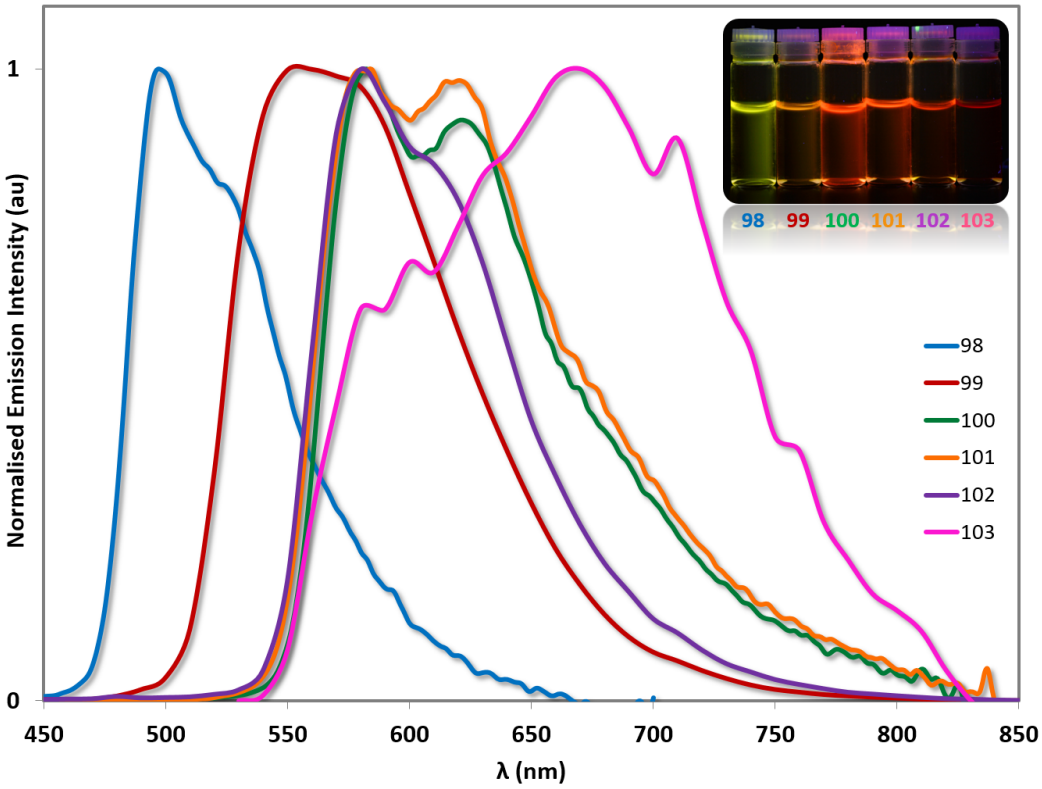

Figure 4.15: Emission spectra of complexes **98** – **103** in deaerated MeCN solution at 298 K. Inset: MeCN solutions of complexes **98** – **103** illuminated under UV light.

the ligand-based orbitals and blue-shifting the emission. Complex **99** by contrast displays a significantly red-shifted emission (λ_{PL} = 560, 580 nm), which is similar to what was reported for **97** (λ_{PL} = 593 nm in DCM). The opposite trend was observed between [Ir(dFppy)$_2$(H$_2$biim)](PF$_6$) (complex **64**) and [Ir(dFppy)$_2$(*o*-Xylbiim)](PF$_6$) (complex **66**) in Chapter 2, where the latter complex exhibited a small *blue-shift* in the emission. This is likely a result of the difference in excited state: complexes **98** and **99** have T$_1$ states comprised of significant ^{3}MLCT contributions (as evidenced by the photophysics and triplet spin density plots), which make them much more sensitive to the electronics of the N^N ligand, while complexes **64** and **66** are overwhelmingly ^{3}LC in nature and thus largely insensitive to the electronics of the ancillary ligand.

The differences observed in the emission of complexes **98** and **99** are surprisingly not mirrored in the analogous comparison between **100** and **101**, which show virtually identical emission spectra (λ_{PL} = 585, 626 nm for **100** and 586, 623 nm for **101**). This change in behaviour suggests that the presence of the naphthyl ring within the C^N ligands induces

Complex	λ_{PL} (nm) [a]	Φ_{PL} (%) [b]	τ_e (μs) [c]	k_r ($/10^5$ s^{-1})	k_{nr} ($/10^5$ s^{-1})
98	500, 527	78	1.26	6.19	1.75
99	560, 580	89	1.83	4.86	0.60
100	585, 626	32	5.10	0.63	1.33
101	586, 623	44	7.65	0.58	0.73
102	580, 620	18	7.93	0.27	1.03
103	670	<1	-	-	-

Table 4.3: Relevant solution-state photophysical data for complexes **98** – **103**. Measurements at 298 K in dearated MeCN. [a] λ_{exc}: 360 nm. [b] $[Ru(bpy)_3](Cl)_2$ was used as the reference (Φ_{PL} = 4.0% in aerated water at 298 K).[262] [c] λ_{exc}: 378 nm.

greater ^{3}LC character into the emitting triplet state, thereby making the emission of these complexes less sensitive to substitution on the ancillary ligand. The spin density distributions for **100** and **101** reveal a decidedly increased LC character of the T_1 state, corroborating these conclusions. Likewise, complex **102** also emits from a ^{3}LC state, exhibiting a very similar emission profile to those of **100** and **101** (λ_{PL} = 580, 620 nm for **102**), and a spin density plot delocalised on the C^N ligand.

Complex **103** shows expectedly the most red-shifted emission and is also the least emissive as a function of increased vibrational coupling to the ground state and hence increased k_{nr}. The spectrum is broad and noisy due to the low emission intensity of the complex. The T_1 state is assigned as a mixed ^{3}LLCT and ^{3}MLCT state, which is mirrored in the spin density calculations carried out on **103**.

The excited state kinetics are revealing for characterising the nature of the emissive state, as well as the effects of substitution on the bibenz ligands. Complex **98** has a high Φ_{PL} and short lifetime (Φ_{PL} = 78%, τ_e = 1.26 µs) which is indicative of a ^{3}CT state. This is also reflected by **98** exhibiting the highest radiative rate constant among complexes **98** – **102** ($k_r = 6.19 \times 10^5$ s^{-1}). The higher Φ_{PL} of **98** compared to that reported for **96** (Φ_{PL} = 33% in DCM) demonstrates the positive impact of the mesityl ring in inhibiting non-radiative decay processes. Alkylation with the *o*-xylylene linkger as in **99** results in an enhanced Φ_{PL} and a longer lifetime value (Φ_{PL} = 89%, τ_e = 1.83 µs). Thus despite the red-shifted emission of **99** compared to **98**, non-radiative decay is suppressed ($k_{nr} = 0.60 \times 10^5$ s^{-1}) as a result of the rigidifcation of the bibenz N^N ligand.

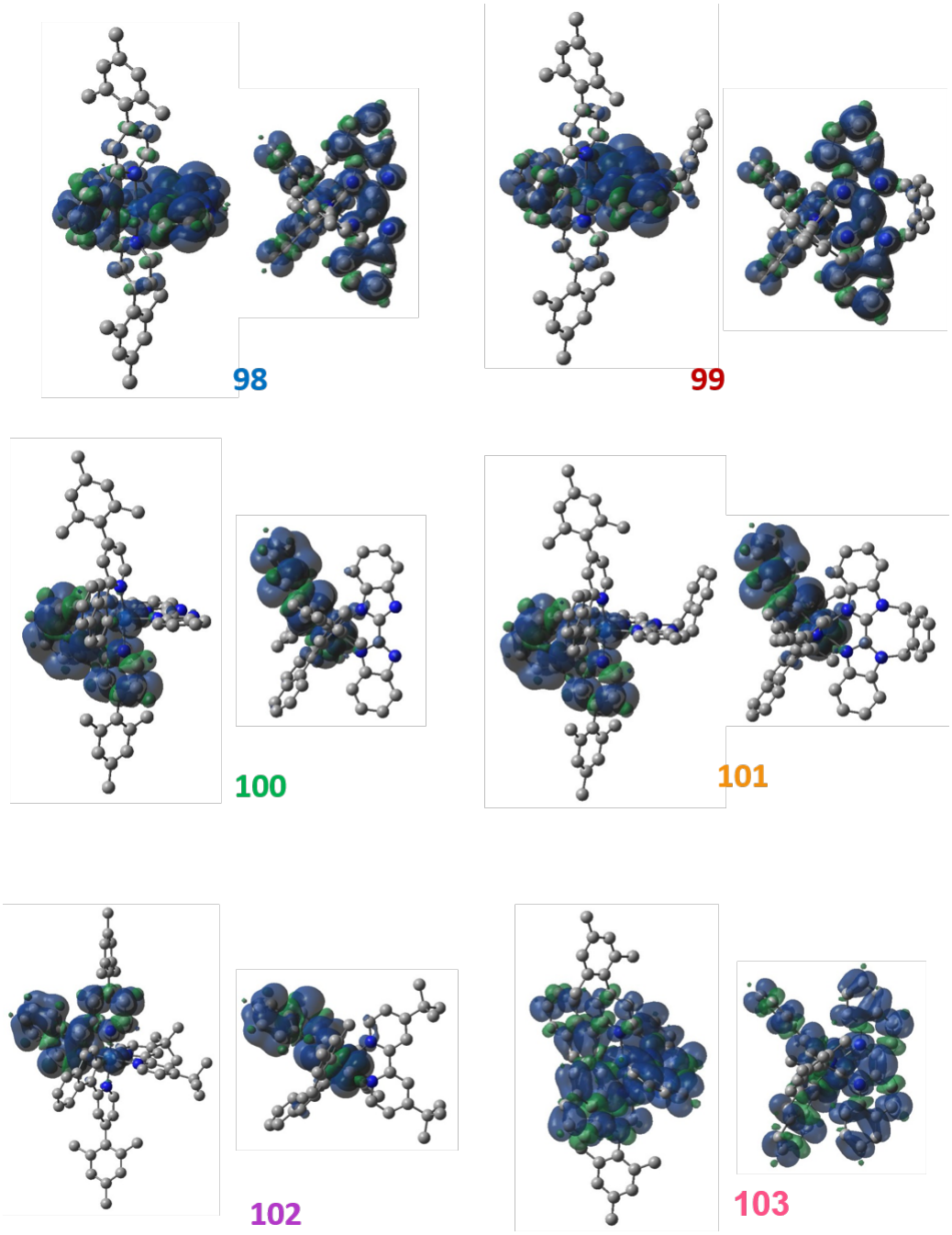

Figure 4.16: Computed spin densities in the lowest triplet state (B3LYP level, H atoms omitted for clarity, isodensity value 4×10^{-4} a.u.); two orientations are shown in each case, a side view (left of the labels) along the plane of the N^N ligand and a top view (right of the labels) down the axis of the mesityl rings of the C^N ligands.

When the Mesnpy C^N ligand is employed, two features become apparent: 1) the emission lifetimes lengthen considerably, due to greater ^{3}LC character in the T_1 state

and 2) the values for k_r are an order of magnitude lower than for complexes **98** and **99** complexes, which is a result of a combination of a more ^{3}LC-type excited state and more prevalent energy gap law effects as a function of the red-shifted emission. For example, the lifetime of **100** (τ_e = 5.10 µs) is much longer than its Mesppy analogue complex **98**. The Φ_{PL} is also lower (Φ_{PL} = 32%) which is primarily a function of the lower radiative rate constant ($k_r = 0.63 \times 10^5$ s^{-1}) associated with this ^{3}LC state. A similar comparison can be made between complexes **99** ($k_r = 4.86 \times 10^5$ s^{-1}) and **101** ($k_r = 0.58 \times 10^5$ s^{-1}). However, analogous to the enhanced Φ_{PL} and τ_e in **99** compared to **98**, these values for **101** (Φ_{PL} = 44%, τ_e = 7.65 µs) are higher than measured for **100**. This is attributed to the lowered non-radiative rate constant for **101** ($k_{nr} = 0.73 \times 10^5$ s^{-1}) compared to **100** ($k_{nr} = 1.33 \times 10^5$ s^{-1}). Complex **102** is much less emissive (Φ_{PL} = 18%) than complexes **100** or **101**, but has an enhanced Φ_{PL} compared to **93** (Φ_{PL} = 1%), indicating that the mesityl group in the Mesnpy C^N ligand is acting to inhibit intermolecular quenching processes in a similar fashion to Mesppy and dFMesppy. Thus, the use of the mesityl group strategy is applicable to emitters across the visible spectrum. Finally, the very poorly emissive properties of complex **103** precluded quantifying precisely its photoluminescence quantum yield and lifetime.

4.4 Conclusions and Further Work

In this chapter, three independent design strategies, relating to the colour and Φ_{PL} of the emitter, have been combined to achieve more efficient orange/red emitting $[Ir(C^N)_2(N^N)]^+$ complexes. Firstly, bibenzimidazole ligands have been studied as replacement N^N ligands in place of dtbubpy, and give complexes with comparable emission wavelengths despite the electron-releasing nature of the imidazole heterocycles. The emission of these complexes can be universally red-shifted by adopting a more conjugated naphthalene ring within the C^N ligand framework in place of phenyl. Secondly, the *o*-xylylene tethering strategy has been shown to be applicable also to bibenzimidazoles, with complexes incorporating *o*-Xylbibenz within the coordination sphere exhibiting higher Φ_{PL} values than analogues bearing H_2bibenz or dtbubpy, as a function of lowered k_{nr} values. Finally, the mesityl group strategy appears to be universally applicable, regardless of the nature of the cyclometalating ring (phenyl, naphthyl) and thus this is a useful additional substitution for further increasing the Φ_{PL} of the complexes. Thus combining these design strategies culminates in an iridium

complex (101) with orange red emission (λ_{PL} = 586, 620 nm) with higher Φ_{PL} than measured or reported for reference complexes emitting at similar energies (Φ_{PL} = 44%). Future work based on these complexes will entail the fabrication of LEECs to discern the efficacy of these complexes in devices. In particular, the improved Φ_{PL} of complex 101 makes it an interesting candidate as it may improve the efficiency of the device.

Chapter 5

Panchromic Absorption from Proton-Switchable Iridium(III) Azoimidazolate Complexes

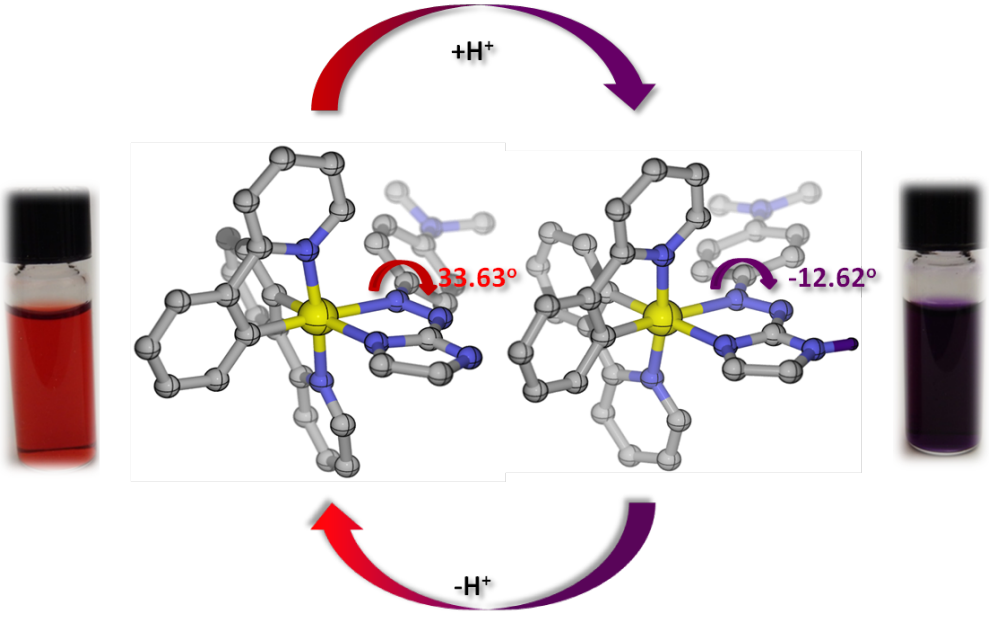

5.1 Introduction

5.1.1 Background

From a colour tuning perspective, the preceding chapters have demonstrated that an electron deficient C^N aryl in concert with electron rich N^N ligands can promote a significant blue-shift in the emission profile of the corresponding complex. Chapter 4 demonstrated that utilising the opposite strategy enables colour tuning of the complexes into the red region of the visible spectrum, and discussed in detail the effects of highly conjugated ligand systems on the emission properties. In this chapter, the use of an ancillary N^N ligand with a pre-designed donor-acceptor (D-A) system is studied to demonstrate a distinct strategy for red-shifting the optoelectronic properties of the system.

Aryldiazo moieties have attracted significant attention as an interesting class of ligand scaffold for metal complexes. Complexes employing such ligands often display broad absorption profiles, dominated by strong CT bands,[263;264] as well as multiple reversible electrochemical reduction processes associated with the typically redox non-innocent nature of these ligands.[265–267] Exploitation of these optoelectronic properties has led to reports of these materials being used as switches in optical recording media,[265;268;269] or as catalysts for small molecule activation where multi-electron processes play a crucial role.[270;271] Interest in such applications is magnified by the potential to utilise the dual coordination modes of the diazo moiety to construct multimetallic complexes that show enhanced CT properties or unique electrochemical behaviour such as mixed metal valency, which is also of use for catalytic applications.[263;272] Finally, significant efforts have been expended in grafting diazo units onto ligands of metal complexes that enable these complexes to act as photoswitches following the *cis-trans* isomerisation of these units.[273;274]

Surprisingly, given the popularity of the use of these ligands with other metals, examples involving their complexation with iridium are scarce and can largely be divided into three main families. The first of these are the tetrahedral complexes such as **104**, where the complexes are capped by a pentamethylcyclpentadienyl (Cp*) ligand. A bidentate aryldiazo ligand and a monodentate ligand such as chloride fill the coordination sphere of these complexes.[270]

Among octahdral Ir(III) complexes, most examples resemble complex **105** where the diazo moiety is integral to a terdentate binding mode and is sandwiched by combinations of phenolate,[275;276] thiolate,[277] deprotonated aniline,[278] or cyclometalated carban-

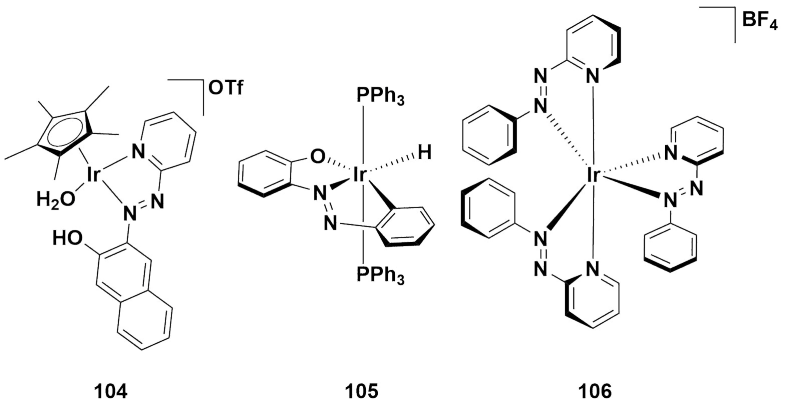

Figure 5.1: Selected examples of iridium complexes bearing aryldiazo-type ligands.

ions.[275;276;278] In this family of iridium complexes the octahedral coordination sphere is completed by monodentate ligands such as chloride, hydride or phosphine. The final class of Ir(III) complexes, exemplified by **106**, involve the use of bidentate aryldiazo ligands, and represent the smallest number of reported examples.[265;279;280]

5.1.2 Chapter Outline

This chapter explores the use of donor-acceptor systems that are effective systems for red-shifting the optoelectronics properties of the system. In particular, such systems can lead to panchromatic absorption profiles. For iridium(III) complexes, this is rare, as they typically exhibit absorption properties with low molar absorptivities in the visible spectrum and blue-shifted absorption onsets (< 550 nm).[281–287] However, panchromically absorbing iridium complexes have been shown to be attainable using bis(iminoarylacenaphthene) (Ar-BIAN) ancillary ligands that contain donor aryl units linked to an acenaphthene acceptor core, thus promoting low energy intraligand charge transfer (ILCT) transitions.[288–290] The most absorptive of this family of complexes employed a dimethylaniline donor (complex **107**), possessing an ILCT absorption band tailing off past 800 nm with a molar absorptivity of 7.1×10^3 M^{-1} cm^{-1} at its λ_{max} at 675 nm.[290] Although this complex was not emissive, such an absorption profile is desirable for solar harvesting applications, and is significant given that iridium complexes typically display attenuated UV-Vis absorption profiles past 530 nm.[286;291]

In this chapter, the aryldiazo ligand 2-[4-(*N*,*N*-dimethylamino)benzeneazo]imidazole (azoimH) is explored as the ancillary ligand. The inherent D-A characteristics of the

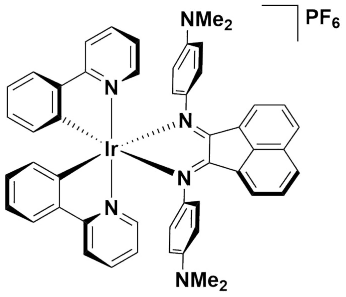

107

Figure 5.2: Example of an iridium complex bearing an Ar-BIAN ligand.[290]

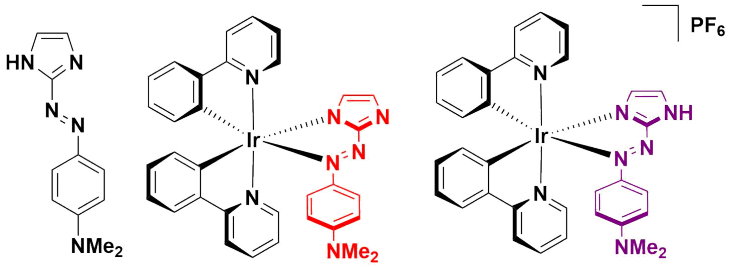

azoimH 108 109

Figure 5.3: The N^N ligand azoimH and the corresponding complexes studied in this chapter.

dimethylamino- donor with an azoimidazolyl acceptor are expected to red-shift the absorption of the corresponding complexes compared to traditional $[Ir(C^N)_2(N^N)]^+$ complexes. The complexes studied have the same C^N ligands, but differ by the protonation state of the imidazole ring (complexes **108** and **109**).

5.2 Synthesis

Cleavage of the $[Ir(ppy)_2(\mu\text{-}Cl)]_2$ dimer in the presence of excess K_2CO_3 and the azoimH ligand results in the formation of neutral $[Ir(ppy)_2(azoim)]$, **108**, in excellent yield.[158;292] In the absence of base, $[Ir(ppy)_2(azoimH)]^+$, **109**, can be isolated as its PF_6^- salt under standard conditions also in high yield. Remarkably, under these complexation conditions the solution turned from red, which is the colour of azoimH ligand, to a dark purple; under the basic conditions described for the synthesis of **108**, the red colour of the solution persisted but noticeably darkened.

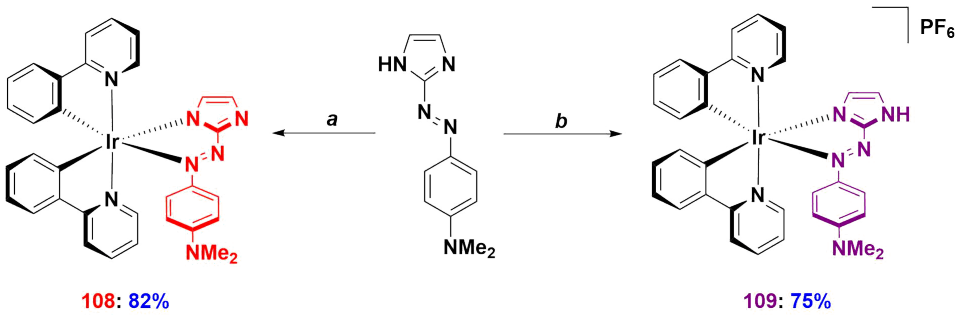

Figure 5.4: Synthesis of **108** and **109**. Reagents and conditions: [a] $[Ir(ppy)_2(\mu\text{-}Cl)]_2$ (1.0 equiv.), azoimH (2.2 equiv.), K_2CO_3 (2.4 equiv.), DCM/MeOH (5:4 v/v), 55 °C, 19 h. [b] i) $[Ir(ppy)_2(\mu\text{-}Cl)]_2$ (1.0 equiv.), azoimH (2.5 equiv.), DCM/MeOH (5:4 v/v), 55 °C, 19 h ii) excess NH_4PF_6. The colour of the N^N ligands in **108** and **109** represents the colour of the corresponding materials in solution and solid state.

5.3 Characterisation

The complex nature of the ^{1}H NMR spectra (Figure 5.5) is indicative of the lowering of the symmetry about the iridium centre following complexation. The 1H NMR spectra for 4 and 5 show similar features, particularly in the aromatic region. At higher frequency, multiplets at both ca. 8.05 and 7.75 ppm in **108** become more resolved in **109**. The distal -NH proton in **109** could not be detected.

Suitable crystals for X-ray analysis were obtained for **108** and **109** (Figure 5.6). The X-ray structures support the absence/presence of the imidazoyl proton in the two respective complexes. The distal -NH of **109** forms a hydrogen bond (1.77(2) Å) with a solvent water molecule. Surprisingly, changing the protonation state leads to a notable conformational change of the ancillary ligand. When the ligand is neutral, as in **109**, it is conformationally flat, but when deprotonated in **108** a larger torsional twist (**108**: 33.6(6)°; **109**: -12.6(5)°) of the aryl ring with respect to the N-N-C-N azoimidazole plane is observed, which is coupled with a pyramidalisation and deconjugation of the -NMe_2 group. This twisting about the azoimidazole-aminophenyl bond is not significantly reflected in the N_{azo}-C_{Ph} distances (**108**: 1.416(6) Å, **109**: 1.405(5) Å) but is more apparent for the deconjugation of the -NMe_2 group, for which significant lengthening of the C_{Ph}-N_{amine} distances is observed for **108** (**108**: 1.385(6) Å, **109**: 1.348(6) Å). The reduced conjugation within the N^N ligand observed in the solid state for **108** may account for the blue-shifted absorption profile of **108** compared with **109** in solution and the solid state (*vide infra*).

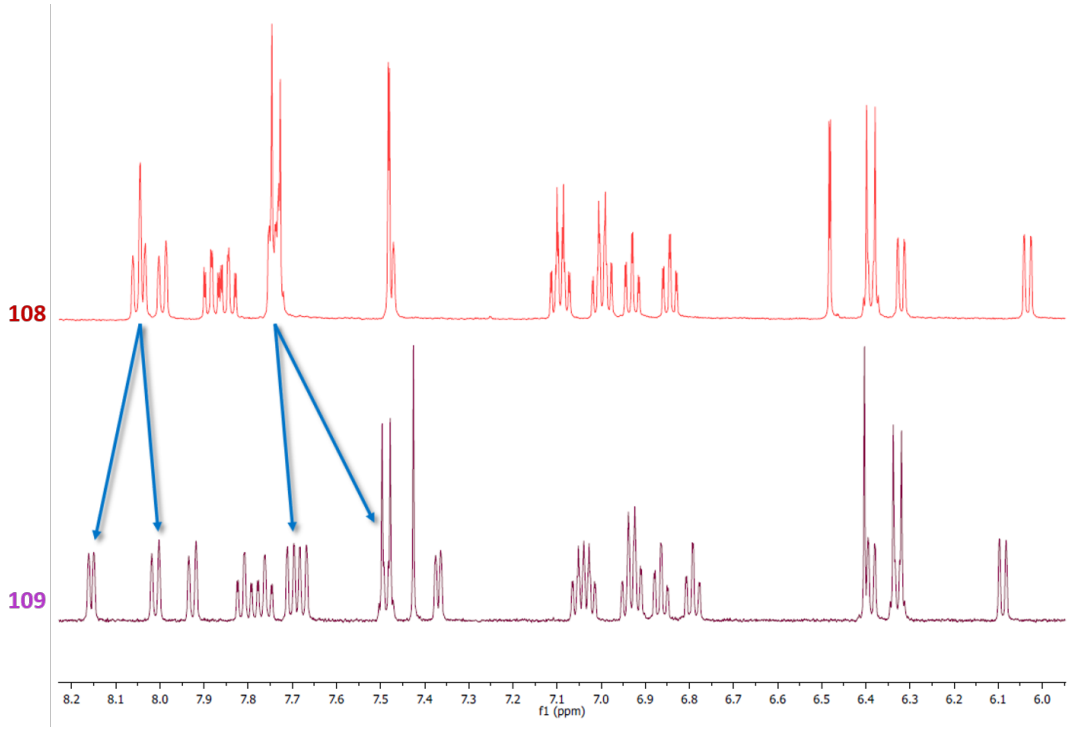

Figure 5.5: Stacked aromatic region of the ^{1}H NMR spectra of complexes **108** (top) and **109** (bottom) in CD_3CN.

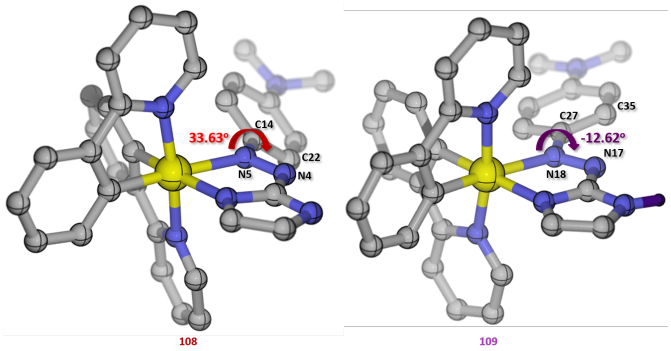

Figure 5.6: X-ray crystal structures of complexes **108** (left) and **109** (right), annotated with N(3)-N(4)-C(4)-C(9) dihedral angles. Solvent molecules, counterions and C-H hydrogen atoms are omitted for clarity.

5.4 Optoelectronic Characterisation and Analysis

The electronic structure of the complexes was probed by DFT calculations. The relevant relative orbital energies of **108** and **109**, and their electronic distribution character are given in Figure 5.7. For both complexes, the HOMO is delocalized across the azoimH ligand, with the strongest contributions arising from the dimethylaniline fragment. The

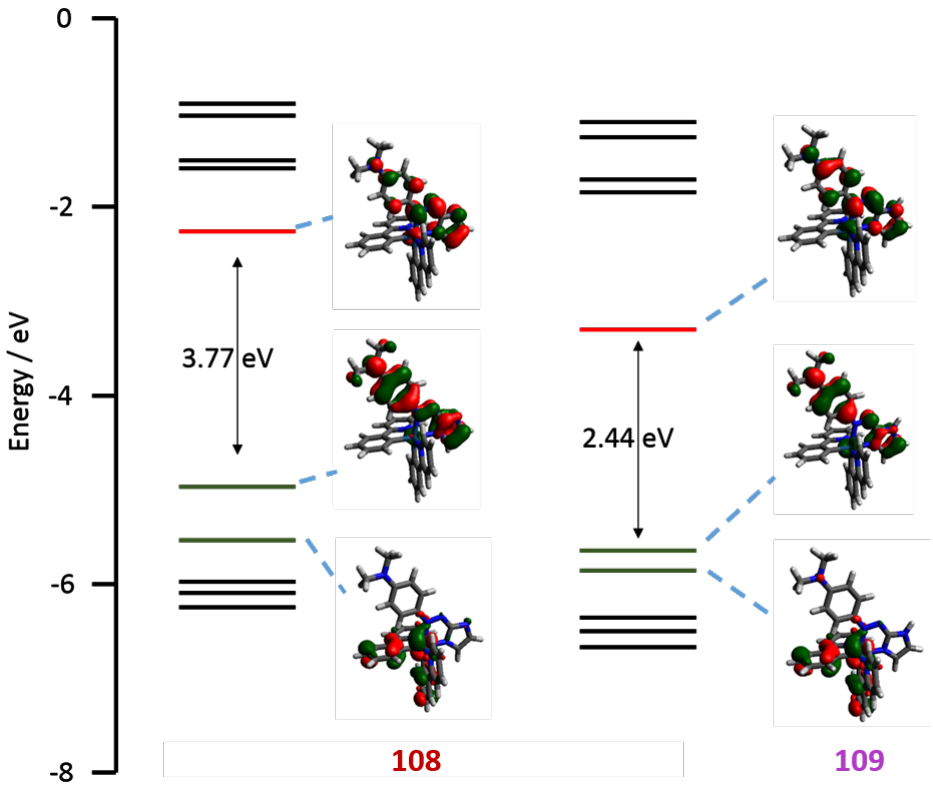

Figure 5.7: Energy level schemes for the Kohn-Sham orbitals of 108 and 109, including selected Kohn-Sham orbitals and the HOMO-LUMO energy gap (singlet ground states, B3LYP level).

LUMO is also delocalized along the azoimH ligand, but resides most significantly on the imidazole fragment. Finally, the HOMO-1 for both complexes is primarily localised on the Ir atom and the phenyl moiety of the ppy ligands; a pattern typically observed in the HOMO of most $[Ir(C^{\wedge}N)(N^{\wedge}N)]^{+}$-type complexes. Although both the HOMO and LUMO of 109 are stabilised upon protonation, the LUMO undergoes greater stabilisation than the HOMO, providing an explanation for the greatly red-shifted absorption spectrum seen for 109 compared to 108 (*vide infra*).

The optoelectronic properties of 108 and 109 are are summarised in Table 5.1. The UV-Vis absorption and emission spectra of 108 and 109, as well as the ligand azoimH, are shown in Figure 5.8. Upon complexation, the absorption profiles of 108 and 109 differ markedly from the parent ligand, particularly in the higher energy regimes: firstly, very intense high energy absorptions for are present both 108 and 109, which are largely absent for the ligand, but are typical of many bis-cyclometalated iridium complexes.[29] Below 350

	108	**109**
λ_{abs} (nm) [ϵ ($/10^4$ M^{-1} cm^{-1}]	256 [4.08], 304(sh) [1.55], 392 [1.04], 493 [2.21], 546(sh) [1.55]	252 [4.00], 297(sh) [1.98], 406 [0.80], 565 [3.38], 616(sh) [1.50]
λ_{PL} (nm) [a]	580	625
Φ_{PL} (%) [a,b]	0.03	0.08
τ_e (ns) [c]	4.82 (11%), 163 (19%), 1403 (69%)	108.7 (22%), 1215 (78%)
τ_e aerated (ns) [c]	0.405 (19%), 4.57 (41%), 45.2 (40%)	8.46 (15%), 31.5 (85%)
$E_{1/2(ox)}$ (V)	0.19	0.62
$E_{1/2(red)}$ (V)	-1.82	-1.03
E_{HOMO} (eV)	-4.99	-5.42
E_{LUMO} (eV)	-2.98	-3.77

Table 5.1: Relevant optoelectronic paramters for complexes **108** and **109** at 298 K. [a] Measurements were carried out in degassed MeCN, except for UV-Vis absorption and aerated lifetimes, which were conducted under air. Electrochemical measurements were performed at 100 mV s^{-1}, using Fc/Fc^+ as an interal standard and are referenced to the Fc/Fc^+ redox couple. [a] λ_{exc}: 360 nm. [b] Quinine sulfate used as the reference (Φ_{PL} = 54.6% in 0.5 M H_2SO_4 at 298 K).[220] [c] λ_{exc}: 378 nm.

nm, these transitions are assigned to spin-allowed π-π^* transitions localized on the ppy ligands, while between 350 – 450 nm mixed ^{1}MLCT and ^{1}LLCT absorptions to the N^N ligand are operative. In addition, there are increased absorptivities for **108** in this region, which is distinct from what is observed at lower energies.

At low energies, the form of the absorption spectra for both the free ligand and the complexes are more similar, albeit with pronounced changes in the absolute energies at which these transitions occur. For the ligand, an intense shoulder (415 nm) and fully resolved band (458 nm) are observed for the ligand. These bands are ascribed as CT transitions between the -NMe_2 donor and the azoimidazole acceptor. Given the similar profiles, the same ILCT-type transitions are presumed to be operative within the complex framework as well, but with significant red-shifting and enhancing of intensity of the transitions for the complexes compared with the free ligand. These low energy absorptions

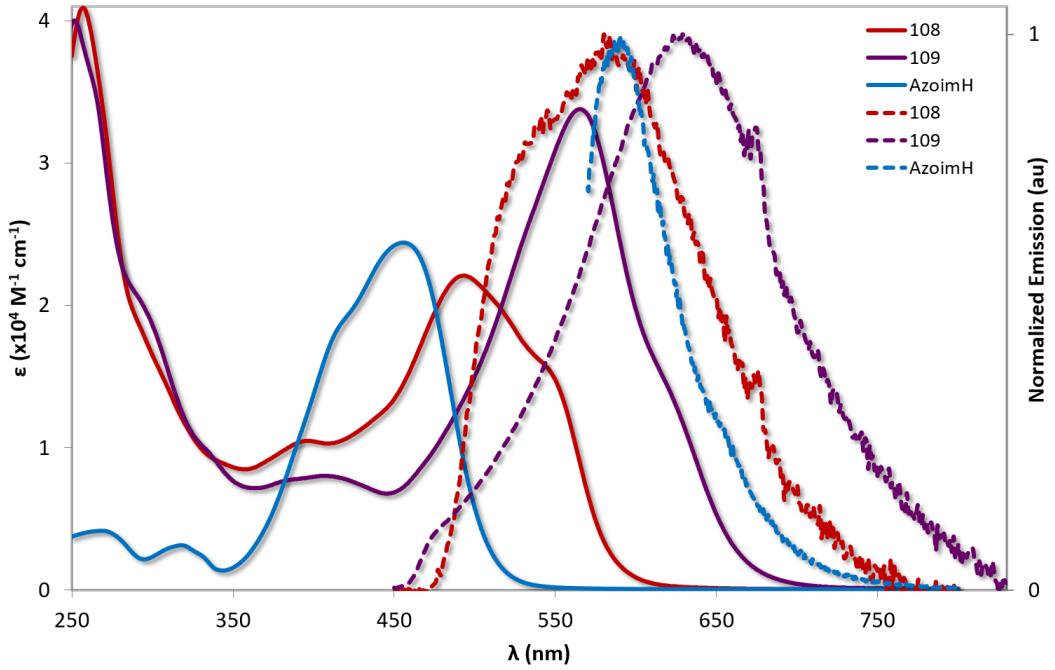

Figure 5.8: Absorption (solid lines) and normalised photoluminescence spectra (dashed lines) of the ligand azoimH in DCM and complexes **108** and **109** in MeCN solution.

(up to 700 nm for **109**) and unprecedentedly high extinction coefficients are in stark contrast to the absorption profiles of the vast majority of bis-cyclometalated iridium(III) complexes previously reported.[293] In **108** this band peaks at 493 nm (2.21×10^4 M^{-1} cm^{-1}), with a shoulder at 546 nm also observed. With **109**, protonation red-shifts these bands by 72 nm (2585 cm^{-1}), with the principal band (565 nm) remarkably intense at 3.38×10^4 M^{-1} cm^{-1}. The high intensity observed for the shoulder at 616 nm for **109** (1.50×10^4 M^{-1} cm^{-1}) compares favourably with complex **107**, which exhibits an albeit red-shifted ILCT absorption (λ_{abs} = 675 nm) but at much lower molar absorptivity (0.71×10^4 M^{-1} cm^{-1}).[290]

The similar profiles of the absorption spectra suggest that the nature of the transitions occurring for both complexes (as well as the ligand) are fundamentally the same, but are found at higher energy when the imidazole ring is formally anionic as in **108**. This implies that the trend in relative conformations seen in the solid state (Figure 5.6) is also somewhat mirrored in solution, with the reduced conjugation in **108** responsible for both the blue-shifted absorption and the lower absorptivity compared to **109**.

To assess the nature of these transitions, TDDFT calculations were performed. In **108**,

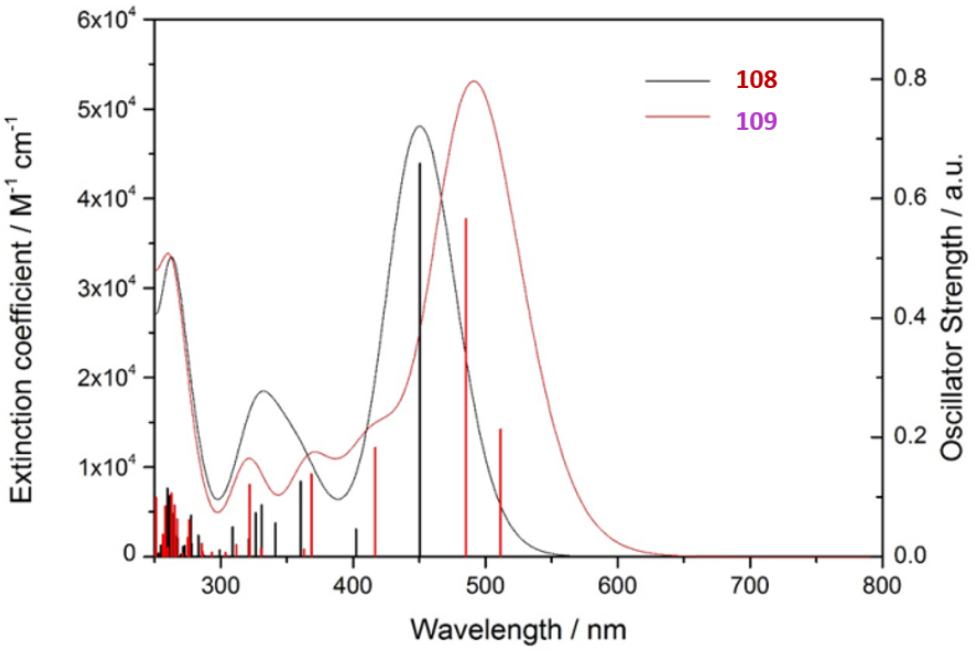

Figure 5.9: Simulated absorption spectra with oscillator strength (vertical lines) for **108** (black) and **109** (red) using the CAM-B3LYP functional.

the lowest energy singlet electronic state arises from a HOMO to LUMO ILCT transition from the donor -ArNMe$_2$ moiety to the azoimidazole acceptor. In **109**, the first two lowest energy states are characterised by transitions arise from a combination of HOMO-1 to LUMO and HOMO to LUMO. Their nature correspond to an admixture of a similar ILCT-type transition observed for **108**, as well as MLCT contributions. The simulated absorption profiles generally reproduce the trends observed experimentally, with **109** red-shifted compared to **108**, but the overall spectra are predicted to be more blue-shifted than experimentally observed (Figure 5.9).

UV-visible absorption titration experiments (Figure 5.10) revealed the reversibility of de/protonating the imidazole ring, and illustrate the large differences in energy of the lowest energy absorption bands between **108** and **109** (2585 cm^{-1}, 72 nm). Such energy differences are uncommon among proton switchable iridium complexes. For example, complex **57**, with an H$_2$biim N^N ligand, undergoes only a modest 498 cm^{-1} (12 nm) bathochromic shift in the emission energy upon mono-deprotonation of the ancillary ligand.[161] A switchable iridium complex bearing a 2-pyridylbenzimidazole ancillary ligand has been reported in which the protonated form emits 3212 cm^{-1} (94 nm) lower in energy (496 nm neutral,

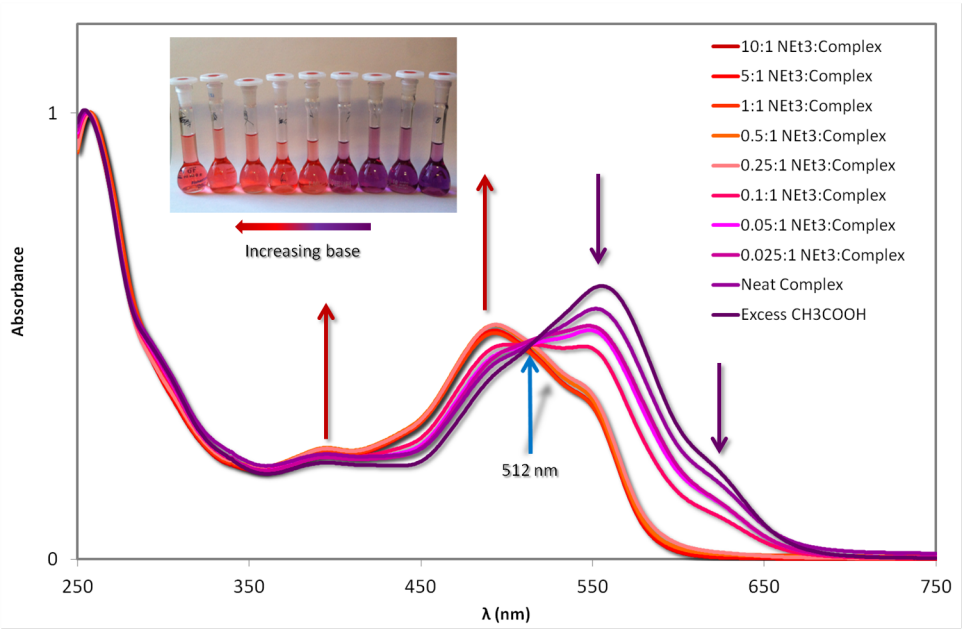

Figure 5.10: UV-Visible absorption titration, showing addition of varying equivalents of NEt_3 to a solution of **109** in MeCN. The spectra are normalised to the band at 257 nm. A curve showing **109** with addition of excess AcOH is shown for reference. Inset: photos of solutions of complex **109** with increasing equivalents of NEt_3.

590 nm charged).[158] Finally, significant stabilisation in energy is reported for a tris-cyclometalated iridium complex bearing an acid-responsive 4-pyridyl group (57 nm, 4223 cm^{-1} for absorption and 87 nm, 2899 cm^{-1} for emission).[294] However, in this instance the pyridyl groups are appended to the cyclometalated phenyl rings, which are typically associated with the HOMO of these complexes, pointing towards HOMO-modulation rather than the LUMO-modulation observed here.

Emission spectroscopy reveals more insight into the excited state properties of these complexes. The ligand itself is poorly emissive, with a weak fluorescence signal detected at 592 nm in DCM. Similarly, the complexes are also poorly emissive ($\Phi_{PL} < 0.1\%$), as is typical of many metal-azo complexes.[279] The multi-exponential decay kinetics observed point towards significant quenching processes deactivating the excited state. Indeed, such behaviour has been studied[264] with an analogous ruthenium complex $[Ru(bpy)_2(pap)](ClO_4)_2$ (where pap is 2-(phenylazo)pyridine). The totally non-emissive nature of this complex is attributed to a combination of conventional energy gap law vibrational quenching due to the red-shifted absorption imparted by the azo ligand, as well as to sequential population of the ^{1}MLCT $\rightarrow^3$ $MLCT_{bpy}$ $\rightarrow^3$ $MLCT_{pap}$ excited states, wherein eventual de-excitation of the

^{3}MLCT$_{pap}$ state occurs non-radiatively within 4.5 ns. In an analogous fashion, it is possible that **108** and **109** undergo a similar process (^{1}MLCT $\rightarrow^3$ MLCT$_{ppy}$ $\rightarrow^3$ MLCT$_{azoim(H)}$). However, in these instances energy transfer from the ^{3}MLCT$_{ppy}$ state to the ^{3}MLCT$_{azoim(H)}$ state is not as efficient as the ruthenium analogue, giving rise to a long-lived phosphorescent component from the ^{3}MLCT$_{ppy}$ state. Such excited state dynamics would account for the peculiarly small Stokes' shifts observed for these complexes (45 nm or 1419 cm^{-1} for **108** and 14 nm or 361 cm^{-1} for **109**). Under aerated conditions, this emission is quenched significantly, which further points to population of a long-lived triplet excited state.

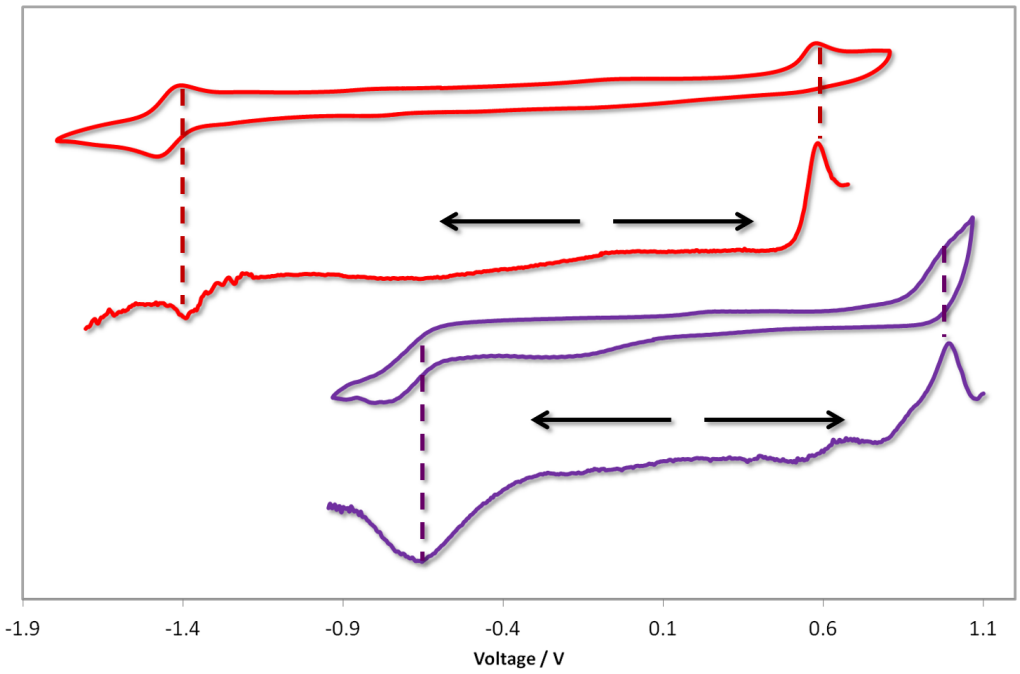

Figure 5.11: Cyclic and differential pulse voltammetry measurements showing first oxidation and reduction potentials of complexes **108** (red) and **109** (purple) in MeCN, referenced with respect to the Fc/Fc$^+$ redox couple. Scan rate: 100 mV s^{-1}. Arrows indicate DPV scan directions.

Cyclic and differential pulse voltammetry (DPV) measurements were undertaken to discern the energy levels of these materials (Figure 5.11 and Table 5.1). The oxidation processes are uncharacteristic of typical bis-cyclometalated iridium(III) complexes. For example, complex **4** possesses a pseudo-reversible first oxidation wave at 0.89 V (*vs* Fc/Fc$^+$) that has been attributed to the Ir^{III}/Ir^{IV} redox couple along with contribution from the phenyl moieties of the cyclometalating ligands.[62] By comparison, here the oxidation waves are at much less positive potential (0.19 V for **108** and 0.62 V for **109**, *vs* Fc/Fc$^+$) and are

completely irreversible. This suggests that the oxidation process is purely ligand-centred. The changes in the electrochemistry as a function of the protonation state of the ancillary ligand can be rationalized as a function of the charge of the complex. When protonated, the complex is +1 charged, and thus a single electron oxidation of **109** would generate a formal +2 cation. This is thermodynamically more difficult than the analogous process of generating a formal +1 cation in the oxidation of **108**, which explains the moderately greater anodic potential observed for **109**. The same arguments hold for the reduction: The positive charge on **109** makes for facile reduction (-1.03 *vs* Fc/Fc^+) to the charge-neutral species compared with reduction of the formally neutral **108** to a radical anion, which occurs at substantially more negative potential (-1.82 vs Fc/Fc^+). The ligand-centred assignment of the electrochemistry, as well as the thermodynamic arguments are in general agreement with energy changes predicted by the DFT calculations (*vide supra*).

5.5 Organic Photovoltaic Devices

Although it is poorly emissive, the panchromatic absorption properties of **109** make it an interesting candidate for solar cell applications. To assess this suitability further, a photophysical study of this complex in thin films was carried out, with a view to employing this material in solution processed organic photovoltaics (OPV). The absorbing layer of these devices generally comprises a mixture of donor material (high HOMO and LUMO) and acceptor material (low HOMO and LUMO), which facilitate rapid separation of electrons and holes upon photogeneration of an exciton. Poly(3-hexylthiophen-2,5-diyl) (P3HT) was chosen as the complementary donor material, since the solution photophysics of **109** suggested it absorbs in the same spectral region as P3HT and thus efficient energy transfer should be possible. Films of P3HT:**109** in a 1:0.5 (by weight). The absorption spectra and photoluminescence spectra of a neat film of P3HT and the blended film are shown in Figure 5.12. The blend demonstrates good overlap with the neat film but has more pronounced vibronic features, leading to slightly more absorption at longer wavelengths.

A necessary condition for efficient charge generation in the OPV device is that there should be efficient quenching of the donor. Accordingly, time-resolved photoluminescence (TRPL) quenching measurements of the blend (P3HT:**109**) compared with the pristine P3HT film were carried out. Figure 5.13 shows increased PL quenching for the blend compared to pristine P3HT; while a lifetime 603 ns was measured for the pristine P3HT

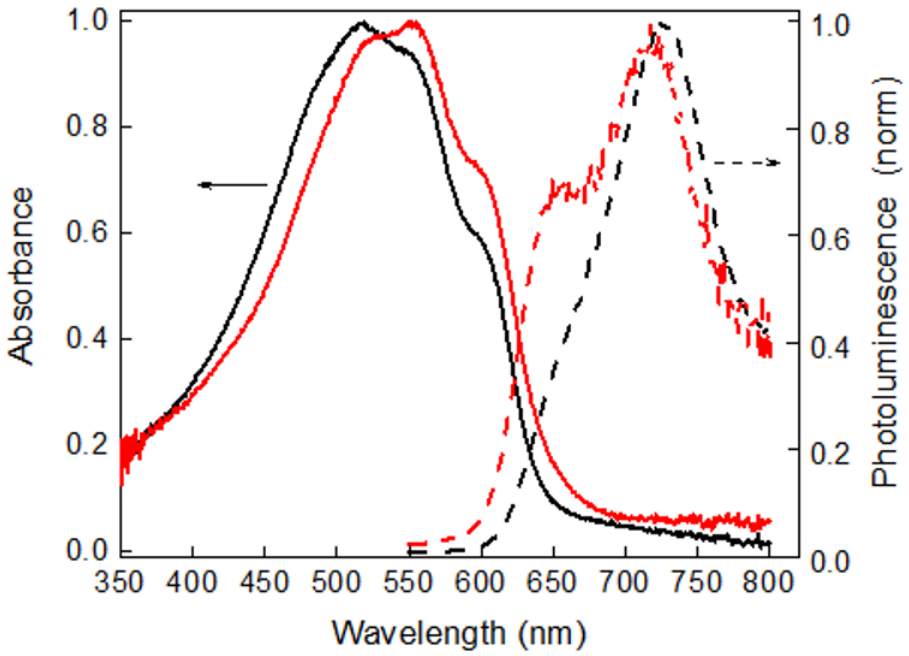

Figure 5.12: Absorption spectra of pristine P3HT (black solid line) and P3HT:**109** (1:0.5) (red solid line) films, and PL spectra of pristine P3HT (black dashed line) and P3HT:**109** (1:0.5) (red dashed line) films on quartz substrates. PL spectra were collected after excitation at 400 nm.

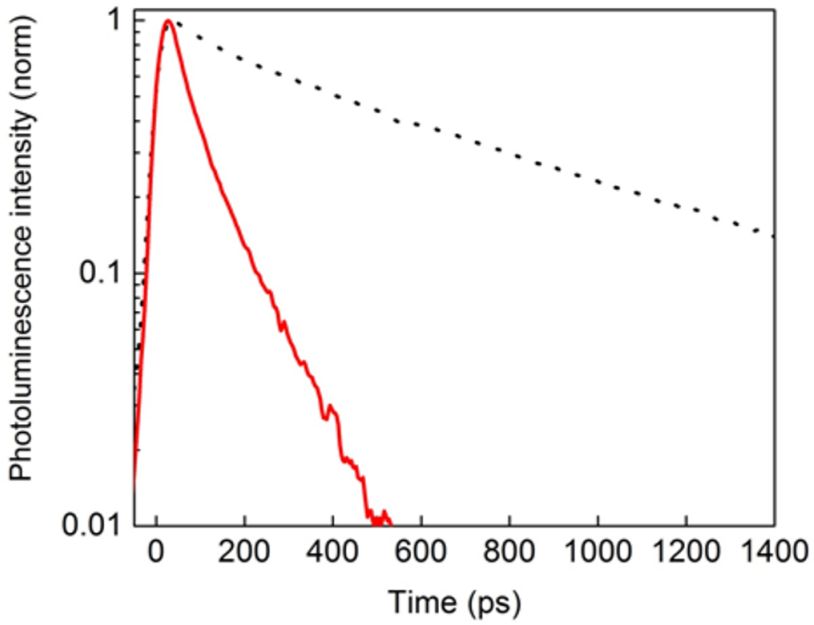

Figure 5.13: TRPL spectra of pristine P3HT (black dashed line) and P3HT:**109** (1:0.5) (red solid line) films on quartz substrates. PL spectra were excited at 400 nm and detected at 650 nm.

film, this was reduced to just 75 ns for the blend. The charge transfer quenching efficiency, η_{et}, can thus be calculated using the following equation:

$$\eta_{et} = 1 - \frac{\int I \cdot dt}{\int I_0 \cdot dt}$$

Where I is the TRPL intensity of the P3HT:**109** film and I_0 is the TRPL intensity of the neat P3HT film. The calculated quenching efficiency was 81% for the blend, pointing towards substantial, but not complete quenching, and indicating that **109** can act as an acceptor in the device. It is likely that quenching here is due to a combination of both charge transfer and energy transfer processes.

The device configuration is given in Figure 5.14, while the current-voltage (I-V) characteristics and device performance are shown in Figure 11. The most striking feature of the OPV performance is the exceptionally high open circuit voltage (V_{oc}) of 1.12 V obtained from the blend (P3HT:5) when compared to the device containing P3HT only (0.93 V). These V_{oc} values are higher than that reported for other solution-processed iridium complexes, which are in the range of 0.7 to 0.8 V.[287;295] This high V_{oc} can be understood from consideration of the energy levels, which are related by:[296]

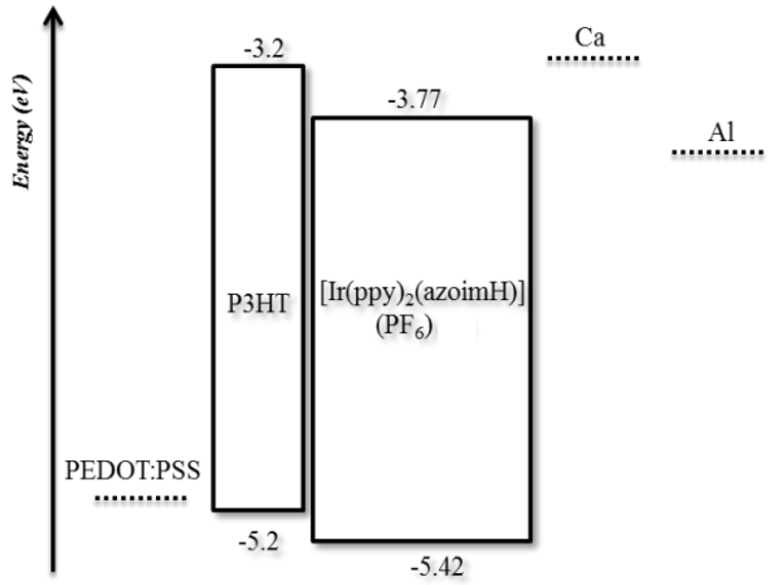

Figure 5.14: HOMO-LUMO energy level band diagram of relevant materials employed in the OPV device.

$$V_{oc} = HOMO_{donor} - LUMO_{acceptor} - 0.3$$

The estimated V_{oc} based on this equation is 1.13 V, which is in good agreement with the experimentally determined value. Such a high observed V_{oc}, particularly compared with other iridium-based devices, is attributable to the device configuration wherein the iridium complex is acting as an acceptor, rather than as a donor as was the case in previous reports.[286;287;295] The strongly stabilized HOMO and LUMO energy levels in **109** make this complex viable from a thermodynamic standpoint to function as an acceptor for the P3HT donor. By contrast, the anionic charge on the imidazolate moiety of **108** destabilises the energy of the HOMO and LUMO to the extent that this is no longer possible.

Unfortunately, despite the high observed V_{oc} of the OPV device and efficient photoluminescence quenching of P3HT by **109**, the overall device performance is poor. In general, low short circuit currents can arise from inefficient charge separation, poor charge transport and leakage of the charge carriers to the electrodes. Although efficient quenching was observed, it is possible that there is considerable energy transfer from P3HT to **109**. In such instances, charge generation would be impaired, which perhaps provides an explanation as to why the device performances is poor. Such a problem could be overcome by designing materials that display even lower HOMO energy levels.

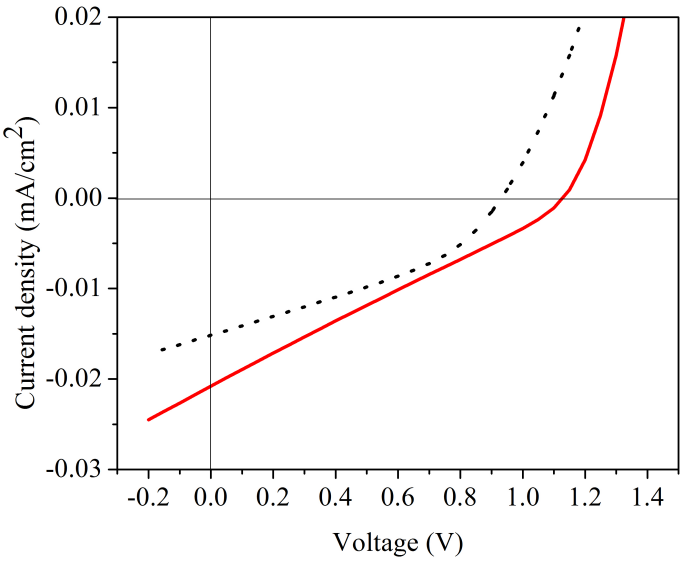

Figure 5.15: I-V characteristics for pristine P3HT (black dashed line) and P3HT:**109** (red solid line) bulk heterojunction solar cells.

5.6 Conclusion

In summary, two novel iridium complexes bearing azoimidazole/imidazolate ligands have been synthesised and characterised. Both complexes are strongly absorptive, with **109** in particular demonstrating absorption up to 700 nm, with very high molar extinction coefficients at long wavelengths (1.50×10^4 M^{-1} cm^{-1} at 616 nm). De/protonation of the imidazole ring is fully reversible, and the energetic differences in the absorption profiles of **108** and **109** upon the addition of acid or base are unusually large, particularly when compared to other iridium-based systems. The strong absorption observed for **109**, as well as its low lying HOMO and LUMO, made it an interesting candidate to explore as an acceptor material for use in OPV devices. Although a high V_{oc} value was obtained, the overall device performance was poor. Nevertheless, the first example of an iridium-based acceptor material is reported, and results suggest enhanced electron transport via judicious ligand design may lead to improved device performance.

Chapter 6

Experimental

6.1 General Synthetic Methods

Commercial chemicals were used as supplied. All reactions were carried out using solvents of reagent grade or better. Flash column chromatography was performed using silica gel (60 Å, 40-63 µm). Analytical thin layer chromatography (TLC) was performed using silica plates with aluminum backings (250 µm with indicator F-254). Compounds were visualized under UV light. ^{1}H, ^{13}C and ^{19}F NMR spectra were recorded on Bruker Avance spectrometers at 300 – 500 MHz, 126 MHz and 376 MHz respectively. The following abbreviations have been used for multiplicity assignments: 's' for singlet, 'd' for doublet, 't' for triplet, 'q' for quartet, 'p' for pentet, 'm' for multiplet and 'br' for broad. Deuterated chloroform ($CDCl_3$), deuterated dichloromethane (CD_2Cl_2), deuterated acetonitrile (CD_3CN), deuterated water (D_2O), deutertated methanol (CD_3OD) and deuterated dimethylsulfoxide (DMSO-d_6) were used as the NMR solvents of record. ^{1}H and ^{13}C NMR spectra were referenced to the solvent peak. High-resolution mass spectra were recorded at the EPSRC UK National Mass Spectrometry Facility at Swansea University on a quadrupole time-of-flight (ESI-Q-TOF), model ABSciex 5600 Triple TOF in positive electrospray ionization mode and spectra were recorded using sodium formate solution as the calibrant. Elemental analyses were performed by Mr. Stephen Boyer, London Metropolitan University. Melting points (Mp) were recorded using open-ended capillaries on an Electrothermal melting point apparatus and are uncorrected.

6.2 Syntheses of Ligands and Organic Intermediates

6.2.1 Suzuki-Miyaura Cross-Coupling Reactions

General Procedure

The boronic acid and aryl halide were added to a round bottom flask along with base and a mixture of 1,4-dioxane and distilled water (4:1 v/v) to obtain a concentration of 0.15 to 0.20 M. The reaction mixture was degassed via three purging cycles of N_2 and vacuum. Under positive N_2 pressure, $Pd(PPh_3)_4$ (5.0 mol%) was added to the flask under positive nitrogen pressure and the flask was sealed. The mixture was refluxed for the specified time, before adding distilled water, extracting with organic solvent and washing with water and saturated aqueous sodium hydrogen carbonate to remove residual boronic acid. Evaporation under reduced pressure gave the crude product, which was purified by flash column chromatography.

2-(2,4-Difluorophenyl)pyridine (dFppy).

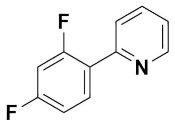

Synthesis of this compound proceeded using 2,4-difluorophenylboronic acid (1.5 equiv.), 2-bromopyridine (1.0 equiv.) and sodium carbonate (2.0 equiv.). The mixture was refluxed for 19 h. The crude was extracted with DCM. The compound was purified by silica gel chromatography (hexanes/ethyl acetate 95:5) gave 0.554 g of pure compound as a colourless oil. **Yield:** 87%. **R_f:** 0.48 (silica, hexanes/ethyl acetate, 80:20). **^{1}H {^{19}F} NMR (500 MHz, $CDCl_3$)** δ **(ppm):** 8.72 (dt, J = 4.5, 1.0 Hz, 1H), 8.03 – 7.99 (m, 1H), 7.75 (d, J = 4.0 Hz, 2H), 7.28 – 7.23 (m, 1H), 7.03 – 6.99 (m, 1H), 6.93 – 6.90 (m, 1H). **^{13}C {^{1}H} NMR (126 MHz, $CDCl_3$)** δ **(ppm):** 164.6, 162.1, 159.5, 152.7, 149.9, 136.6, 132.3, 124.4, 122.6, 112.1, 104.5. **^{19}F {^{1}H} NMR (471 MHz, $CDCl_3$)** δ **(ppm):** -109.3 (d, J = 6.8 Hz, 1F), -113.0 (d, J = 6.8 Hz, 1F). **GC-MS:** (13.6 min) **$[M]^+$:** 191. The characterisation matches that reported.[178]

5-(4-Methylpyridin-2-yl)-2,4-dimethoxypyrimidine (Mepypyrm).

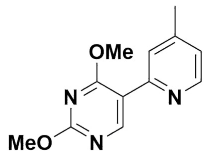

Synthesis of this compound proceeded using 2,4-dimethoxypyrimidine-5-boronic acid (1.2 equiv.), 2-bromo-4-methylpyridine (1.0 equiv.) and potassium carbonate (3.0 equiv.). The mixture was refluxed for 16 h. The crude was extracted with DCM. The compound was purified by silica gel chromatography (Et_2O/DCM, 1:9) followed by a second silica gel column (hexanes/ethyl acetate, gradient 9:1 to 8:2), to give 1.090 g of white crystalline solid. **Yield:** 70%. **R_f:** 0.45 (silica, Et_2O/DCM, 8:2). **^{1}H NMR (400 MHz, $CDCl_3$)** δ **(ppm):** 8.82 (s, 1H), 8.50 (d, J = 5.0 Hz, 1H), 7.59 (s, 1H), 7.03 (d, J = 5.0 Hz, 1H), 4.06 (s, 3H), 4.03 (s, 3H), 2.38 (s, 3H). **^{13}C {^{1}H} NMR (126 MHz, $CDCl_3$)** δ **(ppm):** 168.3, 165.0, 159.9, 151.8, 149.4, 147.5, 124.9, 123.3, 114.9, 55.1, 54.3, 21.4. **MS (TOF ES$^+$):** ***m/z*** **(%)**: 254.2 (100) $[M+Na]^+$. **HR-MS** (ES^+): **$[M+H]^+$ Calculated:** ($C_{12}H_{13}N_3O_2H$) 232.1086; **Found:** 232.1088.

5-(5-(Trifluoromethyl)pyridin-2-yl)-2,4-dimethoxypyrimidine (CF_3pypyrm).

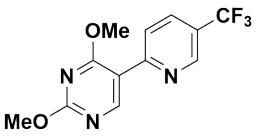

Synthesis of this compound proceeded using 2,4-dimethoxypyrimidine-5-boronic acid (1.2 equiv.), 2-bromo-5-(trifluoromethyl)pyridine (1.0 equiv.) and potassium carbonate (3.0 equiv.). The mixture was refluxed for 16 h. The crude was extracted with ethyl acetate. The compound was purified by silica gel chromatography (Et_2O/DCM, 8:2) followed by a second silica gel column (hexanes/ethyl acetate, 8:2), to give 0.728 g of white crystalline solid. **Yield:** 84%. **R_f:** 0.21 (silica, hexanes/ethyl acetate, 9:2). **^{1}H NMR (300 MHz, $CDCl_3$)** δ **(ppm):** 9.00 (s, 1H), 8.89 – 8.83 (m, 1H), 7.99 (d, J = 8.4 Hz, 1H), 7.89 (dd, J = 8.5, 2.2 Hz, 1H), 4.08 (s, 3H), 4.02 (s, 3H). **^{13}C {^{1}H} NMR (126 MHz, $CDCl_3$)** δ **(ppm):** 168.4, 165.6, 160.7, 155.2, 146.3, 133.5, 124.7, 123.7, 123.2, 113.3, 55.2, 54.4. **^{19}F {^{1}H} NMR (282 MHz, $CDCl_3$)** δ **(ppm):** -62.4 (s, 3F). **MS (TOF EI$^+$):** ***m/z*** **(%)**: 285.1 (100) $[M+H]^+$. **HR-MS** (EI^+): **$[M+H]^+$ Calculated:** ($C_{12}H_{13}N_3O_2H$) 285.0725; **Found:** 285.0727.

2-Chloro-4-(2,4,6-trimethylphenyl)pyridine.

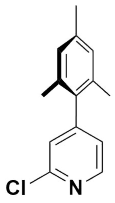

Synthesis of this compound proceeded using 2,4,6-trimethylphenylboronic acid (1.5 equiv.), 2-chloro-4-iodopyridine (1.0 equiv.) and potassium carbonate (3.0 equiv.). Note: an excess of boronic acid is required to ensure full consumption of 2-chloro-4-iodopyridine, since the boronic acid is prone to deborylation *in situ* and separation of 2-chloro-4-(2,4,6-trimethylphenyl)pyridine from 2-chloro-4-iodopyridine by chromatography is not possible. The mixture was refluxed for 72 h. The crude was extracted with toluene. The compound was purified by silica gel chromatography (hexanes/ethyl acetate, 95:5) to give the product as a colourless oil (2.288 g). **Yield:** 59%. $\mathbf{R_f}$**:** 0.37 (silica, hexanes/ethyl acetate, 95:5). ^{1}**H NMR (400 MHz, CDCl$_3$)** δ **(ppm):** 8.40 (d, J = 4.0 Hz, 1H), 7.12 (s, 1H), 7.02 (dd, J = 4.0, 1.2 Hz, 1H) 6.92 (s, 2H) 2.29 (s, 3H), 1.97 (s, 6H). ^{13}**C {^{1}H} NMR (126 MHz, CDCl$_3$)** δ **(ppm):** 152.9, 151.8, 149.8, 138.0, 134.9, 128.5, 125.1, 123.6, 21.0, 20.5. **HR-MS** (APCI$^+$): **[M+H]$^+$ Calculated:** ($C_{14}H_{14}ClNH$) 234.0858; **Found:** 234.0856. The characterisation matches that reported.[172]

2-Phenyl-4-(2,4,6-trimethylphenyl)pyridine (Mesppy).

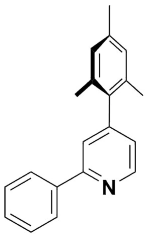

Synthesis of this compound proceeded using phenylboronic acid (1.6 equiv.), 2-chloro-4-(2,4,6-trimethylphenyl)pyridine (1.0 equiv.) and potassium carbonate (2.8 equiv.). The reaction mixture was refluxed for 19 h. The crude was extracted with DCM. The compound was purified by silica gel chromatography (hexanes/ethyl acetate, 9:1) to give the product as a colourless oil (0.283 g). Yield: 96%. **R_f:** 0.38 (silica, hexanes/ethyl acetate, 9:1). **^{1}H NMR (500 MHz, $CDCl_3$) δ (ppm):** 8.85 (dd, J = 5.0, 0.8 Hz, 1H), 8.17 – 8.13 (m, 2H), 7.68 (t, J = 1.2 Hz, 1H), 7.58 – 7.53 (m, 2H), 7.51 – 7.46 (m, 1H) 7.14 (dd, J = 4.9, 1.5 Hz, 1H), 2.44 (s, 3H), 2.15 (s, 6H). **^{13}C {^{1}H} NMR (126 MHz, CD_2Cl_2) δ (ppm):** 157.7, 150.3, 149.9, 139.4, 137.6, 136.5, 135.2, 129.1, 128.8, 128.6, 128.4, 127.0, 123.2, 121.5, 21.1, 20.7. **HR-MS** (FTMS$^+$): **$[M+H]^+$ Calculated:** ($C_{20}H_{19}NH$) 274.1585; **Found:** 274.1585. The characterisation matches that reported.[260]

2-(2,4-Difluorophenyl)-4-(2,4,6-trimethylphenyl)pyridine (dFMesppy).

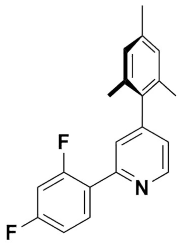

Synthesis of this compound proceeded using 2,4-difluorophenylboronic acid (1.4 equiv.), 2-chloro-4-(2,4,6-trimethylphenyl)pyridine (1.0 equiv.) and potassium carbonate (2.5 equiv.). The reaction mixture was refluxed for 19 h. The crude was extracted with DCM. The compound was purified by silica gel chromatography (hexanes/ethyl acetate, 9:1) to give the product as a colourless oil (2.880 g). Yield: 94%. **R_f:** 0.43 (silica, hexanes/ethyl acetate, 95:5). **^{1}H {^{19}F} NMR (500 MHz, $CDCl_3$) δ (ppm):** 8.75 (dd, J = 7.5, 1.5 Hz, 1H), 8.08 (dt, J = 8.5, 10 Hz, 1H), 7.59 (m, 1H), 7.09 (dd, J = 5.0, 1.5 Hz, 1H), 7.02 (tdd, J = 10.0, 3.3, 1.0 Hz, 1H) 6.97 (d, J = 1.0 Hz, 2H), 6.90 (dt, J = 3.0, 12.5 Hz, 1H), 2.34 (s, 3H), 2.05 (s, 6H). **^{13}C {^{1}H} NMR (126 MHz, $CDCl_3$) δ (ppm):** 164.7, 162.0, 159.5, 152.9, 122.8, 150.2, 150.1, 137.8, 136.4, 135.4, 132.4, 132.4, 132.3, 132.3, 128.5, 125.5, 125.4, 123.7, 112.2, 112.1, 111.9, 111.9, 104.8, 104.5, 104.3, 21.2, 20.8. **^{1}9F {^{1}H} NMR (471 MHz, $CDCl_3$) δ (ppm):** -109.3 (d, J = 9.4 Hz, 1F), -112.7 (d, J = 9.4 Hz, 1F). **HR-MS** ($APCI^+$): **$[M+H]^+$ Calculated:** ($C_{20}H_{17}F_2NH$) 310.1402; **Found:** 310.1402. The characterisation matches that reported.[172]

2-(Naphthalen-1-yl)-4-(2,4,6-trimethylphenyl)pyridine (Mesnpy).

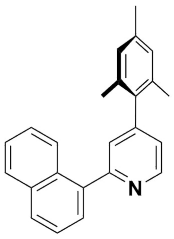

Synthesis of this compound proceeded using napthalen-1-ylboronic acid (1.6 equiv.), 2-chloro-4-(2,4,6-trimethylphenyl)pyridine (1.0 equiv.) and potassium carbonate (2.8 equiv.). The reaction mixture was refluxed for 19 h. The crude was extracted with DCM. The compound was purified by silica gel chromatography (hexanes/ethyl acetate, 9:1) to give the product as white crystals (0.451 g). Yield: 68%. **R_f:** 0.12 (silica, hexanes/ethyl acetate, 9:1). **^{1}H NMR (500 MHz, CD_2Cl_2)** δ **(ppm):** 8.82 (d, J = 5.0 Hz, 1H), 8.19 (d, J = 8.0 Hz, 1H), 7.93 (d, J = 8.0 Hz, 2H), 7.66 (d, J = 7.0 Hz, 1H) 7.60 – 7.55 (m, 1H), 7.54 – 7.47 (m, 2H) 7.41 (s, 1H), 7.17 (dd, J = 5.0, 1.5 Hz, 1H), 6.98 (s, 2H), 2.32 (s, 3H), 2.10 (s, 6H). **^{13}C {^{1}H} NMR (126 MHz, $CDCl_3$)** δ **(ppm):** 159.3, 149.9, 149.6, 138.7, 137.5, 136.4, 135.1, 133.9, 131.2, 128.7, 128.3, 127.5, 126.3, 126.0, 125.8, 125.7, 125.3, 123.2, 20.8, 20.5. **HR-MS** (FTMS$^+$): **$[M+H]^+$ Calculated:** ($C_{24}H_{21}NH$) 324.1717; **Found:** 324.1747.

6.2.2 Miscellaneous Organic Reactions

***o*-Phenylenediamine.**

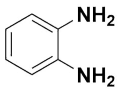

Synthesis of this compound was by a literature method.[259] To a solution of 2-nitroaniline (2.70 g, 20 mmol) in ethanol (25 mL), concentrated HCl (6 mL) and anhydrous $SnCl_2$ (18.34 g, 72 mmol). The reaction was stirred under nitrogen at 60 ℃ for 16 h. Water was added to the reaction mixture and the resulting mixture was poured into a stirring, aqueous solution of NaOH (3 M) resulting in the formation of a white precipitate. Saturated, aqeuous $NaHCO_3$ solution was added for an additional 5 min. The fine white precipitate was removed by filtration through celite. The precipitate was repeatedly washed with DCM, then the organic phases were combined, washed with brine, dried over Na_2SO_4 and concentrated to give the compound as a white solid (2.10 g) The product was filtered and dried to give 2.47 g as a cream white powder. **Yield:** 33%. **Mp:** 99 – 100 ℃. **^{1}H NMR (500 MHz, $CDCl_3$) δ (ppm):** 6.74 – 6.70 (m, 4H), 3.19 (br s, 4H).

1*H*,1'*H*-2,2'-Biimidazole (H_2biim).

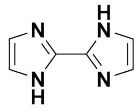

Synthesis of this ligand was as outlined in the literature.[180] To a mixture of ammonium acetate (2.7 equiv.) in distilled water at 40 ℃ was added dropwise 40% aqueous glyoxal solution (1.0 equiv.) over a period of 3 h to give a concentration of 0.1 M. The mixture was allowed to stir for a further 5 h at room temperature. The reaction mixture was filtered and washed multiple times with distilled water and acetone to give 8.31 g of a brown crude product. This material was added to ethylene glycol (0.5 M), heated to 150 ℃ and treated with decolourising carbon. Filtration saw product precipitate immediately, with further washings with distilled water to maximise product precipitation. The product was filtered and dried to give 2.47 g as a cream white powder. **Yield:** 33%. **R_f:** 0.12 (10% MeOH/DCM on silica). **Mp:** 350 – 352 ℃. **Litt.:** > 300 ℃.[179] **^{1}H NMR (500 MHz, DMSO-d_6) δ (ppm):** 12.67 (s, 2H), 7.14 (s, 2H), 7.00 (s, 2H). **^{13}C {^{1}H} NMR (126 MHz, DMSO-d_6) δ (ppm):** 139.8, 128.7, 117.9.

1*H*,1'*H*-2,2'-Bibenzimidazole (H_2biben).

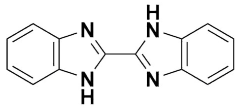

The synthesis of this compound is similar to a previously reported method.[259] To a solution of *o*-phenylenediamine (1.24 g, 11.47 mmol) in methanol (50 mL) was added methyl-2,2,2-trichloroacetimidate (1.01 g, 5.74 mmol, 1.0 equiv.), followed by concentrated HCl (0.05 mL) at 0 ℃ under N_2, and the obtained mixture was stirred at room temperature. To this mixture three portions of K_2CO_3 (393 mg, 2.8 mmol; 786 mg, 5.6 mmol; 786 mg, 5.6 mmol) were added at intervals of 3 h, 3h and 15 h. The reaction mixture was stirred another 24 h after the final addition, and then water and Et_2O were added. The resulting precipitate was filtered, washed with water and Et_2O, and dried in vacuum. Orange solid (1.24 g). **Yield:** 92%. **^{1}H NMR (500 MHz, DMSO-d_6) δ (ppm):** 7.75 (d, J = 7.8 Hz, 2H), 7.55 (d, J = 7.8 Hz, 2H), 7.34 – 7.23 (m, 4H).

1,1'-Dimethyl-2,2'-biimidazole (dMebiim).

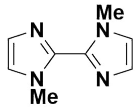

Synthesis of this ligand was as outlined in the literature.[180] 1*H*,1'*H*-2,2'-Biimidazole (l.0 equiv.) was added to a mixture of aqueous sodium hydroxide (5.6 equiv., 35% w/v) in DMF to give a concentration of 0.9 M. This was stirred for 1 h. The mixture turned green and then black over the course of the hour. Methyl iodide (3.0 equiv.) was then added slowly to the reaction mixture. The mixture was left to stir for 19 h at room temperature. The crude reaction mixture was then poured onto distilled water and extracted with chloroform multiple times. The combined organic layers were washed with water and dried over sodium sulfate. Filtration and evaporation under reduced pressure gave the crude product (0.29 g). Purification by flash column chromatography (silica, dichloromethane/ethanol gradient 100:0 to 95:5) afforded 0.19 g of the product as an off-white solid. **Yield:** 79%. $\mathbf{R}_f$**:** 0.25 (10% EtOAc/hexanes on silica). **Mp:** 117 – 118 ℃. ^{1}**H NMR (500 MHz, CDCl$_3$)** δ **(ppm):** 7.11 (s, 2H), 6.96 (s, 2H), 4.04 (s, 6H). ^{13}**C {^{1}H} NMR (126 MHz, CDCl$_3$)** δ **(ppm):** 128.0, 122.8, 35.5. Characterisation matches that previously reported, although only three ^{13}C signals could be detected.[180]

1,1'-(α,α'-*o*-Xylylene)-2,2'-biimidazole (*o*-Xylbiim).

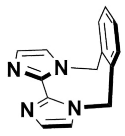

Synthesis of this ligand was as outlined in the literature.[190] To a solution containing α,α'-dibromo-*o*-xylene (1.0 equiv.) in acetonitrile (0.1 M) was added with stirring 1*H*,1'*H*-2,2'-biimidazole (1.2 equiv.) followed by aqueous sodium hydroxide (5.6 equiv., 35% v/w) solution. The temperature was increased to reflux, where after about 10 min a yellow-brown solution formed. The mixture was maintained at reflux overnight, before being cooled to room temperature. After addition of distilled water the mixture was extracted with multiple times with dichloromethane. The organic fractions were combined, dried over anhydrous magnesium sulfate and then evaporated to dryness under reduced pressure. The crude product was washed with portions of diethyl ether, affording 0.23 g of the pure compound as an off-white solid. **Yield:** 35%. **Mp:** 288 – 291 ℃. **Litt.:** 284 – 292 ℃.[180] **^{1}H NMR (500 MHz, DMSO-d_6) δ (ppm):** 7.47 (d, J = 1.0 Hz, 2H), 7.41 – 7.47 (m, 4H), 7.11 (d, J = 0.5 Hz, 2H), 4.97 (s, 4H). **^{13}C {^{1}H} NMR (126 MHz, DMSO-d_6) δ (ppm):** 139.4, 133.9, 130.1, 128.9, 128.7, 122.1, 49.0. Characterisation matches that previously reported.[179]

2,4-Dimethoxypyrimidine-5-boronic acid.

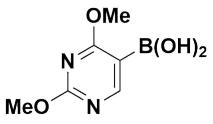

A 2-neck round bottom flask fitted with a magnetic stirrer, septum and stopcock was dried under vacuum and filled with argon. 5-bromo-2,4-dimethoxypyrimidine (2.00 g, 9.13 mmol, 1 equiv.) and dry THF (30 mL) were added to the reaction vessel, and the resulting solution cooled to −78 ℃. *n*-BuLi (2.5 M in hexanes, 4.75 mL, 11.9 mmol, 1.3 equiv.), was then added dropwise to the stirred solution. The resulting dark red solution was stirred at −78 ℃ for 1 h before the addition of $B(OMe)_3$ (1.42 g, 13.7 mmol, 1.5 equiv.). The resulting solution was allowed to warm to RT, and was then stirred under argon for 16 h. HCl (3 M, 40 mL) was then added slowly dropwise and the solution stirred for further 16 h. The reaction mixture was then neutralised by careful addition of Na_2CO_3 (1 M). The organic phase was extracted and the aqueous phase extracted with EtOAc. The organic phases were combined, dried over magnesium sulphate and the solvent removed under reduced pressure to yield a crude yellow solid which was carried forward.

2-[4-(*N*,*N*-dimethylamino)benzeneazo]imidazole, (azoimH).

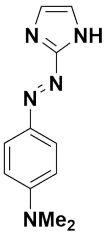

2-Aminoimidazole sulfate (0.54 g, 2.5 mmol) was dissolved in 8 ml HNO_3 (33% aqueous solution, v/v). A solution of $NaNO_2$ (0.35 g, 5.0 mmol) in H_2O (2 ml) was added dropwise to a salt/ice bath. The resultant solution was slowly run into a well-stirred solution of *N*,*N*-dimethylaniline (6.05 g, 50 mmol) in H_2O (25 mL). The solution was made alkaline with concentrated NH_3(aq) during which a bright red precipitate formed. The mixture was extracted with diethyl ether before recrystallizing from ethanol to give red crystals (0.56 g, 52%). **^{1}H NMR (500 MHz, MeOD) δ (ppm):** 7.87 (d, J = 9.1 Hz, 2H), 7.19 (s, 2H), 6.84 (d, J = 9.1 Hz, 2H), 3.13 (s, 6H). **^{13}C {^{1}H} NMR (126 MHz, MeOD) δ (ppm):** 157.0, 155.1, 144.9, 126.6, 113.0, 40.66. **MS EI**: **[M+H]$^+$ Calculated:** ($C_{11}H_{13}N_5$) 215.1; **Found:** 215.1. **Anal. Calc.:** ($C_{11}H_{13}N_5$): C 61.38, H 6.09, N 32.54. **Found:** C 61.15, H 6.24, N 32.66%.

6.3 Syntheses of Organometallic Complexes

6.3.1 μ-Chloro-Bridged Iridium Dimers

General procedure for synthesis of iridium dimers by Nonoyama's method

This procedure is a modified version of that originally reported by Nonoyama.[181] To a flask containing $IrCl_3.3H_2O$ (1.0 equiv.) and C^N ligand(2.2 equiv.) was added 2-ethoxyethanol and distilled water (3:1 v/v) to give a concentration of ca. 0.2 M. The mixture was degassed by repeatedly evacuating the flask, before backfilling with nitrogen. The mixture was heated to reflux, whereupon a yellow precipitate formed after 1 h. The mixture was refluxed for a further 18 h, before cooling. Water was added and the precipitate was collected by filtration. The solid was washed with multiple times with a mixture of water and ethanol (1:1 v/v) and then multiple times with a mixture of hexanes and diethyl ether (1:1 v/v), before drying to give the title compound.

General procedure for synthesis of iridium dimers using [Ir(COD)(Cl)]$_2$

This synthetic protocol is a modification of that reported in the literature.[185] A suspension of bis(1,5-cyclooctadiene)diiridium(I) dichloride (1.0 equiv.) in 2-ethoxyethanol was degassed via vigorous nitrogen bubbling. A solution of C^N ligand (4.0 equiv.) in 2-ethoxyethanol (ca. 1.8 M) was added to the reaction mixture to give a concentration of ca. 0.5 M and the mixture was degassed via nitrogen bubbling again. The reaction mixture was heated to reflux. After 30 min, the reaction mixture turned dark red/black. At 1 h, a precipitate had formed. After 3 h, the reaction mixture was cooled and MeOH was added. The precipitate was filtered, washed with MeOH and acetone, and then multiple times with a mixture of hexanes and diethyl ether (1:1 v/v), before drying to give the title compound.

Tetrakis[2-phenylpyridinato-$N,C^{2'}$]-bis(μ-chloro)diiridium(III), [Ir(ppy)$_2$(μ-Cl)]$_2$.

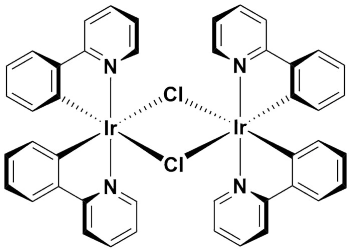

Preparation by Nonoyama's method: yellow powder **Yield:** 81%. **^{1}H NMR (500 MHz, CDCl$_3$) δ (ppm):** 9.26 (dd, J = 5.5, 1.0 Hz, 4H), 7.88 (d, J = 7.5 Hz, 4H), 7.76 (td, J = 7.5, 1.5 Hz, 4H), 7.51 (dd, J = 7.5, 1.5 Hz, 4H), 6.81 âĂŞ 6.75 (m, 8H), 6.58 (td, J = 7.5, 1.5 Hz, 4H), 5.95 (dd, J = 7.5, 1.0 Hz, 4H).

Tetrakis[2-(4',6'-difluorophenyl)-pyridinato-$N,C^{2'}$]-bis(μ-chloro)diiridium(III): [Ir(dFppy)$_2$(μ-Cl]$_2$.

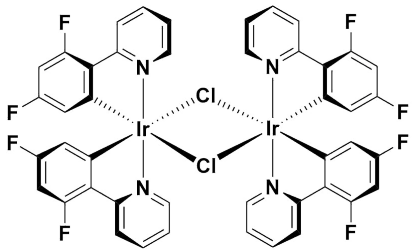

Yellow powder. Preparation by Nonoyama's method: **Yield:** 55%. Preparation using [Ir(COD)(Cl)]$_2$ precursor: **Yield:** 46%. **^{1}H {^{19}F} NMR (500 MHz, CD_2Cl_2)** δ **(ppm):** 9.12 (d, J = 5.0 Hz, 4H), 8.33 (d, J = 8.5 Hz, 4H), 7.88 (t, J = 7.0 Hz, 4H), 6.87 (td, J = 5.8, 1.0 Hz, 4H), 6.38 (td, J = 11.0, 2.0 Hz, 4H) 5.31 (dd, J = 9.3, 2.0 Hz, 4H). **^{19}F {^{1}H} NMR (471 MHz, CD_2Cl_2)** δ **(ppm):** -108.4 (d, J = 9.4 Hz, 4F), -110.6 (d, J = 9.4 Hz, 4F).

Tetrakis[2-(4',6'-dimethoxypyrmidyl)-4-methylpyridinato-$N,C^{2'}$]-bis(μ-chloro)diiridium(III): [Ir(Mepyrim)$_2$(μ-Cl)]$_2$.

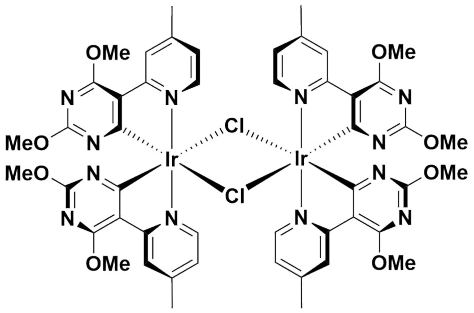

Yellow solid. Preparation using [Ir(COD)(Cl)]$_2$ precursor: **Yield:** 61%. **^{1}H NMR (400 MHz, CD_2Cl_2) δ (ppm):** 8.83 (d, J = 6.0 Hz, 4H), 8.16 (s, 4H), 6.56 (dd, J = 9.6, 2.0 Hz, 4H), 3.98 (s, 12H), 3.41 (s, 12H) 2.62 (s, 12H).

Tetrakis[2-(4',6'-dimethoxypyrmidyl)-5-trifluoromethylpyridinato-$N,C^{2'}$]-bis(μ-chloro)diiridium(III): [Ir(CF_3pyrim)$_2$(μ-Cl]$_2$.

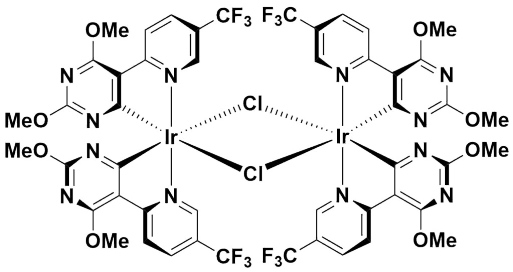

Yellow solid. Preparation using [Ir(COD)(Cl)]$_2$ precursor: **Yield:** 57%. **^{1}H NMR (400 MHz, CD_2Cl_2) δ (ppm):** 9.41 (dd, J = 1.6 0.8 Hz, 4H), 8.46 (dd, J = 8.8, 0.4 Hz, 4H), 7.96 (dd, J = 9.2, 2.0 Hz, 4H), 4.00 (s, 12H), 3.33 (s, 12H). **^{19}F {^{1}H} NMR (371 MHz, CD_2Cl_2) δ (ppm):** -62.4 (s, 12F).

Tetrakis[2-(phenyl)-4-(2,4,6-trimethylphenyl)pyridinato-$N, C^{2'}$]-bis(μ-chloro)diiridium(III): [Ir(Mesppy)$_2$(μ-Cl)]$_2$.

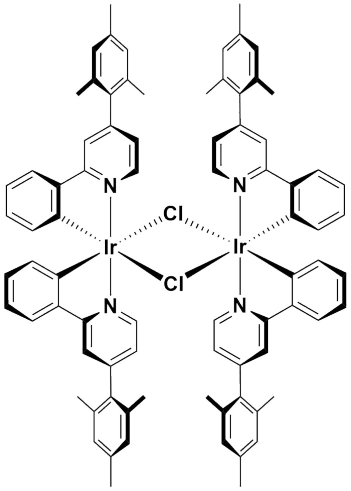

Yellow powder. Preparation using [Ir(COD)(Cl)]$_2$ precursor: **Yield:** 72%. **^{1}H NMR (500 MHz, CD_2Cl_2)** δ **(ppm):** 9.66 (d, J = 5.8 Hz, 4H), 7.74 (d, J = 1.8 Hz, 4H), 7.50 (dd, J = 7.8, 1.3 Hz, 4H), 7.01 (d, J = 14.0 Hz, 8H), 6.84 âĂŞ 6.80 (m, 8H), 6.67 (ddd, J = 8.3, 7.1, 1.4, 4H), 5.91 (dd, J = 7.9, 1.1 Hz, 4H), 2.38 (s, 12H), 2.12 (s, 12H), 2.11 (s, 12H).

Tetrakis[2-(4',6'-difluorophenyl)-4-(2,4,6-trimethylphenyl)pyridinato-$N,C^{2'}$]-bis(μ-chloro)diiridium(III): [Ir(dFMesppy)$_2$(μ-Cl)]$_2$.

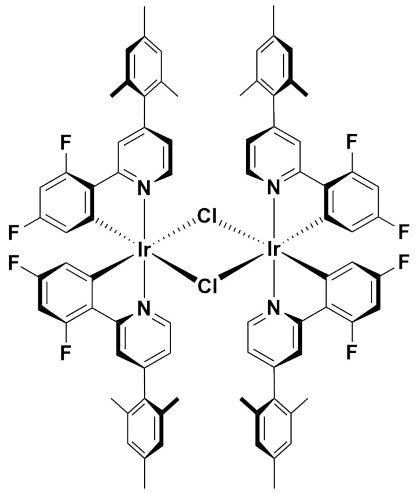

Yellow powder. Preparation using [Ir(COD)(Cl)]$_2$ precursor: **Yield:** 81%. **^{1}H {^{19}F} NMR (400 MHz, CD_2Cl_2)** δ **(ppm):** 9.57 (d, J = 5.6 Hz, 4H), 8.13 (d J = 1.2 Hz, 4H), 7.01 (d, J = 10.0 Hz, 8H), 6.89 (dd, J = 6.0, 2.0 Hz, 4H), 6.38 (d, J = 2.4 Hz, 4H), 5.28 (d, J = 2.4 Hz, 4H), 2.38 (s, 12H), 2.12 (s, 12H), 2.10 (s, 12H). **^{19}F {^{1}H} NMR (471 MHz, CD_2Cl_2)** δ **(ppm):** -108.07 (d, J = 11.13 Hz, 4F), -110.22 (d, J = 7.42 Hz, 4F).

Tetrakis[2-(napthalen-1-yl)-4-(2,4,6-trimethylphenyl)pyridinato-N, C^2']-bis(μ-chloro)diiridium(III): [Ir(Mesnpy)$_2$(μ-Cl)]$_2$.

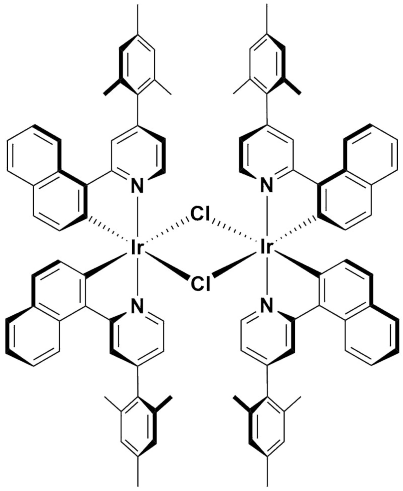

Orange powder. Preparation using Nonoyama's method: **Yield:** 70%. **^{1}H NMR (500 MHz, CD_2Cl_2)** δ **(ppm):** 9.76 (d, J = 5.7 Hz, 4H), 8.46 (d, J = 5.7 Hz, 4H), 8.35 (s, 4H), 7.59 (d, J = 7.9 Hz, 4H), 7.39 (t, J = 7.8 Hz, 4H), 7.22 (t, J = 7.4 Hz, 4H), 7.11 (s, 4H), 7.05 (s, 4H), 7.00 (d, J = 8.6 Hz, 4H), 6.93 (d, J = 5.8 Hz, 4H),5.85 (d, J = 8.6 Hz, 4H), 2.41 (s, 12H), 2.35 (s, 12H), 2.14 (s, 12H).

6.3.2 Iridium Complex Reactions

General Procedure for Synthesis of [Ir(C^N)$_2$(N^N)](PF$_6$) Complexes

To a round bottom flask containing the appropriate dichloro-bridged iridium dimer (1.0 equiv.) and N^N ligand (2.2 equiv.) were added DCM and MeOH (1:1 v/v) to give a suspension with a concentration of ca. 0.02 M. The mixture was degassed via bubbling with N_2 for 10 min, before the reaction vessel was sealed. The reaction mixture was heated to 40 ℃ for 19 h. The solution was cooled to room temperature, and the solvent evaporated. The crude product was purified by flash column chromatography, and the appropriate fractions were collected and the solvent evaporated. This material was dissolved in the minimum volume of MeOH, and added dropwise to vigorously stirring aqueous NH_4PF_6 (1 g / 10 mL). The fine precipitate that formed was left under continuous stirring for 3 h, until the precipitate had sufficiently aggregated. The material was filtered, washed with water and a mixture of hexanes and diethyl ether (1:1 v/v), before drying to give the title compound.

Silver Assisted Synthesis of [Ir(C^N)$_2$(N^N)](PF$_6$) Complexes

To a round bottom flask containing the appropriate dichloro-bridged iridium dimer (1.0 equiv.) and $AgPF_6$ (2.1 equiv.) were added DCM and MeOH (1:1 v/v) to give a suspension with a concentration of ca. 0.15 M. The mixture was degassed via bubbling with N_2 for 10 min, before the reaction vessel was sealed. The reaction mixture was stirred at room temperature in the dark for 3 h. The suspension was filtered through celite and then evaporated to dryness. DCM and the N^N ligand (2.1 equiv.) were added the reaction mixture was stirred at room temperature for a further 3 h. The reaction mixture was evaporated to dryness, before purifying by column chromatography. The fractions were combined, evaporated to dryness and then redissolved in the minimum of DCM. The solutions were cooled to 0 ℃ and then excess hexane was added with stirring until the complexes precipitated. Filtration and drying afforded the title compounds.

Bis[2-phenylpyridinato-$N,C^{2\prime}$]-N,N-(4-((1H-imidazol-2-yl)diazenyl) -dimethylaniline)iridium(III) hexafluorophosphate, [Ir(ppy)$_2$(azoimH)](PF$_6$).

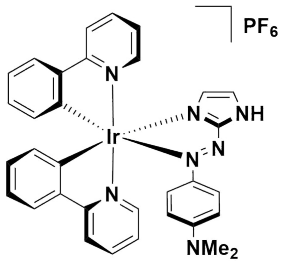

The synthesis of this complex is a modification of the usual method. Upon cooling the solution to room temperature, the crude mixture was evaporated to dryness. The solid was then dissolved in the minimum of MeOH, and added dropwise to an aqueous solution of NH_4PF_6 (10 mL, 1 g/10 mL) with the compound precipitating immediately. Following complete compound addition, the suspension was immersed in a water bath at 0 ℃ and maintained at this temperature for 1 h. The mixture was filtered and washed vigorously with distilled water and Et_2O. The crude material was then recrystallised by dissolving in the minimum of DCM and precipitating with the addition of $^iPr_2O$. Filtration and drying gave the compound as a dark purple solid (0.060 g). Crystals of suitable X-ray quality were grown from slow evaporation of a mixed acetone/heptanes solution. **Yield:** 75%. **Mp:** 159.0 ℃. **R$_f$:** 0.35 (silica, DCM/MeOH, 95:5). **^{1}H NMR (500 MHz, CD$_3$CN) δ (ppm):** 8.04 (t, J = 8.5 Hz, 2H), 8.00 (d, J = 8.0 Hz, 1H), 7.88 (td, J = 7.5, 1.5 Hz, 1H), 7.84 (td, J = 7.5, 1.5 Hz, 1H), 7.75 – 7.72 (m, 4H), 7.48 (d, J = 1.5 Hz, 1H), 7.47 – 7.46 (m, 1H), 7.12 – 7.07 (m, 2H), 7.02 – 6.98 (m, 2H), 6.92 (td, J = 7.5, 1.5 Hz, 1H), 6.84 (td, J = 7.5, 1.5 Hz, 1H), 6.48 (d, J = 1.5 Hz, 1H), 6.38 (d, J = 9.5 Hz, 2H), 6.31 (dd, J = 7.5, 0.5 Hz, 1H), 6.03 (dd, J = 7.5, 1.0 Hz, 1H), 3.04 (s, 6H). **^{13}C {^{1}H} NMR (126 MHz, CD$_3$CN) δ (ppm):** 168.5, 167.5, 161.6, 155.5, 153.5, 151.8, 150.0, 145.0, 144.6, 144.5, 144.2, 139.5, 132.4, 131.6, 131.2, 130.9, 129.0, 127.4, 125.7, 125.3, 124.9, 124.2, 124.1, 123.7, 123.2, 120.8, 120.6, 112.6, 68.7, 40.5, 23.1. **HR-MS** (FTMS$^+$): **[M-PF$_6$]$^+$ Calculated:** ($C_{33}H_{29}N_7Ir$) 716.2110; **Found:** 716.2094.

Bis[2-phenylpyridinato-$N,C^{2\prime}$]-N,N-(4-((1H-imidazolide)diazenyl)-dimethyl aniline)iridium(III), [Ir(ppy)$_2$(azoim)].

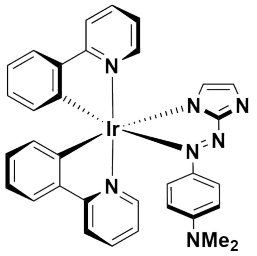

The synthesis of this complex is a modification of the usual method, with the additional use of K_2CO_3 (2.4 equiv.) in the reaction mixture. Upon cooling the solution to room temperature, the crude mixture was evaporated to dryness. The solid was then dissolved in DCM, water was added and the layers were separated. The aqueous layer was extracted multiple times with DCM and then the organic fractions were combined. The organic layer was dried over Na_2SO_4, filtered and evaporated to give a crude product. This product was then recrystallised by dissolving in the minimum of DCM and precipitating with the addition of Et_2O. Filtration and drying gave the compound as a red solid (0.073 g). Crystals of suitable X-ray quality were grown from vapour diffusion of diethyl ether into a concentrated solution of the material in DCM. **Yield:** 82%. **Mp:** 293.1 ℃. **^{1}H NMR (500 MHz, CD_3CN) δ (ppm):** 8.15 (d, J = 6.0 Hz, 1H), 8.00 (d, J = 8.0 Hz, 1H), 7.92 (d, J = 8.5 Hz, 1H), 7.81 (td, J = 7.5, 1.5 Hz, 1H), 7.76 (td, J = 6.5, 1.5, 1H), 7.77 (d, J = 7.5 Hz, 1H), 7.67 (d, J = 7.0 Hz, 1H), 7.50 – 7.47 (m, 2H), 7.42 (s, 1H), 7.36 (d, J = 5.5 Hz, 1H), 7.07 – 7.01 (m, 2H), 6.95 – 6.90 (m, 2H), 6.86 (dd, J = 7.5, 1.0, 1H), 6.79 (dd, J = 7.5, 1.0 Hz, 1H), 6.40 (s, 1H), 6.38 (d, J = 7.0 Hz, 1H), 6.35 – 6.31 (m, 2H) 6.08 (d, J = 7.5 Hz, 1H), 2.88 (s, 6H). **^{13}C {^{1}H} NMR (126 MHz, CD_3CN) δ (ppm):** 151.0, 148.6, 144.2, 143.9, 137.8, 137.7, 137.6, 131.9, 130.8, 129.8, 129.5, 129.3, 124.8, 124.5, 124.0, 123.4, 122.8, 121.8, 121.2, 121.1, 119.4, 119.1, 110.9, 39.4. **HR-MS** (APCI$^+$): **[M+H]$^+$ Calculated:** ($C_{33}H_{28}N_7Ir$) 716.2110; **Found:** 712.2111.

Bis[2-(4',6'-difluorophenyl)-pyridinato-$N,C^{2'}$]-N,N'-(4,4'-di-*tert*-butyl-2,2'-bipyridine)iridium(III) hexafluorophosphate: [Ir(dFppy)$_2$(dtbubpy)](PF$_6$).

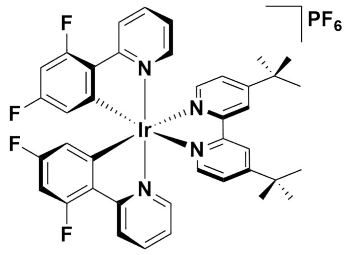

Synthesised using the general method. Yellow powder (0.116 g). **Yield:** 72%. **^{1}H {^{19}F} NMR (400 MHz, CD$_2$Cl$_2$) δ (ppm):** 8.33 (d, J = 8.0, Hz, 2H), 8.31 (d, J = 1.6 Hz, 2H), 7.90 (d, J = 5.6 Hz, 2H), 7.85 (td, J = 8.0, 1.6 Hz, 2H), 7.50 (d, J = 7.5 Hz, 4H), 7.07 (td, J = 5.6, 1.2 Hz, 2H), 6.61 (d, J = 2.0 Hz, 2H), 5.73 (d, J = 2.4 Hz, 2H), 1.44 (s, 18H). **^{13}C {^{1}H} NMR (126 MHz, CD$_2$Cl$_2$) δ (ppm):** 165.2, 165.1, 164.7, 164.6, 163.1, 163.0, 163.0, 162.9, 160.9, 160.8, 156.6, 154.5, 154.4, 150.5, 149.1, 139.5, 128.1, 126.3, 124.3, 124.1, 124.00, 121.8, 114.3, 114.2, 99.5, 99.3, 99.1, 36.1, 30.3. **^{19}F {^{1}H} NMR (371 MHz, CD$_2$Cl$_2$) δ (ppm):** -73.33 (d, J = 697.5 Hz, 6F), -106.46 (d, J = 11.1 Hz, 2F), -108.98 (d, J = 11.1 Hz, 2F). **HR-MS** (FTMS$^+$): **[M-PF$_6$]$^+$ Calculated:** ($C_{40}H_{36}N_4F_4Ir$) 841.2481; **Found:** 841.2502. **Anal. Calc.:** ($C_{40}H_{36}N_4F_{10}IrP$ (MW 985.93): C 48.73, H 3.68, N 5.68. **Found:** C 48.76, H 3.79, N 5.64% (average of two runs).

Bis[2-(4',6'-difluorophenyl)-pyridinato-$N,C^{2'}$]-$N^2,N^{2'}$-(1H,1'H-2,2'-biimidazole) iridium(III) hexafluorophosphate, [Ir(dFppy)$_2$(H$_2$biim)](PF$_6$).

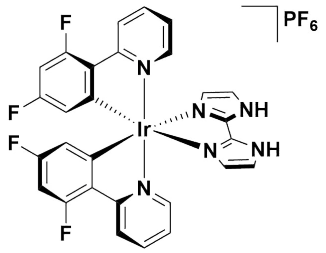

Synthesised using the general method. Yellow powder (0.094 g). **Yield:** 80%. **Mp:** 310 – 311 ℃. **^{1}H {^{19}F} NMR (500 MHz, DMSO-d_6) δ (ppm):** 8.24 (d, J = 8.5 Hz, 2H), 8.0 (td, J = 7.8, 1.5 Hz, 2H), 7.72 (d, J = 5.5 Hz, 2H), 7.45 (s, 2H), 7.28 (td, J = 7.0, 1.0 Hz, 2H), 6.84 (dd, J = 8.8, 2.0 Hz, 2H), 6.55 (d, J = 1.0 Hz, 2H), 5.66 (dd, J = 8.0, 2.5 Hz, 2H). **^{19}F {^{1}H} NMR (471 MHz, DMSO-d_6) δ (ppm):** -70.09 (d, J = 712.2 Hz, 6F), -107.72 (d, J = 9.9 Hz, 2F), -109.7 (d, J = 9.9 Hz, 2F). **HR-MS** (ES-Q-TOF): **[M-PF$_6$]$^+$ Calculated:** ($C_{28}H_{18}N_6F_4Ir$) 707.1158; **Found:** 707.1130.

Bis[2-(4',6'-difluorophenyl)-pyridinato-$N,C^{2'}$]-$N^2,N^{2'}$-(1,1'-dimethyl-2,2'-biimidazole)iridium(III) hexafluorophosphate, [Ir(dFppy)$_2$(dMebiim)](PF$_6$).

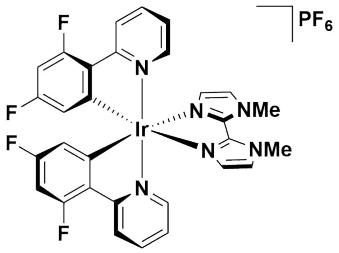

Synthesised using the general method. Yellow powder (0.062 g). **Yield:** 54%. **Mp:** 3225 – 326 ℃. **^{1}H {^{19}F} NMR (500 MHz, DMSO-d_6) δ (ppm):** 8.25 (d, J = 7.5 Hz, 2H), 8.03 (t, J = 7.8 Hz, 2H), 7.74 (d, J = 6.0 Hz, 2H), 7.53 (d, J = 1.5 Hz, 2H), 7.33 (td, J = 1.0, 6.5 Hz, 2H), 6.87 (t, J = 6.0 Hz, 2H) 6.50 (d, J = 1.5 Hz, 2H), 5.63 (dd, J = 8.0, 2.5 Hz, 2H) 4.22 (s, 6H). **^{19}F {^{1}H} NMR (471 MHz, DMSO-d_6) δ (ppm):** -70.14 (d, J = 712.2 Hz, 6F), -107.75 (d, J = 9.9, 2F), -109.77 (d, J = 9.9, 2F). **HR-MS** (ES-Q-TOF): **[M-PF$_6$]$^+$ Calculated:** ($C_{30}H_{22}N_6F_4Ir$) 735.1471; **Found:** 735.1442.

Bis[2-(4',6'-difluorophenyl)-pyridinato-$N,C^{2'}$]-$N^2,N^{2'}$-(1,1'-(α,α'-*o*-Xylylene)-2,2'-biimidazole)iridium(III) hexafluorophosphate, [Ir(dFppy)$_2$(*o*-Xylbiim)](PF$_6$).

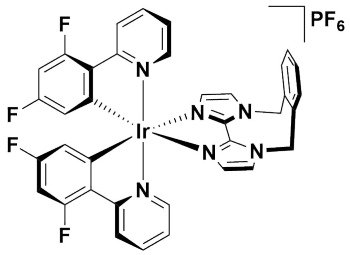

Synthesised using the general method. Yellow powder (0.072 g). **Yield:** 83%. **Mp:** 359 – 360 ℃. **^{1}H {^{19}F} NMR (500 MHz, DMSO-d_6, 372 K) δ (ppm):** 8.22 (d, J = 8.0 Hz, 2H), 7.97 (t, J = 7.5 Hz, 2H), 7.76 (d, J = 1.0 Hz, 2H), 7.69 – 7.57 (m, 3H), 7.56 – 7.46 (m, 3H), 7.17 (s, br, 2H), 6.79 – 6.73 (m, 2H), 6.51 (d, J = 1.0 Hz, 2H), 5.86 (s, br, 4H), 5.67 – 5.64 (m, 2H). **^{19}F {^{1}H} NMR (471 MHz, DMSO-d_6) δ (ppm):** -70.13 (d, J = 712.2 Hz, 6F), -107.60 (m, 2F), -109.7 (m, 2F). **HR-MS** (ES-Q-TOF): **[M-PF$_6$]$^+$ Calculated:** ($C_{36}H_{24}N_6F_4Ir$) 809.1628; **Found:** 809.1597.

Bis[2-(4',6'-dimethoxy-3',5'-pyrimidyl)-4-methylpyridinato-$N,C^{2'}$]-N,N'-(4,4'-di-*tert*-butyl-2,2'-bipyridine)iridium(III) hexafluorophosphate: [Ir(Mepypyrm)$_2$(dtbubpy)](PF$_6$).

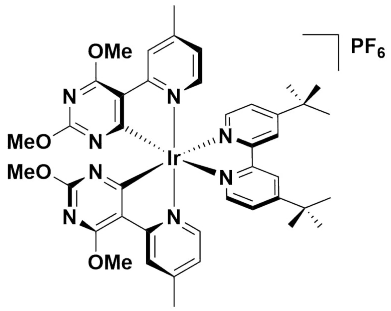

Synthesis was a deviation from the general method. After the reaction was completed, the solution was evaporated, before DCM and excess Et_2O until a precipitate formed. This precipitate was filtered, before washing first with water to dissolve any salt residues, and then again with excess ether. The product was then dissolved in the minimum of MeCN, and crystallised from solution by slow evaporation of Et_2O. Off-white solid (0.076 g). **Yield:** 98%. **^{1}H NMR (500 MHz, CD_3CN) δ (ppm):** 8.49 (d, J = 1.5, Hz, 2H), 8.20 (s, 2H), 7.97 (d, J = 6.0 Hz, 2H), 7.52 (dd, J = 6.0, 2.0 Hz, 2H), 7.39 (d, J = 6.0 Hz, 2H), 6.79 (dd, J = 6.0, 2.0 Hz, 2H), 4.06 (s, 6H), 3.61 (s, 6H), 2.45 (s, 18H), 1.41 (s, 18H). **^{13}C {^{1}H} NMR (126 MHz, CD_2Cl_2) δ (ppm):** 189.8, 166.4, 165.5, 163.5, 156.0, 151.6, 149.4, 126.3, 122.8, 123.4, 122.9, 119.8, 118.3, 54.8, 54.2, 36.5, 30.3, 21.4. **HR-MS** (FTMS$^+$): **[M-PF$_6$]$^+$ Calculated:** ($C_{42}H_{48}N_8O_4Ir$) 921.3425; **Found:** 921.3402. **Anal. Calc.:** ($C_{42}H_{48}N_8F_6O_4IrP$ (MW 1066.08): C 47.32, H 4.54, N 10.51. **Found:** C 47.14, H 4.47, N 10.40% (average of two runs).

Bis[2-(4',6'-dimethoxy-3',5'-pyrimidyl)-4-methylpyridinato-N,C^2']-N^2,N^2'-(1,1'-(α,α'-*o*-Xylylene)-2,2'-biimidazole)iridium(III) hexafluorophosphate: [Ir(Mepyrim)$_2$(*o*-Xylbiim)](PF$_6$).

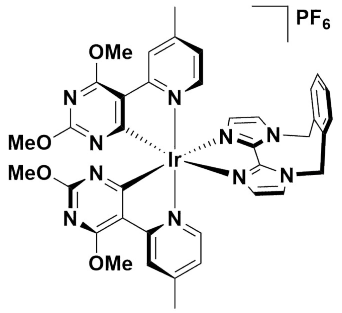

Synthesis was a deviation from the general method. After the reaction was completed, the solution was evaporated, before DCM and excess$_2$O until a precipitate formed. This precipitate was filtered, before washing first with water to dissolve any salt residues, and then again with excess ether. The product was then dissolved in the minimum of MeCN, and crystallised from solution by slow evaporation of Et$_2$O. Off-white powder (0.050 g). **Yield:** 67%. **^{1}H NMR (500 MHz, DMSO-d_6, 363 K) δ (ppm):** 8.08 (s, 2H), 7.76 (d, J = 1.5 Hz, 2H), 7.63 (t, J = 3.5 Hz, 2H), 7.46 (dd, J = 5.5, 3.5 Hz, 2H), 7.33 (br s, 2H), 6.85 (br s, 2H), 6.69 (br s, 2H), 5.85 (br s, 4H), 4.06 (s, 6H), 3.60 (s, 6H), 2.45 (s, 6H). **^{13}C {^{1}H} NMR (126 MHz, CD$_2$Cl$_2$) δ (ppm):** 206.9, 187.8, 165.5, 163.3 (C^a), 163.1 (C^b), 162.5, 149.9 (C^a), 149.7 (C^b), 149.1 (C^a) 148.8 (C^b), 139.7, 133.9 (C^a) 133.7 (C^b), 131.6, 131.3, 128.0, 126.0 (C^a), 125.6 (C^b), 122.9, 122.7 (C^a) 122.1 (C^b), 119.6 (C^a) 119.5 (C^b), 51.2, 31.0, 21.6. **HR-MS** (FTMS$^+$): **[M-PF$_6$]$^+$ Calculated:** (C$_{38}$H$_{36}$N$_{10}$O$_4$Ir) 889.2545; **Found:** 889.2536. **Anal. Calc.:** (C$_{38}$H$_{36}$N$_{10}$F$_6$O$_4$IrP (MW 1033.95): C 44.14, H 3.51, N 13.55. **Found:** C 44.20, H 3.45, N 13.61% (average of two runs).

Bis[2-(4',6'-dimethoxy-3',5'-pyrimidyl)-5-trifluoromethylpyridinato-$N,C^{2'}$]-N,N'-(4,4'-di-*tert*-butyl-2,2'-bipyridine)iridium(III) hexafluorophosphate: [Ir(CF_3pypyrm)$_2$(dtbubpy)](PF_6).

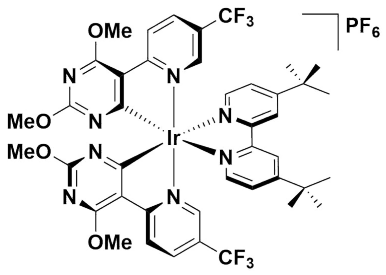

Synthesis was a deviation from the general method. After the reaction was completed, the solution was evaporated, before DCM and excess Et_2O until a precipitate formed. This precipitate was filtered, before washing first with water to dissolve any salt residues, and then again with excess ether. The product was then dissolved in the minimum of MeCN, and crystallised from solution by slow evaporation of Et_2O. Pale yellow solid (0.070 g). **Yield:** 95%. **^{1}H {^{19}F} NMR (500 MHz, CD_2Cl_2) δ (ppm):** 8.52 (d, J = 2.0, Hz, 2H), 8.50 (s, 2H), 8.08 (dd, J = 9.0, 2.0 Hz, 2H), 8.04 (d, J = 5.5 Hz, 2H), 7.69 (s 2H), 7.60 (dd, J = 5.6, 1.6 Hz, 2H), 4.06 (s, 6H), 3.54 (s, 6H), 1.43 (s, 18H). **^{13}C {^{1}H} NMR (126 MHz, CD_2Cl_2) δ (ppm):** 189.8, 167.3, 166.7, 165.2, 163.3, 155.5, 151.0, 145.9, 135.7, 125.6, 123.7, 123.1, 122.8, 122.4, 122.2, 121.5, 118.0, 54.1, 53.7, 35.6, 29.4. **^{19}F {^{1}H} NMR (371 MHz, CD_2Cl_2) δ (ppm):** -63.30 (s, 6F), -72.92 (d, J = 697.5 Hz, 6F). **HR-MS** (FTMS$^+$): **[M-PF_6]$^+$ Calculated:** ($C_{42}H_{42}N_8F_6O_4Ir$) 1029.2859; **Found:** 1029.2863. **Anal. Calc.:** ($C_{42}H_{42}N_8F_{12}O_4IrP$ (MW 1174.02): C 42.97, H 3.61, N 9.54. **Found:** C 42.93, H 3.44, N 9.34% (average of two runs).

Bis[2-(4',6'-dimethoxy-3',5'-pyrimidyl)-5-trifluoromethylpyridinato-$N,C^{2'}$]-$N^2,N^{2'}$-(1,1'-(α,α'-*o*-Xylylene)-2,2'-biimidazole)iridium(III) hexafluorophosphate: [Ir(CF_3pypyrm)$_2$(*o*-Xylbiim)](PF_6).

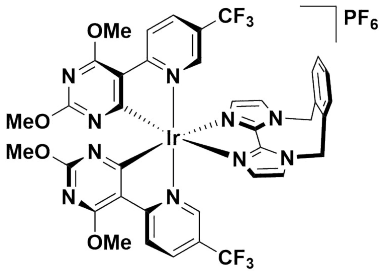

Synthesis was a deviation from the general method. After the reaction was completed, the solution was evaporated, before DCM and excess H_2O until a precipitate formed. This precipitate was filtered, before washing first with water to dissolve any salt residues, and then again with excess ether. The product was then dissolved in the minimum of MeCN, and crystallised from solution by slow evaporation of Et_2O. Pale yellow powder (0.050 g). **Yield:** 70%. **^{1}H (500 MHz, DMSO-d_6, 372 K) δ (ppm):** 8.05 (s, 2H), 7.74 (d, J = 1.0 Hz, 2H), 7.62 (t, J = 4.0 Hz, 2H), 7.49 (dd, J = 5.5, 3.5 Hz, 2H), 7.38 (br s, 2H), 6.83 (br s, 2H), 6.64 (d, J = 1.5 Hz, 2H), 5.82 (br s, 4H), 4.01 (s, 6H), 3.53 (s, 6H). **^{13}C {^{1}H} NMR (126 MHz, CD_3CN) δ (ppm):** 207.4, 189.8, 168.3 (C^a), 168.1 (C^b), 167.4, 163.9, 148.0 (C^a), 146.9 (C^b), 141.1 (C^a) 140.9 (C^b), 136.2 (C^a) 136.0 (C^b), 134.9, 131.8, 131.70, 128.2, 127.8 (C^a), 127.4 (C^b), 126.8, 124.5, 122.5, 54.9, 54.4, 51.1. **^{19}F {^{1}H} NMR (371 MHz, CD_2Cl_2) δ (ppm):** -62.97 (s, 3F), -63.39, (s, 3F), -72.92 (d, J = 697.5 Hz, 6F). **HR-MS** (FTMS$^+$): **[M-PF_6]$^+$ Calculated:** ($C_{38}H_{30}N_{10}F_6O_4Ir$) 997.1980; **Found:** 997.1955. **Anal. Calc.:** ($C_{38}H_{30}N_{10}F_{12}O_4IrP$ (MW 1141.90): C 39.97, H 2.65, N 12.27. **Found:** C 40.25, H 3.01, N 12.40% (average of two runs).

Bis[2-(phenyl)-4-(2,4,6-trimethylphenyl)pyridinato-$N,C^{2\,\prime}$]-N,N'-(1H,1'H-2,2'-bibenzimidazole)iridium(III) hexafluorophosphate, [Ir(Mesppy)$_2$(H$_2$bibenz)](PF$_6$).

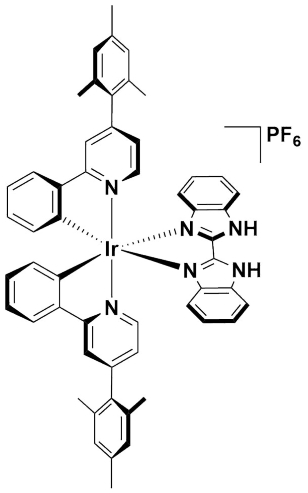

Synthesised using the silver method. Yellow solid (0.055 g). **Yield:** 60%. **Mp:** 331 – 333 ℃ (decomp.). **R$_f$:** 0.63 (silica, DCM/MeOH, 9:1). **^{1}H NMR (500 MHz, CD$_2$Cl$_2$)** δ **(ppm):** 11.55 (s, br 2H), 7.75 – 7.68 (m, 8H), 7.42 (t, J = 7.7 Hz, 2H), 7.08 – 7.15 (m, 4H), 7.01 (t, J = 7.4 Hz, 2H), 6.97 (s, 2H), 6.91 (s, 2H), 6.75 (dd, J = 5.9, 1.6 Hz, 2H), 6.55 (d, J = 7.4 Hz, 2H), 6.42 (d, J = 8.4 Hz, 1H), 2.30 (s, 6H), 2.10 (s, 6H), 1.87 (s, 6H). **^{13}C {^{1}H} NMR (126 MHz, CD$_2$Cl$_2$)** δ **(ppm):** 168.5, 151.9, 149.8, 147.8, 145.4, 144.3, 141.0, 138.5, 135.5, 135.5, 135.4, 134.6, 132.5, 130.3, 128.8, 128.7, 126.9, 125.0, 124.9, 122.7, 121.0, 118.4, 113.8, 21.1, 20.7. **HR-MS** (FTMS$^+$): **[M-PF$_6$]$^+$ Calculated:** ($C_{54}H_{46}N_6Ir$) 971.3412; **Found:** 971.3408. **Anal. Calc.:** ($C_{54}H_{46}N_6F_6IrP$ (MW 1116.19): C, 58.11; H, 4.15; N, 7.53. **Found:** C, 57.98; H, 4.16; N, 7.51% (average of two runs).

Bis[2-(phenyl)-4-(2,4,6-trimethylphenyl)pyridinato-$N,C^{2'}$]-N,N'-(1,1'-(α,α'-*o*-Xylylene)-2,2'-bibenzimidazole)iridium(III) hexafluorophosphate, [Ir(Mesppy)$_2$(*o*-Xylbibenz)](PF$_6$).

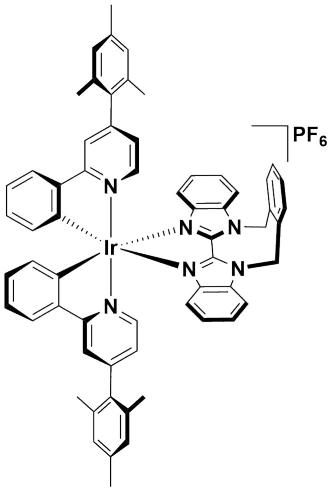

Synthesised using the silver method. Yellow solid (0.044 g). **Yield:** 62%. **Mp:** 264 – 267 ℃ (decomp.). **R$_f$:** 0.57 (silica, DCM/MeOH, 9:1). **^{1}H NMR (500 MHz, DMSO-d_6, 372 K) δ (ppm):** 8.36 (d, J = 8.5 Hz, 2H), 7.92 – 7.88 (m, 4H), 7.71 (dd, J = 5.6, 3.4 Hz, 2H), 7.57 – 7.50 (m, 4H), 7.45 (dd, J = 5.7, 3.3 Hz, 2H), 7.10 (t, J = 8.0 Hz, 2H), 7.05 (t, J = 8.0 Hz, 2H), 6.98 – 6.89 (m, 6H), 6.75 (dd, J = 6.0, 1.9 Hz, 2H), 6.40 (dd, J = 7.6, 1.2 Hz, 2H), 6.36 (d, J = 8.4 Hz, 2H), 6.24 (d, J = 3.0 Hz, 2H), 2.28 (s, 3H), 1.89 (br s, 12H). **^{13}C {^{1}H} NMR (126 MHz, CD$_2$Cl$_2$) δ (ppm):** 168.3, 151.8, 149.6, 149.0, 145.1, 144.9, 140.6, 138.5, 136.2, 135.5, 135.3, 134.5, 132.3, 131.3, 131.3, 130.3, 128.8, 128.7, 127.1, 126.0, 124.9, 122.7, 121.0, 119.2, 111.6, 47.5, 21.1, 20.7, 20.6. **HR-MS** (FTMS$^+$): **[M-PF$_6$]$^+$ Calculated:** ($C_{62}H_{52}N_6Ir$) 1073.3882; **Found:** 1073.3873. **Anal. Calc.:** ($C_{62}H_{52}N_6F_6IrP$ (MW 1218.32): C, 61.12; H, 4.39; N, 6.90. **Found:** C, 61.14; H, 4.03; N, 6.84% (average of two runs).

Bis[2-(4',6'-difluorophenyl)-4-(2,4,6-trimethylphenyl)pyridinato-$N,C^{2'}$]-N,N'-(4,4'-di-*tert*-butyl-2,2'-bipyridine)iridium(III) hexafluorophosphate, [Ir(dFMesppy)$_2$(dtbubpy)](PF$_6$).

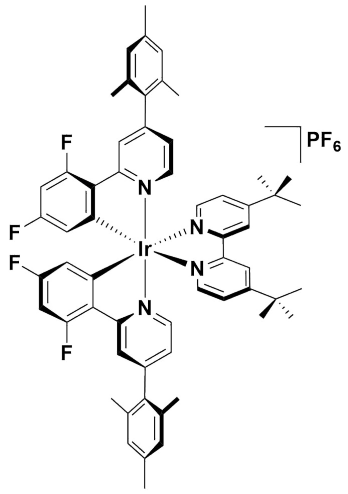

Synthesised using the general method. Yellow flakes (0.111 g). **Yield:** 77%. **^{1}H {^{19}F} NMR (400 MHz, CD_2Cl_2)** δ **(ppm):** 8.37 (d, J = 1.6, Hz, 2H), 8.14 (d, J = 1.6 Hz, 2H), 8.02 (d, J = 6.0 Hz, 2H), 7.55 (dd, J = 5.8, 2.4 Hz, 4H), 6.98 (d, J = 16.0 Hz, 4H), 6.91 (dd, J = 4.4, 2.0 Hz, 2H), 6.61 (d, J = 2.4 Hz, 2H), 5.77 (d, J = 2.0 Hz, 2H), 2.32 (s, 6H), 2.11 (s, 6H), 1.94 (s, 6H), 1.46 (s, 18H). **^{13}C {^{1}H} NMR (126 MHz, CD_2Cl_2)** δ **(ppm):** 165.3, 165.1, 165.1, 164.7, 164.7, 163.2, 163.1, 162.9, 162.8, 160.8, 160.7, 155.9, 154.6, 154.5, 153.6, 150.7, 149.0, 138.8, 135.3, 135.1, 135.1, 129.0, 128.9, 128.2, 126.3, 125.6, 125.5, 125.4, 121.9, 114.3, 114.1, 99.5, 99.3, 99.1, 36.1, 30.4, 21.2, 20.7, 20.5. **^{19}F {^{1}H} NMR (371 MHz, CD_2Cl_2)** δ **(ppm):** -73.34 (d, J = 719.7 Hz, 6F),-106.38 (d, J = 11.1 Hz, 2F), -108.65 (d, J = 11.1 Hz, 2F). **HR-MS** (FTMS$^+$): **[M-PF$_6$]$^+$ Calculated:** ($C_{58}H_{56}N_4F_4Ir$) 1077.4069; **Found:** 1077.4041. **Anal. Calc.:** ($C_{58}H_{56}N_4F_{10}IrP$ (MW 1222.29): C 56.99, H 4.62, N 4.58. **Found:** C 56.85, H 4.51, N 4.64% (average of two runs).

Bis[2-(4',6'-difluorophenyl)-4-(2,4,6-trimethylphenyl)pyridinato-N,C^2']-N^2,N^2'-(1,1'-(α,α'-*o*-Xylylene)-2,2'-biimidazole)iridium(III) hexafluorophosphate,

[Ir(dFMesppy)$_2$(*o*-Xylbiim)](PF$_6$).

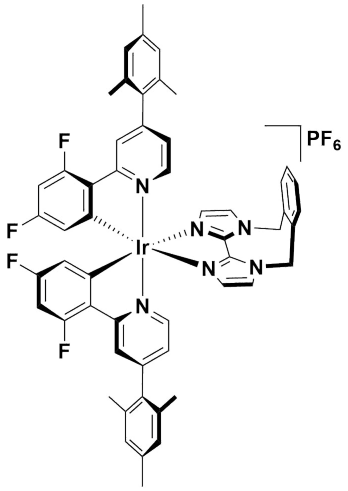

Synthesised using the general method. Yellow flakes (0.094 g). **Yield:** 66%. **^{1}H {^{19}F} NMR (500 MHz, DMSO-d_6, 372 K) δ (ppm):** 7.91 (s, 2H), 7.80 (s, 2H), 7.62 (t, J = 6.0 Hz, 2H), 7.46 (dd, J = 5.5, 3.5 Hz, 2H), 7.05 – 6.94 (m, 8H), 6.75 (td, J = 11.0, 2.0 Hz, 2H), 6.62 (s, 2H), 5.88 (s, 4H), 5.75 (dd, J = 8.8, 1.5 Hz, 2H), 2.31 (s, 6H), 1.99 (s, 12H). **^{13}C {^{1}H} NMR (126 MHz, CD$_2$Cl$_2$) δ (ppm):** 164.6, 164.6, 152.8, 152.7, 149.8, 148.7, 138.6, 138.6, 135.6, 135.4, 135.1, 134.1, 133.9, 131.5, 131.4, 128.8, 127.9, 127.8, 126.0, 125.7, 125.5, 124.9, 125.0, 124.6, 114.4, 114.2, 114.1, 98.8, 98.5, 98.3, 51.4, 51.3, 21.2, 20.6. **^{19}F {^{1}H} NMR (371 MHz, CD$_2$Cl$_2$) δ (ppm):** -72.83 (d, J = 701.2 Hz, 6F), -107.70 (d, J = 9.7 Hz, 1F), -108.36 (d, J = 9.7 Hz, 1F), -109.82 – -109.98 (m, 2F). **HR-MS** (FTMS$^+$): **[M-PF$_6$]$^+$ Calculated:** ($C_{55}H_{44}N_6F_4Ir$) 1045.3191; **Found:** 1045.3160. **Anal. Calc.:** ($C_{55}H_{44}N_6F_{10}IrP$ (MW 1190.16): C 54.50, H 3.73, N 7.06. **Found:** C 54.85, H 4.11, N 7.46% (average of two runs).

Bis[2-(naphthalen-1-yl)-4-(2,4,6-trimethylphenyl)pyridinato-*N*,C^2']-*N*,*N*'-(4,4'-di-*tert*-butyl-2,2'-bipyridine)iridium(III) hexafluorophosphate, [Ir(Mesnpy)$_2$(dtbubpy)](PF$_6$).

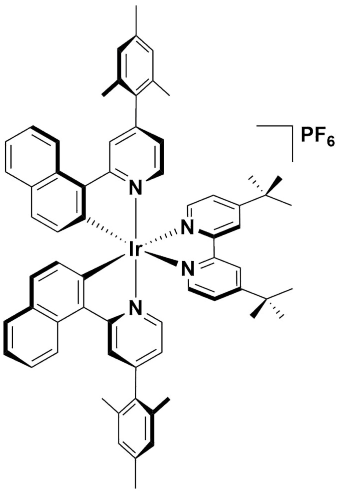

Synthesised using the silver method. Red solid (0.047 g). **Yield:** 62%. **Mp:** 372 – 374 ℃ (decomp.). **R$_f$:** 0.30 (silica, DCM/MeOH, 9:1). **^{1}H NMR (500 MHz, CD$_2$Cl$_2$) δ (ppm):** 8.45 (d, J = 8.7 Hz, 2H), 8.36 (dd, J = 7.4, 1.8 Hz, 4H), 7.88 (d, J = 5.9 Hz, 2H), 7.78 (dd, J = 8.1, 1.4, 2H), 7.72 (d, J = 5.8 Hz, 2H), 7.5 (ddd, J = 8.5, 6.8, 1.5 Hz, 2H), 7.42 (dd, J = 5.9 1.9 Hz, 2H), 7.38 (ddd, J = 8.0, 6.9, 1.0 Hz, 2H), 7.35 (d, J = 8.4 Hz, 2H), 7.03 (d, J = 9.0 Hz, 4H), 6.88 (dd, J = 5.9, 1.8 Hz, 2H), 6.39 (d, J = 8.3 Hz, 1H), 2.35 (s, 6H), 2.19 (s, 6H), 2.06 (s, 6H). **^{13}C {^{1}H} NMR (126 MHz, CD$_2$Cl$_2$) δ (ppm):** 168.9, 164.5, 155.9, 155.7, 155.3, 150.7, 149.4, 138.5, 137.7, 135.4, 135.2, 135.1, 131.8, 131.6, 130.5, 130.0, 129.9, 128.8, 128.7, 127.6, 125.8, 125.4, 124.0, 123.8, 121.7, 121.2, 35.8, 30.2, 21.0, 20.5. **HR-MS** (FTMS$^+$): **[M-PF$_6$]$^+$ Calculated:** ($C_{66}H_{64}N_4Ir$) 1105.4760; **Found:** 1105.4743. **Anal. Calc.:** ($C_{66}H_{64}N_4F_6IrP$ (MW 1250.45): C, 63.40; H, 5.16; N, 4.48. **Found:** C, 63.05; H, 5.19; N, 4.51% (average of two runs).

Bis[2-(naphthalen-1-yl)-4-(2,4,6-trimethylphenyl)pyridinato-$N,C^{2'}$]-N,N'-(2,2'-biquinoline)iridium(III) hexafluorophosphate, [Ir(Mesnpy)$_2$(biq)](PF$_6$).

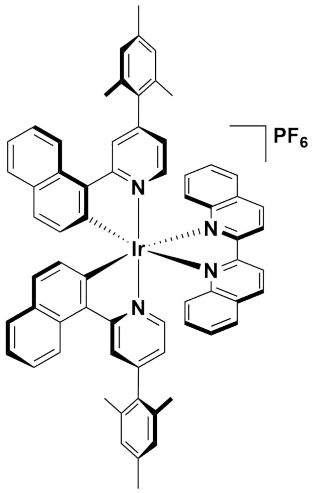

Synthesised using the silver method. Brick red solid (0.028 g). **Yield:** 37%. **Mp:** 231 – 232 ℃ (decomp.). **R$_f$:** 0.37 (silica, DCM/MeOH, 9:1). **^{1}H NMR (500 MHz, CD$_2$Cl$_2$)** δ **(ppm):** 8.76 – 8.69 (m, 4H), 8.28 (d, J = 8.6 Hz, 2H), 8.22 (d, J = 1.7 Hz, 2H), 7.98 – 7.86 (m, 6H), 7.75 (dd, J = 8.1, 1.4 Hz, 2H), 7.44 (t, J = 7.0 Hz, 4H), 7.38 – 7.31 (m, 4H), 7.02 – 6.90 (m, 6H), 6.72 (dd, J = 5.9, 1.7 Hz, 2H), 6.63 (d, J = 8.4 Hz, 4H), 2.31 (s, 6H), 2.19 (s, 6H), 1.75 (s, 6H). **^{13}C {^{1}H} NMR (126 MHz, CD$_2$Cl$_2$)** δ **(ppm):** 168.6, 160.0, 153.3, 152.5, 150.9, 148.5, 141.8, 138.7, 137.1, 135.4, 135.2, 135.2, 131.9, 131.8, 131.6, 130.7, 130.2, 130.0, 129.9, 129.5, 128.9, 128.9, 128.8, 128.3, 127.8, 125.4, 124.1, 123.1, 122.1, 121.8, 21.2, 20.8, 20.5. **HR-MS** (FTMS$^+$): **[M-PF$_6$]$^+$ Calculated:** ($C_{66}H_{52}N_4Ir$) 1093.3821; **Found:** 1093.3809. **Anal. Calc.:** ($C_{66}H_{52}N_4F_6IrP$ (MW 1238.35): C, 64.01; H, 4.23; N, 4.52. **Found:** C, 63.89; H, 4.13; N, 4.65% (average of two runs).

Bis[2-(naphthalen-1-yl)-4-(2,4,6-trimethylphenyl)pyridinato-*N*,C^2']-*N*,*N*'-(1*H*,1'*H*-2,2'-bibenzimidazole)iridium(III) hexafluorophosphate, [Ir(Mesnpy)$_2$(H$_2$bibenz)](PF$_6$).

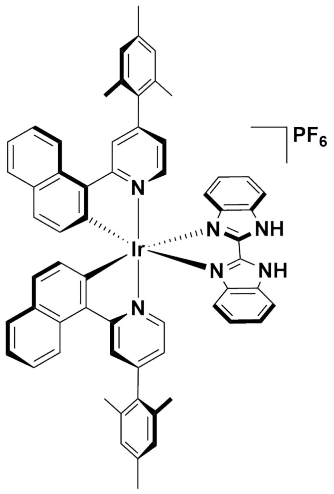

Synthesised using the silver method. Orange solid (0.029 g). **Yield:** 310%. **Mp:** 281 – 283 ℃ (decomp.). **R$_f$:** 0.60 (silica, DCM/MeOH, 9:1). **^{1}H NMR (500 MHz, CD$_2$Cl$_2$) δ (ppm):** 8.40 (d, J = 8.7 Hz, 2H), 8.30 (s, 2H), 7.91 (d, J = 5.9 Hz, 2H), 7.83 (d, J = 8.0 Hz, 2H), 7.70 (d, J = 8.3 Hz, 2H), 7.47 (t, J = 7.8 Hz, 2H), 7.41 – 7.36 (m, 4H), 7.33 (t, J = 7.0 Hz, 2H), 6.98 (d, J = 13.2 Hz, 4H), 6.82 (t, J = 7.8 Hz, 2H), 6.78 (d, J = 5.5 Hz, 2H), 6.51 (d, J = 8.4 Hz, 2H), 6.04 (d, J = 8.4 Hz, 2H), 2.32 (s, 6H), 2.16 (s, 6H), 1.98 (s, 6H). **^{13}C {^{1}H} NMR (126 MHz, CD$_2$Cl$_2$) δ (ppm):** 169.4, 151.9, 150.5, 140.9, 139.2, 138.5, 135.9, 135.6, 135.4, 131.9, 131.6, 130.7, 130.1, 130.0, 128.8, 128.8, 127.6, 126.7, 125.5, 125.1, 124.0, 123.7, 122.0, 118.1, 113.9, 21.2, 20.8, 20.7. **HR-MS** (FTMS$^+$): **[M-PF$_6$]$^+$ Calculated:** (C$_{62}$H$_{50}$N$_6$Ir) 1071.3726; **Found:** 1071.3722. **Anal. Calc.:** (C$_{62}$H$_{52}$N$_6$F$_6$IrP (MW 1216.31): C, 61.22; H, 4.14; N, 6.99. **Found:** C, 61.65; H, 4.25; N, 6.96% (average of two runs).

Bis[2-(naphthalen-1-yl)-4-(2,4,6-trimethylphenyl)pyridinato-$N,C^{2'}$]-N,N'-(1,1'-(α,α'-*o*-Xylylene)-2,2'-bibenzimidazole)iridium(III) hexafluorophosphate, [Ir(Mesnpy)$_2$(*o*-Xylbibenz)](PF$_6$).

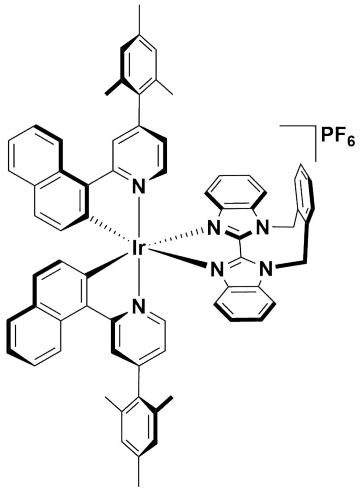

Synthesised using the silver method. Orange solid (0.029 g). **Yield:** 310%. **Mp:** 281 – 283 ℃ (decomp.). **R$_f$:** 0.60 (silica, DCM/MeOH, 9:1). **^{1}H NMR (500 MHz, DMSO-d_6, 372 K) δ (ppm):** 8.36 (dd, J = 8.6, 3.7 Hz, 4H), 8.16 (d, J = 1.8 Hz, 2H), 7.86 (d, J = 8.0 Hz, 2H), 7.77 – 7.70 (m, 4H), 7.53 (t, J = 8.5 Hz, 2H), 7.50 – 7.35 (m, 8H), 6.99 (s, 4H), 6.86 – 6.77 (m, 4H), 6.50 (d, J = 8.4 Hz, 2H), 6.26 (s, 4H), 6.06 (d, J = 8.4 Hz, 2H), 2.30 (s, 6H), 1.94 (br s, 12H). **^{13}C {^{1}H} NMR (126 MHz, CD$_2$Cl$_2$) δ (ppm):** 169.2, 153.9, 151.8, 150.5, 144.9, 140.4, 139.0, 138.5, 136.1, 135.8, 135.5, 135.4, 134.5, 131.9, 131.5, 131.4, 131.3, 130.5, 130.0, 128.8, 128.8, 127.7, 127.1, 125.9, 125.2, 124.1, 123.7, 121.9, 118.9, 111.6, 47.5, 21.2, 20.7, 20.7. **HR-MS** (FTMS$^+$): **[M-PF$_6$]$^+$ Calculated:** ($C_{70}H_{56}N_6Ir$) 1173.4196; **Found:** 1173.4182. **Anal. Calc.:** ($C_{70}H_{56}N_6F_6IrP$ (MW 1318.44): C, 63.77; H, 4.28; N, 6.37. **Found:** C, 63.55 H, 4.40; N, 6.25% (average of two runs).

6.4 General Spectroscopic Methods

Photophysical Measurements

All samples were prepared in HPLC grade solvents with varying concentrations on the order of µM. Absorption spectra were recorded at RT using a Shimadzu UV-1800 double beam spectrophotometer. Molar absorptivity determination was verified by linear least-squares fit of values obtained from at least three independent solutions at varying concentrations with absorbances of less than 1.0 for each absorption band.

The sample solutions for the emission spectra were degassed by vigorous bubbling for ca. 20 min. Steady-state emission was recorded at 77 K or 298 K using an Edinburgh Instruments F980 or a Gilden Photonics fluoroSENS spectrophotometer. All samples for steady-state measurements were excited at 360 nm OR 440 NM using a xenon lamp, while samples for time-resolved measurements were excited at 378 nm using a PDL 800-D pulsed diode laser, and recorded using a time-correlated single photon counting (TCSPC) method. Emission quantum yields were determined using the optically dilute method.[297;298] A stock solution with absorbance of ca. 0.5 on the excitation band was prepared and then four dilutions were prepared with dilution factors of 5, 6.6, 10 and 20 to obtain solutions with absorbances of ca. 0.1 0.075, 0.05 and 0.025, respectively. The Beer-Lambert law was found to be linear at the concentrations of the solutions. The emission spectra were then measured after the solutions were degassed by nitrogen purging for ca. 20 min per sample prior to spectrum acquisition. For each sample, linearity between absorption and emission intensity was verified through linear regression analysis and additional measurements were acquired until the Pearson regression factor (R^2) for the linear fit of the data set surpassed 0.9. Individual relative quantum yield values were calculated for each solution and the values reported represent the slope value. The equation:

$$\Phi_s = \Phi_r \left(\frac{A_r}{A_s}\right)\left(\frac{I_s}{I_r}\right)\left(\frac{n_s}{n_r}\right)^2$$

was used to calculate the relative quantum yield of each of the sample, where Φ is the absolute quantum yield of the reference, n is the refractive index of the solvent, A is the absorbance at the excitation wavelength, and I is the integrated area under the corrected emission curve. The subscripts s and r refer to the sample and reference, respectively. For

the reference sample, either a solution of quinine sulfate in 0.5 M H_2SO_4 ($\Phi_r = 54.6\%$)[220] or $[Ru(bpy)_3]Cl_2$ in air-satured water ($\Phi_r = 2.8\%$)[299;300] was used.

Samples for solid-state measurements were prepared by spin-coating solutions of each complex (5 mg / 1 mL) onto quartz substrates. Steady-state emission and time-resolved emission spectra were recorded at 298 K using an Edinburgh Instruments F980. All samples for steady-state measurements were excited at 360 nm xenon lamp while samples for time-resolved measurements were excited at 378 nm using a PDL 800-D pulsed diode laser, and were recorded under air. Photoluminescence quantum yields were measured using an integrating sphere, under a nitrogen atmosphere.

Electrochemical Measurements

Cyclic voltammery (CV) and differential pulse voltammetry (DPV) measurements were performed on an Electrochemical Analyzer potentiostat model 600D from CH Instruments. Solutions for were prepared in MeCN or DCM and degassed with solvent-saturated nitrogen by bubbling for ca. 10 min prior to scanning. Tetra(*n*-butyl)ammoniumhexafluorophosphate ($TBAPF_6$; ca. 0.1 M in MeCN) was used as the supporting electrolyte. A Pt wire was used as the pseudo-reference electrode; a Pt wire coil was used as the counter electrode and a Pt disk electrode was used for the working electrode. The redox potentials are reported relative to a saturated calomel electrode (SCE) electrode with a ferrocenium/ferrocene (Fc^+/Fc) redox couple as an internal reference (0.38 V vs SCE).[219]

Bibliography

[1] J. Paris and W. W. Brandt, *J. Am. Chem. Soc.*, 1959, **81**, 5001.

[2] K. Kalyanasundaram, *Coord. Chem. Rev.*, 1982, **46**, 159.

[3] I. M. Dixon, J.-P. Collin, J.-P. Sauvage, L. Flamigni, S. Encinas and F. Barigelletti, *Chem. Soc. Rev.*, 2000, **29**, 385.

[4] X. He and V. W.-W. Yam, *Coord. Chem. Rev.*, 2011, **255**, 2111.

[5] H. Yersin and D. Braun, *Coord. Chem. Rev.*, 1991, **111**, 39.

[6] V. W.-W. Yam and K. M.-C. Wong, *Chem. Commun.*, 2011, **47**, 11579.

[7] H. Sasabe and J. Kido, *Chem. Mater.*, 2010, **23**, 621.

[8] C. K. Prier, D. A. Rankic and D. W. C. MacMillan, *Chem. Rev.*, 2013, **113**, 5322.

[9] J. A. G. Williams, S. Develay, D. L. Rochester and L. Murphy, *Coord. Chem. Rev.*, 2008, **252**, 2596.

[10] M. K. Nazeeruddin and M. Grätzel, in *Photofunctional Transition Metal Complexes*, Springer, 2007, p. 113.

[11] J. J. Concepcion, J. W. Jurss, M. K. Brennaman, P. G. Hoertz, A. O. T. Patrocinio, N. Y. Murakami Iha, J. L. Templeton and T. J. Meyer, *Acc. Chem. Res.*, 2009, **42**, 1954.

[12] J. W. Tucker and C. R. J. Stephenson, *J. Org. Chem.*, 2012, **77**, 1617.

[13] D. Sykes and M. D. Ward, *Chem. Commun.*, 2011, **47**, 2279.

[14] D. Sykes, A. J. Cankut, N. M. Ali, A. Stephenson, S. J. Spall, S. C. Parker, J. A. Weinstein and M. D. Ward, *Dalton Trans.*, 2014, **43**, 6414.

[15] J. R. Piper, L. Cletheroe, C. G. Taylor, A. J. Metherell, J. A. Weinstein, I. V. Sazanovich and M. D. Ward, *Chem. Commun.*, 2017, **53**, 408.

[16] J. Otsuki, T. Akasaka and K. Araki, *Coord. Chem. Rev.*, 2008, **252**, 32.

[17] C. Joachim, J. Gimzewski and A. Aviram, *Nature*, 2000, **408**, 541.

[18] S. Fraysse, C. Coudret and J.-P. Launay, *J. Am. Chem. Soc.*, 2003, **125**, 5880.

[19] P. Belser, L. De Cola, F. Hartl, V. Adamo, B. Bozic, Y. Chriqui, V. M. Iyer, R. T. F. Jukes, J. Kuhni, M. Querol, S. Roma and N. Salluce, *Adv. Funct. Mater.*, 2006, **16**, 195.

[20] V. Balzani, M. Clemente-León, A. Credi, B. Ferrer, M. Venturi, A. H. Flood and J. F. Stoddart, *Proc. Nat. Acad. Sci.*, 2006, **103**, 1178.

[21] J. Sun, Y. Wu, Z. Liu, D. Cao, Y. Wang, C. Cheng, D. Chen, M. R. Wasielewski and J. F. Stoddart, *J. Phys. Chem. A*, 2015, **119**, 6317.

[22] G.-J. Zhou, Q. Wang, W.-Y. Wong, D. Ma, L. Wang and Z. Lin, *J. Mater. Chem.*, 2009, **19**, 1872.

[23] R. D. Costa, E. Orti, H. J. Bolink, F. Monti, G. Accorsi and N. Armaroli, *Angew. Chem. Int. Ed.*, 2012, **51**, 8178.

[24] K. K.-W. Lo, M.-W. Louie and K. Y. Zhang, *Coord. Chem. Rev.*, 2010, **254**, 2603.

[25] M. H. Keefe, K. D. Benkstein and J. T. Hupp, *Coord. Chem. Rev.*, 2000, **205**, 201.

[26] M. Grätzel, *Bull. Jpn. Soc. Coord. Chem.*, 2008, **51**, 3.

[27] A. F. Rausch, H. H. H. Homeier and H. Yersin, in *Photophysics of Organometallics*, Springer, 2010, pp. 193–235.

[28] A. Barbieri, G. Accorsi and N. Armaroli, *Chem. Commun.*, 2008, 2185.

[29] L. Flamigni, A. Barbieri, C. Sabatini, B. Ventura and F. Barigelletti, in *Photochemistry and Photophysics of Coordination Compounds II*, Springer, 2007, pp. 143–203.

[30] S. Campagna, F. Puntoriero, F. Nastasi, G. Bergamini and V. Balzani, in *Photochemistry and Photophysics of Coordination Compounds I*, Springer, 2007, pp. 117–214.

[31] V. Balzani, G. Bergamini, S. Campagna and F. Puntoriero, in *Photochemistry and Photophysics of Coordination Compounds I*, Springer, 2007, pp. 1–36.

[32] M. Kasha, *Discuss, Faraday Soc.*, 1950, **9**, 14.

[33] L. F. Gildea and J. A. G. Williams, *Organic Light-Emitting Diodes (OLEDs): Materials, Devices and Applications*, 2013, 76.

[34] H. Yersin, A. F. Rausch, R. Czerwieniec, T. Hofbeck and T. Fischer, *Coord. Chem. Rev.*, 2011, **255**, 2622.

[35] H. Yersin, *Highly Efficient OLEDs with Phosphorescent Materials*, John Wiley & Sons, 2008.

[36] T. Hofbeck and H. Yersin, *Inorg. Chem.*, 2010, **49**, 9290.

[37] F. So, J. Kido and P. Burrows, *MRS Bull.*, 2008, **33**, 663.

[38] C. J. Humphreys, *MRS Bull.*, 2008, **33**, 459.

[39] M. Wright and A. Uddin, *Sol. Energ. Mat. Sol. Cells*, 2012, **107**, 87.

[40] G. Niu, X. Guo and L. Wang, *J. Mater. Chem. A*, 2015, **3**, 8970.

[41] M. S. Shur and R. Zukauskas, *Proc. IEEE*, 2005, **93**, 1691.

[42] J. Y. Tsao, *IEEE Circuit. Dev.*, 2004, **20**, 28.

[43] M. R. Krames, O. B. Shchekin, R. Mueller-Mach, G. O. Mueller, L. Zhou, G. Harbers and M. G. Craford, *J. Display Technol.*, 2007, **3**, 160.

[44] T.-H. Han, Y. Lee, M.-R. Choi, S.-H. Woo, S.-H. Bae, B. H. Hong, J.-H. Ahn and T.-W. Lee, *Nat. Photonics*, 2012, **6**, 105.

[45] J. W. Park, D. C. Shin and S. H. Park, *Semicond. Sci. Technol.*, 2011, **26**, 034002.

[46] H. Sasabe and J. Kido, *Eur. J. Org. Chem.*, 2013, **2013**, 7653.

[47] S. Reineke, F. Lindner, G. Schwartz, N. Seidler, K. Walzer, B. Lüssem and K. Leo, *Nature*, 2009, **459**, 234.

[48] D. Fyfe, *Nat. Photonics*, 2009, **3**, 453.

[49] A. K. Bansal, W. Holzer, A. Penzkofer and T. Tsuboi, *Chem. Phys.*, 2006, **330**, 118.

[50] M. A. Baldo, D. F. O'brien, Y. You, A. Shoustikov, S. Sibley, M. E. Thompson and S. R. Forrest, *Nature*, 1998, **395**, 151.

[51] M. A. Baldo, S. Lamansky, P. E. Burrows, M. E. Thompson and S. R. Forrest, *Appl. Phys. Lett.*, 1999, **75**, 4.

[52] T. Sajoto, P. I. Djurovich, A. B. Tamayo, J. Oxgaard, W. A. Goddard III and M. E. Thompson, *J. Am. Chem. Soc.*, 2009, **131**, 9813.

[53] H. Sasabe and J. Kido, *J. Mater. Chem. C*, 2013, **1**, 1699.

[54] G. M. Farinola and R. Ragni, *Chem. Soc. Rev.*, 2011, **40**, 3467.

[55] H.-C. Su, C.-C. Wu, F.-C. Fang and K.-T. Wong, *Appl. Phys. Lett.*, 2006, **89**, 261118.

[56] E. Baranoff, S. SuaÌĂrez, P. Bugnon, C. Barolo, R. Buscaino, R. Scopelliti, L. Zuppiroli, M. Graetzel and M. K. Nazeeruddin, *Inorg. Chem.*, 2008, **47**, 6575.

[57] S. Tang, J. Pan, H. A. Buchholz and L. Edman, *J. Am. Chem. Soc.*, 2013, **135**, 3647.

[58] X. Yang, X. Xu and G. Zhou, *J. Mater. Chem. C*, 2015, **3**, 913.

[59] Y. Tao, C. Yang and J. Qin, *Chem. Soc. Rev.*, 2011, **40**, 2943.

[60] G. Schwartz, K. Fehse, M. Pfeiffer, K. Walzer and K. Leo, *Appl. Phys. Lett.*, 2006, **89**, 3509.

[61] J. D. Slinker, J. Rivnay, J. S. Moskowitz, J. B. Parker, S. Bernhard, H. D. Abruña and G. G. Malliaras, *J. Mater. Chem.*, 2007, **17**, 2976.

[62] A. F. Henwood and E. Zysman-Colman, *Top. Curr. Chem.*, 2016, **374**, 1.

[63] T. Hu, L. He, L. Duan and Y. Qiu, *J. Mater. Chem.*, 2012, **22**, 4206.

[64] D. A. Bernards, J. D. Slinker, G. G. Malliaras, S. Flores-Torres and H. D. Abruna, *Appl. Phys. Lett.*, 2004, **84**, 4980.

[65] Q. Sun, Y. Li and Q. Pei, *J. Display Technol.*, 2007, **3**, 211–224.

[66] S. Tang and L. Edman, *Top. Curr. Chem.*, 2016, **374**, 1.

[67] Q. Pei, G. Yu, C. Zhang, Y. Yang and A. J. Heeger, *Science*, 1995, **269**, 1086.

[68] S. Bernhard, J. A. Barron, P. L. Houston, H. D. Abruna, J. L. Ruglovksy, X. Gao and G. G. Malliaras, *J. Am. Chem. Soc.*, 2002, **124**, 13624.

[69] D. Ma, T. Tsuboi, Y. Qiu and L. Duan, *Adv. Mater.*, 2017, **29**, 1603253.

[70] A. J. Norell Bader, A. A. Ilkevich, I. V. Kosilkin and J. M. Leger, *Nano Lett.*, 2010, **11**, 461.

[71] G. Qian, Y. Lin, G. Wantz, A. R. Davis, K. R. Carter and J. J. Watkins, *Adv. Funct. Mater.*, 2014, **24**, 4484.

[72] M. F. AyguÌĹler, M. D. Weber, B. M. Puscher, D. D. Medina, P. Docampo and R. D. Costa, *J Phys. Chem. C*, 2015, **119**, 12047.

[73] H. Zhang, H. Lin, C. Liang, H. Liu, J. Liang, Y. Zhao, W. Zhang, M. Sun, W. Xiao, H. Li *et al.*, *Adv. Funct. Mater.*, 2015, **25**, 7226.

[74] F. G. Gao and A. J. Bard, *J. Am. Chem. Soc.*, 2000, **122**, 7426.

[75] A. B. Tamayo, S. Garon, T. Sajoto, P. I. Djurovich, I. M. Tsyba, R. Bau and M. E. Thompson, *Inorg. Chem.*, 2005, **44**, 8723.

[76] D. R. Blasini, J. Rivnay, D.-M. Smilgies, J. D. Slinker, S. Flores-Torres, H. D. Abruña and G. G. Malliaras, *J. Mater. Chem.*, 2007, **17**, 1458.

[77] C.-Y. Liu and A. J. Bard, *J. Am. Chem. Soc.*, 2002, **124**, 4190.

[78] S. van Reenen, P. Matyba, A. Dzwilewski, R. A. Janssen, L. Edman and M. Kemerink, *J. Am. Chem. Soc.*, 2010, **132**, 13776.

[79] A. Sandström, A. Asadpoordarvish, J. Enevold and L. Edman, *Adv. Mater.*, 2014, **26**, 4975.

[80] A. Asadpoordarvish, A. Sandström, C. Larsen, R. Bollström, M. Toivakka, R. Österbacka and L. Edman, *Adv. Funct. Mater.*, 2015, **25**, 3238.

[81] G. E. Schneider, H. J. Bolink, E. C. Constable, C. D. Ertl, C. E. Housecroft, A. Pertegàs, J. A. Zampese, A. Kanitz, F. Kessler and S. B. Meier, *Dalton Trans.*, 2014, **43**, 1961.

[82] J. Slinker, D. Bernards, P. L. Houston, H. D. Abruña, S. Bernhard and G. G. Malliaras, *Chem. Commun.*, 2003, 2392.

[83] E. Baranoff, H. J. Bolink, E. C. Constable, M. Delgado, D. Häussinger, C. E. Housecroft, M. K. Nazeeruddin, M. Neuburger, E. Ortí, G. E. Schneider *et al.*, *Dalton Trans.*, 2013, **42**, 1073.

[84] J. M. Fernández-Hernández, S. Ladouceur, Y. Shen, A. Iordache, X. Wang, L. Donato, S. Gallagher-Duval, M. de Anda Villa, J. D. Slinker, L. De Cola *et al.*, *J. Mater. Chem. C*, 2013, **1**, 7440.

[85] S. Evariste, M. Sandroni, T. W. Rees, C. Roldán-Carmona, L. Gil-Escrig, H. J. Bolink, E. Baranoff and E. Zysman-Colman, *J. Mater. Chem. C*, 2014, **2**, 5793.

[86] J. D. Slinker, A. A. Gorodetsky, M. S. Lowry, J. Wang, S. Parker, R. Rohl, S. Bernhard and G. G. Malliaras, *J. Am. Chem. Soc.*, 2004, **126**, 2763.

[87] R. D. Costa, E. Ortí, H. J. Bolink, S. Graber, S. Schaffner, M. Neuburger, C. E. Housecroft and E. C. Constable, *Adv. Funct. Mater.*, 2009, **19**, 3456.

[88] Y. Shen, D. D. Kuddes, C. A. Naquin, T. W. Hesterberg, C. Kusmierz, B. J. Holliday and J. D. Slinker, *Appl. Phys. Lett.*, 2013, **102**, 203305.

[89] R. D. Costa, E. Ortí, D. Tordera, A. Pertegás, H. J. Bolink, S. Graber, C. E. Housecroft, L. Sachno, M. Neuburger and E. C. Constable, *Adv. Energy Mater.*, 2011, **1**, 282.

[90] S. Ladouceur and E. Zysman-Colman, *Eur. J. Inorg. Chem.*, 2013, **2013**, 2985.

[91] S. Ladouceur, D. Fortin and E. Zysman-Colman, *Inorg. Chem.*, 2010, **49**, 5625.

[92] J. Zhang, L. Zhou, H. A. Al-Attar, K. Shao, L. Wang, D. Zhu, Z. Su, M. R. Bryce and A. P. Monkman, *Adv. Funct. Mater.*, 2013, **23**, 4667.

[93] D. Tordera, J. J. Serrano-PeÌĄrez, A. Pertegas, E. Ortí, H. J. Bolink, E. Baranoff, M. K. Nazeeruddin and J. Frey, *Chem. Mater.*, 2013, **25**, 3391.

[94] D. Rota Martir, C. Momblona, A. Pertegás, D. B. Cordes, A. M. Z. Slawin, H. J. Bolink and E. Zysman-Colman, *ACS Appl. Mater. Interfaces*, 2016, **8**, 33907.

[95] C. M. Cardona, W. Li, A. E. Kaifer, D. Stockdale and G. C. Bazan, *Adv. Mater.*, 2011, **23**, 2367.

[96] J.-L. Bredas, *Mater. Horiz.*, 2014, **1**, 17.

[97] C.-T. Liao, H.-F. Chen, H.-C. Su and K.-T. Wong, *Phys. Chem. Chem. Phys.*, 2012, **14**, 1262.

[98] A. Pertegás, N. M. Shavaleev, D. Tordera, E. Ortí, M. K. Nazeeruddin and H. J. Bolink, *J. Mater. Chem. C*, 2014, **2**, 1605.

[99] C.-C. Ho, H.-F. Chen, Y.-C. Ho, C.-T. Liao, H.-C. Su and K.-T. Wong, *Phys. Chem. Chem. Phys.*, 2011, **13**, 17729.

[100] M. S. Lowry and S. Bernhard, *Chem. Eur. J.*, 2006, **12**, 7970.

[101] J. Frey, B. F. E. Curchod, R. Scopelliti, I. Tavernelli, U. Rothlisberger, M. K. Nazeeruddin and E. Baranoff, *Dalton Trans.*, 2014, **43**, 5667.

[102] C. Hansch, A. Leo and R. W. Taft, *Chem. Rev.*, 1991, **91**, 165.

[103] M. Bixon, J. Jortner, J. Cortes, H. Heitele and M. Michel-Beyerle, *J. Phys. Chem.*, 1994, **98**, 7289.

[104] J. V. Caspar and T. J. Meyer, *J. Phys. Chem.*, 1983, **87**, 952.

[105] A. Batagin-Neto, A. Assis, J. F. d. Lima, C. J. Magon, L. Yan, M. Shao, B. Hu and C. Graeff, *J. Phys. Chem. A*, 2014, **118**, 3717.

[106] L. J. Soltzberg, J. D. Slinker, S. Flores-Torres, D. A. Bernards, G. G. Malliaras, H. D. Abruña, J.-S. Kim, R. H. Friend, M. D. Kaplan and V. Goldberg, *J. Am. Chem. Soc.*, 2006, **128**, 7761.

[107] W. Zhao, C.-Y. Liu, Q. Wang, J. White and A. J. Bard, *Chem. Mater.*, 2005, **17**, 6403.

[108] J. Lee, H.-F. Chen, T. Batagoda, C. Coburn, P. I. Djurovich, M. E. Thompson and S. R. Forrest, *Nat. Mater.*, 2016, **15**, 92.

[109] B. Geffroy, P. Le Roy and C. Prat, *Polym. Int.*, 2006, **55**, 572.

[110] L. He, L. Duan, J. Qiao, R. Wang, P. Wei, L. Wang and Y. Qiu, *Adv. Funct. Mater.*, 2008, **18**, 2123.

[111] H.-B. Wu, H.-F. Chen, C.-T. Liao, H.-C. Su and K.-T. Wong, *Org. Electron.*, 2012, **13**, 483.

[112] L. He, J. Qiao, L. Duan, G. Dong, D. Zhang, L. Wang and Y. Qiu, *Adv. Funct. Mater.*, 2009, **19**, 2950.

[113] L. He, L. Duan, J. Qiao, G. Dong, L. Wang and Y. Qiu, *Chem. Mater.*, 2010, **22**, 3535.

[114] F. Zhang, L. Duan, J. Qiao, G. Dong, L. Wang and Y. Qiu, *Org. Electron.*, 2012, **13**, 1277.

[115] F. Zhang, L. Duan, J. Qiao, G. Dong, L. Wang and Y. Qiu, *Org. Electron.*, 2012, **13**, 2442.

[116] L. He, L. Duan, J. Qiao, D. Zhang, L. Wang and Y. Qiu, *Chem. Commun.*, 2011, **47**, 6467.

[117] C.-T. Liao, H.-F. Chen, H.-C. Su and K.-T. Wong, *Phys. Chem. Chem. Phys.*, 2012, **14**, 9774.

[118] J.-S. Lu, H.-F. Chen, J.-C. Kuo, R. Sun, C.-Y. Cheng, Y.-S. Yeh, H.-C. Su and K.-T. Wong, *J. Mater. Chem. C*, 2015, **3**, 2802.

[119] H.-C. Su, H.-F. Chen, P.-H. Chen, S.-W. Lin, C.-T. Liao and K.-T. Wong, *J. Mater. Chem.*, 2012, **22**, 22998.

[120] H.-C. Su, H.-F. Chen, Y.-C. Shen, C.-T. Liao and K.-T. Wong, *J. Mater. Chem.*, 2011, **21**, 9653.

[121] C.-T. Liao, H.-F. Chen, H.-C. Su and K.-T. Wong, *J. Mater. Chem.*, 2011, **21**, 17855.

[122] V. Sivasubramaniam, F. Brodkorb, S. Hanning, H. P. Loebl, V. van Elsbergen, H. Boerner, U. Scherf and M. Kreyenschmidt, *J. Fluorine Chem.*, 2009, **130**, 640.

[123] Y. Zheng, A. S. Batsanov, R. M. Edkins, A. Beeby and M. R. Bryce, *Inorg. Chem.*, 2011, **51**, 290.

[124] N. Darmawan, C.-H. Yang, M. Mauro, M. Raynal, S. Heun, J. Pan, H. Buchholz, P. Braunstein and L. De Cola, *Inorg. Chem.*, 2013, **52**, 10756.

[125] A. M. Bünzli, E. C. Constable, C. E. Housecroft, A. Prescimone, J. A. Zampese, G. Longo, L. Gil-Escrig, A. Pertegás, E. Ortí and H. J. Bolink, *Chem. Sci.*, 2015, **6**, 2843.

[126] H. J. Bolink, E. Coronado, R. D. Costa, E. Ortí, M. Sessolo, S. Graber, K. Doyle, M. Neuburger, C. E. Housecroft and E. C. Constable, *Adv. Mater.*, 2008, **20**, 3910.

[127] R. D. Costa, E. Ortí, H. J. Bolink, S. Graber, C. E. Housecroft and E. C. Constable, *Adv. Funct. Mater.*, 2010, **20**, 1511.

[128] H.-C. Su, F.-C. Fang, T.-Y. Hwu, H.-H. Hsieh, H.-F. Chen, G.-H. Lee, S.-M. Peng, K.-T. Wong and C.-C. Wu, *Adv. Funct. Mater.*, 2007, **17**, 1019.

[129] H. J. Bolink, E. Coronado, R. D. Costa, N. Lardiés and E. OrtiÌĄ, *Inorg. Chem.*, 2008, **47**, 9149.

[130] D. Tordera, J. Frey, D. Vonlanthen, E. Constable, A. Pertegás, E. Ortí, H. J. Bolink, E. Baranoff and M. K. Nazeeruddin, *Adv. Energy Mater.*, 2013, **3**, 1338.

[131] H.-C. Su, H.-F. Chen, C.-C. Wu and K.-T. Wong, *Chem. Asian J.*, 2008, **3**, 1922.

[132] R. D. Costa, E. Ortí, H. J. Bolink, S. Graber, C. E. Housecroft, M. Neuburger, S. Schaffner and E. C. Constable, *Chem. Commun.*, 2009, 2029.

[133] R. D. Costa, E. OrtiÌĄ, H. J. Bolink, S. Graber, C. E. Housecroft and E. C. Constable, *J. Am. Chem. Soc.*, 2010, **132**, 5978.

[134] L. Sun, A. Galan, S. Ladouceur, J. D. Slinker and E. Zysman-Colman, *J. Mater. Chem.*, 2011, **21**, 18083.

[135] D. Tordera, S. Meier, M. Lenes, R. D. Costa, E. Ortí, W. Sarfert and H. J. Bolink, *Adv. Mater.*, 2012, **24**, 897.

[136] D. Tordera, A. Pertegás, N. M. Shavaleev, R. Scopelliti, E. Ortí, H. J. Bolink, E. Baranoff, M. Grätzel and M. K. Nazeeruddin, *J. Mater. Chem.*, 2012, **22**, 19264.

[137] E. Zysman-Colman, J. D. Slinker, J. B. Parker, G. G. Malliaras and S. Bernhard, *Chem. Mater.*, 2007, **20**, 388.

[138] R. D. Costa, A. PertegaÌĄs, E. OrtiÌĄ and H. J. Bolink, *Chem. Mater.*, 2010, **22**, 1288.

[139] R. D. Costa, F. J. Céspedes-Guirao, E. Ortí, H. J. Bolink, J. Gierschner, F. Fernández-Lázaro and A. Sastre-Santos, *Chem. Commun.*, 2009, 3886.

[140] K. Hasan, L. Donato, Y. Shen, J. D. Slinker and E. Zysman-Colman, *Dalton Trans.*, 2014, **43**, 13672.

[141] S. Graber, K. Doyle, M. Neuburger, C. E. Housecroft, E. C. Constable, R. D. Costa, E. OrtiÌĄ, D. Repetto and H. J. Bolink, *J. Am. Chem. Soc.*, 2008, **130**, 14944.

[142] J. L. Rodríguez-Redondo, R. D. Costa, E. Ortí, A. Sastre-Santos, H. J. Bolink and F. Fernández-Lázaro, *Dalton Trans.*, 2009, 9787.

[143] M. Mydlak, C. Bizzarri, D. Hartmann, W. Sarfert, G. Schmid and L. De Cola, *Adv. Funct. Mater.*, 2010, **20**, 1812.

[144] J. M. Fernández-Hernández, C.-H. Yang, J. I. Beltrán, V. Lemaur, F. Polo, R. FroÌĹhlich, J. Cornil and L. De Cola, *J. Am. Chem. Soc.*, 2011, **133**, 10543.

[145] S. Ladouceur, D. Fortin and E. Zysman-Colman, *Inorg. Chem.*, 2011, **50**, 11514.

[146] C. D. Ertl, J. Cerdá, J. M. Junquera-Hernández, A. Pertegás, H. J. Bolink, E. C. Constable, M. Neuburger, E. Ortí and C. E. Housecroft, *RSC Adv.*, 2015, **5**, 42815.

[147] D. Tordera, A. M. Bünzli, A. Pertegás, J. M. Junquera-Hernández, E. C. Constable, J. A. Zampese, C. E. Housecroft, E. Ortí and H. J. Bolink, *Chem. Eur. J.*, 2013, **19**, 8597.

[148] L. Donato, P. Abel and E. Zysman-Colman, *Dalton Trans.*, 2013, **42**, 8402.

[149] C. E. Welby, L. Gilmartin, R. R. Marriott, A. Zahid, C. R. Rice, E. A. Gibson and P. I. Elliott, *Dalton Trans.*, 2013, **42**, 13527.

[150] F. Kessler, R. D. Costa, D. Di Censo, R. Scopelliti, E. Ortí, H. J. Bolink, S. Meier, W. Sarfert, M. Grätzel, M. K. Nazeeruddin *et al.*, *Dalton Trans.*, 2012, **41**, 180.

[151] C.-H. Yang, J. Beltran, V. Lemaur, J. Cornil, D. Hartmann, W. Sarfert, R. FroÌĹhlich, C. Bizzarri and L. De Cola, *Inorg. Chem.*, 2010, **49**, 9891.

[152] S. B. Meier, W. Sarfert, J. M. Junquera-Hernández, M. Delgado, D. Tordera, E. Ortí, H. J. Bolink, F. Kessler, R. Scopelliti, M. Grätzel, M. K. Nazeeruddin and E. Baranoff, *J. Mater. Chem. C*, 2013, **1**, 58.

[153] S. Derossi, H. Adams and M. D. Ward, *Dalton Trans.*, 2007, 33.

[154] K. Heussner, K. Peuntinger, N. Rockstroh, L. C. Nye, I. Ivanovic-Burmazovic, S. Rau and C. Streb, *Chem. Commun.*, 2011, **47**, 6852.

[155] H. Sun, S. Liu, W. Lin, K. Y. Zhang, W. Lv, X. Huang, F. Huo, H. Yang, G. Jenkins, Q. Zhao *et al.*, *Nat. Commun.*, 2014, **5**, 3601.

[156] S. A. Rommel, D. Sorsche, N. Rockstroh, F. W. Heinemann, J. Kübel, M. Wächtler, B. Dietzek and S. Rau, *Eur. J. Inorg. Chem.*, 2015, 3730.

[157] Y. Cui, H.-J. Mo, J.-C. Chen, Y.-L. Niu, Y.-R. Zhong, K.-C. Zheng and B.-H. Ye, *Inorg. Chem.*, 2007, **46**, 6427.

[158] L. Murphy, A. Congreve, L.-O. Pålsson and J. A. G. Williams, *Chem. Commun.*, 2010, **46**, 8743.

[159] X. Wang, J. Jia, Z. Huang, M. Zhou and H. Fei, *Chem. Eur. J.*, 2011, **17**, 8028.

[160] O. S. Wenger, *Acc. Chem. Res.*, 2013, **46**, 1517.

[161] J. C. Freys, G. Bernardinelli and O. S. Wenger, *Chem. Commun.*, 2008, 4267.

[162] S.-J. Yun, H.-J. Seo, M. Song, S.-H. Jin and Y. I. Kim, *Bull. Korean Chem. Soc.*, 2012, **33**, 3645.

[163] V. N. Kozhevnikov, M. C. Durrant and J. A. G. Williams, *Inorg. Chem.*, 2011, **50**, 6304.

[164] P.-H. Lanoë, C. M. Tong, R. W. Harrington, M. R. Probert, W. Clegg, J. A. G. Williams and V. N. Kozhevnikov, *Chem. Commun.*, 2014, **50**, 6831.

[165] R. E. Daniels, S. Culham, M. Hunter, M. C. Durrant, M. R. Probert, W. Clegg, J. A. G. Williams and V. N. Kozhevnikov, *Dalton Trans.*, 2016, **45**, 6949.

[166] G.-G. Shan, H.-B. Li, H.-Z. Sun, H.-T. Cao, D.-X. Zhu and Z.-M. Su, *Dalton Trans.*, 2013, **42**, 11056.

[167] J. A. G. Williams, A. J. Wilkinson and V. L. Whittle, *Dalton Trans.*, 2008, 2081.

[168] D. A. Vezzu, J. C. Deaton, J. S. Jones, L. Bartolotti, C. F. Harris, A. P. Marchetti, M. Kondakova, R. D. Pike and S. Huo, *Inorg. Chem.*, 2010, **49**, 5107.

[169] T. Fleetham, L. Huang and J. Li, *Adv. Funct. Mater.*, 2014, **24**, 6066.

[170] S. C. Kui, P. K. Chow, G. Cheng, C.-C. Kwok, C. L. Kwong, K.-H. Low and C.-M. Che, *Chem. Commun.*, 2013, **49**, 1497.

[171] G. St-Pierre, S. Ladouceur, D. Fortin and E. Zysman-Colman, *Dalton Trans.*, 2011, **40**, 11726.

[172] V. N. Kozhevnikov, Y. Zheng, M. Clough, H. A. Al-Attar, G. C. Griffiths, K. Abdullah, S. Raisys, V. Jankus, M. R. Bryce and A. P. Monkman, *Chem. Mater.*, 2013, **25**, 2352.

[173] E. Baranoff and B. F. Curchod, *Dalton Trans.*, 2015, **44**, 8318.

[174] A. F. Henwood, S. Evariste, A. M. Slawin and E. Zysman-Colman, *Faraday Discuss.*, 2014, **174**, 165.

[175] H. Benjamin, Y. Zheng, A. S. Batsanov, M. A. Fox, H. A. Al-Attar, A. P. Monkman and M. R. Bryce, *Inorg. Chem.*, 2016, **55**, 8612.

[176] D. R. Martir, A. K. Bansal, V. Di Mascio, D. B. Cordes, A. F. Henwood, A. M. Slawin, P. C. Kamer, L. Martínez-Sarti, A. Pertegás, H. J. Bolink *et al.*, *Inorg. Chem. Front.*, 2016, **3**, 218.

[177] A. F. Henwood, A. K. Bansal, D. B. Cordes, A. M. Slawin, I. D. Samuel and E. Zysman-Colman, *J. Mater. Chem. C*, 2016, **4**, 3726.

[178] Y. You and S. Y. Park, *J. Am. Chem. Soc.*, 2005, **127**, 12438.

[179] R. P. Thummel, V. Goulle and B. Chen, *J. Org. Chem.*, 1989, **54**, 3057.

[180] J.-C. Xiao and J. M. Shreeve, *J. Org. Chem.*, 2005, **70**, 3072.

[181] M. Nonoyama, *Bull. Chem. Soc. Jpn.*, 1974, **47**, 767.

[182] L. Li, F. Wu, S. Zhang, D. Wang, Y. Ding and Z. Zhu, *Dalton Trans.*, 2013, **42**, 4539.

[183] H. Oh, K.-M. Park, H. Hwang, S. Oh, J. H. Lee, J.-S. Lu, S. Wang and Y. Kang, *Organometallics*, 2013, **32**, 6427.

[184] S. A. Denisov, Y. CudreÌĄ, P. Verwilst, G. Jonusauskas, M. Marín-SuaÌĄrez, J. F. FernaÌĄndez-SaÌĄnchez, E. Baranoff and N. D. McClenaghan, *Inorg. Chem.*, 2014, **53**, 2677.

[185] E. Baranoff, B. F. Curchod, J. Frey, R. Scopelliti, F. Kessler, I. Tavernelli, U. Rothlisberger, M. GraÌĹtzel and M. K. Nazeeruddin, *Inorg. Chem.*, 2011, **51**, 215.

[186] D. Tordera, M. Delgado, E. Ortí, H. J. Bolink, J. Frey, M. K. Nazeeruddin and E. Baranoff, *Chem. Mater.*, 2012, **24**, 1896.

[187] H. Gutowsky and C. Holm, *J. Chem. Phys.*, 1956, **25**, 1228.

[188] H. J. Bolink, L. Cappelli, S. Cheylan, E. Coronado, R. D. Costa, N. Lardiés, M. K. Nazeeruddin and E. Ortí, *J. Mater. Chem.*, 2007, **17**, 5032.

[189] X. Wang, Y.-L. Chang, J.-S. Lu, T. Zhang, Z.-H. Lu and S. Wang, *Adv. Funct. Mater.*, 2014, **24**, 1911.

[190] H. V. Phan, P. Chakraborty, M. Chen, Y. M. Calm, K. Kovnir, L. K. Keniley, J. M. Hoyt, E. S. Knowles, C. Besnard, M. W. Meisel *et al.*, *Chem. Eur. J.*, 2012, **18**, 15805.

[191] E. Laurila, L. Oresmaa, M. Niskanen, P. Hirva and M. Haukka, *Cryst. Growth Des.*, 2010, **10**, 3775.

[192] N. Sengottuvelan, H.-J. Seo, S.-K. Kang and Y.-I. Kim, *Bull. Korean Chem. Soc.*, 2010, **31**, 2309.

[193] T. Kundu, S. M. Mobin and G. K. Lahiri, *Dalton Trans.*, 2010, **39**, 4232.

[194] L. He, D. Ma, L. Duan, Y. Wei, J. Qiao, D. Zhang, G. Dong, L. Wang and Y. Qiu, *Inorg. Chem.*, 2012, **51**, 4502.

[195] P. Hohenberg, *Phys. Rev*, 1965, **140**, A1133–A1138.

[196] W. Kohn and L. J. Sham, *Phys. Rev.*, 1965, **140**, A1133.

[197] J. Andzelm, E. Wimmer and D. Salahub, by DR Salahub and MC Zerner, ACS Symposium Series, 1989, p. 228.

[198] R. E. Stratmann, G. E. Scuseria and M. J. Frisch, *J. Chem. Phys.*, 1998, **109**, 8218.

[199] R. Bauernschmitt and R. Ahlrichs, *Chem. Phys. Lett.*, 1996, **256**, 454.

[200] M. E. Casida, C. Jamorski, K. C. Casida and D. R. Salahub, *J. Chem. Phys.*, 1998, **108**, 4439.

[201] M. Frisch, G. Trucks, H. Schlegel, G. Scuseria, M. Robb, J. Cheeseman, V. Zakrzewski, J. Montgomery Jr, R. E. Stratmann, J. Burant *et al.*, *Inc., Pittsburgh, PA*, 1998, **12**, year.

[202] A. D. Becke, *J. Chem. Phys.*, 1993, **98**, 5648.

[203] C. Lee, W. Yang and R. G. Parr, *Phys. Rev. B*, 1988, **37**, 785.

[204] B. Miehlich, A. Savin, H. Stoll and H. Preuss, *Chem. Phys. Lett.*, 1989, **157**, 200.

[205] J. S. Binkley, J. A. Pople and W. J. Hehre, *J. Am. Chem. Soc.*, 1980, **102**, 939.

[206] W. J. Stevens, H. Basch and M. Krauss, *J. Chem. Phys.*, 1984, **81**, 6026.

[207] W. J. Stevens, M. Krauss, H. Basch and P. G. Jasien, *Can. J. Chem.*, 1992, **70**, 612.

[208] T. R. Cundari and W. J. Stevens, *J. Chem. Phys.*, 1993, **98**, 5555.

[209] M. S. Gordon, J. S. Binkley, J. A. Pople, W. J. Pietro and W. J. Hehre, *J. Am. Chem. Soc.*, 1982, **104**, 2797.

[210] W. J. Pietro, M. M. Francl, W. J. Hehre, D. J. DeFrees, J. A. Pople and J. S. Binkley, *J. Am. Chem. Soc.*, 1982, **104**, 5039.

[211] K. D. Dobbs and W. J. Hehre, *J. Comp. Chem.*, 1986, **7**, 359.

[212] K. D. Dobbs and W. J. Hehre, *J. Comp. Chem.*, 1987, **8**, 880.

[213] R. H. W. J. Ditchfield, W. J. Hehre and J. A. Pople, *J. Chem. Phys.*, 1971, **54**, 724.

[214] W. J. Hehre, R. Ditchfield and J. A. Pople, *J. Chem. Phys.*, 1972, **56**, 2257.

[215] P. C. Hariharan and J. A. Pople, *Theo. Chim. Acta.*, 1973, **28**, 213.

[216] P. Hariharan and J. Pople, *Mol. Phys.*, 1974, **27**, 209.

[217] M. S. Gordon, *Chem. Phys. Lett.*, 1980, **76**, 163.

[218] J. Tomasi, B. Mennucci and R. Cammi, *Chem. Rev.*, 2005, **105**, 2999.

[219] V. V. Pavlishchuk and A. W. Addison, *Inorg. Chim. Acta*, 2000, **298**, 97.

[220] W. H. Melhuish, *J. Phys. Chem.*, 1961, **65**, 229.

[221] H. Yu, C. Liu, Z. Yu, L. Zhang *et al.*, *J. Mater. Chem. C*, 2017, DOI: 10.1039/C6TC04732G.

[222] M. Ouyang, L. Zeng, K. Qiu, Y. Chen, L. Ji and H. Chao, *Eur. J. Inorg. Chem.*, 2017, 1764.

[223] J. Mei, Y. Hong, J. W. Lam, A. Qin, Y. Tang and B. Z. Tang, *Adv. Mater.*, 2014, **26**, 5429.

[224] Y. Q. Zhang, G. Y. Zhong and X. A. Cao, *J. Appl. Phys.*, 2010, **108**, 083107.

[225] Y. Kawamura, K. Goushi, J. Brooks, J. J. Brown, H. Sasabe and C. Adachi, *Appl. Phys. Lett.*, 2005, **86**, 071104.

[226] M. A. Baldo, M. E. Thompson and S. R. Forrest, *Nature*, 2000, **403**, 750.

[227] G. Nasr, A. Guerlin, F. Dumur, L. Beouch, E. Dumas, G. Clavier, F. Miomandre, F. Goubard, D. Gigmes, D. Bertin *et al.*, *Chem. Commun.*, 2011, **47**, 10698.

[228] R. Tao, J. Qiao, G. Zhang, L. Duan, L. Wang and Y. Qiu, *J. Phys. Chem. C*, 2012, **116**, 11658.

[229] N. M. Shavaleev, G. Xie, S. Varghese, D. B. Cordes, A. M. Z. Slawin, C. Momblona, E. Ortí, H. J. Bolink, I. D. W. Samuel and E. Zysman-Colman, *Inorg. Chem.*, 2015, **54**, 5907.

[230] J. O. Huh, M. H. Lee, H. Jang, K. Y. Hwang, J. S. Lee, S. H. Kim and Y. Do, *Inorg. Chem.*, 2008, **47**, 6566.

[231] N. Luo, Y. Lan, R. Tang, L. He and L. Duan, *Chem. Commun.*, 2016, **52**, 14466.

[232] D. Ma, C. Zhang, Y. Qiu and L. Duan, *J. Mater. Chem. C*, 2016, **4**, 5731.

[233] D. Ma, L. Duan and Y. Qiu, *J. Mater. Chem. C*, 2016, **4**, 5051.

[234] W.-Y. Wong, G.-J. Zhou, X.-M. Yu, H.-S. Kwok and Z. Lin, *Adv. Funct. Mater.*, 2007, **17**, 315.

[235] T.-Y. Li, X. Liang, L. Zhou, C. Wu, S. Zhang, X. Liu, G.-Z. Lu, L.-S. Xue, Y.-X. Zheng and J.-L. Zuo, *Inorg. Chem.*, 2014, **54**, 161.

[236] C.-H. Yang, M. Mauro, F. Polo, S. Watanabe, I. Muenster, R. FroÌĹhlich and L. De Cola, *Chem. Mater.*, 2012, **24**, 3684.

[237] M. L. P. Reddy and K. S. Bejoymohandas, *J. Photochem. Photobiol. C*, 2016, **29**, 29.

[238] K. S. Bejoymohandas, A. Kumar, S. Varughese, E. Varathan, V. Subramanian and M. L. P. Reddy, *J. Mater. Chem. C*, 2015, **3**, 7405.

[239] Q.-L. Xu, X. Liang, S. Zhang, Y.-M. Jing, X. Liu, G.-Z. Lu, Y.-X. Zheng and J.-L. Zuo, *J. Mater. Chem. C*, 2015, **3**, 3694.

[240] Q.-L. Xu, X. Liang, L. Jiang, Y. Zhao and Y.-X. Zheng, *RSC Adv.*, 2015, **5**, 89218.

[241] B. J. Coe, M. Helliwell, S. Sánchez, M. K. Peers and N. S. Scrutton, *Dalton Trans.*, 2015, **44**, 15420.

[242] B. J. Coe, M. Helliwell, J. Raftery, S. Sánchez, M. K. Peers and N. S. Scrutton, *Dalton Trans.*, 2015, **44**, 20392.

[243] C.-H. Chang, Z.-J. Wu, C.-H. Chiu, Y.-H. Liang, Y.-S. Tsai, J.-L. Liao, Y. Chi, H.-Y. Hsieh, T.-Y. Kuo, G.-H. Lee, H.-A. Pan, P.-T. Chou, J.-S. Lin and M.-R. Tseng, *ACS Appl. Mater. Interfaces*, 2013, **5**, 7341.

[244] T. Duan, T.-K. Chang, Y. Chi, J.-Y. Wang, Z.-N. Chen, W.-Y. Hung, C.-H. Chen and G.-H. Lee, *Dalton Trans.*, 2015, **44**, 14613.

[245] Q.-L. Xu, X. Liang, L. Jiang, Y. Zhao and Y.-X. Zheng, *Dalton Trans.*, 2016, **45**, 7366.

[246] X. Wang, S. Feng, X. Wang, C. Wang, L. Wang and J. Zhang, *Comp. Theor. Chem.*, 2017, **1105**, 69.

[247] M. S. Lowry, J. I. Goldsmith, J. D. Slinker, R. Rohl, R. A. Pascal, G. G. Malliaras and S. Bernhard, *Chem. Mater.*, 2005, **17**, 5712.

[248] N. Miyaura, T. Yanagi and A. Suzuki, *Synth. Commun.*, 1981, **11**, 513.

[249] Ł. Skórka, M. Filapek, L. Zur, J. G. Małecki, W. Pisarski, M. Olejnik, W. Danikiewicz and S. Krompiec, *J. Phys. Chem. C*, 2016, **120**, 7284.

[250] K. Hasan, A. K. Bansal, I. D. Samuel, C. Roldán-Carmona, H. J. Bolink and E. Zysman-Colman, *Sci. Rep.*, 2015, **5**, 12325.

[251] S. Medina-Rodríguez, S. A. Denisov, Y. Cudré, L. Male, M. Marín-Suárez, A. Fernández-Gutiérrez, J. F. Fernández-Sánchez, A. Tron, G. Jonusauskas, N. D. McClenaghan and E. Baranoff, *Analyst*, 2016, **141**, 3090.

[252] H.-C. Su, H.-F. Chen, F.-C. Fang, C.-C. Liu, C.-C. Wu, K.-T. Wong, Y.-H. Liu and S.-M. Peng, *J. Am. Chem. Soc.*, 2008, **130**, 3413.

[253] G. Zhang, H. Zhang, Y. Gao, R. Tao, L. Xin, J. Yi, F. Li, W. Liu and J. Qiao, *Organometallics*, 2013, **33**, 61–68.

[254] E. E. Langdon-Jones, A. J. Hallett, J. D. Routledge, D. A. Crole, B. D. Ward, J. A. Platts and S. J. A. Pope, *Inorg. Chem.*, 2012, **52**, 448.

[255] Z. Li, P. Cui, C. Wang, S. Kilina and W. Sun, *J. Phys. Chem. C*, 2014, **118**, 28764.

[256] C.-H. Leung, H.-J. Zhong, H. Yang, Z. Cheng, D. S.-H. Chan, V. P.-Y. Ma, R. Abagyan, C.-Y. Wong and D.-L. Ma, *Angew. Chem. Int. Ed.*, 2012, **51**, 9010.

[257] L. K. McKenzie, I. V. Sazanovich, E. Baggaley, M. Bonneau, V. Guerchais, J. A. G. Williams, J. A. Weinstein and H. E. Bryant, *Chem. Eur. J.*, 2017, **23**, 234.

[258] D.-P. Gong, T.-B. Gao, D.-K. Cao and M. D. Ward, *Dalton Trans.*, 2017, **46**, 275.

[259] D. K. Frantz, A. Linden, K. K. Baldridge and J. S. Siegel, *J. Am. Chem. Soc.*, 2012, **134**, 1528.

[260] D. Rota Martir, G. J. Hedley, D. B. Cordes, A. M. Z. Slawin, D. Escudero, D. Jacquemin, T. Kosikova, D. Philp, D. M. Dawson, S. E. Ashbrook, I. D. W. Samuel and E. Zysman-Colman, *Dalton Trans*, 2016, **45**, 17195.

[261] A. F. Henwood and E. Zysman-Colman, *Chem. Commun.*, 2017, **53**, 807.

[262] K. Suzuki, A. Kobayashi, S. Kaneko, K. Takehira, T. Yoshihara, H. Ishida, Y. Shiina, S. Oishi and S. Tobita, *Phys. Chem. Chem. Phys.*, 2009, **11**, 9850.

[263] S. Kohlmann, S. Ernst and W. Kaim, *Angew. Chem. Int. Ed.*, 1985, **24**, 684.

[264] R. Ghosh and D. K. Palit, *Phys. Chem. Chem. Phys.*, 2014, **16**, 219.

[265] S. Goswami, D. Sengupta, N. D. Paul, T. K. Mondal and S. Goswami, *Chem. Eur. J.*, 2014, **20**, 6103.

[266] S. Patra, B. Sarkar, S. Maji, J. Fiedler, F. A. Urbanos, R. Jimenez-Aparicio, W. Kaim and G. K. Lahiri, *Chem. Eur. J.*, 2006, **12**, 489.

[267] S. Roy, I. Hartenbach and B. Sarkar, *Eur. J. Inorg. Chem.*, 2009, **2009**, 2553.

[268] F. Huang, Y. Wu, D. Gu and F. Gan, *Thin Solid Films*, 2005, **483**, 251.

[269] F. Huang, Y. Wu, D. Gu and F. Gan, *Materials letters*, 2004, **58**, 2461–2465.

[270] W.-B. Yu, Q.-Y. He, H.-T. Shi, Y. Pan and X. Wei, *Dalton Trans.*, 2014, **43**, 12221.

[271] G. Albertin, S. Antoniutti, M. Bortoluzzi, J. Castro-Fojo and S. Garcia-Fontán, *Inorg. Chem.*, 2004, **43**, 4511.

[272] W. Kaim, *Coord. Chem. Rev.*, 2001, **219**, 463.

[273] S. Kume and H. Nishihara, *Dalton Trans.*, 2008, 3260.

[274] T. Yutaka, I. Mori, M. Kurihara, J. Mizutani, N. Tamai, T. Kawai, M. Irie and H. Nishihara, *Inorg. Chem.*, 2002, **41**, 7143.

[275] S. Baksi, D. K. Seth, H. Tadesse, A. J. Blake and S. Bhattacharya, *J. Organomet. Chem.*, 2010, **695**, 1111.

[276] R. Acharyya, F. Basuli, R.-Z. Wang, T. C. Mak and S. Bhattacharya, *Inorg, Chem.*, 2004, **43**, 704.

[277] D. Sardar, P. Datta, P. Mitra and C. Sinha, *Polyhedron*, 2010, **29**, 3170.

[278] J. L. Pratihar, P. Pattanayak, D. Patra, R. Rathore and S. Chattopadhyay, *Inorg. Chim. Acta*, 2011, **367**, 182.

[279] M. Panda, N. D. Paul, S. Joy, C.-H. Hung and S. Goswami, *Inorg. Chim. Acta*, 2011, **372**, 168.

[280] M. Panda, C. Das, G.-H. Lee, S.-M. Peng and S. Goswami, *Dalton Transactions*, 2004, 2655–2661.

[281] E. Baranoff, J.-H. Yum, M. Graetzel and M. K. Nazeeruddin, *J. Organomet. Chem.*, 2009, **694**, 2661.

[282] Z. Ning, Q. Zhang, W. Wu and H. Tian, *J. Organomet. Chem.*, 2009, **694**, 2705.

[283] D. Wang, Y. Wu, H. Dong, Z. Qin, D. Zhao, Y. Yu, G. Zhou, B. Jiao, Z. Wu, M. Gao and G. Wang, *Org. Electron.*, 2013, **14**, 3297.

[284] E. I. Mayo, K. Kilså, T. Tirrell, P. I. Djurovich, A. Tamayo, M. E. Thompson, N. S. Lewis and H. B. Gray, *Photochem. Photobiol. Sci.*, 2006, **5**, 871.

[285] N. Wang, J. Yu, Y. Zheng, Z. Guan and Y. Jiang, *J. Phys. Chem. C*, 2012, **116**, 5887.

[286] T. B. Fleetham, Z. Wang and J. Li, *Inorg. Chem.*, 2013, **52**, 7338.

[287] H. Zhen, Q. Hou, K. Li, Z. Ma, S. Fabiano, F. Gao and F. Zhang, *J Mater. Chem. A*, 2014, **2**, 12390.

[288] K. Hasan and E. Zysman-Colman, *Inorg. Chem.*, 2012, **51**, 12560.

[289] K. Hasan and E. Zysman-Colman, *J. Phys. Org. Chem.*, 2013, **26**, 274.

[290] K. Hasan and E. Zysman-Colman, *Eur. J. Inorg. Chem.*, 2013, **2013**, 4421.

[291] E. Baranoff, J.-H. Yum, I. Jung, R. Vulcano, M. Grätzel and M. Nazeeruddin, *Chem. Asian J.*, 2010, **5**, 496.

[292] S. Ladouceur, L. Donato, M. Romain, B. P. Mudraboyina, M. B. Johansen, J. A. Wisner and E. Zysman-Colman, *Dalton Trans.*, 2013, **42**, 8838.

[293] Y. You and W. Nam, *Chem Soc. Rev.*, 2012, **41**, 7061.

[294] A. Nakagawa, Y. Hisamatsu, S. Moromizato, M. Kohno and S. Aoki, *Inorg. Chem.*, 2013, **53**, 409.

[295] M. Qian, R. Zhang, J. Hao, W. Zhang, Q. Zhang, J. Wang, Y. Tao, S. Chen, J. Fang and W. Huang, *Adv. Mater.*, 2015, **27**, 3546.

[296] M. C. Scharber, D. Mühlbacher, M. Koppe, P. Denk, C. Waldauf, A. J. Heeger and C. J. Brabec, *Adv. Mater.*, 2006, **18**, 789.

[297] J. N. Demas and G. A. Crosby, *J. Phys. Chem.*, 1971, **75**, 991.

[298] S. Fery-Forgues and D. Lavabre, *J. Chem. Educ.*, 1999, **76**, 1260.

[299] K. Nakamaru, *Bull. Chem. Soc. Jpn.*, 1982, **55**, 2697.

[300] H. Ishida, S. Tobita, Y. Hasegawa, R. Katoh and K. Nozaki, *Coord. Chem. Rev.*, 2010, **254**, 2449.

Chapter 7

Appendix

7.1 Characterisation Data

Relevant characterisation data is contained in electronic form in a CD at the end of this thesis.

7.2 Publications and Patents Arising from Work in this PhD

1. A Comprehensive Review of Luminescent Iridium Complexes Used in Light-Emitting Electrochemical Cells (LEECs), Adam F. Henwood and Eli Zysman-Colman, in *Iridium(III) in Optoelectronic and Photonic Applications*, pp, 275 – 357.

2. Phosphorescent Platinum(II) Complexes Bearing Pentafluorosulfanyl Substituted Cyclometalating Ligands, Adam F. Henwood, James Webster, David Cordes, Alexandra M. Z. Slawin, Denis Jacquemin and Eli Zysman-Colman, *RSC Adv.*, 2017, **7**, 25566.

3. Lessons Learned in Tuning the Optoelectronic Properties of Phosphorescent Iridium(III) Complexes, Adam F. Henwood and Eli Zysman-Colman, *Chem Commun.*, 2017, **53**, 807.

4. Luminescent Iridium Complexes Used in Light Emitting Electrochemical Cells (LEECs), Adam F. Henwood and Eli Zysman-Colman, *Top. Curr. Chem.*, 2016, **374**, 1.

5. Solubilised Bright Blue-Emitting Iridium Complexes for Solution Processed OLEDs, Adam F. Henwood, Ashu K. Bansal, David B. Cordes, Alexandra M. Z. Slawin, Ifor D. W. Samuel, Eli Zysman-Colman, *J. Mater. Chem. C*, 2016, **4**, 3726.

6. Enhancing the Photoluminescence Quantum Yields of Blue-Emitting Cationic Iridium(III) Complexes Bearing Bisphosphine Ligands, Diego Rota Martir, Ashu K. Bansal, Vincent

Di Mascio, David B. Cordes, Adam F. Henwood, Alexandra M. Z. Slawin, Paul C. J. Kamer, Laura Martinez-Sarti, Antonio Pertegas, Henk J. Bolink, Ifor D.W. Samuel and Eli Zysman-Colman, *Inorg. Chem. Frontiers*, 2016, **3**, 218.

7. Luminescent Complexes and Display Devices, Adam F. Henwood and Eli Zysman-Colman, US Pat., 14, 944, 427, 2016.

8. Unprecedented Strongly Panchromic Absorption from Proton-Switchable Iridium(III) Azoimidazolate Complexes, Adam F. Henwood, Yue Hu, Muhammad T. Sajjad, Gopala Krishna V. V. Thalluri, Sanjay S. Ghosh, David B. Cordes, Alexandra M. Z. Slawin, Ifor D. W. Samuel, Neil Robertson, Eli Zysman-Colman, *Chem. Eur. J*, 2015, **21**, 19128.

9. Palladium(0) NHC Complexes: A New Avenue to Highly Efficient Phosphorescence, Adam F. Henwood, Mathieu Lesieur, Ashu K. Bansal, David G. Thompson, Duncan Graham, Alexandra M. Z. Slawin, Ifor D. W. Samuel, Catherine S. J. Cazin and Eli Zysman-Colman, *Chem. Sci.*, 2015, **6**, 3248.

10. One-Pot Synthesis of Highly Emissive Dipyridinium Dihydrohelicenes, Amedeo Santoro, Rianne Lord, Jonathan Loughrey, Patrick McGowan, Malcolm Halcrow, Adam F. Henwood, Connor Thomson, Eli Zysman-Colman, *Chem. Eur. J.*, 2015, *21*, 7035.

11. Rigid Biimidazole Ancillary Ligands as an Avenue to Bright Deep Blue Cationic Iridium (III) Complexes, Adam F. Henwood, Sloane Evariste, Alexandra M. Z. Slawin and Eli Zysman-Colman, *Faraday Discuss.*, 2014, **174**, 165.

7.3 Contributions to Conferences

1. Macrocyclic and Supramolecular Chemistry (MASC) 2016, Edinburgh, United Kingdom (15 – 16 December 2016): *Improving the Efficiency of Blue-Emitting Iridium Complexes* (Poster Presentation).

2. St. Andrews Postgraduate Symposium, St. Andrews, United Kingdom (6 – 7 December 2016): *Making Iridium Brighter* (Oral Presentation, runner up prize).

3. 6^{th} EuCHEMs Chemistry Conggress, Seville, Spain (11 – 15 September 2016): *Phosphorescent Transition Metal Complexes Bearing Pentafluorosulfanyl Substituents* (Oral Presentation).

4. Molecular Photophysics Conference, Newcastle, United Kingdom (19 April 2016): *Palladium(0) Complexes: An Underexplored Route to Efficient Phosphorescence and Applications*

to OLEDs (Poster Presentation).

5. 2nd Asian-European Symposium on Organic Electronics, Edinburgh, United Kingdom (27 – 29 October 2015): *Bright Deep Blue Iridium Complexes for Solution Processed Lighting Devices* (Oral Presentation).

6. 21st ISPPCC, Krakow, Poland (5 July – 9 July 2015): *Palladium(0) Complexes: An Underexplored Route to Efficient Phosphorescence and Applications to OLEDs* (Poster Presentation).

7. 5st EuCHEMs Chemistry Congress, Istanbul, Turkey (31 August – 4 September 2014): *Rigid Biimidazole Ancillary Ligands as an Avenue to Bright Deep Blue Cationic Iridium(III) Complexes* (Oral Presentation).